# Microstructure, Thermal Stability and Consolidation of Nanostructured and Ultrafine Structured Cu based Metal Matrix Composite and Alloy Powders Produced by High Energy Mechanical Milling

A thesis submitted in fulfilment of the
requirements for the degree of

**Doctor of Philosophy**

in Materials and Process Engineering

at

**The University of Waikato**

by

**Aamir Mukhtar**

---

**The University of Waikato**
**2010**


THE UNIVERSITY OF
WAIKATO
*Te Whare Wānanga o Waikato*

**To my Father**

## *Abstract*

Ultrafine grained and/or nanostructured Cu and Cu-(2.5-10)vol.%$Al_2O_3$ composite balls/granules/powder particles were produced using two high energy mechanical milling (HEMM) routes respectively. The microstructural evolution of the as-milled Cu and Cu-$Al_2O_3$ composite balls/granules/powder particles produced using Route 1 (12hours) and Route 2 (Route 1 + 12 hours milling under another condition) of milling was studied using scanning electron microscopy (SEM), transmission electron microcopy (TEM), scanning transmission electron microscopy (STEM) and energy dispersive X-ray (EDX) mapping. The study confirmed that HEMM can be effectively used to disperse (2.5-10)vol.%$Al_2O_3$ nanoparticles into a ultrafine grained or nanocrystalline Cu matrix after both routes of milling.

The as-milled Cu and Cu-$Al_2O_3$ composite balls/granules/powder particles were heat treated at 150, 300, 400 and 500°C for 1 hour, respectively, to determine the thermal stability of the microstructure and corresponding microhardness change as a function of annealing temperature. It was found that for Cu and Cu-2.5vol.%$Al_2O_3$ composites after heat treatment at 150°C, the Cu grain sizes decreased due to recrystallisation, and increasing the annealing temperature to 300°C causes slight coarsening of the Cu grains. Further increasing the annealing temperature to 500°C caused significant coarsening of the Cu grains and the $Al_2O_3$ nanoparticles. With increasing the volume fraction of $Al_2O_3$ nanoparticles, (i) the thermal stability of the Cu-$Al_2O_3$ composite increases, (ii) the microstructure of the Cu matrix became finer, and (iii) the coarsening of Cu grains in the composite powder particles after annealing at 500°C become less severe.

The average microhardness of the Cu-$Al_2O_3$ composites decreased after annealing at 150°C due to decrease of dislocation density, then remained almost unchanged with increasing the annealing temperatures to 300°C and 400°C. Further increasing the annealing temperature to 500°C caused significant decrease in average microhardness due to reduction in dislocation density and grain coarsening, suggesting that Cu-$Al_2O_3$ composites are thermally stable at temperatures up to 400°C.

Pure copper powder and Cu-$Al_2O_3$ composite powders produced using Route 2 were compacted by hot pressing at 350°C followed powder compact forging. Increasing the volume fraction of $Al_2O_3$, the average microhardness increased for the forged Cu-$Al_2O_3$ composites. A decrease in tensile fracture strength was examined for the Cu-$Al_2O_3$ composites with the increase of the volume fraction of $Al_2O_3$ as 2.5% to 10%.

Nanostructured Cu-(1-4)at.%Pb alloy powder particles were produced using Route 1 of high energy mechanical milling. The microstructural evolution and thermal stability of microstructure of powder particles as a function of annealing temperature were examined. It was found that heat treatment at 150°C caused slight coarsening of the Cu grains, and increasing the annealing temperatures to 300 and 500°C caused significant coarsening of the Cu grains. The average microhardness of the Cu-Pb alloy powder particles decreased after annealing at 150°C due to decrease of dislocation density, and then remained almost unchanged with increasing the annealing temperature to 300°C. Further increasing the annealing temperatures to 400°C and 500°C caused significant decrease in average microhardness due to reduction in dislocation density and grain coarsening, suggesting that Cu-Pb alloy powders are thermally stable at temperatures up to 300°C.

# *List of Publications*

**1**. A. Mukhtar, D.L. Zhang, C. Kong and P. Munroe, "Effect of Composition on the Morphology and Hardness of Nanostructured Cu based Composite and Alloy Powders/Granules Produced by High Energy Mechanical Milling", *Advanced Materials Research*, Vols. **29-30**, 2007, 143-146.

**2**. A. Mukhtar, D.L. Zhang, C. Kong and P. Munroe, "Variation in Hardness of Ultrafine Grained Cu-$Al_2O_3$ Composite Hollow Balls and Granules Produced by High Energy Mechanical Milling", *Materials Forum*, Vol. **32**, 2008, 105-109.

**3.** A. Mukhtar, D.L. Zhang, C. Kong and P. Munroe, "Microstructural Stability and Microhardness of Ultrafine Grained and Nanostructured Cu-5vol.%$Al_2O_3$ Composite Lumps/Powders Produced by High Energy Mechanical Milling", *Proc. International Conference on Nanoscience and Nanotechnology*, 2008, 59-62.

**4.** D.L. Zhang, A. Mukhtar, C. Kong and P. Munroe, "Synthesis and Thermal Stability of Cu-(2.5-10)vol.%$Al_2O_3$ Nanocomposite Powders by High Energy Mechanical Milling", *Journal of Physics : Conference Series*, Vol. **144**, 2009, 012028.

**5.** A. Mukhtar, D.L. Zhang, C. Kong and P. Munroe, "Thermal Stability and Microhardness of Cu-10vol.%$Al_2O_3$ Nanocomposite Produced by High Energy Mechanical Milling", *Journal of Physics : Conference Series*, Vol. **144**, 2009, 012082.

**6.** A. Mukhtar, D.L. Zhang, C. Kong and P. Munroe, "Microstructural Evolution during High Energy Mechanical Milling and Heat Treatment of Cu-(5,10)vol.% $Al_2O_3$ Nanocomposite Powders", *International Journal of Modern Physics B*, Vol. **23**, 2009, 1789-1795.

**7.** A. Mukhtar, D.L. Zhang, C. Kong and P. Munroe, "Microstructure and Thermal Stability of Nanostructured Cu-7.5vol.%$Al_2O_3$ Composite Powders Produced by High Energy Mechanical Milling", *Materials Science and Engineering : Conference series*, Vol. **4**, 2009, 012005.

**8.** A. Mukhtar, D.L. Zhang, C. Kong and P. Munroe, "Effect of Processing Condition and Composition on the Microhardness of Cu-$Al_2O_3$ Nanocomposite Powders Particles Produced by High Energy Mechanical Milling", *International Journal of Modern Physics B*, in press

## *Acknowledgements*

I would like to thank my chief supervisor Prof Deliang Zhang, whose guidance, encouragement and future vision during this PhD study has kept me motivated and focused. I would like to extend my grateful thanks to associate supervisor Dr. Brian Gabbitas for providing advice when I needed.

I would like to extend my appreciation to Prof Paul Munroe and Dr. Charlie Kong, University of New South Wales, Sydney, for their collaboration during my PhD study, all of which made an important contribution to finish this project.

Special thanks to my father, wife and kids for their patience and moral support during my PhD study. Undertaking and completing this research project was possible because of the assistance from a number of people, so I would like to take this opportunity to express my gratitude and organise them for their individual roles :

- Prof Janis Swan, Mary Dalbeth and Cheryl Ward for their administrative support,
- Brett, Helen, Paul, Yuanji, Brian, Chris and Allan for their technical support,
- Dr. Hongbao Yu and Bhupinder Singh for their assistance during experiments,
- Metal group including Dr. Peng Cao, Stella, Vijay, Asma, Maslayti and Tasnim for their full cooperation.

Many thanks to Prof Brian Cantor, University of York, UK, Prof Enrique Lavernia, University of California, USA, Prof David St John, University of Queensland, Australia, Prof Jun Shen, Harbin Institute of Technology, China, Prof Yuyong Chen, Harbin Institute of Technology, China, Dr Terry Lowe, Los Alamos National Laboratory, USA, Prof Ian Brown, Industrial Research Limited, New Zealand, Prof Claude Esling, Université de Metz, France, Prof Kee Do Woo, Chonbuk National University, South Korea, Prof. Werner Skrotzki, Technical University, Germany and Dr. Zbigniew Pedzich, AGH University of Science and Technology, Poland for helpful discussions and communications.

# *Table of Contents*

# *List of Figures*

# *List of Tables*

## Abbreviations

| | |
|---|---|
| CMC | Ceramic matrix composite |
| HEMM | High energy mechanical milling |
| HIP | Hot isostatic pressing |
| HVAF | High velocity air fuel |
| JCPDS | Joint Committee on Powder Diffraction Standards |
| MA | Mechanical alloying |
| MMCs | Metal matrix composites |
| MMCNs | Metal matrix nanocomposites |
| nc | Nanocrystalline |
| NsM | Nanostructured materials |
| PM | Powder metallurgy |
| SPD | Severe plastic deformation |
| SADP | Selected Area Diffraction Pattern |
| SPS | Spark plasma sintering |
| UFG | Ultrafine grained |
| UTS | Ultimate tensile strength |

# Chapter One

# Introduction and Literature Review

## 1.1 Introduction

Nanocrystalline metals and alloys and nanocomposites (grain sizes and particle sizes < 100 nm) have the potential of revolutionising the performance of traditional coarse grained metals and alloys (grain size > 1 μm) due to the dramatic enhancement of chemical, physical and mechanical properties. The properties include strength and hardness [1-7], magnetic properties [3,8,9], optical properties [10,11], catalytic properties [12] and high corrosion resistance [13]. Nanotechnology, rapidly thrusting its applications in all aspects of life including engineering and medicine, is the creation of new materials, devices and systems at the molecular level. Back in 1959 at California Institute of Technology Nobel prize laureate, Richard Feynman, predicted that there is plenty of room to investigate at the bottom of the material size scale. The term nanotechnology refers broadly to the use of materials with nanoscale dimensions, a size range from 1 to 100 nm. Since the grain (or particle) sizes are so small, a significant volume of the microstructure in nanostructured materials (NsM) is composed of interfaces, mainly grain boundaries and interphase boundaries, which mean that a large volume fraction of the atoms resides in the grain boundaries or interphase boundaries.

In the last two-three decades, nanostructure science and technology has become one of the most rapidly growing research areas in the field of materials science and engineering partly due to the pioneering work of Gleiter and coworkers in early 1980's [14], who synthesized NsM by consolidation of powders. NsM include powders, layered (lamellar) films, wires or tubes and bulk materials [15]. Nanomaterials and most of the applications derived from them are still in an early stage of technical development. There are several issues that remain to be addressed before nanomaterials will become useful for industrial sectors. These issues include synthesis of high purity materials economically and environment friendly, characterization of the new structures and properties and fabrication of fully dense and fully bonded products from nanostructured powders or

nanopowders without losing the nanostructure [16]. Recent developments in science have advanced capabilities to fabricate and control material systems at nanometer scale [17]. Fabrication technology can strongly affect the microstructures of the materials, thus innovation for manufacturing of free-standing parts and composites with retained nanostructure remains a challenge. Although substantial progress has been made in understanding the structure-property relationships in nanomaterials, further progress is needed in the field to address the issues mentioned above.

We chose to study Cu-$Al_2O_3$ metal matrix composite because this material has a potential to offer high strength, good ductility and high electrical and/or thermal conductivity, which are ideal for applications in making resistance welding electrodes, electrical switches and microwave and x-ray components. High electrical and thermal conductivity of the Cu phase and high strength and high thermal and chemical stability of the $Al_2O_3$ phase are combined to produce nanostructured Cu-$Al_2O_3$ metal matrix composites. Thus nanostuctured Cu-$Al_2O_3$ composites have the potential to offer both high strength and high electrical conductivity. In order to achieve high fracture toughness and low processing cost, the $Al_2O_3$ phase in the microstructure should be in particulate form, and the particle size should be small.

High energy mechanical milling (HEMM) was used to prepare nanostructured Cu-based composite/alloy powders in this research, using $Al_2O_3$ nanoaprticles as ceramic reinforcement. Although HEMM is one of the most widely used techniques for processing metal matrix nanocomposites with a dispersion of ceramic nanoparticles such as $Al_2O_3$ nanoaprticles in a ductile metal matrix such as Cu, there has been no systematic study on the microstructural evolution of the nanocomposite powder particles during milling. Since the ultrafine and nanostructured powders need to be consolidated at elevated temperatures by thermomechanical processing, it is important to understand their microstructural stability at different temperatures, which was the main objective of this research. On the other hand, since for most applications the nanocomposite powders need to be consolidated into bulk materials at elevated temperatures and the microstructures of the nanocomposite powder particles produced using nonequilibrium processes such as HEMM are metastable, it is also important to

understand the microstructural evolution of the nanocomposite powders during heat treatment at different temperatures.

This thesis has seven chapters. Chapter one presents a literature review for the nanostructured metal-matrix composites, their fabrication and properties. While chapter two describes the materials used, experimental procedures and equipment required to complete this research. Chapter three presents and discusses the results of a study on the morphology, microstructural evolution and changes in microhardness for as-milled ultrafine grained (UFG) and nanostructured Cu-$Al_2O_3$ composite powder particles during the HEMM. Chapter four presents and discusses the results of a study on the thermal stability of the UFG and nanostructured Cu-$Al_2O_3$ composite powder particles. While chapter five presents and discusses the results of a study on the microstructural evolution, changes in microhardness and thermal stability of nanostructured Cu-Pb alloy powder particles. Chapter six presents the results of a preliminary study on consolidation of the UFG and nanostructured Cu-(2.5-10)vol.%$Al_2O_3$ composite powders and the mechanical properties of the consolidated materials. Chapter seven summarizes the conclusions and recommendations for the future work.

## 1.2 Literature Review

### 1.2.1 Introduction

Increasing industrial demands for high temperature applications, high heat cycle resistance, high temperature gradients, high wear resistance, impact resistance, etc., require applications of new materials. Conventional metallic materials cannot resist such extreme operating conditions. They have to be replaced by new metal-matrix composite (MMC) or ceramic-matrix composite (CMC) materials. When fine ceramic or other hard particles are embedded into soft metal matrix to form MMC, the properties of the matrix materials can be substantially improved/strengthened [18-22]. The mechanical properties of MMCs can be further enhanced even with a very low volume fraction by decreasing the size of ceramic particulates and/or matrix grains from micrometer to nanometer level [23-29], termed as metal matrix nanocomposites (MMNCs). The sizes of matrix grains can be refined to submicrometer or nanometer regime using severe plastic deformation (SPD) or mechanical alloying (MA) processes [30,31].

The general microstructure of a nanocomposite, as shown in Figure 1.1, consists of nanometre sized (< 100 nm in diameter) particles dispersed throughout a matrix. Nanoparticles may be distributed within the grains, along grain boundaries or both. Nanocomposites structures, as introduced by K. Niihara [10] and shown in Figure 1.2, could sharply improve various mechanical characteristics [32].

MMNCs are most promising in producing balanced mechanical properties between nano- and micro-structured materials, for example, enhanced hardness, Young's modulus, 0.2% yield strength, ultimate tensile strength and ductility [28,33-38], due to addition of nano-sized reinforcement particles into the matrix. Recently metal matrix nanocomposites are being explored for structural applications in aerospace, automotive sectors, and other industrial applications.

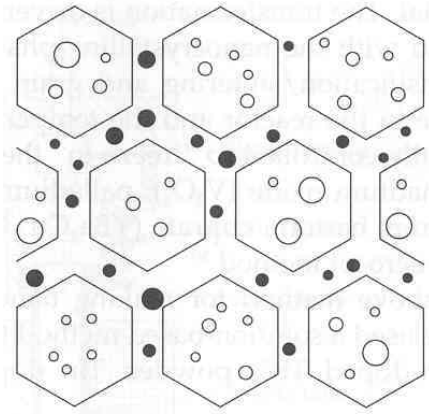

Figure 1.1: Schematic structure (not to scale) of nanacomposite [32]

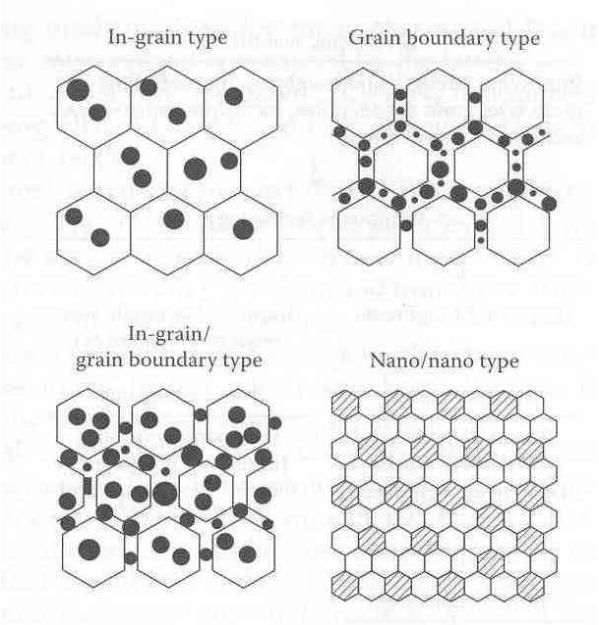


Figure 1.2: Type charts of nanocomposites [32]

Research on metal-ceramic nanocomposites is very active in international materials science and engineering community due to the potential of commercial opportunities and the challenge that this class of materials can offer [39]. There are several types of metal-ceramic nanocomposites, nanometer sized ceramic particles dispersed in a metal matrix, nanometer sized metal (or semiconductor) wires in a ceramic matrix, nanometer scaled multilayer metal-ceramic composites, and so on. Figure 1.3 illustrates the three types of metal-ceramic nanocomposites categorized by the form of nanosized phase or particles, wires or thin layers [39].

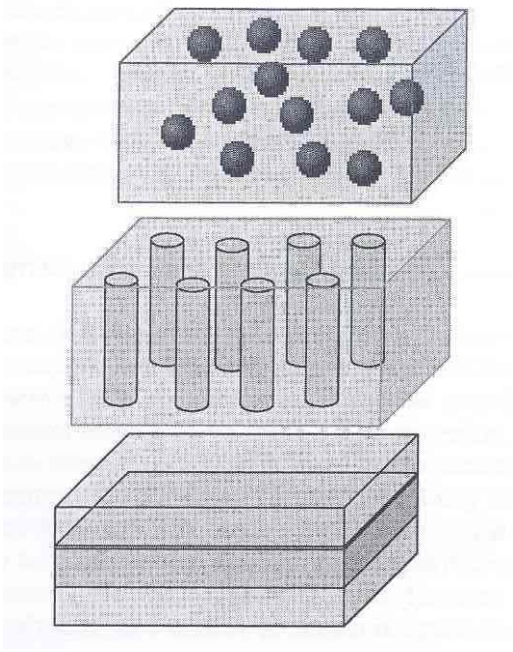

Figure 1.3: Schematic illustration of three major types of metal-ceramic nanocomposite [39], (a) nanoparticles embedded in a matrix, (b) nanowires embedded in a matrix, (c) nanometer sized multilayer thin films.

## 1.2.2 Fabrication of MMNCs

Metal matrix nanocomposites (MMNCs) can be synthesized via either ex-situ or in-situ processing routes. Ex-situ route involves the introduction of ceramic nanoparticles into metals during composite processing. Such particles are synthesized separately prior to composite fabrication. In contrast, in-situ nanoparticles synthesized by means of mechanical alloying and friction stir processing are found to distribute more uniformly in metal matrix, while this uniform dispersion of nanoparticles can lead to metal-matrix nanocomposites having enhanced mechanical strength and ductility. The fabrication of such nanocomposites could create new technological opportunities and challenges, as a strong bond between in-situ nanoparticles and metal matrix is necessary to achieve an effective load transfer mechanism in the nanocomposites. Solidification processing methods, such as stir mixing, squeeze casting and pressure infiltration are also used in the fabrication of MMNCs.

Powder blending and consolidation is one of the commonly used techniques for the fabrication of MMNCs. In this process, one of the starting powders consists of nanoparticles (usually called nanopowder). Powders of the metallic matrix and reinforcement are first blended and fed into a mold of the desired shape. Blending can be carried out dry or in liquid suspension. After blending, the mixture can also

be consolidated directly by hot pressing or hot isostatic pressing (HIP) to obtain high density. Because of the large surface area and high total surface energy associated with the nanoparticles, agglomeration is very common, and it is difficult to break up the agglomerates and disperse the nanoparticles homogenously in a metal matrix. Figure 1.4(a) shows the microstructure of a Mg-3vol.%SiC nanocomposite produced using powder blending [26]. Powder blending has also been used to produce metal-carbon nanotube composites [40] as shown in Figure 1.4(b).

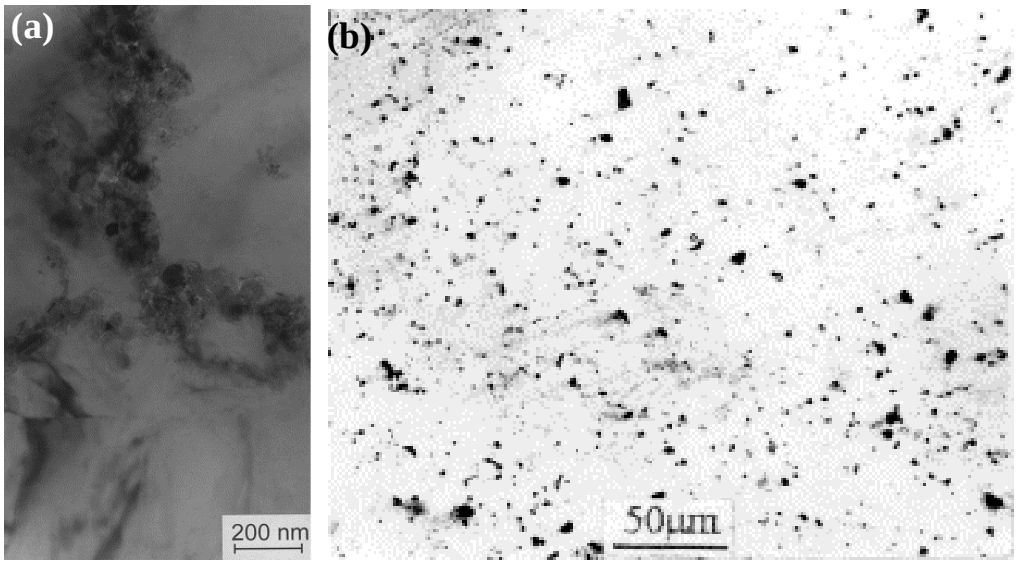


Figure 1.4: Nanocomposites produced by powder blending (a) Mg-3vol.%SiC nanocomposite [26], and (b) Optical micrograph of the nanotube/Cu [40].

Spray deposition is another technique used to synthesize MMNCs. Spray deposition methods are characterized by rapid solidification, low oxide contents and significant porosity levels. Depositions of this type are typically consolidated to full density in subsequent processing. In this process a stream of metal droplets impinges on a substrate in two distinct ways, depending on whether the droplet stream is produced from the molten bath or by continuous feeding of cold metal into a zone of rapid heat injection. Spray deposition has some advantages. They include high interface strength between particles and matrix and the interface is free of any interfacial phase, while a fine microstructure due to rapid solidification in combination with a high bonding strength between the reinforcement and the matrix can be obtained. The Al-5.5wt%Cu/$TiAl_3$ composites made by spray deposition exhibited much finer grain [41] (Figure 1.5(b)), as compared to composites fabricated by stir casting (Figure 1.5(a)).

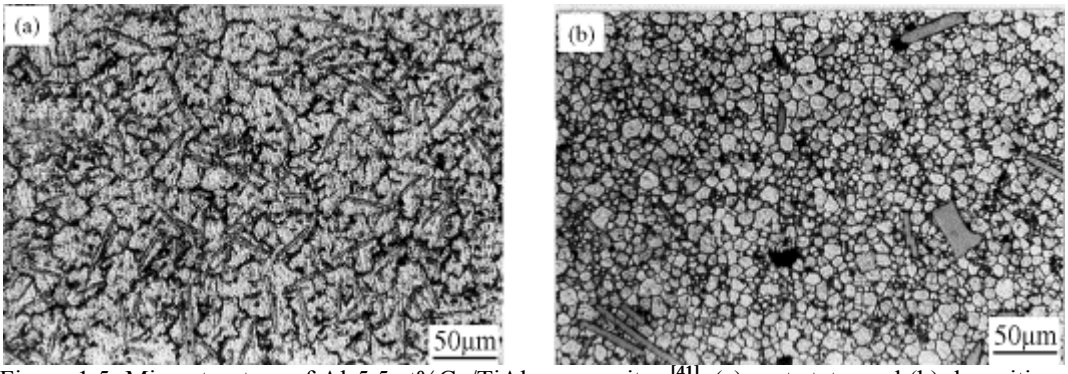


Figure 1.5: Microstructure of Al-5.5wt%Cu/$TiAl_3$ composites [41], (a) cast state, and (b) deposition state.

Squeeze casting is also used to fabricate MMNCs. In squeeze casting, a hydraulically activated ram applies a low and controlled pressure to the molten metal to attain infiltration. As infiltration is completed, a high pressure is applied to eliminate the shrinkage porosity that can occur when the liquid metal contracts as it transforms into the solid state (absence of porosity). In squeeze casting/infiltration, the metals used include aluminum, magnesium, copper and silver, while reinforcement material includes carbon, graphite and ceramics, such as carbides, oxides and nitrides. SEM micrographs (Figures 1.6(a) and 1.6(b)) show a transition zone near the interface between the SiC ceramic network and Cu matrix [42].

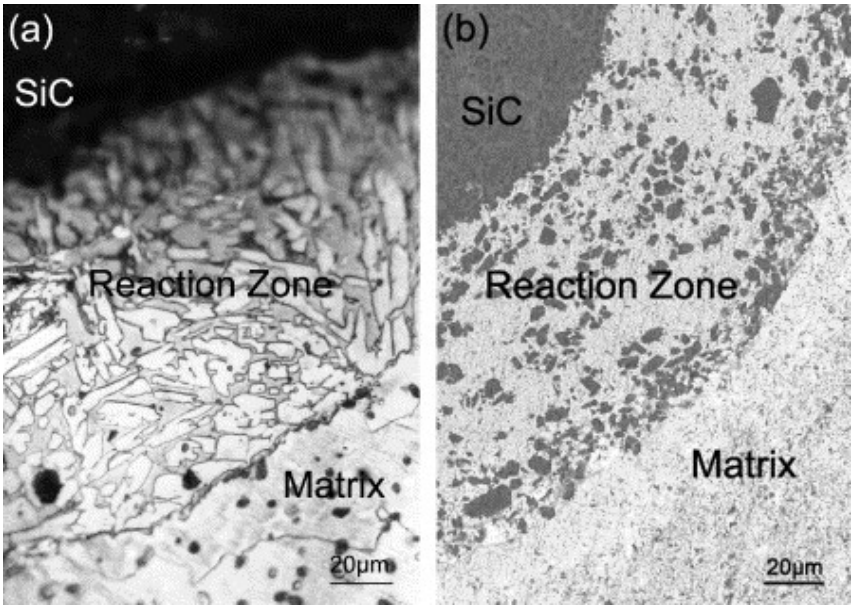


Figure 1.6: Metallographic (a) and SEM (b) morphologies near Cu-matrix composite interface [42].

Electron beam/physical vapor deposition is a prominent technique among the vapor deposition techniques for the fabrication of MMNCs. This process involves continuous passage of fiber through a region of high partial vapor pressure of the metal to be deposited, where condensation takes place so as to produce a

relatively thick coating on the fiber. Composite fabrication is usually completed by assembling the coated fibers into an array and consolidating in a hot press or HIP operation. The main advantages are that there is little mechanical disturbance of the interfacial region which may be quite significant when the fibers have a diffusion barrier layer and a wide range of alloys compositions can be used [43]. For the metal-ceramic nanocomposites, high frequency ultrasonic waves can be employed to disperse ceramic nanoparticles uniformly in molten metals [44,45]. Researchers are fabricating metal matrix nanocomposites that incorporate nanoparticles and nanotubes for structural applications, as these materials exhibit even greater improvements in their physical, mechanical and tribological properties as compared to composites with micron-sized reinforcements [26,40,46-50].

### 1.2.2.1 Fabrication of MMNC powders

With the arrival of the 21st century, powder metallurgy (PM) has emerged as technologically based industry and advanced in all sectors, while HEMM is a powder processing process in which reactant powders are milled under inert atmosphere as one of the SPD processing processes. HEMM is different from simple mechanical powder blending, even though it also often starts with a mixture of metal and ceramic powders. The principle of underlying the effectiveness of HEMM in synthesizing metal matrix nanocomposite powder involves (i) mechanical mixing of powder particles of different compositions, (ii) incorporating nanoparticles into the metal matrix through plastic deformation, fracturing and cold welding of metallic powder particles and breaking of agglomerates of nanoparticles, (iii) uniformly dispersing ceramic nanoparticles in the metal matrix in each of the powder particles again through randomly moving the nanoparticles by plastic deformation, fracturing and cold welding of the metal matrix composite powder particles. A variety of ball mills have been developed for different purposes including tumbler mill, vibratory mill, planetary mill, uniball mill, attritor mill, shaker mills, etc [51].

HEMM has been widely used in producing nanostructured powders [52-54]. Since early 1990s, HEMM has also been used to produce high quality bulk UFG and NsM from ductile powders such as Cu, Zn and Al powders [55-64]. During the HEMM, an extremely high strain rate up to ~$10^4$ $s^{-1}$ can be achieved [65]. HEMM, a simple room temperature technique with inexpensive equipment, has been

widely used to synthesize NsM by structural disintegration of coarse-grained structure as a result of SPD [66-75].

HEMM is one of the most versatile methods to fabricate MMNCs powders. Researchers have used HEMM to fabricate Cu based nanocomposite powders, such as Cu-Fe [76], Cu-Ta [77], Cu-FeC [78] and $Cu_{50}Ag_{50}$ [79] nanocomposites. For the Cu-Ta nanocomposite powders [77], it was observed that increasing the amount of Ta in the composite powder resulted in a finer crystallite size of both Cu and Ta. WC-Co nanocomposite powders [80] were prepared using high energy ball milling and with the increase of milling time nearly equiaxed nanocrystalline grains of WC were obtained. Recently Aqeeli et al. [81] developed new Al–Mg–Zr nanocomposite materials using high energy mechanical milling, and the phase evolution during milling and heat treatment of the powders was studied.

Cu-$Al_2O_3$ nanocomposite lumps/powder particles were produced [55,56,82] using HEMM and has been studied by examining changes in macrostructure and microstructure. Ying and Zhang [83] reported that HEMM in conjunction with the traditional PM process is an effective technique for producing Cu-$Al_2O_3$ metal matrix nanocomposite material with a high volume fraction (up to 20vol.%) of $Al_2O_3$ particles from Cu, Al and CuO powders. Rajkovic et al. [84,85] investigated reinforced Cu matrix with different size and amount of $Al_2O_3$ particles using high energy ball milling in air. Fine layered structure was observed in Cu-5wt.%$Al_2O_3$ composite powder particles [85] after 5 hours of milling. The same research group examined the change of Cu-3wt.%$Al_2O_3$ composite powder particles [84] morphology with increasing milling time. The size of the Cu-3wt.%$Al_2O_3$ composite powder particles increases after 3 hours of milling.

Ni and Fe powders were mixed with an $Al_2O_3$ powder to produce Fe-$Al_2O_3$ [86] and Ni-$Al_2O_3$ [87] nanocomposite powders using high energy ball milling. Nanosized Ni particles and $Al_2O_3$ particles were obtained in Ni-$Al_2O_3$ nanocomposite [87] powder particles milled for 15 hours. Microstructural evolution was investigated during HEMM of Al-5vol.%$Al_2O_3$ composite powders [88]. Figure 1.7 shows the morphology of Al-$Al_2O_3$ composite powder at different milling times. The deformation of the particles (Figure 1.7(a)) and the flake-like particles (Figure 1.7(b)) were observed.

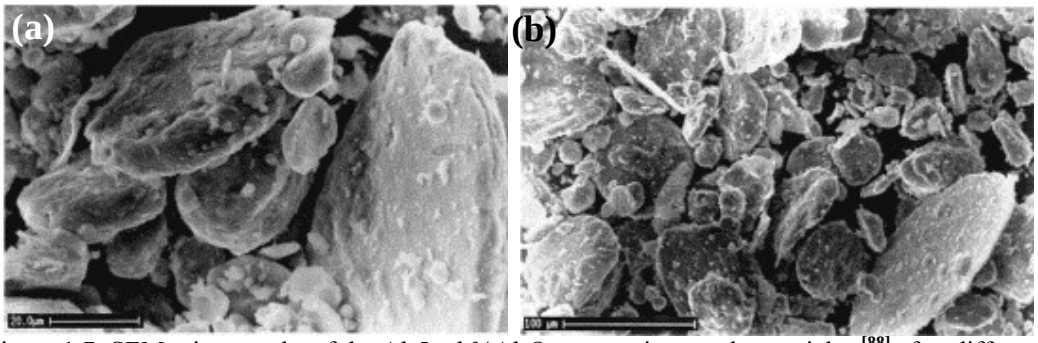


Figure 1.7: SEM micrographs of the Al-5vol.%$Al_2O_3$ composite powder particles [88] after different milling durations, (a) 8 hours, and (b) 16 hours.

To achieve desired mechanical properties of MMNCs, reinforcing nanoparticles must be distributed uniformly within metal matrix of the composites. HEMM is a well developed process for dispersing nanoparticles more uniformly in metal matrix [25,26,83,89-92] and also effective to induce in-situ nanoparticles in the composites during milling. Zhang et al [90] investigated the microstructure development of $Ti_3Al$-10vol.%SiC composite powder during milling, as shown in Figure 1.8. Ti and Al phases were heavily deformed in the early stage of milling, forming multilayer metal-metal composite structure (Figure 1.8(a)). With further milling, the irregular layered structure between Al and Ti became finer and less apparent, and the degree of incorporation of the SiC particles and the metallic phase increased significantly, as shown in Figures 1.8(b)-(d).

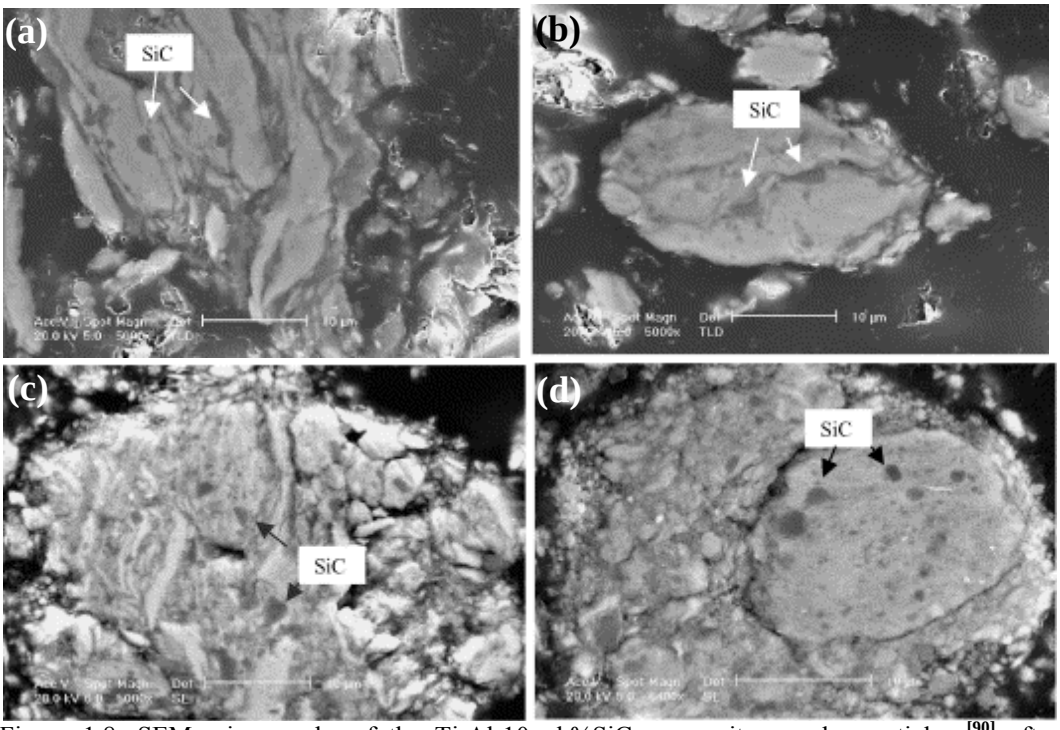


Figure 1.8: SEM micrographs of the $Ti_3Al$-10vol.%SiC composite powder particles [90] after different milling durations, (a) 2 hours, (b) 4 hours, (c) 8 hours, and (d) 16 hours.

Naser et al. [93,94] reported that nanoscaled $Al_2O_3$ powders were distributed in microscaled Cu powders by ball milling/mixer followed by uniaxially hot extrusion. Uniform distribution of commercial $Al_2O_3$ particles was observed for Cu-3wt.%$Al_2O_3$ [84] and Cu-5wt.%$Al_2O_3$ [85] composite powder mixture during milling. Mg-TiC nanocomposites [34] were prepared using HEMM with a dispersion of ultra-fine nanometer-sized TiC particles. Microstructural investigation showed that the nano-sized SiC particles had been dispersed homogeneously in the Al-5083 matrix [89] reinforced regions in the nanostructured composites synthesized via cryomilling. Ferkel and Mordike [26] investigated the microstructure and strengthening behaviour of Mg reinforced with 3vol.%SiC nanoparticles. Mg powder was mixed with SiC nanopowder, followed by ball milling and hot extrusion.

Researchers have also used mechanochemical and thermochemical methods to produce MMNCs. Cu-$Al_2O_3$ composites including nanostructured Cu-$Al_2O_3$ composite powders has been prepared using mechanochemical method [95,97]. Lü et al. [28] synthesized Mg-Al-Ti nanocomposites by mechanochemical milling of elemental powders of Mg, Al and Ti. Formation of $TiH_2$ was observed after milling and the concentration of $TiH_2$ was found to further increase after sintering. Li and coworkers [98] prepared Co-$TiO_2$ nanocomposites by mechanochemical synthesis. The microwave characteristics of the Co-$TiO_2$ nanocomposite-paraffin wax mixture were studied in the 0.1-18 GHz frequency range.

### 1.2.2.2 Consolidation of Powder Mixture and MMNC Powders

Consolidation of nanostructured powders into fully dense bulk materials is of primary interest for the development of bulk materials and near-net shape parts for technological applications. Attempts to produce and densify nanopowders started as early as 1968 [99]. All compaction techniques make use of temperature, pressure and shear. The essence of all compaction techniques is to apply high pressure for densification, and rather high temperature to soften the material so that plastic deformation allows better filling, and material flow by diffusion helps to remove the remaining porosity [100]. The diffusion processes will not only assist densification, but also allow grain coarsening to occur. As such, the temperature and time span of the consolidation process have to be adjusted carefully in order to achieve a balance between densification and grain growth. However, using high

pressure for consolidation bears the problem of cracking as the pressure is released [101-104]. At the other extreme of the temperature-pressure requirements are processes of pressureless sintering, hot isostatic pressing, or uniaxial hot pressing, where rather high temperatures are required to compensate for low pressures [102].

Consolidation of high energy mechanically milled powders is an essential process for achieving the desirable mechanical, physical and chemical properties. Mechanically milled powders, irregular in shape and heavily work hardened, have unique sintering behaviour. Therefore the consolidation of nanocomposite powders into fully dense material is very essential to keep the nanostructure of the material in order to retain the unique properties of nanostructure and ultrafine structure. Consolidation of nanocomposite powders under the applications of temperature and pressure generally can yield nearly fully dense compacts. One of the key factors in consolidating NsM is that you need diffusion to achieve atomic level bonding between powder particles, but at the same time, diffusion also causes coarsening of grains and interfacial reactions. However, recrystallization and grain-growth occur readily during high temperature consolidation, particularly those prepared from the HEMM process. Studying the materials produced by consolidation of powders, is important in the sense that it can provide vital information for understanding the process of powder consolidation by thermomechanical processing at temperatures significantly lower than the temperatures used in conventional powder extrusion and powder forging processes.

In particular forging and extrusion methods, with high pressures and shear strains are imposed at moderate temperatures to achieve good densification and interparticle bonding [105,106]. In many cases, improvements in density and particle bonding not only require optimized consolidation techniques and parameters, but also great care has to be taken with respect to clean powder handling and compaction conditions. This often requires the use of closed-loop processing or ultrahigh vacuum systems to ensure a high purity and good dynamic degassing [106]. For nanocrystalline materials, the driving force for coarsening is high, because of the high surface area, and growth can occur even at temperatures as low as room temperature [106-108]. Grain growth can be hindered by a narrow size distribution [108] and by impurities [106]. Almost any deviation from pure single-

phase material will reduce the tendency for grain growth, which includes porosity [109], second phase [110] and solute [111] drag. Hence, incorporating a significant volume fraction of fine second phase particles enables one to retain a fine grain size both during and after processing [105,112-114].

To achieve full density and minimal grain growth, the technique of hot pressing give distinct advantages in comparison to pressureless sintering. With this technique of hot pressing, near-theoretical densities and grain sizes less than 100 nm have been achieved for the mechanically alloyed powders [115-117] and nanocrystalline (nc) bulk materials [118-120]. Hot isostatic pressing (HIP) densification involves longer times and therefore grain growth is more likely to occur than in hot pressing, with final grain size in dense materials reaching almost in microns [121-123]. However after carefully controlling the HIP parameters, particularly temperature, the grain sizes of 100-300 nm were obtained in ball milled TiAl and $Ti_3Al$ [124], Fe-10wt.%Cu [125], $Si_3N_4$-SiC nanocomposites [126]. Comparing other techniques, such as HIP, hot extrusion is applied at lower temperatures as it involves high stresses. Hot extrusion has been primarily used to consolidate metal nanoparticles [127-130]. Grain sizes less than 100 nm were achieved at 1120K using 0.5 GPa stress in Ni and Fe [127].

Sinter forging has received substantial attention, both theoretically and experimentally, because the stress levels required for densification are lower than in HIP [131]. Sinter forging was very effective in achieving full or near full densities and grain sizes less than 100 nm in both ceramics [132-134] and metals [76,118,135].

Consolidation behavior of two types of nanoscale Fe powders, vacuum condensed and ball-milled was studied [136] and high hardness was reported for the ball-milled material. The mechanically alloyed Cu-1.6wt.%Li powders [137] were hot-consolidated by uniaxial hot pressing at different temperatures. Compaction at higher temperatures increases the possibility of particle melting, leading to an increase in porosity/cracking. Consolidation of a Cu-20vol.%NbC composite powder [138] produced using high energy planetary mill was systematically studied by pressing the powder at different pressures. Higher compaction pressure has increased the hardness. The NbC particles are coarse and close to the size of NbC raw material, shown in Figure 1.9(a). Hong et al [139] produced nanostructured W-

10wt.%Cu composite powders, and samples were sintered at 1450°C, showing porosity in Figure 1.9(b).

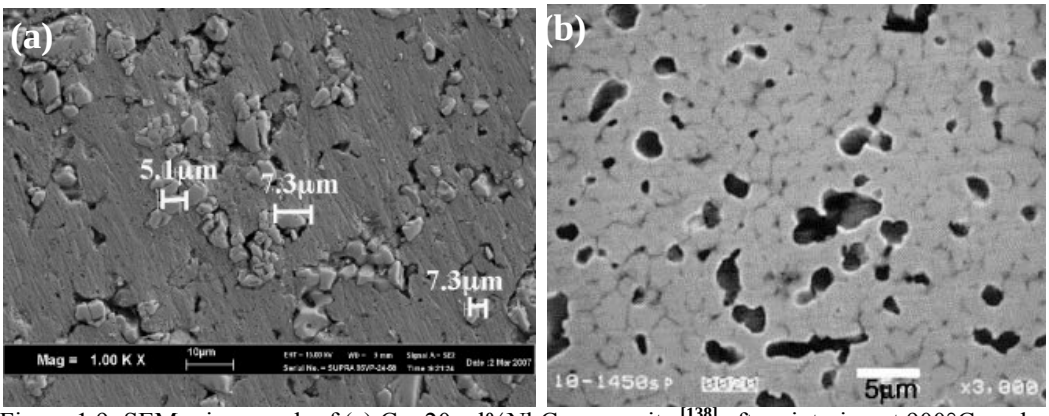


Figure 1.9: SEM micrograph of (a) Cu–20vol%NbC composite [138] after sintering at 900°C, and (b) W-20wt.%Cu composite [139] sintered at 1450°C.

Powder blending or HEMM plus powder consolidation has been widely used in preparing metal-ceramic nanocoposites [24,26,56,82,84,87,140-144]. Zhang et al. [56] demonstrated that the consolidation of the Cu-2.5vol.%$Al_2O_3$ powder by high energy ball milling which leads to formation of lumps, then by cold welding and re-shaping of the lumps into small balls, and finally by cold welding of small balls into larger balls. The two types of defects in the consolidated lumps and balls in the large balls, concentrated voids and crack-like voids, show that the material undergoes a large amount of plastic flow during the process of consolidation. The consolidation of the Cu-2.5vol.%$Al_2O_3$ powder can also been achieved by a combination of cryomilling and room temperature milling, but the consolidation process is slower due to increased hardness of the powder particles. Kleiner et al. [140] produced and consolidated an Al-$Al_3Ti$-$Al_2O_3$ nanocomposite from readily available and inexpensive aluminium powder and nanosized $TiO_2$, and obtained a fine grained and thermally stable microstructure with a controllable amount of dispersoids.

One of the most promising consolidation technologies is spark plasma sintering (SPS), a pressure assisted route whose peculiar features are a high heating rate, a low sintering temperature and a short isothermal holding at the sintering temperature. Libardi et al. [145] used SPS for the production of bulk Fe samples preserving the original microstructure. Nanostructured powders were obtained by milling of an iron powder prealloyed with 1.5wt.%Mo and by milling of the same base powder with the addition of 1.5wt.% of silica nanoparticles.

### 1.2.3 Thermal Stability of Nanostructured Metallic Materials and MMCs

Nanostructured metallic materials exhibit unique physical, mechanical and chemical properties, which are closely related to the extremely fine grain size and the large volume fraction of grain boundaries. So it is legitimate to maintain the microstructure at nanometer scale during the structural applications of NsM at elevated temperature. Thermal stability is important for consolidation of nanostructured powders which involves not only the stability of the grain structure, that is the microstructure, but also the stability of the structure of the grain boundaries in NsM. Knowledge of the thermal stability of NsM is important for both technological and scientific reasons. Looking at technological point, thermal stability is important for consolidation of nanostructured powders without coarsening the microstructure. On the other hand scientifically, it would be necessary to check whether the grain growth behaviour in NsM is similar to that in coarse-grained materials. Therefore it becomes imperative to create such NsM which are resistant to grain growth at elevated temperatures.

There are two basic ways in which grain growth can be reduced. The first one involves a kinetic approach in which the grain boundaries are pinned by various methods to decrease grain boundary mobility, which include chemical ordering, solute drag, porosity drag and second phase drag. The second is thermodynamic approach in which the driving force for grain growth is lowered by reducing the grain boundary energy and mainly depending on solute segregation. Reducing the grain boundary energy should minimize grain growth, since the driving force for grain growth is directly proportional to the grain boundary energy. Therefore the addition of the solute atoms that segregate to the grain boundaries will affect the grain boundary energy. It has been suggested that a stabilization of grain boundaries in milled materials could occur at very low grains due to decrease in grain boundary free volume, the occurrence of which was inferred from the scaling of resistivity with grain size [146].

Basically grain growth and phase transformations will alter the properties of NsM when exposed at elevated temperatures. Chen and Spaepen [147] reported that metals and compounds, exhibit a remarkable resistance to grain growth, manifested by a relatively high onset temperature of grain growth, maximum reaching as high as $0.6T_m$, (where $T_m$ is the melting temperature of pure metal in Kelvin scale).

Thermal stability of nc-Ni [148] was investigated in the temperature range of 0.2-0.45 $T_m$, and the normal grain growth was reported in the range of 0.32 and 0.34 $T_m$. Grain size of nc-Ni powders [149] prepared by cryomilling remained unchanged when annealed at 0.56 $T_m$. Chauhan and Mohamed [150] reported the thermal stability of nc-Ni and investigated that the activation energy for grain growth obtained at temperatures above 0.3 $T_m$ was significantly higher. Nanograins of commercially pure Al [151] produced by HEMM can be stabilized up to a temperature as high as 0.78 $T_m$ and grain growth was studied. The high grain size stability is considered to be due to the pinning forces arising from impurities as well as ultrafine dispersoids formed during milling process. Gleiter [14] reported that nc-Fe was thermally stable up to 0.26 $T_m$. After increasing the temperature to 0.37 $T_m$ and annealing for 10 hours, the grain size of nc-Fe increased by five times, while the material became microcrystalline when annealed at 0.42 $T_m$.

Nanograined $Cu_3Ge$ [152] produced through HEMM showed extraordinary thermal stability of grain size at 0.76 $T_m$. Nanocrystalline Mg-Al-Ti composites [153] synthesized by HEMM showed thermal stability at 0.76 $T_m$. The thermal stability of the $Cu_{47}Ti_{33}Zr_{11}Ni_8Si_1$ composite [154] powder reinforced with 25vol.% nanosized Cu was not affected upon the addition of the second phase particles. Crystallization was reported with increasing nucleation rate. Cui et al. [155] investigated the thermal stability of nanostructured NiCrC coating prepared by high velocity air-fuel (HVAF) spraying of cryomilled feedstock powders. Recrystallization and normal grain growth were observed after heat treatment at 0.55 $T_m$ for up to 100 hours. Recently, Darling et al. [156] demonstrated grain-size stability in nc Fe–Zr alloys, produced by HEMM, that extends to annealing temperatures nearing their melting points. Particle pinning, solute drag and reduction in grain-boundary energy have been proposed as stabilization mechanisms. The stabilization in Fe–Zr alloys is attributed to a reduction in grain-boundary energy due to Zr segregation.

### 1.2.4 Properties of Nanostructured Metallic Materials and MMCs

The landmark paper by Gleiter [14] redirected a new vision to the field of materials science for its global research. Grain size reduction is one of the effective ways to strengthen metals and alloys because grain boundaries act as obstacles to dislocation motion. The mechanical properties of nc metals and alloys and

nanocomposites have been studied for over a decade, and extremely high strength and hardness have been found in metals and alloys with the grain size in nm scale [2-6,157,158]. Many research groups have shown that the mechanical properties can be further enhanced by decreasing the size of particulates from micrometer to nanometer level [23-29]. Recently MMNCs are being explored for structural applications in aerospace, automotive sectors, and other industrial applications.

### 1.2.4.1 Mechanical Properties

The mechanical properties of metallic materials are influenced by grain boundaries, solute atoms, dislocations, second-phase particles, dispersoids, etc. The most measured mechanical property of NsM as a function of grain size is hardness, e.g. [159,160], and it has been shown that hardness and strength of NsM is much higher than those of the conventional grain size counterpart. Microhardness measurement of Cu-2.5vol.%$Al_2O_3$ composite lumps produced by cryomilling was slightly higher than that of the balls produced by room temperature milling [56]. Nanocomposite powders of Cu-$Al_2O_3$ [82] showed that average hardness increased for the hot pressed consolidated materials, with increasing vol.% of $Al_2O_3$**.** The hardness of the Cu-Ta nanocomposites [77] was higher than that of the Cu-Ta microcomposites. Al-$Al_3Ti$-$Al_2O_3$ nanocomposite showed a high hardness at room and elevated temperature and therefore considered to be a promising light-weight material for elevated temperature applications.

Grain size is known to have a significant effect on the mechanical behaviour of materials, in particular, on the yield stress. Weertman and coworkers [106] observed that nc Cu and Pd samples were remarkably stronger than their coarse-grained counterparts. Suryanarayana et al. [161] reported compressive yield strength of ~ 500 MPa from nc-Cu sample. Youssef et al. [61] synthesized artifact-free bulk nc-Cu samples that exhibited tensile yield strength about 11 times higher than that of conventional coarse-grained copper. The yield strength for nc $Cu_3Ge$ [152] was reported as 2 GPa, while typical nc-Cu equates to 0.77 GPa. Nanoindentation was also performed, yielding an elastic modulus of ~110 GPa. As an extreme example, the yield strength of nc-Cu (23 nm) has been found to be 22 times that of conventional grain size Cu (20 μm) [62]. A bulk nc Al-5%Mg alloy [162] showed the tensile yield strength as 620 MPa (four times that of the coarse-grained Al-5083 alloy). Recently Lavernia et al. [163] reported the yield strength of 1065 MPa for a

tri-modal composite which consists of 10% $B_4C$ particles, 50% unmilled coarse-grained 5083 Al and the balance nanostructured 5083 Al.

The tensile strength of the Al-6.5vol.%SiC nanocomposite powder [91] was 26% higher than that of nc Al-5083 without reinforcement. An ultimate tensile strength of 2332 MPa was observed in $(Cu_{60}Zr_{30}Ti_{10})_{0.95}Ta_5$ amorphous matrix composite [164]. A nc Co-Cu alloy [165] exhibited a high 0.2% proof stress of 1420 MPa and an ultimate tensile strength (UTS) of 1875 MPa. However, an UTS of 740 MPa was reported in nc Al-5%Mg alloy [162]. Zhang and coworkers [166] reported that $Al/Al_{85}Ni_{10}La_5$ nanocomposites exhibit ultrahigh compression strength, suggesting that the composite is a promising candidate material for high temperature applications.

Ductility is a property of NsM which might be predicted to be enhanced by extrapolation of its grain size dependence in conventional materials. Bohn et al. [167] predicted that extrapolation of the grain size, or the scale of the microstructure, to the nanoscale will lead to an increase in ductility. In the conventional metals with micrometer sized grains, mostly a reduction in grain size leads to an increase in ductility. Thus one should expect an increase in ductility with the reduction of the grain size to nanoscale. However, the ductility of nc metals is small for most of metals [168]. Three major sources of limited ductility in NsM were identified by Koch [169], namely: (1) artifacts from processing (e.g., pores), (2) tensile instability, and (3) crack nucleation or shear instability. One of the ways to increase the ductility is to decrease the strain hardening rate in order for the specimen to sustain more plastic strain prior to necking [170]. The work on Al-6.5vol.%SiC nanocomposite [91] showed that the existence of coarse-grained regions improves the ductility of the composite. The study on nc Al-5%Mg alloy [162] showed that a significant tensile ductility was obtained, with an elongation to failure value of 8.5%. Cheng et al. [63] showed a tensile elongation in nc-Cu to failure of 6% and with the refined microstructure, the strain rate sensitivity was increased to ~0.026.

Developing an understanding of the damage tolerance of NsM is essential for evaluating their overall usefulness as structural materials or coatings in engineering components. Many attractive features of NsM, such as high strength, high hardness, and improved resistance to wear and corrosion damage, would likely be rendered nonviable if the damage tolerance of these materials does not meet certain minimum acceptable levels for particular applications. Fracture is a

complex phenomenon of initiation and propagation of micro(nano)voids or micro(nano)cracks leading to the separation of a body into two or more parts. For NsM, , the situation is more complex. In the absence of heterogeneous nucleation sites, the scale of the fracture surfaces is, by virtue of the reduced grain size, reduced. Figures 1.10 show fractographs of nc-Ni [171] that are classified as transgranular ductile. The spacing/size of dimples, however, is considerably larger than the grain size in their specimens. Annealing at 200°C retains the dimpled structure if no dopants are present. WC-Co nanocomposites [80] showed an increase in the fracture toughness (14 $MPa.m^{1/2}$). An enhanced fracture strain of 15.3% was observed for $(Cu_{60}Zr_{30}Ti_{10})_{0.95}Ta_5$ amorphous matrix composite [164].

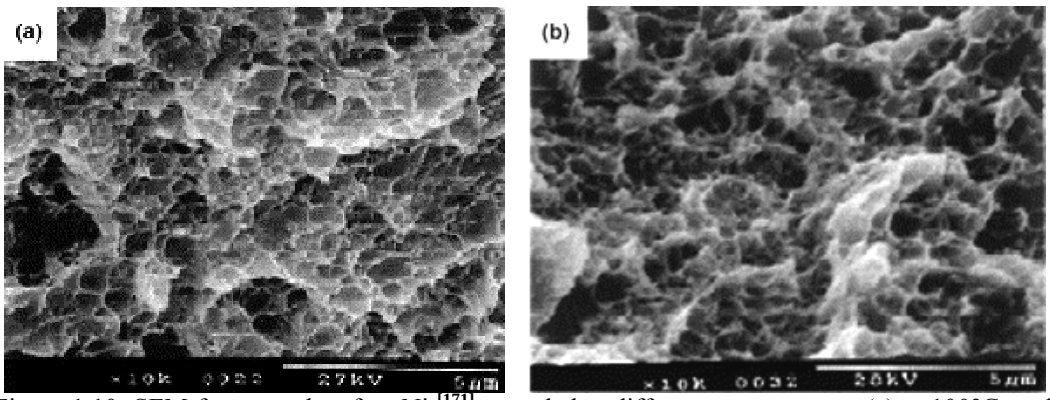

Figure 1.10: SEM fractographs of nc-Ni [171] annealed at different temperatures, (a) at 100°C, and (b) at 200°C.

NsM has shown a dramatic enhancement in strength, ductility, toughness and even superplasticity [14,172-175]. Valiev et al. [176] presented the new results on superplasticity in several nanostructured Al and Ti alloys focusing on microstructure evolution and strain hardening, as well as the challenges of their application. The results demonstrated the possibilities of new applications of superplastic forming using NsM.

### 1.2.4.2 Electrical Properties

The average value of electrical conductivity of compacts processed from Cu-5wt.%$Al_2O_3$ powders [85] was 88% IACS (International Annealed Copper Standard), which is a rather significant increase if compared with value of 60% IACS of compact processed from as-received and non-milled powders. The electrical resistivity of the Cu-Ta nanocomposites is slightly higher than that of the Cu-Ta microcomposites [77].

## 1.3 Objectives of the Study

The aim of this study is to achieve an in-depth understanding of the effects of second phase particles/ceramic nanoparticles on the microstructure and thermal stability of nanostructured Cu based composites and alloys produced by HEMM. As mechanical properties and electrical properties are critically important when metallic materials are used to make structural components, therefore it is legitimate to maintain the microstructure at a nanometer scale during the structural applications of NsM at elevated temperatures. In the present study, the Cu and Cu-$Al_2O_3$ composite powders were also consolidated and the mechanical behaviour of the consolidated samples was investigated to gain some preliminary understanding of the consolidation behaviour of the nanostructured and UFG Cu based composites.

## 1.4 References


1. H. Gleiter, *Acta Mater*., **48**, 2000, 1

2. H. Conrad, *Mater. Sci. Eng. A* **341**, 2003, 216

3. K.S. Kumar, H. Van Swygenhoven and S. Suresh, *Acta Mater.*, **51**, 2003, 5743

4. G.He, W. Löser, J. Eckert, *Acta Mater.*, **51**, 2003, 5223

5. D. Roy, R. Mitra, T. Chudoba, Z. Witczak, W. Lojkowski, H.J. Fecht and I. Manna, *Mater. Sci. Eng. A* **497**, 2008, 93

6. M.A. Meyers, A. Mishra and D.J. Benson, *Prog. Mater. Sci.*, **51**, 2006, 427

7. T. Sekino, T. Nakajima and K. Niihara, *Mater. Lett.*, **29**, 1996, 165

8. A. Inoue, *Mater. Sci. Eng. A* **304-306**, 2001, 1

9. Y. Yoshizawa, S. Fujii, D.H. Ping, M. Ohnuma and K. Hono, *Mater. Sci. Eng. A* **375-377**, 2004, 207

10. K. Niihara, *J. Ceram. Soc. of Japan*, **99**, 1991, 974

11. D.N. Lambeth, E.M.T. Velu, G.H. Bellesis, L.L. Lee and D.E. Laughlin, *J. Appl. Phys.*, **79(8)**, 1996, 4496

12. S. Ozkar, G.A. Ozin, R.A. Prokopowicz, *Chem. Mater.*, **4**, 1992, 1380

13. D. Zander and U. Köster, *Mater. Sci. Eng. A* **375-377**, 2004, 53

14. H. Gleiter, *Prog. Mater. Sci.*, **33**, 1989, 223

15. C.C. Koch, *Nanostructured Materials, Processing, Properties and Applications*, 2002, Noyes Publications, NY.

16. S.C. Tjong and H. Chen, *Mater. Sci. Eng. R* **45**, 2004, 1

17. K.P. Chong, *J. Phys. and Chem. of Solids.*, **65,** 2004, 1501

18. M.R. Piggot, *Load-Bearing Fiber Composites*, 1980, Pergamon Press, Oxford.

19. R.J. Arsenault, *Mater. Sci. Eng.*, **64**, 1984, 171

20. V.C. Nardone and K.M. Prewo, *Scripta Metallur.*, **20**, 1986, 43

21. A.I. Ibrahim, F.A. Mohamed and E.J. Lavernia, *J. Mater. Sci.*, **26**, 1991, 1137

22. N. Ramakrishnan, *Acta Mater.*, **44**, 1996, 69

23. S.C. Tjong and Z.Y. Ma, *Mater. Sci. Eng. R* **29,** 2000, 49

24. Z.Y. Ma, Y.L. Li, Y. Liang, F. Zheng, J. Bi and S.C. Tjong, *Mater. Sci. Eng. A* **219**, 1996, 229

25. D.C. Jia, *Mater. Sci. Eng. A* **289**, 2000, 83

26. F. Ferkel and B.L. Mordike, *Mater. Sci. Eng. A* **298**, 2001, 193

27. Y.C. Kang and S.L. Chan, *Mater. Chem. Phys.*, **85**, 2004, 438

28. L. Lü, M.O. Lai and W. Liang, *Compos. Sci. Tech.*, **64(13-14)**, 2004, 2009

29. S.F. Hassan and M. Gupta, *Mater. Sci. Eng. A* **392**, 2005, 163

30. R.Z. Valiev, *Mater. Sci. Eng. A* **234**, 1997, 59

31. V.V. Stolyarov, Y.T. Zhu, T.C. Lowe, R.K. Islamgaliev and R.Z. Valiev, *Mater. Sci. Eng. A* **282**, 2000, 78

32. M. Schwartz, *New Materials, Processes and Methods Technology*, pg.37, 2006, Taylor and Francis, CRC Press.

33. T. Sekino and K. Niihara, *Nanostruct. Mater.*, **6**, 1995, 663

34. S. Hwang, C. Nishimura and P.G. McCormick, *Scripta Mater.*, **44**, 2001, 2457

35. F. Audebert, F. Prima, M. Galano, M. Tomut, P.J. Warren and I.C. Stone, *Mater. Trans.*, **43**, 2002, 2017

36. I. Shao, P.M. Vereecken, C.L. Chien, P.C. Searson and R.C. Cammarata, *J. Mater. Res.*, **17,** 2002, 1412

37. S.F. Hassan and M. Gupta, *Mater. Sci. Technol.*, **20,** 2004, 1383

38. X.C. Li, Y. Yang and X.D. Cheng, *J. Mater. Sci.*, **39,** 2004, 3211

39. D.L. Zhang, In. B. Cantor, ed. *Novel Nanocrystalline Alloys and Magnetic Nanomaterials*, 2005, Institute of Physics Publishing.

40. S.R. Dong, J.P. Tu and X.B. Zhang, *Mater. Sci. Eng. A* **313**, 2001, 83

41. S. Zhang, Y. Chen and Q. Li, *J. Mater. Process. Technol.*, **137,** 2003, 168

42. H. Xing, X. Cao, W. Hu, L. Zhao and J. Zhang, *Mater. Lett.*, **59,** 2005, 1563

43. L. Calliari, G. Speranza, L. Minati, V. Micheli, A. Baranov and S. Fanchenko, *App. Surface Sci.*, **255,** 2008, 2214

44. J. Lan, Y. Yang and X. Li, *Mater. Sci. Eng. A* **386**, 2004, 284

45. Y. Yang, J. Lan and X. Li, *Mater. Sci. Eng. A* **380**, 2004, 378

46. T. Kuzumaki, H. Ichinose and K. Ito, *Adv. Eng. Mater.*, **2(7)**, 2000, 416

47. V. Bhattacharya and K. Chattopadhyay, *Scripta Mater.*, **44**, 2001, 1677

48. M. Takagi, Y. Kawamura and A. Inoue, *Scripta Mater.*, **44**, 2001, 2145

49. S.I. Cha, S.N. Arshad and S.H. Hong, *Adv. Mater.,* **17(11)**, 2005, 1377

50. K.T. Kim, S.I. Cha and S.H. Hong, *Mater. Sci. Eng. A* **449-451**, 2007, 46

51. W.E. Kuhn, I.L. Friedman, W. Summers and A. Szegvari, *Powder Metullargy*, ASM Metals Handbook, Vol.**7**, pg.56, 1985, Metals Park, OH.

52. C.C. Koch, *Nanostruct. Mater.*, **2(2)**, 1993, 109

53. C.C. Koch, *Nanostruct. Mater.*, **9**, 1997, 13

54. D.L. Zhang, *Prog. Mater. Sci.*, **49(3-4)**, 2004, 537

55. D.L. Zhang, C.C. Koch, R.O. Scattergood and K.M. Youssef, *J. Metastable and Nanocryst. Mater.*, **24-25**, 2005, 639

56. D.L. Zhang, S. Raynova, C.C. Koch, R.O. Scattergood and K.M. Youssef, *Mater. Sci. Eng. A* **410-411**, 2005, 375

57. X. Zhang, H. Wang, M. Kassem, J. Narayan and C.C. Koch, *Scripta Mater.*, **46(9)**, 2002, 661

58. J.Y. Huang, Y.K. Wu and H.Q. Ye, *Mater. Sci. Eng. A,* **199(2)**, 1995, 165

59. A.M. Harris, G.B. Schaffer and N.W. Page, *Scripta Mater.*, **34(1)**, 1996, 67

60. D.Y. Ying and D.L. Zhang, *J. of Alloys and Compd.*, **311(2)**, 2000, 275

61. K.M. Youssef, R.O. Scattergood, K.L. Murty, J.A. Horton and C.C. Koch, *Appl. Phys. Lett.*, **87(9)**, 2005, 091904-1

62. K.M. Youssef, R.O. Scattergood, K.L. Murty and C.C. Koch, *Appl. Phys. Lett.*, **85(6)**, 2004, 929

63. S. Cheng, E. Ma, Y.M. Wang, L.J. Kecskes, K.M. Youssef, C.C. Koch, U.P. Trociewitz and K. Han, *Acta Mater.*, **53(5)**, 2005, 1521

64. P.A. Carvalho, I. Fonseca, M.T. Marques, J.B. Correia, A. Almeida and R. Vilar, *Acta Mater.*, **53(4)**, 2005, 967

65. D.R. Maurice and T.H. Courtney, *Metall. Trans.,* **21A**, 1990, 289

66. T. D. Shen and C.C. Koch, *Acta Mater.*, **44**, 1996, 753

67. D. Oleszak and P.H. Shingu, *J. Appl. Phys.*, **79(6)**, 1996, 2975

68. S. Hwang, C. Nishimura, P.G. McCormick, *Mater. Sci. Eng. A* **318**, 2001, 22

69. X. Zhang, H. Wang, M. Kassem, J. Narayan and C.C. Koch, *J. Mater. Res.*, **16**, 2001, 3485

70. X. Zhang, H. Wang, R.O. Scattergood, J. Narayan and C.C. Koch, *Mater. Sci. Eng. A* **344**, 2003, 175

71. K. Morsi, S. Shinde and E.A. Olevsky, *Mater. Sci. Eng. A* **426**, 2006, 283

72. Z. Liu, S. Raynova, D.L. Zhang and B. Gabbitas, *Mater. Sci. Eng. A* **449-451**, 2007, 1107

73. L. Yu. Pustov, V.V. Tcherdyntsev, S.D. Kaloshkin, E.I. Estrin, A.I. Laptev and D.V. Gunderov, *Mater. Sci. Eng. A* **481-482**, 2008, 732

74. Sh. Mukhtarov and V. Valitov, *Mater. Sci. Eng. A* **503**, 2009, 181

75. X. Liu, M.Q. Zeng, Y. Ma and M. Zhu, *Mater. Sci. Eng. A*, **506**, 2009, 1

76. L. He and E. Ma, *Nanostruct. Mater.*, **7(3)**, 1996, 327

77. T. Venugopal, K.P. Rao and B.S. Murty, *Acta Mater.*, **55(13)**, 2007, 4439

78. J.B. Correia, M.T. Marques, P.A. Carvalho and R. Vilar, *J. of Alloys and Compd.*, **434-35**, 2007, 301

79. S. Zghal, R. Twesten, F. Wu and P. Bellon, *Acta Mater.,* **50(19)**, 2002, 4711

80. M.S. El-Eskandarany, Amir A. Mahday, H. A. Ahmed and A.H. Amer, *J. Alloys Compd.*, **312**, 2000, 315

81. N. Al-Aqeeli, G.M. Suarez, C. Suryanarayana and R.A.L. Drew, *Mater. Sci. Eng. A* **480**, 2008, 392

82. S.J. Hwang and J. Lee, *Mater. Sci. Eng. A* **405**, 2005, 140

83. D.Y. Ying and D.L. Zhang, *Mater. Sci. Eng. A* **286**, 2000, 152

84. V. Rajkovic, D. Bozic and M.T. Jovanovic, *J. Mater. Process. Technol.,* **200**, 2008, 106

85. V. Rajkovic, D. Bozic and M.T. Jovanovic, *J. of Alloys and Compd.*, **459**, 2008, 177

86. P. Matteazzi and M. Alcalà, *Mater. Sci. Eng. A* **230**, 1997, 161

87. J. Li, F. Li and K. Hu, *J. Mater. Process. Technol.,* **147**, 2004, 236

88. Z.R. Hesabi, A. Simchi and S.M. Reihani, *Mater. Sci. Eng. A* **428**, 2006, 159

89. F. Tang, M. Hagiwara and J.M. Schoenung, *Mater. Sci. Eng. A* **407**, 2005, 306

90. D.L. Zhang, J. Liang and J. Wu, *Mater. Sci. Eng. A* **375**, 2004, 911

91. F. Tang, M. Hagiwara and J.M. Schoenung, *Scripta Mater.*, **53**, 2005, 619

92. M. Krasnowski and T. Kulik, *J. of Alloys and Compd.*, **448**, 2008, 227

93. J. Naser, W. Riehemann and H. Ferkel, *Mater. Sci. Eng. A* **234–236**, 1997, 467

94. J. Naser, H. Ferkel and W. Riehemann, *Mater. Sci. Eng. A* **234-236**, 1997, 470

95. P.K. Jena, E.A. Brocchi, I.G. Solórzano and M.S. Motta, *Mater. Sci. Eng. A* **371**, 2004, 72

96. F. Shehata, A. Fathy, M. Abdelhameed and S.F. Moustafa, *Mater. and Design*, **30**, 2009, 2756

97. D.W. Lee and B.K. Kim, *Mater. Lett.*, **58**, 2004, 378

98. X. Ni, J. Ma, J. Li, D. Jiao, J. Huang and X. Zhang, *J. Alloys Compd.*, **468**, 2009, 386

99. P.E.D. Morgan, *Superplasticity in Ceramics*, In. J.J. Burke, L. Norman and V. Weiss, eds. *Ultrafine Grained Ceramics,* pg.251-271, 1968, Syracuse University Press, Syracuse.

100. F.B. Swinkels, D.S. Wilkinson, E. Arzt and M.F. Ashby, *Acta Metall.*, **31**, 1983, 1829

101. E.Y. Gutmanas, L.I. Trusov, and I. Gotman, *Nanostruct. Mater.*, **4**, 1994, 893

102. R.K. Sadangi, B.H. Kear, L.E. McCandlish, *Nanostruct. Mater.*,**2**, 1993, 563

103. R.B. Schwarz, P. Kasiraj, T. Vreeland and T.J. Ahrens, *Acta Metall.*, **32**, 1984, 1243

104. M. Jain and T. Christman, *Acta Metall. Mater.*, **42**, 1994, 1901

105. D.G. Morris and M.A. Morris, *Acta. Metall. Mater.*, **39(8)**, 1991, 1763

106. P.G. Sanders, G. Fougere, L.J. Thompson, J.E. Eastman and J. Weertman, *Nanostruct. Mater.*, **8**, 1997, 243

107. R. Birringer, *Mater. Sci. Eng. A*, **117**, 1989, 33

108. V.Y. Gertsman and R. Birringer, *Scripta Metall. Mater.*, **30(5)**, 1994, 577

109. H.J. Höfler and R.S. Averback, *Scripta Metall. Mater.*, **24(12),** 1990, 2401

110. K. Boylan, D. Ostrander, U. Erb, G. Palumbo and K.T. Aust, *Scripta Metall. Mater.*, **25(12),** 1991, 2711

111. A. Michels, C.E. Krill, H. Ehrhardt, R. Birringer and D.T. Wu, , *Acta Mater.*, **47(7)**, 1999, 2143

112. K. Lu, *Nanostruct. Mater.*, **2**, 1993, 643

113. U. Grundmann, M. Heilmaier and L. Schultz, *Scripta Metall. Mater.*, **37**, 1997, 103

114. M. Heilmaier, H. Saage and J. Eckert, *Mater. Sci. Eng. A*, **239-240**, 1997, 652

115. G. Liang, Q. Meng, Z. Li and E. Wang, *Nanostruct. Mater.,* **5(6)**, 1995, 673

116. L. He and E. Ma, *Mater. Sci. Eng. A* **204**, 1995, 240

117. L. He and E. Ma, *J. Mater. Res.*, **11**, 1996, 72

118. J. Rawers, G. Slavens, D. Govier, C. Dogan and R. Doan, *Met. Mater. Trans.*, **27A**, 1996, 3126

119. R.J. Perez, B. Huang and E.J. Lavernia, *Nanostruct. Mater.*, **7(5)**, 1996, 565

120. K. Aoki, Y. Itoh, J. Park, Y. Kawamura, A. Inoue and T. Masumoto, *Intermetallics*, **4**, 1996, S103

121. S.C. Danforth, W. Symons and K.J. Nilsen, *Processing of Silicon Nitride powders,* In. J.G.P. Binner, ed. *Advanced Ceramic Processing and Technology* **1**, pg.39-71, 1990, Noyes, Park Ridge, NJ.

122. A. Kaiser, R. Vassen, D. Stöver and H.P. Buchkremer, *Nanostruct. Mater.*, **4**, 1994, 795

123. I. Borner and J. Eckert, *Mater. Sci. Forum*, **235-238**, 1997, 79

124. C. Suryanarayana, G.E Korth and F.H. Froes, *Nanostruct. Mater.*, **2**, 1993, 527

125. J.E. Carsley, W. Milligan and E. Aifantis, *Met. Mater. Trans.*, **26A**, 1995, 2479

126. A. Kaiser, R. Vassen, D. Stöver, H.P. Buchkremer, J. Förster and J. Uhlenbusch, *Nanostruct. Mater.*, **6**, 1995, 917

127. M.I. Alymov and O.N. Leontieva, *Nanostruct. Mater.*, **6**, 1995, 393

128. H. Nagahama, K. Ohtera and K. Higashi, *Phil. Mag. Lett.*, **67**, 1993, 225

129. M.A. Morris and D.G. Morris, *Mater. Sci. Eng. A* **111**, 1989, 115

130. A. Kato, A. Inoue and T. Masumoto, *Mater. Sci. Eng. A* **179-180**, 1994, 112

131. J. R. Groza, In. C.C. Koch, ed. *Nanostructured Materials, Processing, Properties and Applications*, William Andrew Publishing, 2002.

132. G. Skandan, *Nanostruct. Mater.*, **5**, 1995, 111

133. M. Uchic, P. Kurath and R.S. Averback, *Scripta Metall. Mater.*, **26**, 1992, 791

134. A.J.A. Winnubst, Y.J. He and H. Verweij, *Ceramics Intern.*, **23**, 1997, 215

135. G.R. Shaik and W.W. Milligan, *Met. Mater. Trans.*, **28A**, 1997, 895

136. Z. Livne, A. Munitz, and R.J. Fields, *Nanostruct. Mater.*, **10**, 1998, 503

137. C. Camurri, M. Ortiz, and C. Carrasco, *Mater. Characterization*, **51(2-3)**, 2003, 171

138. H. Zuhailawati and T.L. Yong, *Mater. Sci. Eng. A* **505**, 2009, 27

139. S.H. Hong, B.K. Kim and Z.A. Munir, *Mater. Sci. Eng. A* **405**, 2005, 325

140. S. Kleiner, F. Bertocco, F.A. Khalid and O. Beffort, *Adv. Eng. Mater.*, **7(5)**, 2005, 380

141. E. Arzt and P. Grahle, *Acta Mater.*, **46(8)**, 1998, 2717

142. D.L. Zhang and D.Y. Ying, *Mater. Sci. Eng. A* **301**, 2001, 90

143. T.J. Goodwinn, S.H. Yoo, P. Matteazzi and J.R. Groza, *Nanostruct. Mater.*, **8**, 1997, 559

144. M.S. El-Eskandarany, *J. Alloys Compd.*, **391**, 2005, 228

145. S. Libardi, M. Zadra, F. Casari and A. Molinari, *Mater. Sci. Eng. A* **478**, 2008, 243

146. C.E. Krill and R.Birringer, *Mater. Sci. Forum* **225**, 1996, 263

147. L.C. Chen and F. Spaepen, *J. Appl. Phys.,* **69**, 1991, 679

148. U. Klement, U. Erb, A.M. El-Sherik and K.T. Aust, *Mater. Sci. Eng. A* **203**, 1995, 177

149. J. Lee, F. Zhou, K.H. Chung, N.J. Kim and E.J. Lavernia, *Metall. Mater. Trans.* **32A**, 2001, 3109

150. M. Chauhan and F.A. Mohamed, *Mater. Sci. Eng. A* **427**, 2006, 7

151. F. Zhou, J. Lee and E.J. Lavernia, *Scripta Mater.*, **44**, 2001, 2013

152. K.A. Darling, R.K. Guduru, C.L. Reynolds Jr, V.M. Bhosle, R.N. Chan, R.O. Scattergood, C.C. Koch, J. Narayan and M.O. Aboelfotoh, *Intermetallics*, **16(3)**, 2008, 378

153. M.A. Thein, L. Lu and M.O. Lai, *Comp. Sci. Tech.,* **66**, 2006, 531

154. S. Venkataraman, E. Rozhkova, J. Eckert, L. Schultz and D.J. Sordelet, *Intermetallics,* **13(8)**, 2005, 833

155. H. Cui, K. Tao, X. Zhou and J. Zhang, *Rare Metals*, **27(4)**, 2008, 418

156. K.A. Darling, R.N. Chan, P.Z. Wong, J.E. Semones, R.O. Scattergood and C.C. Koch, *Scripta Mater.*, **59**, 2008, 530

157. F.D. Torre, H.Van Swygenhoven and M. Victoria, *Acta Mater.,* **50**, 2002, 3957

158. C.A. Schuh, T.G. Nieh and H. Iwasaki, *Acta Mater.,* **51**, 2003, 431

159. W.W. Milligan, In. I. Milne, R.O. Ritchie and B. Karihaloo eds. *Mechanical Behavior of bulk Nanocrystalline and Ultra-fine Grain Metals,* pg.529-550, 2003, Elsevier, Amsterdam.

160. D.G. Morris, ed. *Mechanical behaviour of Nanostructured Materials*, 1998, Trans. Tech. Publications, Zurich.

161. R. Suryanarayana, C.A. Frey, S.M. Sastry, B.E. Waller and W.E. Buhro, *Processing and Properties of Nanocrystalline Materials*. In C. Suryanarayana, J. Singh, F.H. Froes, Warrendale: TMS, 1996

162. K.M. Youssef, R.O. Scattergood, K.L. Murty and C.C. Koch, *Scripta Mater.*, **54(2)**, 2006, 251

163. E.J. Lavernia, B.Q. Han and J.M. Schoenung, *Mater. Sci. Eng. A* **493**, 2008, 207

164. J.C. Lee, Y.C. Kim, J.P. Ahn and H.S. Kim, *Acta Mater.*, **53**, 2005, 129

165. Y. Nakamoto, M. Yuasa, Y. Chen, H. Kusuda and M. Mabuchi, *Scripta Mater.*, **58(9)**, 2008, 731

166. Z. Zhang, B.Q. Han, D. Witkin, L. Ajdelsztajn and E.J. Lavernia, *Scripta Mater.*, **54(5)**, 2006, 869

167. R. Bohn, M. Oehring, Th. Pfullmann, F. Appel and R. Bormann, In. C. Suryanarayana et al. eds. *Processing of Nanocrystalline Materials*, pg.355-366, 1995, TMS, Warrendale, PA.

168. C.C. Koch, D.G. Morris, K. Lu and A. Inoue, *MRS Bull.,* **24**, 1999, 54

169. C.C. Koch, *Nanocryst. Mater.*, **18**, 2003, 9

170. M.W. Chen, E. Ma, K.J. Hemker, H.W. Sheng and Y.M. Wang, *Science,* **300(5623)**, 2003, 1275

171. C. Xiao, R.A. Mirshams, S.H. Whang and W. M. Yin, *Mater. Sci. Eng. A* **301**, 2001, 35

172. I.A. Ovid'ko, *Science*, **295(5564)**, 2002, 2386

173. J.R. Weertman, D. Farkas, K.J. Hemker, H. Kung, M. Mayo, R. Mitra and H. Van Swygenhoven, *MRS Bull.*, **24**, 1999, 44

174. R. Bohn, T. Haubold, R. Birringer and H. Gleiter, *Scripta Metall. Mater.*, **25(4)**, 1991, 811

175. R.W. Siegel and G.E. Fougere, eds. *Nanophase Materials*, pg.233–261, 1993, Kluwer Academic Publishers.

176. R.Z. Valiev, R.K. Islamgaliev and I.P. Semenova, *Mater. Sci. Eng. A* **463**, 2007, 2

# Chapter Two
# Materials and Experimental Procedure

Outlined in this chapter are the materials and the experimental procedures used to prepare samples and the techniques employed for analysing the samples during this research work.

## 2.1 Starting Materials

As starting materials, powders of Cu, $Al_2O_3$ and Pb were used in producing the Cu-$Al_2O_3$ composite balls/granules/powders and Cu-Pb alloy powders by HEMM. The details of the powders are shown in Table 2.1.

Table 2.1: Starting materials used in the HEMM experiments.

| Powders | Manufacturer | Purity | Particle Size |
|---|---|---|---|
| Cu | MERCK, Germany | 99.7 % | < 63 μm |
| $Al_2O_3$ | ALLIED, USA | 99.9 % | ~ 50nm |
| Pb | MERCK, Germany | 99.0 % | < 100 μm |

## 2.2 Material Preparation

### 2.2.1 High Energy Mechanical Milling

HEMM was carried out in a PM 100 Retsch Planetary ball mill (Germany), as shown in Figure 2.1(a). A hardened steel vial, as shown in Figure 2.1(b), with a cylindrical cavity of 60 mm in depth and 100 mm in diameter and stainless steel balls with different diameters (12.5 mm and 25 mm), as shown in Fig. 2.1(c), were used for the milling. A rotational speed of 400 rpm was used for the milling. The vial which contained steel balls and 100 g of powder mixture was sealed in a glove box filled with high purity argon, ($O_2$ content < 100ppm). Cu powder and Cu-$Al_2O_3$ powder mixtures with four nominal compositions: Cu-2.5vol.%$Al_2O_3$, Cu-5vol.%$Al_2O_3$, Cu-7.5vol.%$Al_2O_3$ and Cu-10vol.%$Al_2O_3$ were milled using two milling routes, respectively. In Route 1, the powder mixture, first mixed for 6 hours with a rotational speed of 100 rpm, was milled for 12 hours using 60 steel balls with a diameter of 12.5 mm. In Route 2, the 12 hours milled powder was further milled for 12 hours using 12 balls with a diameter of 12.5 mm and 6 balls with a diameter of 25 mm. In both routes, the steel ball to powder weight ratio was 5:1. Between Route 1 and Route 2,

the balls were changed in a glove box filled with high purity argon, ($O_2$ content < 100ppm). The milling process was interrupted after 6 hours to take a small amount of sample, ~ 4g, In few experiments, the Cu powder was milled with 0.6wt% of steric acid which worked as a process control agent (PCA) using Route 1 conditions.


Figure 2.1: (a) PM 100 Retsch Planetary ball mill (b) the steel vial and (c) Steel balls with diameter, 12.5 mm and 25 mm, respectively.

For preparing Cu-Pb alloy powders, Cu and Pb powder mixtures with three nominal compositions: Cu-1at.%Pb, Cu-2at.%Pb and Cu-4at.%Pb were milled. The milling was performed for up to 12 hours, using a rotational speed of 400 rpm and a ball to powder weight ratio of 5:1. The diameters of the steel balls during milling remained 12.5 mm, while the milling process was interrupted after 6 hours to take a small amount of sample, ~ 4g, for analysis. Figure 2.2 presents the flow chart for the preparation of the UFG and nanostructured Cu-$Al_2O_3$ composite samples and Cu-Pb alloy powders using two HEMM routes followed by annealing and powder consolidation experiments.

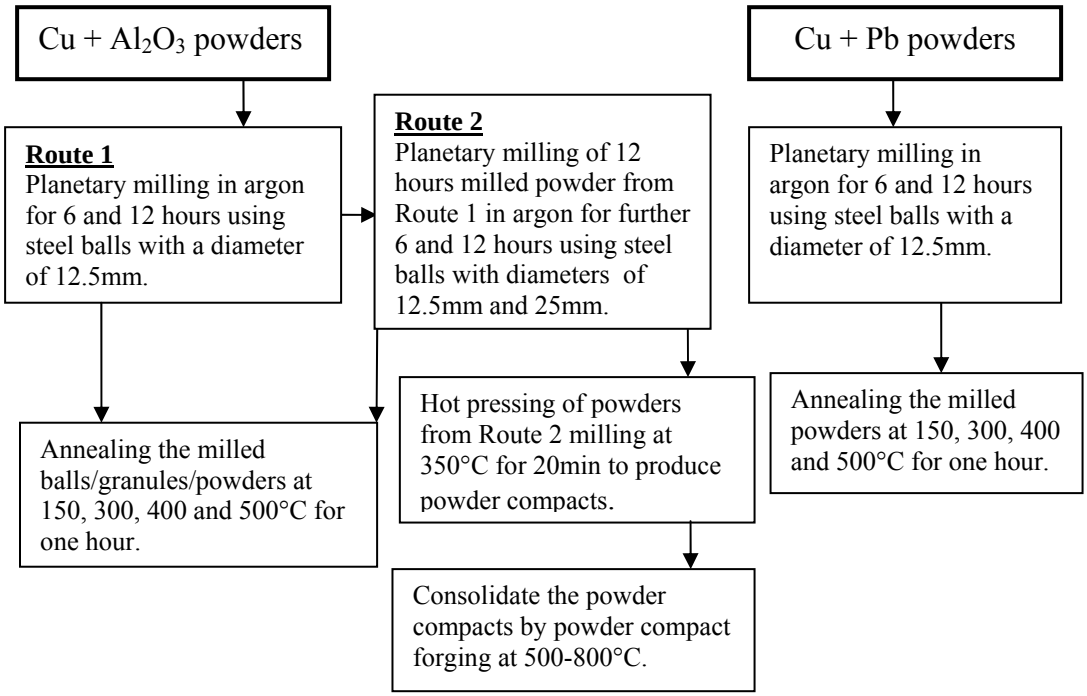


Figure 2.2: Schematic flow sheet of material preparation, annealing and powder consolidation experiments.

### 2.2.2 Heat Treatment

Heat treatment of the samples were carried out in a stainless steel vacuum tube furnace (Ceramic Engineering, Australia), as shown in Figure 2.3(a). The furnace was programmed to operate at a heating and cooling rate of 10°C/min and can be held at temperatures up to 1000°C for required duration. The as-milled samples were annealed at different temperatures in the range of 150-500°C for 1 hour with a vacuum of $10^{-6}$ mbar.

### 2.2.3 Powder consolidation

Pure copper powder and Cu-(2.5-10)vol.%$Al_2O_3$ composite powders (Route 2) were first compacted using a H13 steel die with a cylindrical cavity of 25 mm in diameter and uniaxially hot pressed at 350°C for 20 minutes under pressure of 300 MPa, using a hydraulic press, as shown in Figure 2.3(b). The Cu-(2.5-10)vol.%$Al_2O_3$ composite compacts, having a shallow hole for thermocouple, were enclosed in hydraulic press chamber, under argon atmosphere and were heated from room temperature to forging temperature (700°C/800°C) with an induction heating (coil).

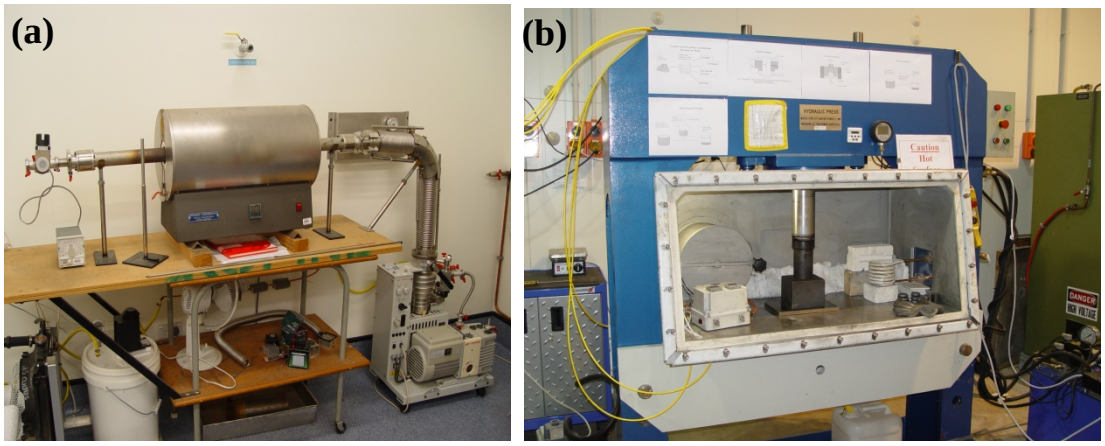


Figure 2.3: (a) Steel tube furnace used for heat treatment of Cu powder, Cu-$Al_2O_3$ composites and Cu-Pb alloys, and (b) Hydraulic press.

## 2.3 Microstructure Characterization

### 2.3.1 Sample Preparation

The as-milled and annealed ball/granule/powder samples were cold mounted in Epoxy resin and hardened for 24 hours. The resin cylinder was carefully ground using

grid 600, 1000, 2000 and 4000 SiC papers [Struers] in running water to reveal the cross section of the particles, followed by polishing using $Al_2O_3$ paste. The polished "mirror" surface of each sample was made parallel to the bottom side of the mount, so that the even height is made available for the microhardness testing, XRD analysis and microscopy examination.

### 2.3.2 Optical Microscopy

Optical microscope examination was carried out using an Olympus BX60 microscope, which was equipped with a Polariod digital camera (NIKON).

### 2.3.3 X-ray Diffractometry

X-ray diffraction of balls/granules/powder samples was performed using a Philip's X-pert system diffractometer using Cu Kα radiation (λ = 1.5406 Å), a copper single crystal monochromator and operating at 40 kV and 40 mA. The patterns were obtained using 0.03° step size averaging for 1.0 seconds per increment. Samples are scanned as powders were pressed into Al holders with sample space dimensions of 2.0 mm x 1.5 mm, with a shallow depth of 0.1 mm.

### 2.3.4 Scanning Electron Microscopy

Microstructure characterisation of Cu balls/powders, Cu-$Al_2O_3$ composite balls/ granules/powders and Cu-Pb alloy powders was carried out using a Hitachi S4700 scanning electron microscope (SEM) with an operating voltage of 20 kV. Energy dispersive x-ray analysis (EDAX) was carried out using a Kevex microanalyser attachment.

### 2.3.5 Transmission Electron Microscopy and Scanning Transmission Electron Microscopy

Specimens for TEM analyses were made in a FEI Nova xT Nanolab 200 dual beam focused in beam (FIB) microscope. Thin membranes with a cross sectional thickness of about 50 nm were cut from the embedded powder particles with a Ga ion beam operating at 30 kV, and was retrieved out of the tranch using a Kleindiek ex-situ nanomanipulator, and then deposited onto a standard 150 mesh Au grid covered with a carbon film. A Philips CM200 FEG TEM equipped with an EDAX energy

dispersive X-ray spectrum (EDS) system operating at 200 kV was used for both microstructure and compositional analyses. A weak beam current was selected to stabilize the microstructure and avoid over heating the sensitive crystal structure. The TEM specimens were prepared and examined in Electron Microscope Unit, University of New South Wales, Sydney, Australia.

### 2.3.6 Microhardness Measurements

The microhardness measurement has become an effective way to observe the behavior of the material prepared under different conditions and heat treated under different temperatures. The Vickers hardness test [1] is a static hardness test for ceramics, which employs a square-based diamond pyramid indentor with an angle 136° between opposite faces. The Vickers hardness is defined as the applied load P divided by the surface area of the indent impression as given below:

$$HV = \frac{1854.4P}{d^2} \quad \text{.....Equation 2.2}$$

where d is the mean diagonal length of indentation, μm.

The microhardness of the samples was examined using digital Vickers microindentation tester, LECO LM700, with a load of 25 gf and dwell time of 20 s. 15 indents for each sample were produced for one average microhardness measurement.

### 2.3.7 Thermal Analysis

The thermal analysis was performed in TA Instruments DSC 2920 Scanning Differential Calorimeter (DSC) under flowing argon at a rate of 50 ml/sec. The heating and cooling rates used were 20°C/min for normal examination. Cu-$Al_2O_3$ samples were heated in Cu pans, while Cu-Pb samples were heated in Al pans.

### 2.3.8 Mechanical Testing

Tensile specimens, as shown in Figure 2.4, were cut from the forged Cu-$Al_2O_3$ composite disks using CNC electric discharge machining (EDM) wire cutter (DK 77 series). The tensile specimens had a gauge length of 9 mm, and a rectangular cross-section of 2 mm in thickness and 2 mm in width with the gauge length. The tensile test specimens were tested at room temperature using an Instron 4204 testing machine with a 5 kN load cell and at a crosshead speed of 5 $mm.min^{-1}$ which was equivalent of

a strain rate of $6\times10^{-5}$ $s^{-1}$ at room temperature. All reported data were the average of at least two test results.


Figure 2.4: Tensile specimen from forged Cu-$Al_2O_3$ composite disk.

## 2.4 Reference

1. R.J. Brook, *Concise Encyclopedia of Advanced Ceramic Materials*, pg. 206-209, 1991, Pergamon Press, Oxford.

# Chapter Three

# Morphology, Microstructure and Microhardness of Cu-(2.5-10)vol.%$Al_2O_3$ Composite Balls/Granules/ Powders Produced by HEMM

## 3.1 Introduction

Mechanical milling is a complex process involving optimization of a number of process variables, such as milling time, milling atmosphere, nature and amount of processing control agent (PCA), etc, to achieve the desired powder characteristics. In this chapter, the results of a study on the effect of milling time and composition on the morphology, microstructure and microhardness of UFG and nanostructured Cu-(2.5-10)vol.%$Al_2O_3$ composite balls/granules/ powders are described. Based on SEM, TEM and STEM examination, the microstructural evolution of the materials produced by two different milling routes is studied in detail. The change in microhardness of the as-milled balls/granules/powder particles of different compositions and for different milling times and conditions was also examined.

## 3.2 Morphology

### 3.2.1 Pure Copper

Pure Cu powder was milled for up to 24 hours using two different routes of HEMM. Bulk nearly-spherical hollow balls, having a diameter in the range of 1-3 mm, were obtained after first 6 hours of milling using Route 1, as shown in Figures 3.1(a) and 3.1(c). The diameter of the hollow balls increased to the range of 1-6.5 mm after 12 hours of milling, using Route 1, as shown in Figures 3.1(b) and 3.1(d). As shown in Figures 3.1(c) and 3.1(d), hollow balls had a wall thickness in the range of 0.5-1.5 mm. With further milling using larger balls but same ball to powder ratio (Route 2) for 6 hours, the Cu hollow balls were converted into granules of sizes in the range of 1.5-3 mm in diameter, as shown in Figure 3.1(e). With further increasing the milling time to 24 hours, Cu granules were converted into Cu powder with a particle size in range of 300 μm-1.0 mm, as shown in Figure 3.1(f). On the other hand, by adding 0.6wt%PCA to the powder, the Cu powder failed to be consolidated in-situ, and the coarser Cu powder was converted into fine Cu flakes after 6 hours and 12 hours (Figure 3.1(g)) of milling, using Route 1.

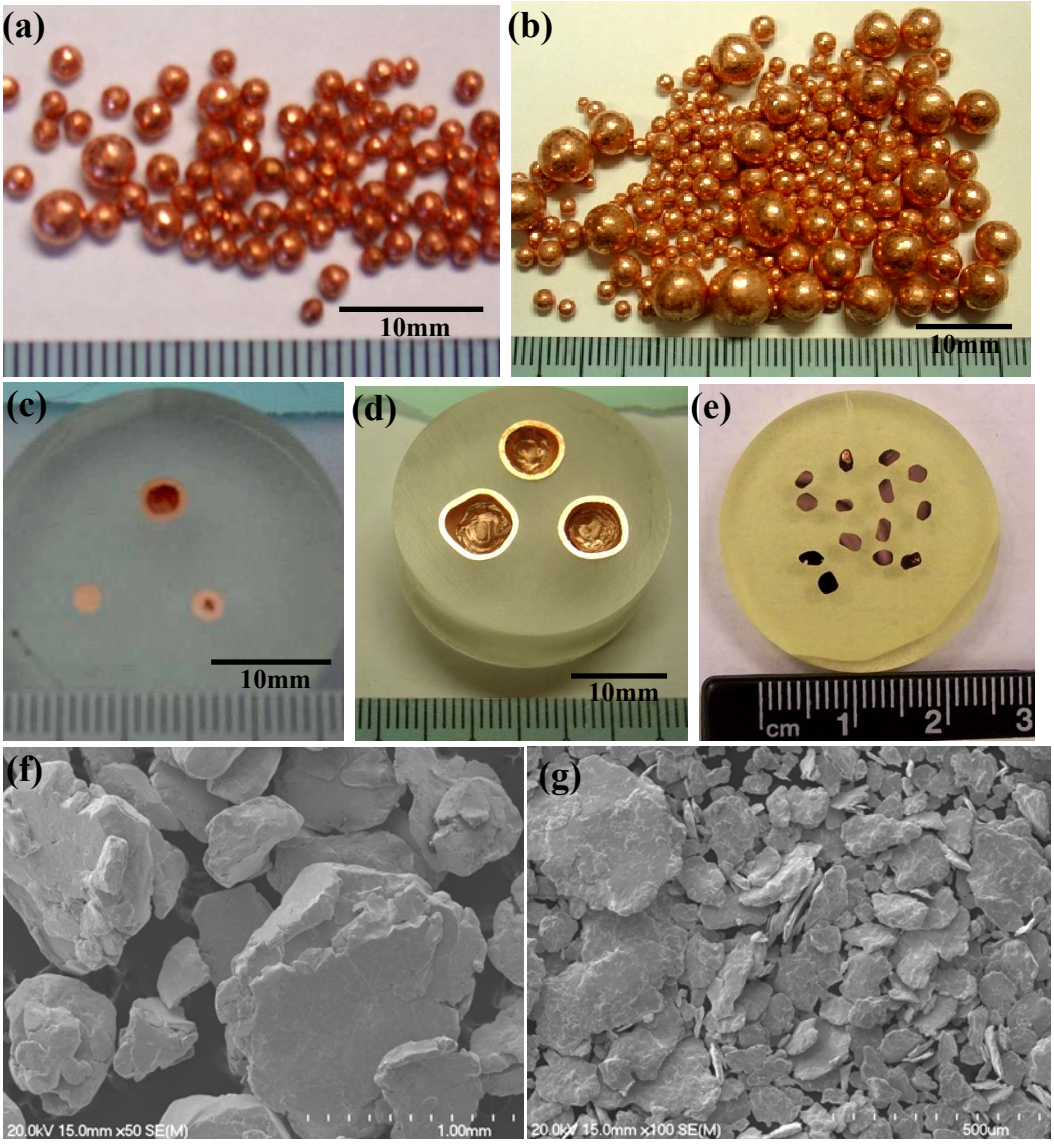


Figure 3.1: Cross section images of the bulk Cu balls/granules and SEM micrographs of Cu powder produced by HEMM using Route 1 or Route 2, (a) after 6 hours milling, Route 1, (b) after 12 hours milling, Route 1, (c) cross section after 6 hours milling, Route 1, (d) cross section after 12 hours milling, Route 1, (e) cross section after 18 hours milling, Route 2, (f) after 24 hours milling, Route 2, and (g) Cu powder with 0.6wt%PCA after 12 hours milling, Route 1.

### 3.2.2 Cu-(2.5-10)vol.%$Al_2O_3$ Composites

During the milling process, the mixture of Cu and $Al_2O_3$ powders with a composition of 2.5vol.%$Al_2O_3$ developed first into near-spherical hollow balls with a diameter in the range of 1-3mm after 6 hours of milling (Route 1), and with a diameter in the range of 1-6 mm after 12 hours of milling, as shown in Figure 3.2. The hollow balls had a wall thickness in the range of 0.5-1.5 mm. For Cu-5vol.%$Al_2O_3$ powder mixture, 6 hours of milling led to formation of granules with diameters in the range of 0.5-4.5 mm, and with further milling to 12 hours, most of the small granules joined to become larger granules, and the diameters of the granules were in the range of 1-7 mm, as shown in Figure 3.3.

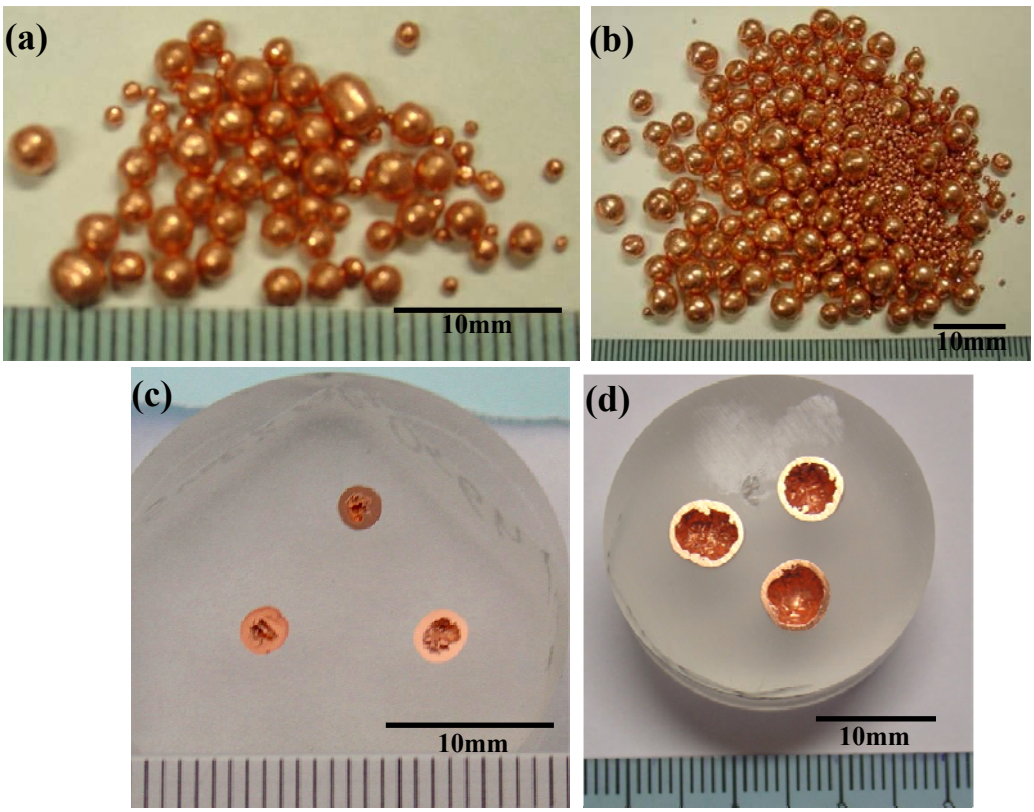


Figure 3.2: Images of the Cu-2.5vol.%$Al_2O_3$ composite balls and their cross section morphologies produced by HEMM using Route1, (a) after 6 hours milling, (b) after 12 hours milling, (c) cross section after 6 hours milling, and (d) cross section after 12 hours milling.

Cross section examination of the Cu-5vol.%$Al_2O_3$ composite granules showed some concentrated cavities and elongated voids, as shown in Figures 3.3(c)-(f). With further milling for up to 12 hours using larger balls (Route 2), the Cu-2.5vol.%$Al_2O_3$ and Cu-5vol.%$Al_2O_3$ large balls/granules produced in the 12 hours of milling using Route 1 were converted into powders with particle sizes in the range of 40-200 μm, as shown in Figure 3.4. On the other hand, with the increase of the volume fraction of $Al_2O_3$ from 5% to 7.5% or 10%, coarse powders were formed during the first 6 hours and 12 hours of milling (Route 1), as shown in Figure 3.5. These coarse powders were converted into fine powders, with further milling for 12 hours to a total time of 24 hours (Route 2), as shown in Figure 3.5. The sizes of 24 hour milled Cu-2.5vol.%$Al_2O_3$ powder particles were in the range of 40-200 μm. With the increase of the volume fraction of $Al_2O_3$ from 2.5% to 5% or 7.5%, the particle sizes decreased to the range of 40-150 μm or 25-75 μm, respectively. However, the average particle sizes of the Cu-10vol.%$Al_2O_3$ composite powder milled for 24 hours are very similar to those of Cu-7.5vol.%$Al_2O_3$ composite powder milled for 24 hours.

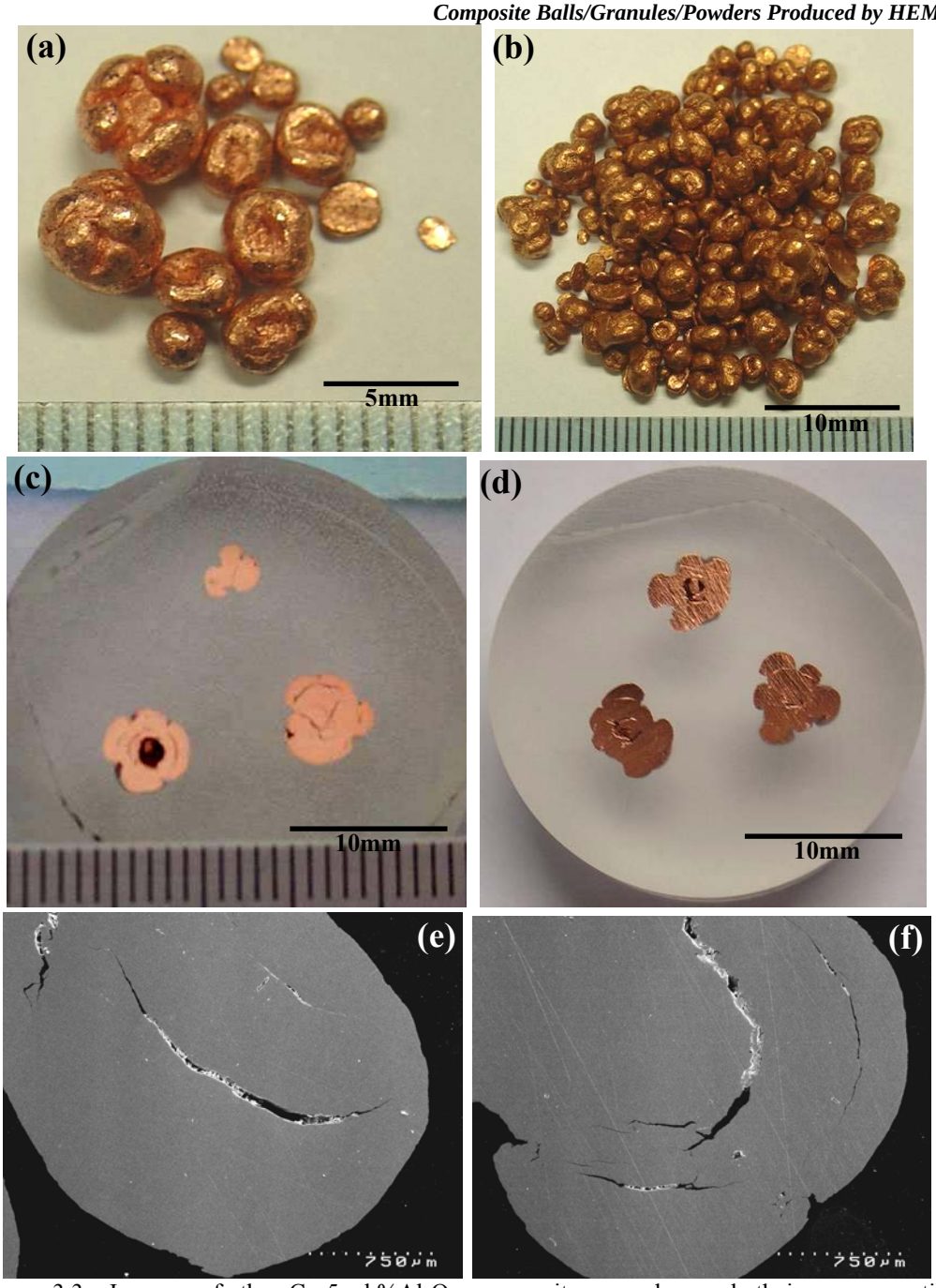


Figure 3.3: Images of the Cu-5vol.%$Al_2O_3$ composite granules and their cross section morphologies produced by HEMM using Route 1, (a) after 6 hours milling, (b) after 12 hours milling, (c) cross section after 6 hours milling, (d) cross section after 12 hours milling, (e) cross section after 6 hours milling, and (f) cross section after 12 hours milling.

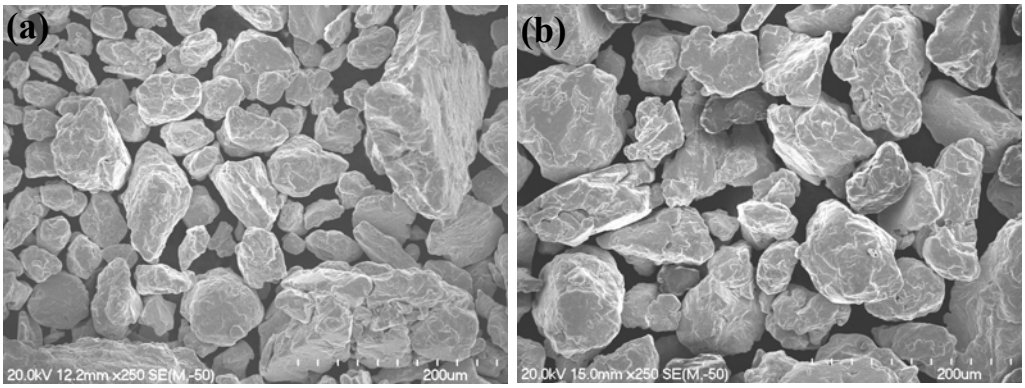


Figure 3.4: SEM micrographs of (a) Cu-2.5vol.%$Al_2O_3$ and (b) Cu-5vol.%$Al_2O_3$ composite powder particles produced by HEMM after 24 hours, Route 2.

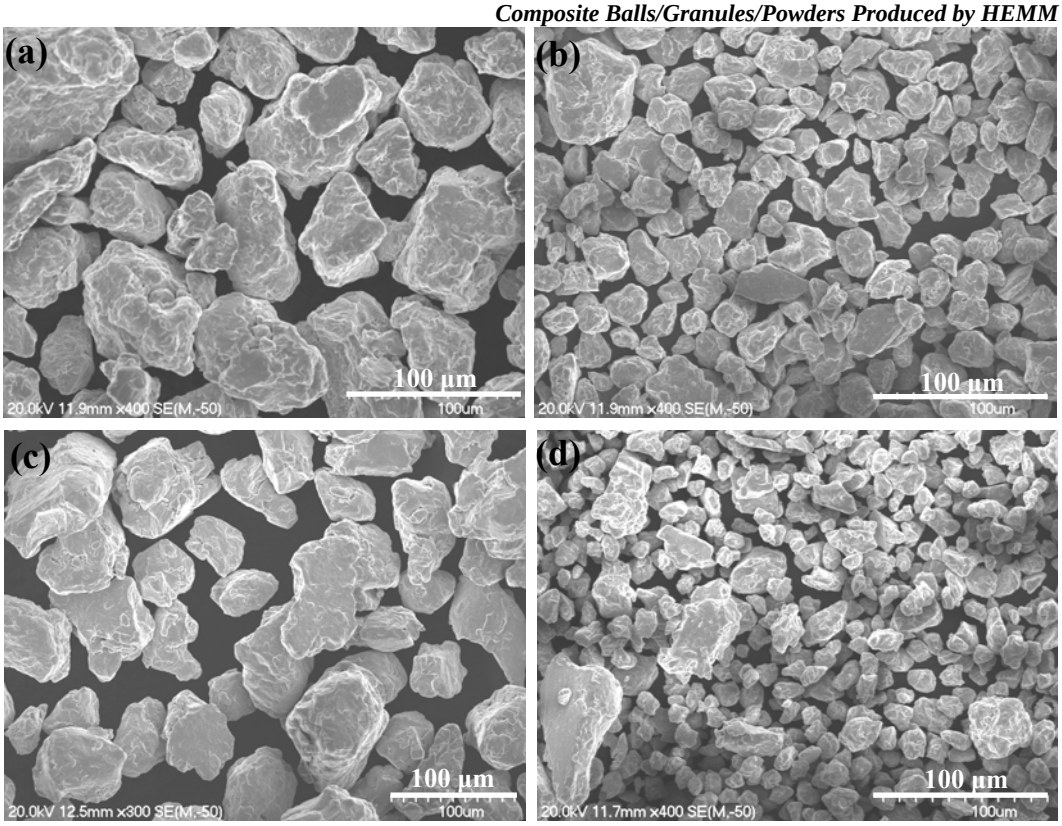


Figure 3.5: SEM micrographs of Cu-$Al_2O_3$ composite powder particles produced by HEMM, (a) Cu-7.5vol.%$Al_2O_3$ after 12 hours, Route 1, (b) Cu-7.5vol.%$Al_2O_3$ after 24 hours, Route 2, (c) Cu-10vol.%$Al_2O_3$ after 12 hours, Route 1, and (d) Cu-10vol.%$Al_2O_3$ after 24 hours, Route 2.

# 3.3 Microstructural Evolution during HEMM

## 3.3.1 Pure Copper

Figure 3.6 shows the XRD patterns of as-milled Cu hollow balls/powder produced by HEMM with different milling times using Route 1 and Route 2, respectively. It was observed from the broadening of the XRD peaks that the grain size clearly decreased after 18 hours of milling. Estimated grain sizes of Cu hollow balls and powders were determined using Scherrer equation [1], as given below :

$$d = \frac{0.9\lambda}{\beta Cos\,\theta} \quad \text{.....Equation 3.1}$$

where β is the full-width of the peak at half maximum intensity, $\lambda$ the wavelength of the X-ray used, $d$ the estimated grain size and $\theta$ the Bragg angle. Based on Scherrer equation, the estimated grain sizes of the 12 hours milled Cu hollow balls and 24 hours milled Cu powder particles were ~ 70 nm and 48 nm, respectively.

The average grain sizes and lattice strains of Cu hollow balls and powders were determined using the Williamson-Hall method [2]. According to Williamson-Hall method, $\frac{\beta Cos\theta}{\lambda}$ and $\frac{\xi Sin\,\theta}{\lambda}$ have a linear relationship expressed by the following equation :

$$\beta Cos\ \theta = \frac{0.9\lambda}{d} + \xi Sin\ \theta \quad \text{.....Equation 3.2}$$

where β is the full-width of the peak at half maximum intensity, $\lambda$ the wavelength of the X-ray used, $d$ the average grain size, $\theta$ the Bragg angle and $\xi$ the average strain. As an example, Figure 3.7 shows the $\frac{\beta Cos\theta}{\lambda}$ vs $\frac{Sin\,\theta}{\lambda}$ data points for the Cu balls produced after 6 hours and 12 hours of milling respectively. Based on this estimation, the average grain sizes of the 12 hours milled Cu hollow balls and 24 hours milled Cu powder particles were ~ 235 nm and 120 nm, respectively, and their lattice strains were 0.391% and 0.581%, respectively, as shown in Figures 3.8(a) and 3.8(b)). The average grain size showed a decreasing trend with the increase of milling hours for the Cu balls/powder particles, as shown in Figure 3.8(a). However a significant increase in lattice strain was observed for Cu powder particles produced after 24 hours, Route 2, as shown in Figure 3.8(b).

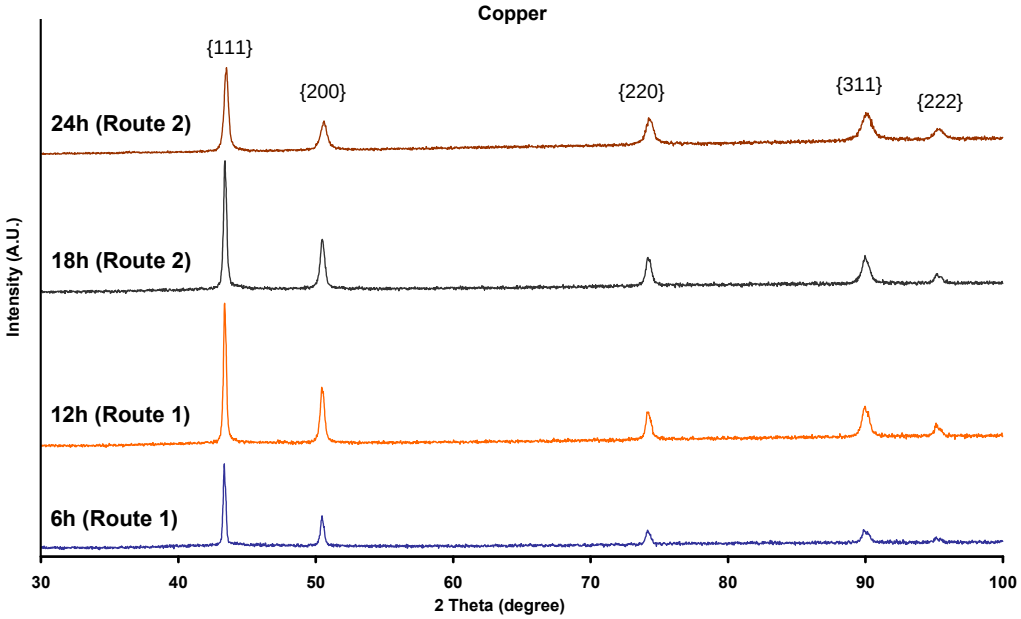


Figure 3.6: X-ray diffraction patterns of as-milled Cu hollow balls/powder produced by HEMM with different milling times using Route 1 and Route 2.

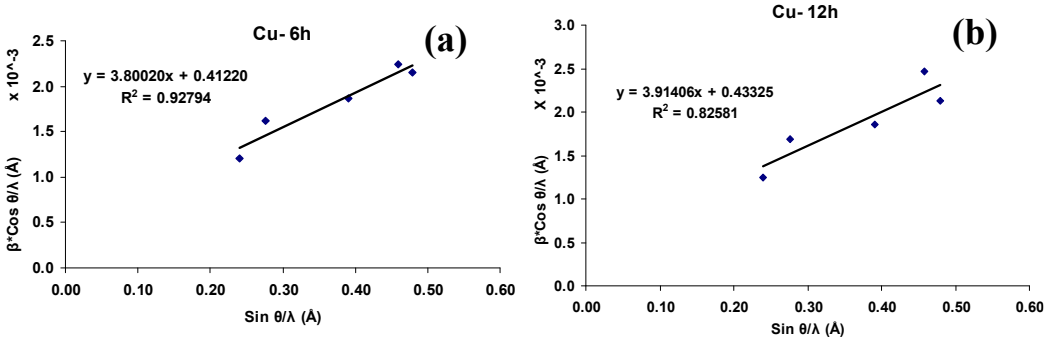


Figure 3.7: $\frac{\beta Cos\theta}{\lambda}$ vs $\frac{Sin\,\theta}{\lambda}$ plot of as-milled Cu balls produced by HEMM with different milling times using Route 1 ; (a) after 6 hours milling, and (b) after 12 hours milling.

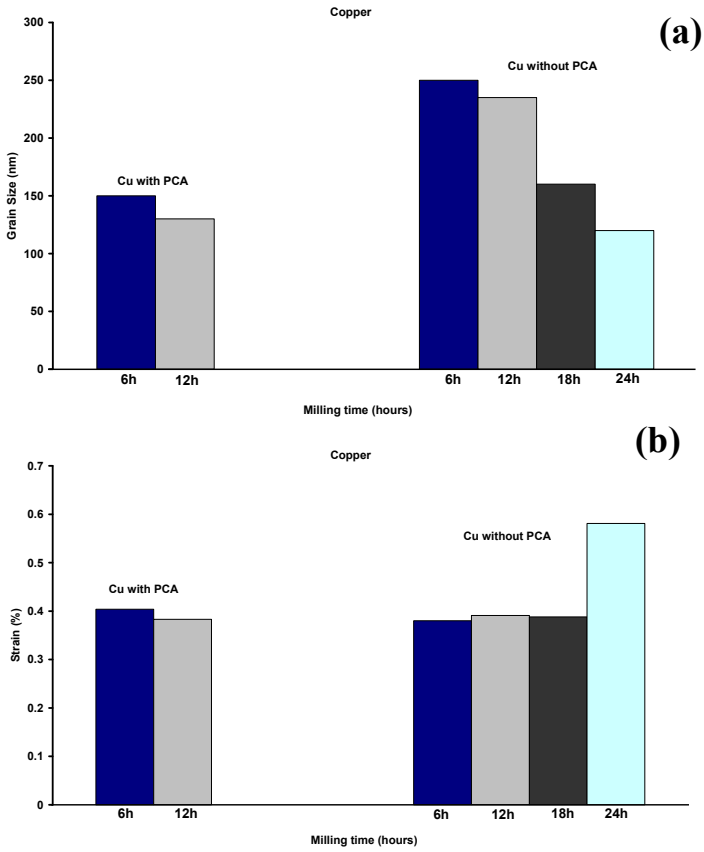


Figure 3.8: (a) Average grain size and (b) lattice strains of Cu powder with 0.6wt%PCA produced using Route 1, and Cu hollow balls/powder particles produced using Route 1 and Route 2, respectively, by HEMM with different milling times.

Microstructural examination was performed on a randomly selected as-milled Cu hollow ball, with a diameter of 6.5 mm, produced after 12 hours of milling (Route 1). Figure 3.9(a) shows the TEM bright field micrograph of the specimen cut from inside the wall of hollow ball. It was observed that the bulk material had a structure consisting of elongated Cu subgrains with a thickness in the range of 400-600 nm. The subgrains contain a high density of dislocations. TEM examination showed that the grain sizes of Cu powder particles after 24 hours of milling (Route 2) were in the range of 100-300 nm, as shown in Figure 3.9(c). So with the increase of milling time and milling severity from 12 to 24 hours, the Cu grains became much finer and in the ultrafine grained (UFG) scale (<500 nm). The indexed diffraction pattern for Cu powder particles in the [011] beam direction is shown in Figure 3.9(b). Almost continuous rings were observed for the as-milled Cu powders produced using Route 2 (Figure 3.9(d)), showing strong reflections for Cu ({111}, {200}, {220}, {311}), based on JCPDS files of Cu (04-0836), as shown in Appendix A.

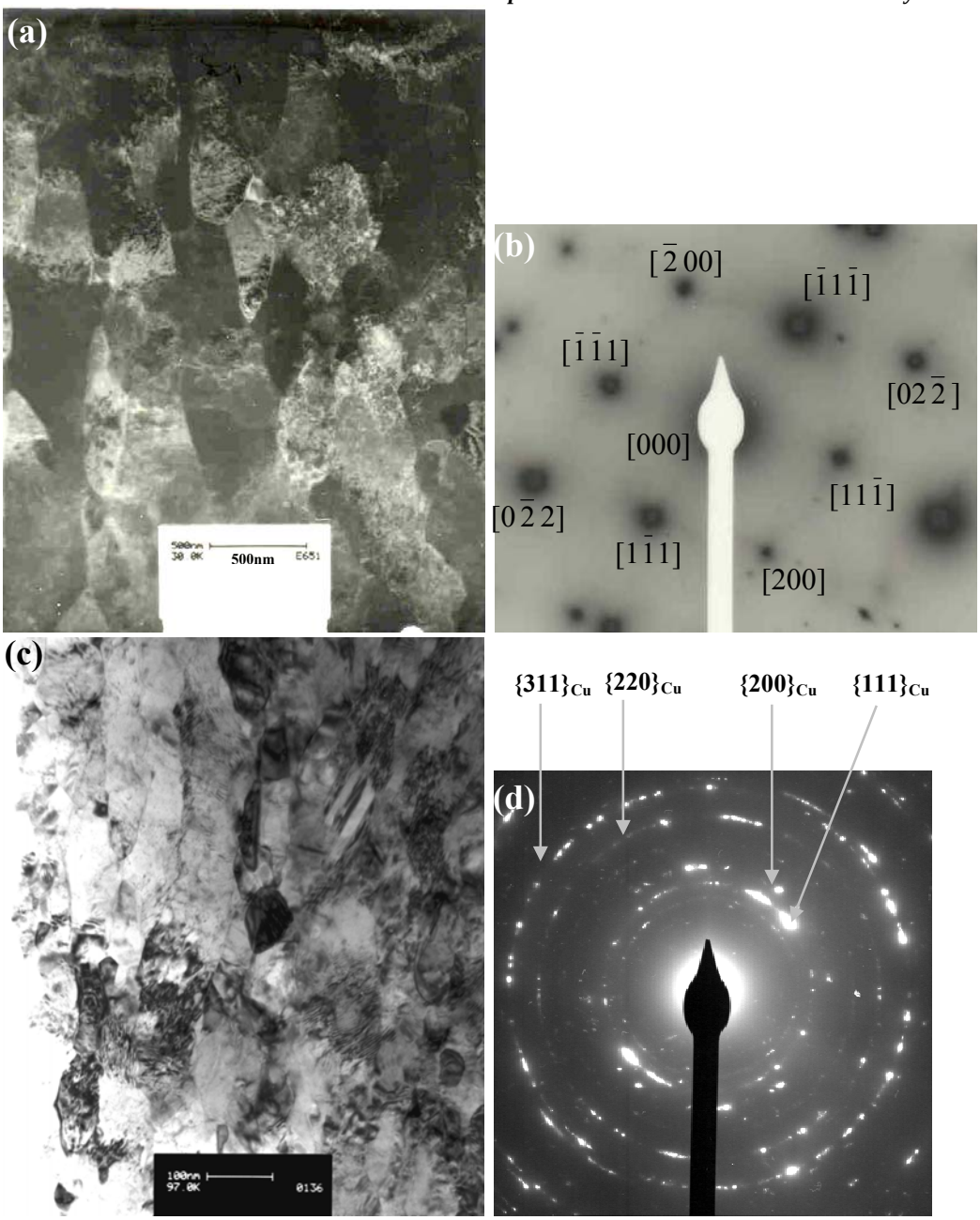


Figure 3.9: TEM bright field images and SADPs of Cu balls/powder particles produced by HEMM, ((a) and (b)) after 12 hours milling, Route 1, and ((c) and (d)) after 24 hours milling, Route 2, respectively.

Figure 3.10 shows the XRD patterns of Cu powder with 0.6wt%PCA produced by HEMM for different milling times using Route 1. The broadening of the XRD peaks was almost unchanged with the increase of milling time from 6 to 12 hours. Based on Scherrer equation, the estimated grain sizes of the Cu powder with 0.6wt%PCA produced after 6 hours and 12 hours were ~ 66 nm and 56 nm, respectively. On the other hand, based on the estimation of Williamson-Hall method and broadening of the XRD peaks, the average grain size of as-milled Cu powder with 0.6wt%PCA produced after 6 hours and 12 hours was ~ 150 nm and 130 nm, respectively, as shown in Figure 3.8(a). However, the lattice strain

remained almost unchanged around 0.40% with the increase of milling from 6 hours to 12 hours, as shown in Figures 3.8(b).

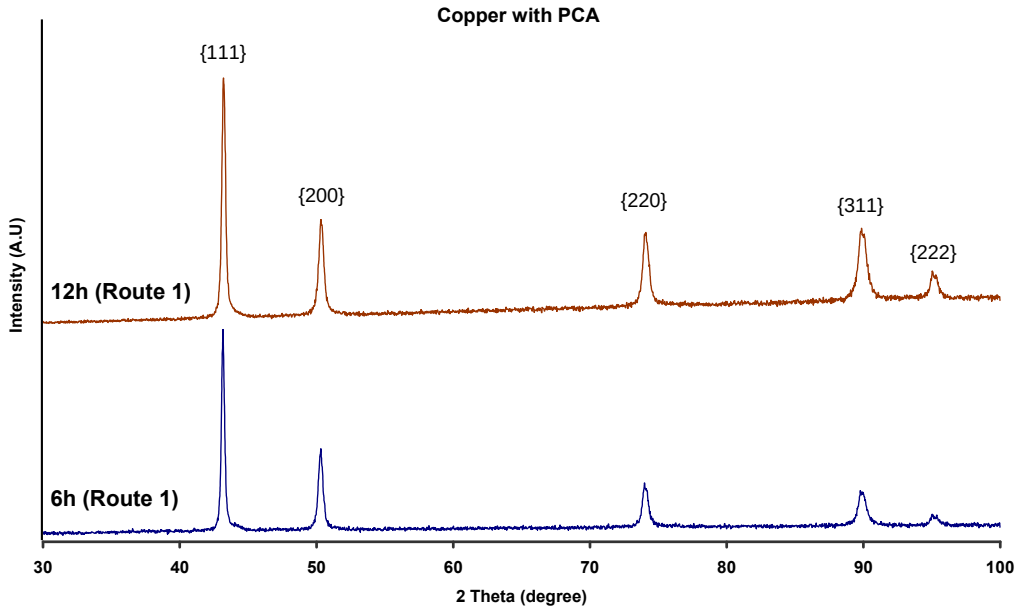


Figure 3.10: X-ray diffraction patterns of as-milled Cu powder with 0.6wt%PCA produced by HEMM with different milling times using Route 1.

On the other hand, TEM bright field images of the Cu powder with 0.6wt%PCA produced after HEMM for 12 hours showed that they consisted of elongated grains with thickness in the range of 100-250 nm (Figure 3.11(a)). Based on TEM examination, Cu grain size produced using PCA reduced to less than half value as compared to that bulk Cu material produced using Route 1 after same milling time of 12 hours. The SADP (Figure 3.11(b)) of the specimen showed semi-continuous rings and strong reflections for Cu ({111}, {200}, {220}, {311}), confirming the refinement of the microstructure.

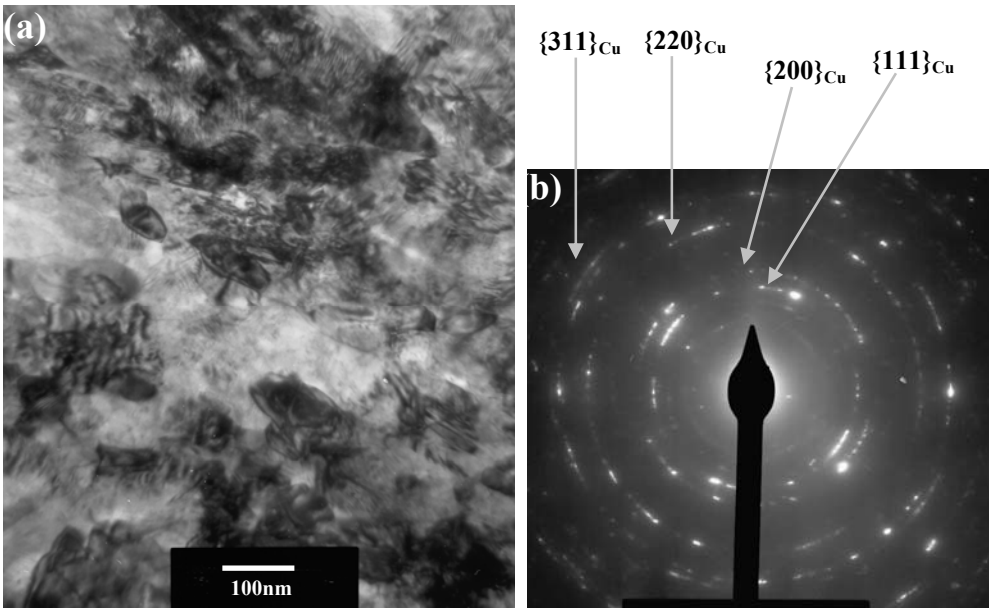


Figure 3.11: TEM bright field images and SADP of as-milled UFG Cu powder with 0.6wt%PCA produced by HEMM after 12 hours of milling using Route 1.

## 3.3.2 Cu-2.5vol.%$Al_2O_3$ Composite

Figure 3.12 shows the XRD patterns of Cu-2.5vol.%$Al_2O_3$ composite balls/powder produced with different milling times using Route 1 and Route 2. The XRD patterns only showed Cu peaks, due to the small fraction and extremely small size of $Al_2O_3$ nanoparticles. XRD analysis of the as-milled nanostructured Cu-2.5vol.%$Al_2O_3$ composite powder showed that extensive milling in Route 2 caused clear broadening of the Cu peaks in the XRD pattern, indicating that the grain sizes of the powder decreased with the increase of milling time. Based on Scherrer equation, the estimated grain sizes of the Cu-2.5vol.%$Al_2O_3$ composite balls/powder produced after 12 hours and 24 hours were ~ 64 nm and 40 nm, respectively. Based on the broadening of the XRD peaks of the Cu phase and Williamson-Hall method, the average grain size and lattice strain of the Cu matrix of the Cu-2.5vol.%$Al_2O_3$ composite balls/powder produced after 12 hours (Route 1) and 24 hours (Route 2) of milling were estimated, and the results are shown in Figures 3.13(a) and 3.13(b). With the increase of milling severity from Route 1 to Route 2, the average grain size reduced to half value for the composite powder particles as compared to composite balls, as shown in Figure 3.13(a). However there was no significant change in lattice strain and values were within the range of 0.351-0.473%, for the composite balls/powder particles produced using Route 1 and Route 2, as shown in Figure 3.13(b).

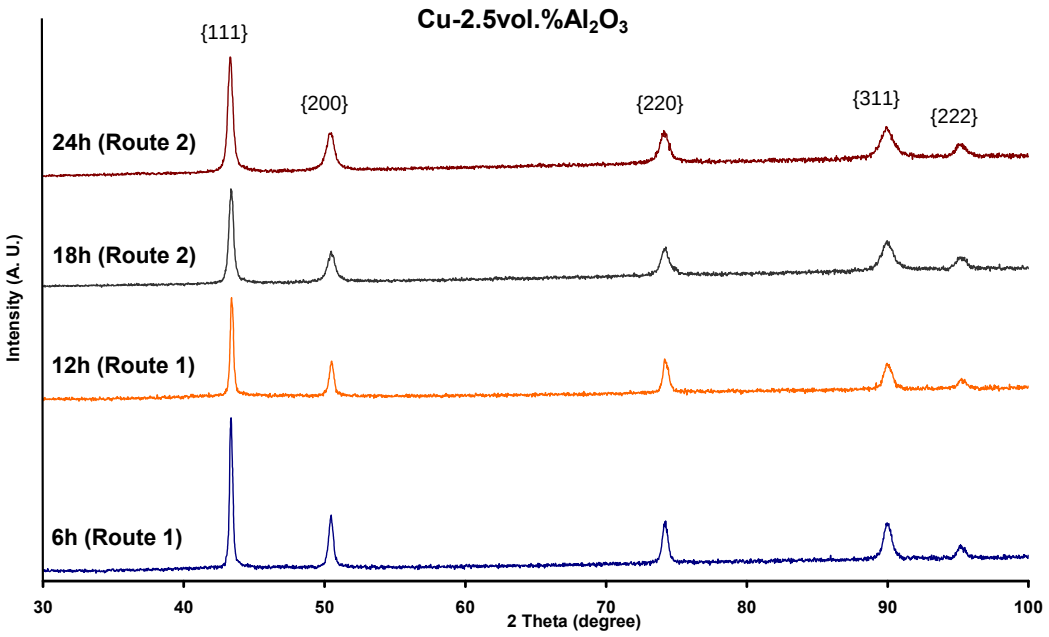


Figure 3.12: X-ray diffraction patterns of as-milled Cu-2.5vol.%$Al_2O_3$ composite balls/powder produced by HEMM with different milling times using Route 1 and Route 2.

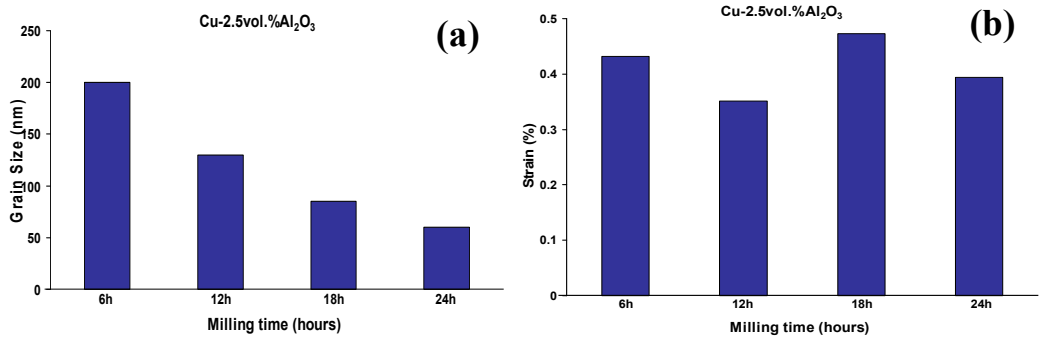


Figure 3.13: (a) Average grain size and (b) lattice strain of Cu-2.5vol.%$Al_2O_3$ composite balls/powder particles produced by HEMM with different milling times using Route 1 and Route 2.

A microstructural examination was performed on a randomly selected as-milled Cu-2.5vol.%$Al_2O_3$ composite ball produced after 12 hours of milling (Route 1) with a maximum diameter of 6 mm, as shown in Figure 3.2(d). TEM specimens were cut at three locations across the wall of the hollow ball using focus ion beam. Figures 3.14(a)-(c) show the TEM images of the specimens from these three locations. Based on the TEM examination, it was clear that the bulk material had an UFG structure consisting of elongated Cu subgrains containing a high density of dislocations and the thickness of the subgrains were in the range of 100-500 nm. This shows that the average grain size estimated using the broadening of the XRD peaks and Williamson-Hall method (Figure 3.39) is clearly smaller than the actual average Cu grain size examined by TEM, and this discrepancy is likely due to overestimate of the broadness of XRD peaks which is directly attributed to the size of the grains. It appears that the thickness of the elongated Cu subgrains near the internal surface is smaller (Figure 3.14(c)) than that near the middle line of the wall (Figure 3.14(b)) and the external surface (Figure 3.14(a)) of the ball. These results indicated that the amount of plastic deformation experienced by the material near the internal surface is substantially larger than that experienced by the material away from the internal surface.

TEM examination of the 24 hours milled Cu-2.5vol.%$Al_2O_3$ composite powder particles showed that the grain size of the Cu matrix decreased to the range of 50-150 nm (Figure 3.15(a)). This again shows that the average grain size estimated using the XRD peaks and Williamson-Hall method is slightly smaller than the actual average grain size. TEM examination confirmed the reduction of grain size of Cu matrix for the Cu-2.5vol.%$Al_2O_3$ composite powder produced using Route 2, in nanoscale (<100 nm), as compared to composite balls produced using Route 1, in UFG scale (< 500 nm). Figure 3.15(b) shows the indexing of a typical SADP of

as-milled Cu-2.5vol.%$Al_2O_3$ composite powder particles produced after 24 hours (Route 2). Based on the SADP it can be seen that strong reflections ({111}, {200}, {220}, {311}) could be correlated to Cu matrix while weak reflections ({104}, {300}) are from fine $Al_2O_3$ nanoparticles, based on JCPDS files of Cu (04-0836) and $Al_2O_3$ (46-1212), as shown in Appendix A.

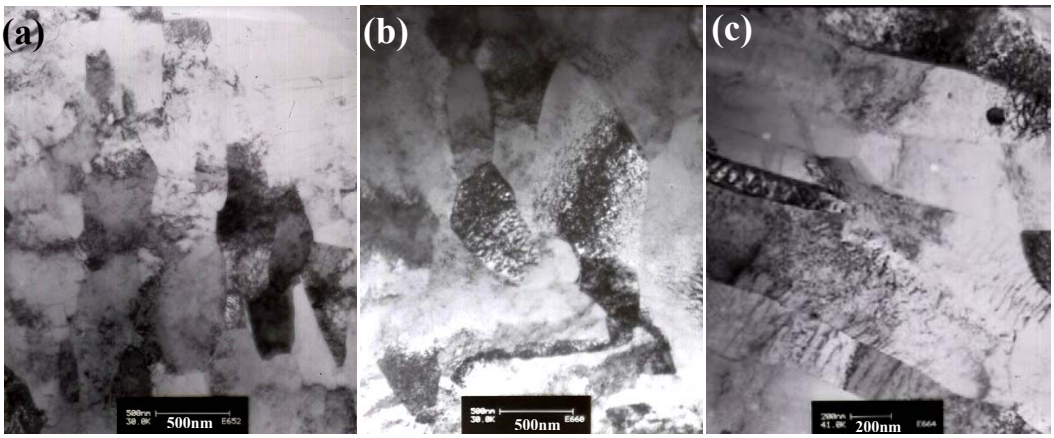


Figure 3.14: Bright field TEM images of specimens obtained at different locations of the wall of a 12 hours milled Cu-2.5vol.%$Al_2O_3$ composite ball, (a) near the external surface of the ball, (b) near the middle line of the wall, and (c) near the internal surface of the ball.

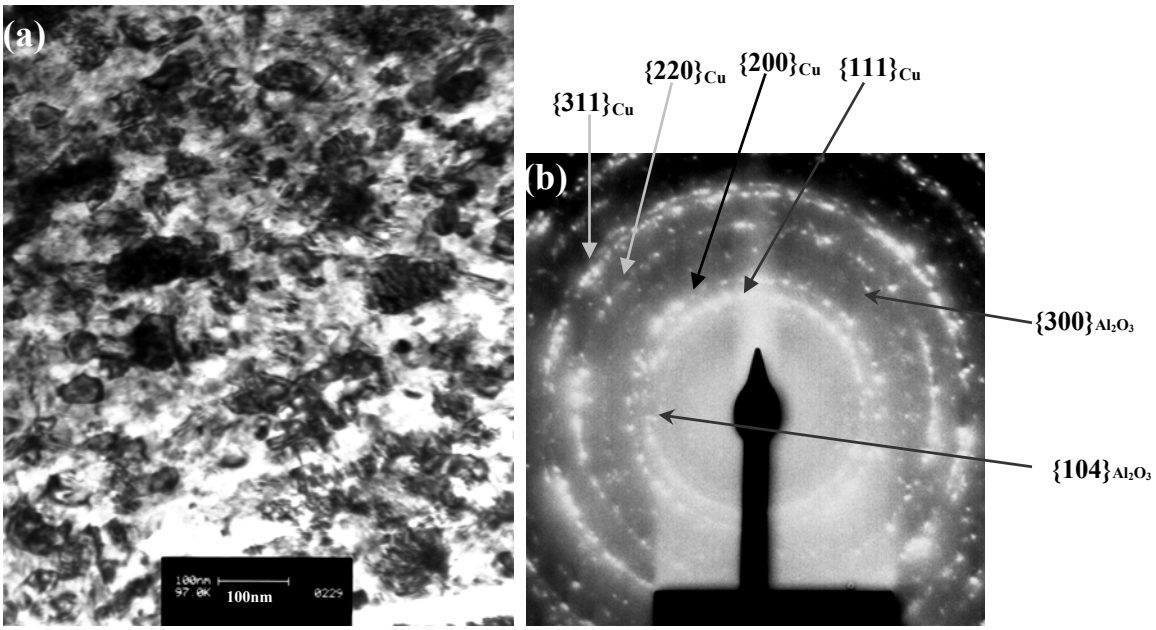


Figure 3.15: TEM bright field image and SADP of as-milled Cu-2.5vol.%$Al_2O_3$ composite powder produced by HEMM after 24 hours of milling using Route 2.

The STEM image (Figure 3.16(a)) of the Cu-2.5vol.%$Al_2O_3$ composite powder particles produced after 24 hours of milling showed that the bright particles are $Al_2O_3$ nanoparticles as confirmed from the X-ray elemental mapping for Al. A uniform distribution of $Al_2O_3$ nanoparticles was achieved, as shown by the elemental mapping (Figure 3.16(c)). It also shows that the small $Al_2O_3$ particles had sizes in the range of 10-50 nm.

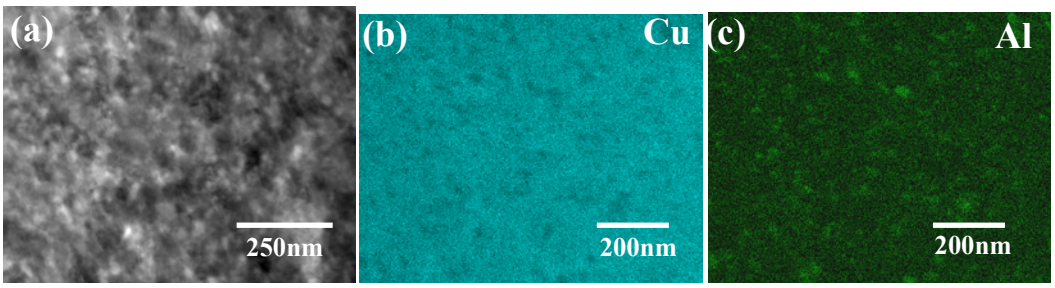


Figure 3.16: STEM image (a) and X-ray elemental (Cu and Al) maps ((b) and (c)) of Cu-2.5vol.%$Al_2O_3$ composite powder particles produced by HEMM after 24 hours of milling, Route 2.

SEM examination of the cross section of as-milled Cu-2.5vol%$Al_2O_3$ composite powder particles produced after 24 hours was carried out to determine the volume fraction and distribution of large $Al_2O_3$ particles, with sizes greater than 100 nm. It was found that there were < 0.5 vol.% of such large particles in the microstructure, and their sizes were in the range of 100-500 nm, as shown in Figures 3.17. They were randomly distributed.

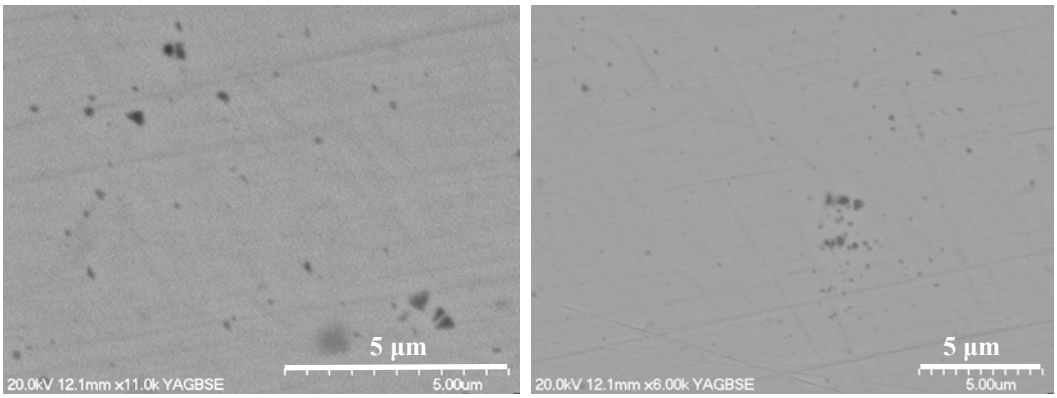


Figure 3.17: SEM backscattered electron images of the cross sections of Cu-2.5vol.%$Al_2O_3$ composite powder particles produced by HEMM after 24 hours of milling, Route 2.

### 3.3.3 Cu-5vol.%$Al_2O_3$ Composite

Figure 3.18 shows the XRD patterns of Cu-5vol.%$Al_2O_3$ composite granules/powder produced with different milling times using Route 1 and Route 2. The XRD patterns only showed Cu peaks, due to the small fraction and extremely small size of $Al_2O_3$ nanoparticles. Extensive milling in Route 2 caused clear broadening of the Cu peaks in the XRD patterns of the as-milled Cu-5vol.%$Al_2O_3$ composite powder, indicating that the grain sizes of the powder decreased with the increase of milling time. Based on Scherrer equation, the estimated grain sizes of the Cu-5vol.%$Al_2O_3$ composite granules/powder produced after 12 hours and 24 hours were ~ 60 nm and 40 nm, respectively. Based on the broadening of the XRD peaks of the Cu phase and Williamson-Hall method, the average grain size and lattice strain of the Cu matrix of the Cu-5vol.%$Al_2O_3$ composite

granules/powder produced after 12 hours (Route 1) and 24 hours (Route 2) of milling were estimated, and the results are shown in Figures 3.19(a) and 3.19(b). The trend of decreasing the average grain size with the increase of milling hours continued and a significant decrease was observed for the composite powder particles produced using Route 2, as shown in Figure 3.19(a). However the decreasing trend of lattice strain was not significant with the increase of milling hours, as shown in Figure 3.19(b).

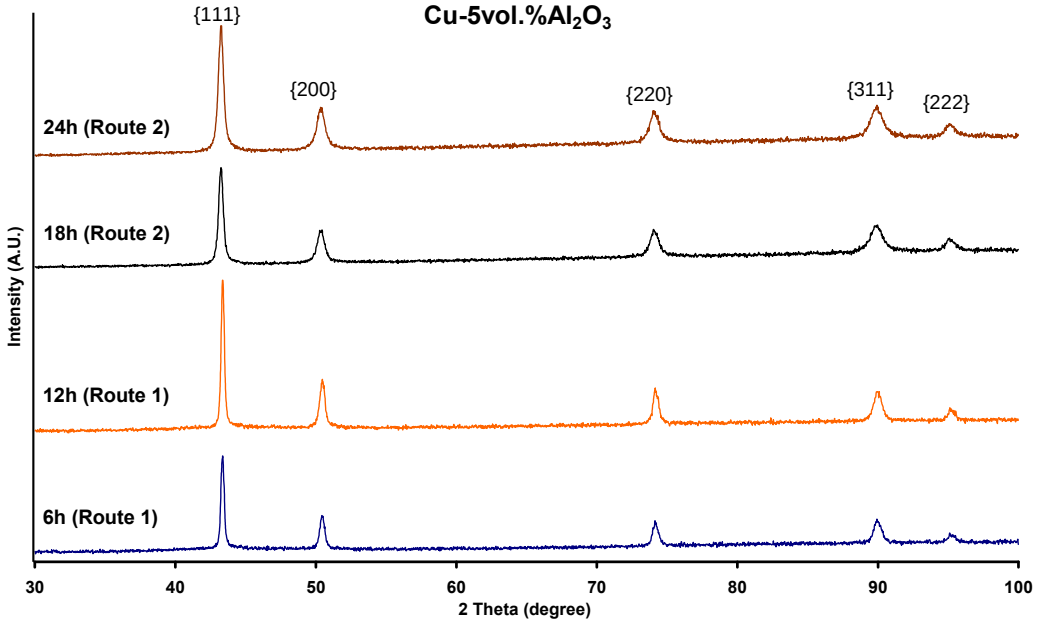


Figure 3.18: X-ray diffraction patterns of as-milled Cu-5vol.%$Al_2O_3$ composite granules/powder produced by HEMM with different milling times using Route 1 and Route 2.

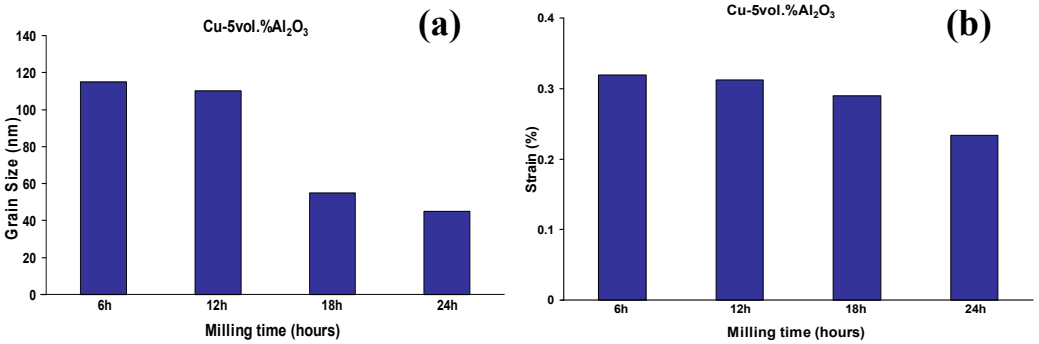


Figure 3.19: (a) Average grain size and (b) lattice strain of Cu-5vol.%$Al_2O_3$ composite granules/powder particles produced by HEMM with different milling times using Route 1 and Route 2.

TEM microstructural examination of the 12 hours milled Cu-5vol.%$Al_2O_3$ composite granules showed that the grain sizes of the Cu matrix were in the range of 100-300 nm (Figure 3.20(a)). With further increasing the milling time to 24 hours, the grain sizes of the Cu matrix of the composite powder particles decreased to 50-150 nm (Figure 3.20(c)), which confirmed that the estimated grain size using the XRD peaks and Williamson-Hall method is clearly smaller

than the actual average grain size, as shown later in Figure 3.39. TEM bright field images confirmed that increasing the milling time and milling severity from 12 hours (Route 1) to 24 hours (Route 2) reduced the grain size of Cu matrix, mainly due to the larger plastic deformation and recrystallisation experienced by the material.

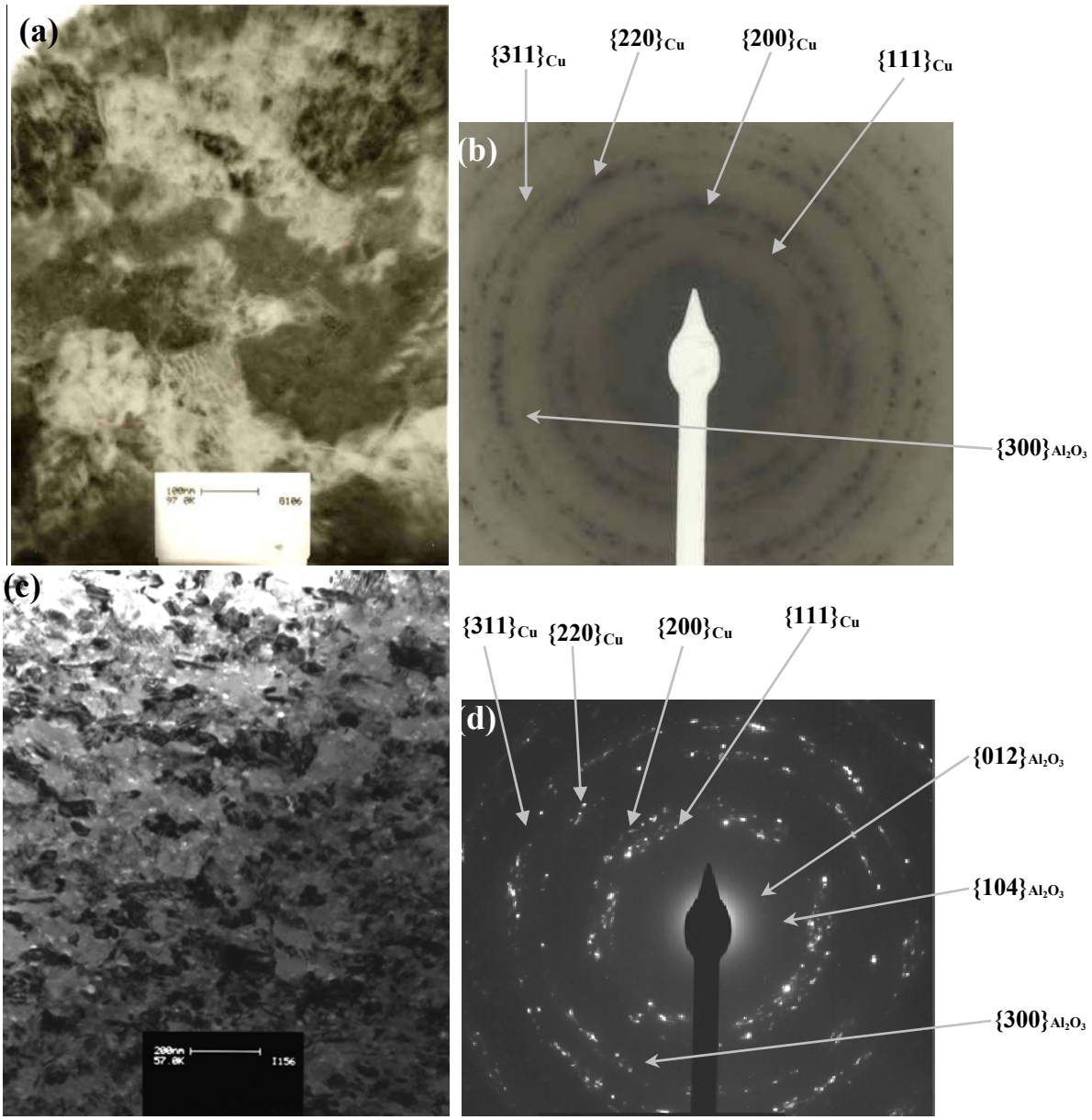


Figure 3.20: TEM bright field images and SADPs of Cu-5vol.%$Al_2O_3$ composite granules/powder particles produced by HEMM, ((a) and (b)) after 12 hours milling, Route 1, ((c) and (d)) after 24 hours milling, Route 2, respectively.

Based on TEM examination the reduction of grain size of Cu matrix for the Cu-5vol.%$Al_2O_3$ composite powder produced using Route 2, was in nanoscale (<100 nm), as compared to composite granules produced using Route 1, which was in UFG scale (< 500 nm). On the other hand, it was also observed that with the increase of milling hours from Route 1 to Route 2 and increasing volume fraction of $Al_2O_3$ from 2.5% to 5%, the estimated grain size of the Cu matrix decreased

significantly, as calculated by using the broadening of the XRD peaks of the Cu phase and Williamson-Hall method and further confirmed by TEM examination. SADPs (Figures 3.20(b) and 3.20(d)) confirmed that strong reflections ({111}, {200}, {220}, {311}) could be correlated to Cu matrix while weak reflections ({012}, {104}, {300}) were from fine $Al_2O_3$ nanoparticles, based on JCPDS files of Cu (04-0836) and $Al_2O_3$ (46-1212), as shown in Appendix A.

Figures 3.21((a)-(c)) and 3.21((d)-(f)) show the STEM images and X-ray elemental mapping (Cu and Al) of the Cu-5vol.%$Al_2O_3$ composite granules produced after 6 hours and 12 hours. In the STEM images, as shown in Figures 3.21(a) and 3.21(d), the bright particles are $Al_2O_3$ nanoparticles, as confirmed from their X-ray elemental mapping for Al. It appeared that with a short milling time of 6 hours, the $Al_2O_3$ nanoparticles were predominately distributed along the grain boundaries, while increasing the milling time to 12 hours, a large fraction of $Al_2O_3$ nanoparticles were distributed inside the grains and the majority of the $Al_2O_3$ particles had sizes in the range of 10-40 nm (Figure 3.21(f)). Increasing the milling time to 12 hours, led to more homogenous distribution of $Al_2O_3$ nanoparticles in Cu matrix, as confirmed by X-ray elemental mapping of Al.

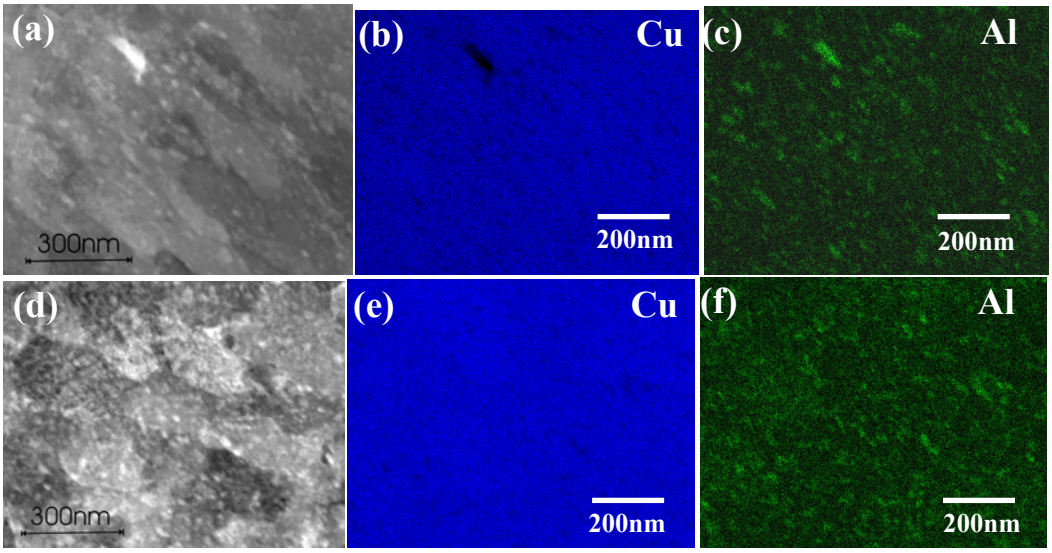


Figure 3.21: STEM images and X-ray elemental maps (Cu and Al) of Cu-5vol.%$Al_2O_3$ composite granules produced by HEMM with different milling times using Route 1, ((a)-(c)) after 6 hours, and ((d)-(f)) after 12 hours.

SEM examination of the cross section of the as-milled Cu-5vol.%$Al_2O_3$ composite powder particles produced after 24 hours was carried out to determine the volume fraction and distribution of the large size of $Al_2O_3$ particles, with sizes in the range of 100-400 nm, as shown in Figures 3.22. This revealed that there was < 0.5 vol.% of such large $Al_2O_3$ particles in the microstructure.

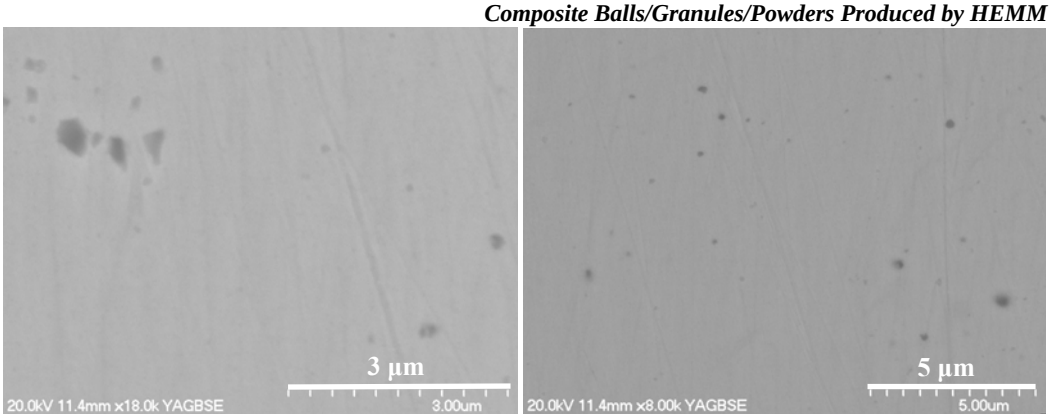


Figure 3.22: SEM backscattered electron images of the cross sections of Cu-5vol.%$Al_2O_3$ composite powder particles produced by HEMM after 24 hours of milling, Route 2.

## 3.3.4 Cu-7.5vol.%$Al_2O_3$ Composite

The broadening of the Cu peaks in the XRD pattern of Cu-7.5vol.%$Al_2O_3$ composite powder did not become more significant with increasing the milling time from 6 to 24 hours, as shown in Figure 3.23. Based on Scherrer equation, the estimated grain sizes of the Cu-7.5vol.%$Al_2O_3$ composite powders produced after 12 hours and 24 hours were ~ 40 nm and 35 nm, respectively. On the other hand, based on the broadening of the XRD peaks of the Cu phase and Williamson-Hall method, the average grain size and lattice strain of the Cu matrix of the Cu-7.5vol.%$Al_2O_3$ composite powders produced after 12 hours (Route 1) and 24 hours (Route 2) of milling were estimated, and the results are shown in Figures 3.24(a) and 3.24(b). The decreasing trend of the average grain sizes with the increase of milling hours was not significant for the composite powders produced using Route 1 and Route 2 of milling, as shown in Figure 3.24(a).

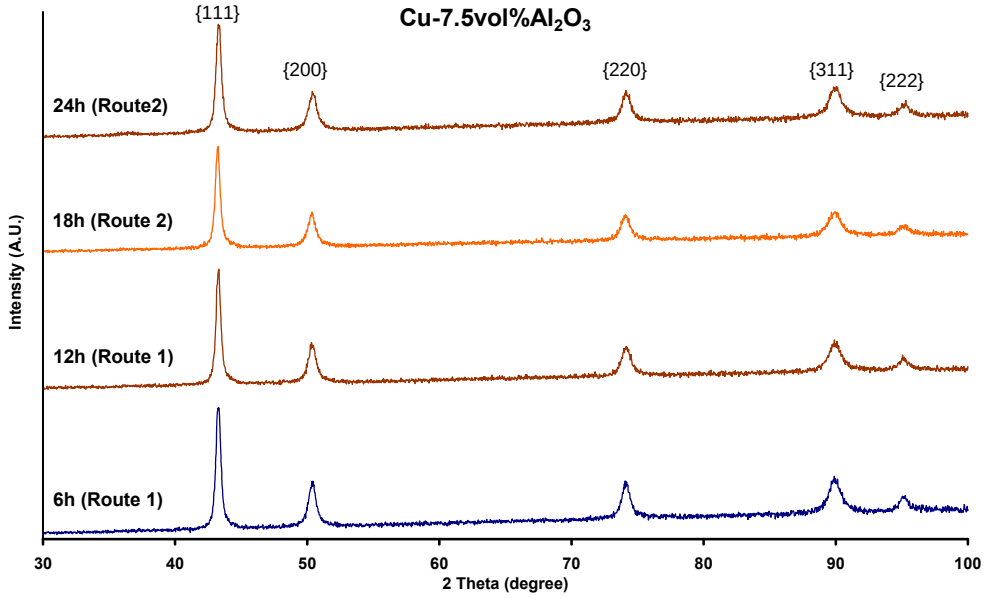


Figure 3.23: X-ray diffraction patterns of as-milled Cu-7.5vol.%$Al_2O_3$ composite powder produced by HEMM with different milling times using Route 1 and Route 2.

With the increase of milling severity from Route 1 to Route 2, the lattice strain for the composite powders remained almost unchanged within the range of 0.311-0.354% due to strain hardening.

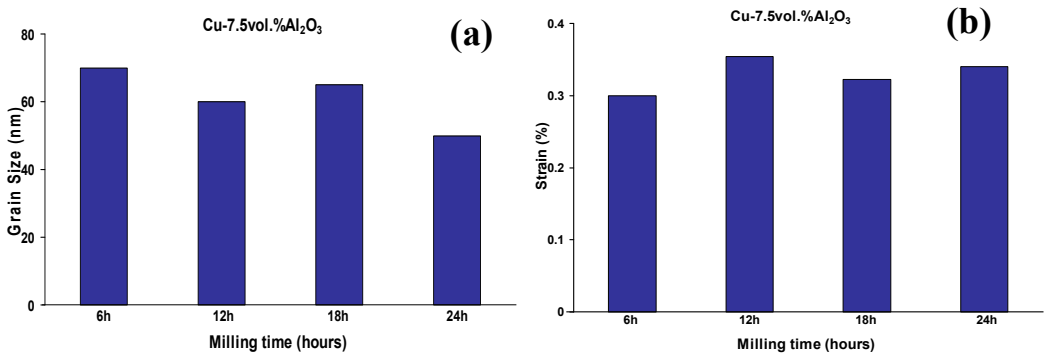


Figure 3.24: Average grain size and lattice strain of Cu-7.5vol.%$Al_2O_3$ composite powder particles produced by HEMM with different milling times using Route 1 and Route 2.

However, TEM bright field images of as-milled Cu-7.5vol.%$Al_2O_3$ composite powder particles produced after 12 hours and 24 hours of milling confirmed that Cu grains remained within the range of 50-150 nm (Figures 3.25 (a) and 3.25(c)), while majority of the Cu grain sizes were smaller than 100 nm of nanostructured composite powder produced using Route 1. The TEM results of Cu grain sizes are close to the estimated Cu grain size using the XRD peaks and Williamson-Hall method. SADPs show that almost continuous rings were observed for the as-milled composite powders produced using Route 1 and Route 2, as shown in Figures 3.25(b) and 3.25(d). SADPs of as-milled Cu-7.5vol.%$Al_2O_3$ composite powder particles produced after 12 hours (Route 1) and 24 hours (Route 2) showed that strong reflections ({111}, {200}, {220}, {311}) could be correlated to Cu matrix while weak reflections ({104}, {300}) were from fine $Al_2O_3$ nanoparticles, based on JCPDS files of Cu (04-0836) and $Al_2O_3$ (46-1212), as shown in Appendix A.

Figures 3.26(a) and 3.26(d) show the SEM micrographs of the coarse and fine as-milled Cu-7.5vol.%$Al_2O_3$ composite powder particles produced after 12 hours (Route 1) and 24 hours (Route 2) of milling, respectively, while Figures 3.26((b) and (c)) and 3.26((e) and (f)) show their corresponding energy dispersive X-ray elemental mapping (Cu and Al). $Al_2O_3$ nanoparticles were incorporated into each of the as-milled powder particles, forming a nanostructured Cu-$Al_2O_3$ composite structure, as shown in Figures 3.26(c) and 3.26(f).

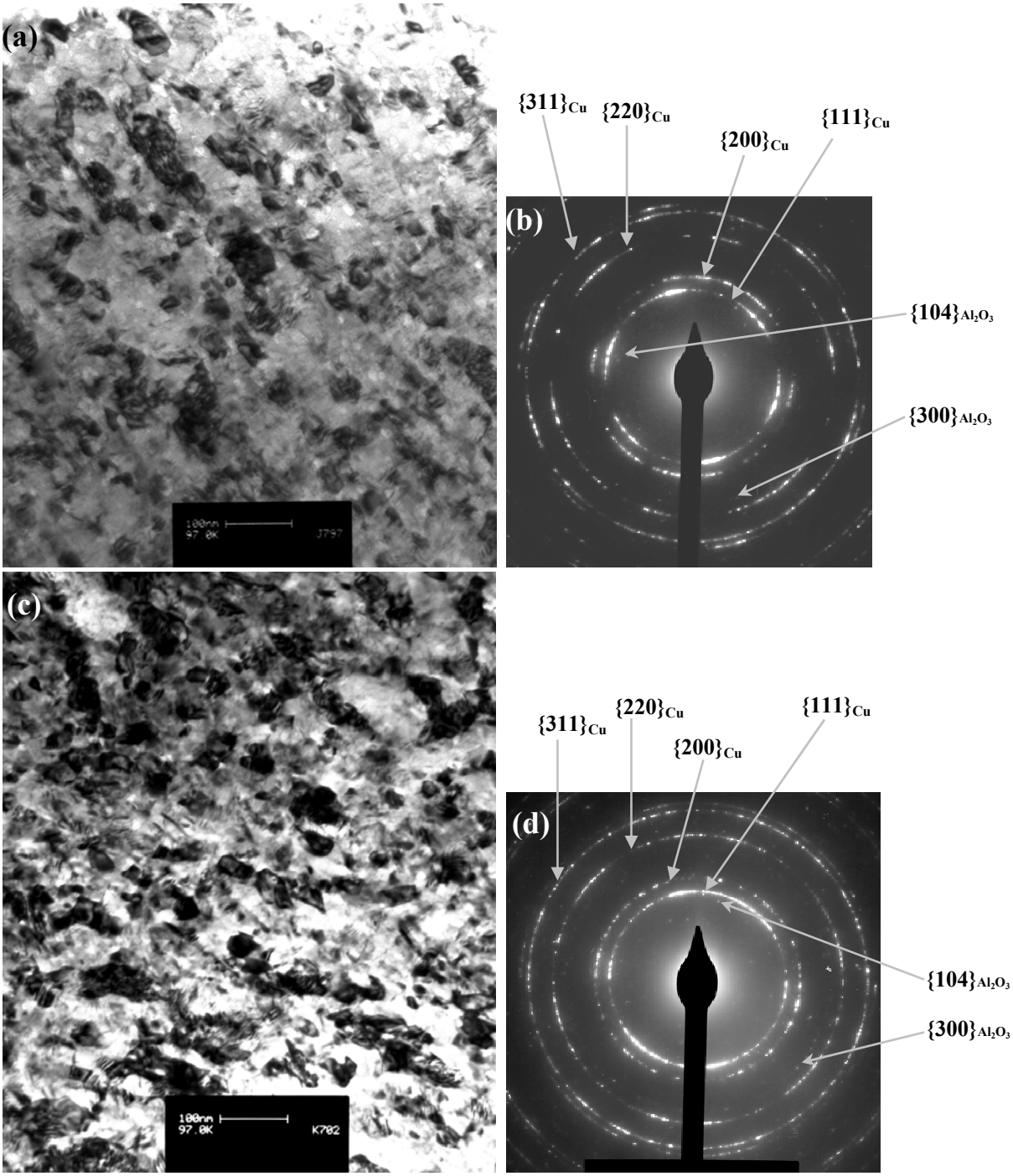


Figure 3.25: TEM bright field images and SADPs of nanostructured Cu-7.5vol.%$Al_2O_3$ composite powder particles produced by HEMM, ((a) and (b)) after 12 hours milling, Route 1, ((c) and (d)) after 24 hours milling, Route 2, respectively.

In the STEM images shown in Figures 3.27(a) and 3.27(d), the bright particles are $Al_2O_3$ nanoparticles which are uniformly distributed in Cu matrix, as confirmed by the X-ray elemental mapping (Al), shown in Figures 3.27(c) and 3.27(f). The $Al_2O_3$ nanoparticles within the range of 10-30 nm are predominantly along the grain boundaries in composite powder particles produced after 12 hours and 24 hours of milling.

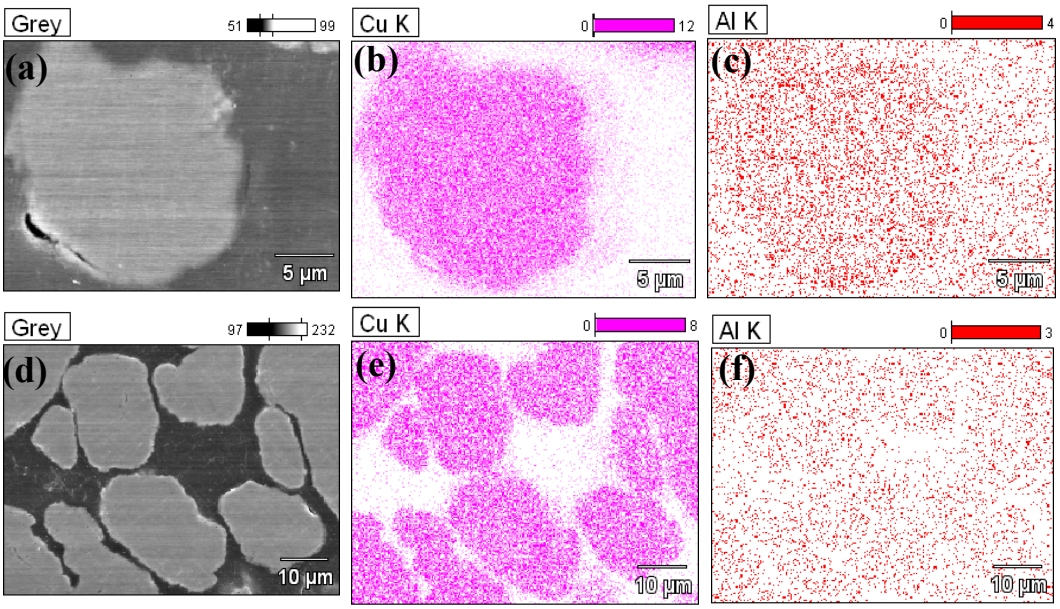


Figure 3.26: SEM micrographs and corresponding energy dispersive X-ray elemental (Cu and Al) maps of the cross section of nanostructured Cu-7.5vol.%$Al_2O_3$ composite powder particles produced by HEMM, ((a)-(c)) after 12 hours milling, Route 1, ((d)-(f)) after 24 hours milling, Route 2, respectively.

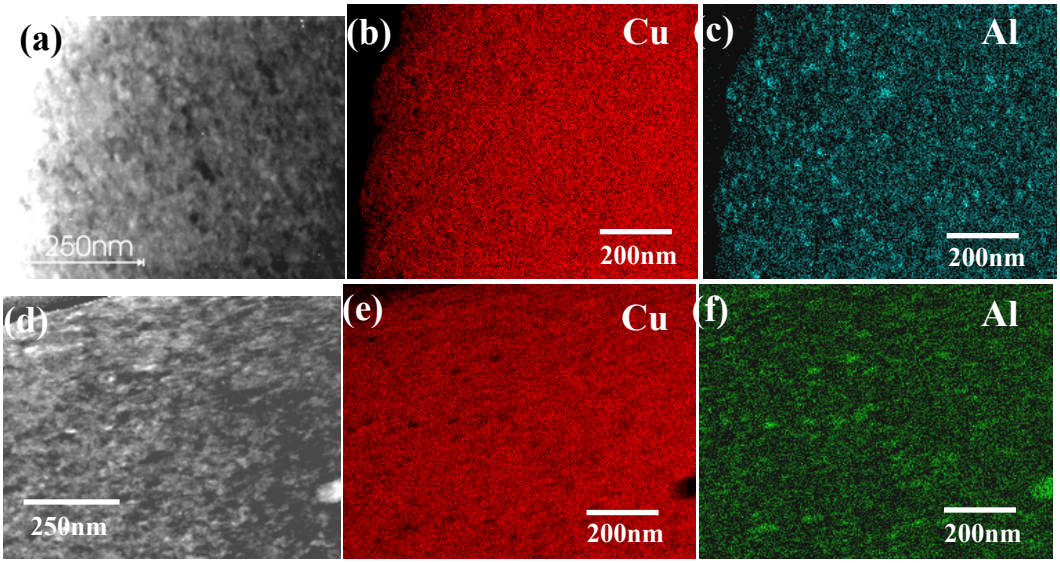


Figure 3.27: STEM images and X-ray elemental (Cu and Al) maps of Cu-7.5vol.%$Al_2O_3$ composite powder particles produced by HEMM with different milling times, ((a)-(c)) after 12 hours milling, Route 1, and ((d)-(f)) after 24 hours milling, Route 2, respectively.

SEM examination of the cross section of the Cu-7.5vol.%$Al_2O_3$ composite powder particles produced after 12 hours and 24 hours of milling (Figures 3.28(a) and 3.28(b)), respectively, observed a small fraction of $Al_2O_3$ particles (< 0.5 vol.%) within the range of 80-500 nm. It appears that increasing the milling time and effectiveness through the use of Route 2 milling, the fraction of the larger sized $Al_2O_3$ particles remained almost unchanged, but their sizes became smaller.

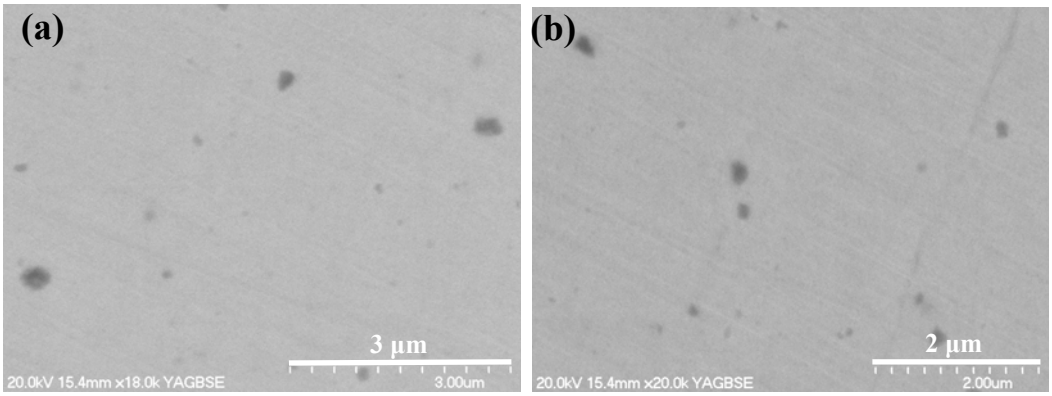


Figure 3.28: SEM backscattered electron images of the cross sections of Cu-7.5vol.%$Al_2O_3$ composite powder particles produced by HEMM after different milling times, (a) after 12 hours, Route 1, (b) after 24 hours, Route 2.

## 3.3.5 Cu-10vol.%$Al_2O_3$ Composite

Figure 3.29 shows the XRD patterns of Cu-10vol.%$Al_2O_3$ composite powder produced with different milling times using Route 1 and Route 2. The XRD patterns only showed Cu peaks, due to the small fraction and extremely small size of $Al_2O_3$ nanoparticles. The broadening of the Cu peaks in the XRD pattern did not become more significant with the increase of the milling time from 6 to 24 hours. Based on Scherrer equation, the estimated grain sizes of the Cu-10vol.%$Al_2O_3$ composite powders produced after 12 hours and 24 hours were ~ 45 nm and 40 nm, respectively. On the other hand, based on the broadening of the XRD peaks of the Cu phase and Williamson-Hall method, the average grain size and lattice strain of the Cu matrix of the Cu-10vol.%$Al_2O_3$ composite powders produced after 12 hours (Route 1) and 24 hours (Route 2) of milling were estimated, and the results are shown in Figures 3.30(a) and 3.30(b). Almost a similar trend was observed in the average grain sizes and lattice strains for the composite powders produced after 12 hours (Route 1) and 24 hours (Route 2) of milling, as shown in Figures 3.30(a) and 3.30(b). The average grain sizes and lattice strains for the composite powders increased with the increase of milling time from 6 to 12 hours, due to strain hardening. However, with the increase of milling severity from Route 1 to Route 2, a decreasing trend was observed in the average grain sizes and lattice strain for the composite powder, suggesting the refinement in microstructure with change of larger steel balls during HEMM.

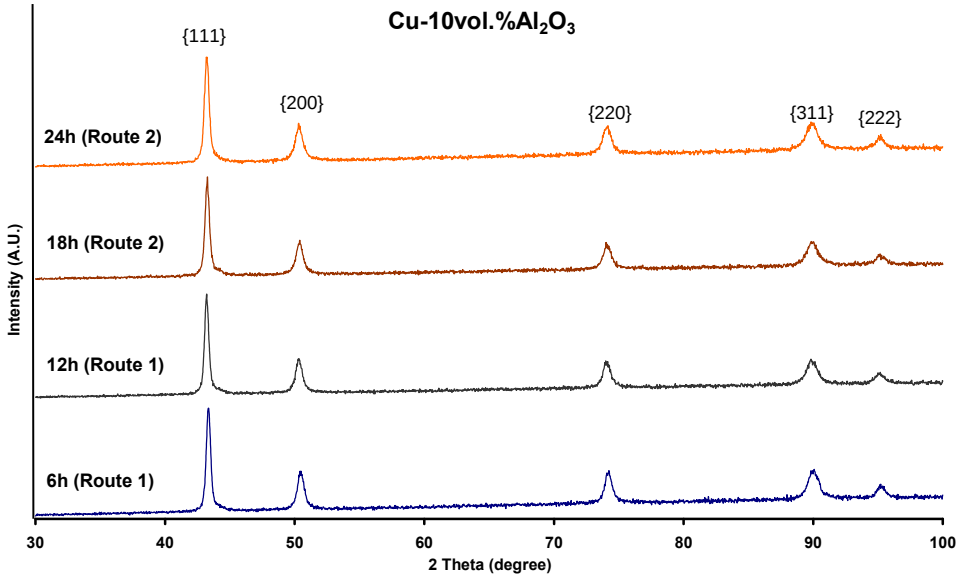


Figure 3.29: X-ray diffraction patterns of as-milled Cu-10vol.%$Al_2O_3$ composite powder produced by HEMM with different milling times using Route 1 and Route 2, respectively.

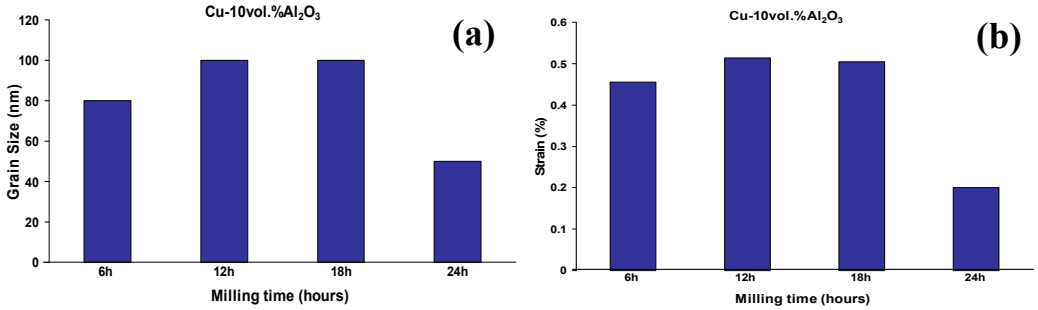


Figure 3.30: (a) Average grain size and (b) lattice strain of Cu-10vol.%$Al_2O_3$ composite powder particles produced by HEMM with different milling times using Route 1 and Route 2.

TEM bright field images show that grains of the Cu matrix are in the range of 50-150 nm (Figure 3.31(a)) for the coarse powder produced using Route 1, while the majority of the Cu grains had sizes smaller than 100 nm (Figure 3.31(c)) for the fine powder produced using Route 2. The Cu grain sizes measured from the TEM images were close to the estimated grain size using the XRD peaks and Williamson-Hall method. Almost continuous rings were observed for the as-milled composite powders produced using Route 1 and Route 2, as shown in SADPs (Figures 3.31(b) and 3.31(d)), which indicated that the major contribution came from fine crystallites of Cu and $Al_2O_3$ in the deformed structure.

Figures 3.32(a) and 3.32(d) show the SEM micrographs of the coarse and fine as-milled Cu-10vol.%$Al_2O_3$ composite powder particles produced after 12 hours (Route 1) and 24 hours (Route 2) of milling, respectively, while Figures 3.32((b) and (c)) and 3.32((e) and (f)) show their corresponding energy dispersive X-ray elemental mapping (Cu and Al). $Al_2O_3$ nanoparticles were incorporated into each of the as-milled powder particles, forming a nanostructured Cu-$Al_2O_3$ composite structure, as shown in Figures 3.32(c) and 3.32(f).

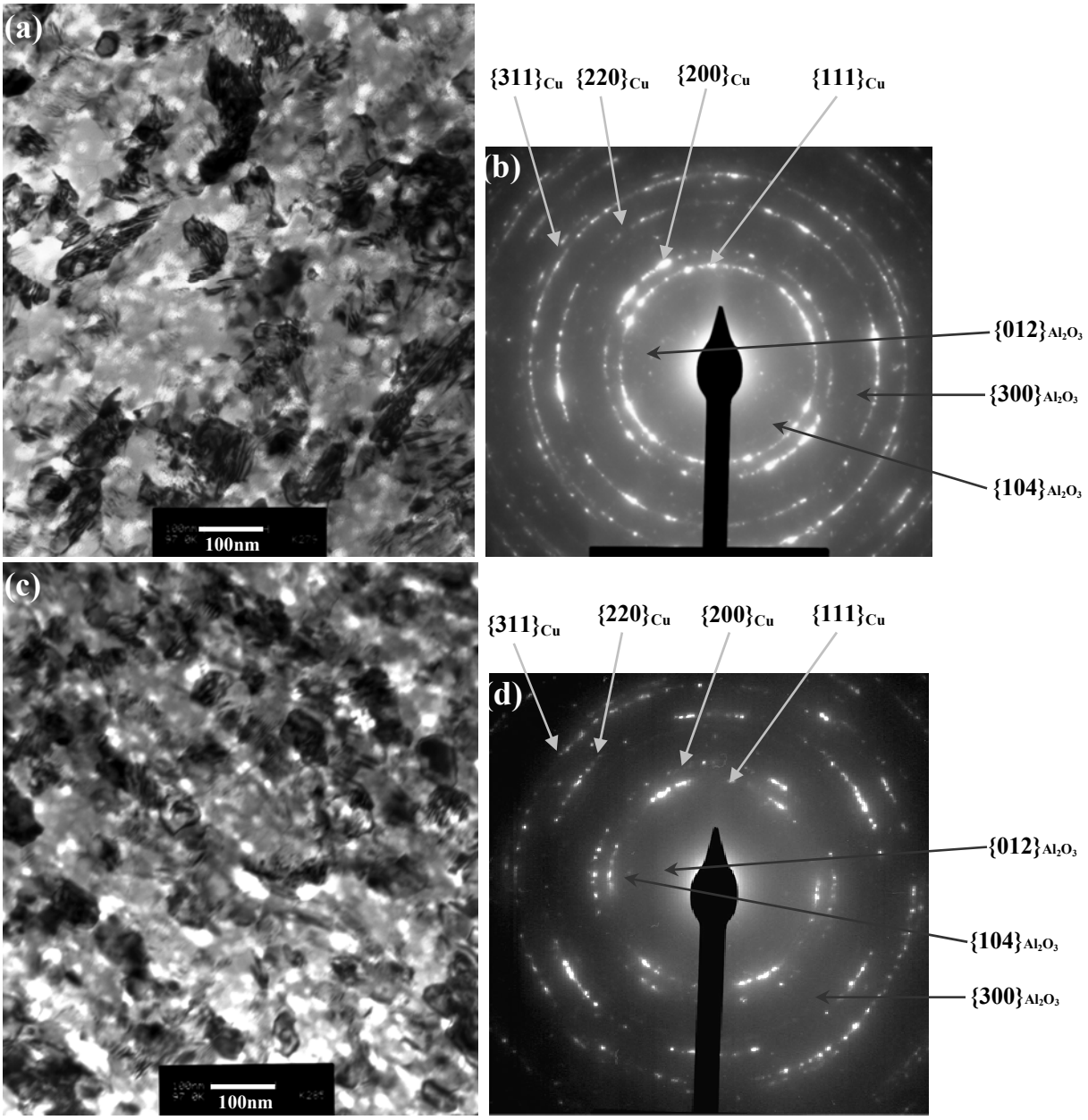


Figure 3.31: TEM bright field images and SADPs of Cu-10vol.%$Al_2O_3$ composite powder particles produced by HEMM, ((a) and (b)) after 12 hours, Route 1, ((c) and (d)) after 24 hours, Route 2, respectively.

In the STEM images shown in Figures 3.33(a) and 3.33(d), the bright particles are $Al_2O_3$ nanoparticles, as confirmed from the X-ray elemental mapping for Al. The $Al_2O_3$ nanoparticles were uniformly distributed in Cu matrix and predominantly along the grain boundaries, as shown in Figures 3.33(c) and 3.33(f). SEM examination of the cross section of the as-milled Cu-10vol.%$Al_2O_3$ composite powder particles produced after 12 hours and 24 hours of milling, showed that the sizes of large $Al_2O_3$ particles were in the range of 80-400 nm, as shown in Figures 3.34(a) and 3.34(b), respectively. This revealed that there was < 1vol.% of such large $Al_2O_3$ particles in the microstructure.

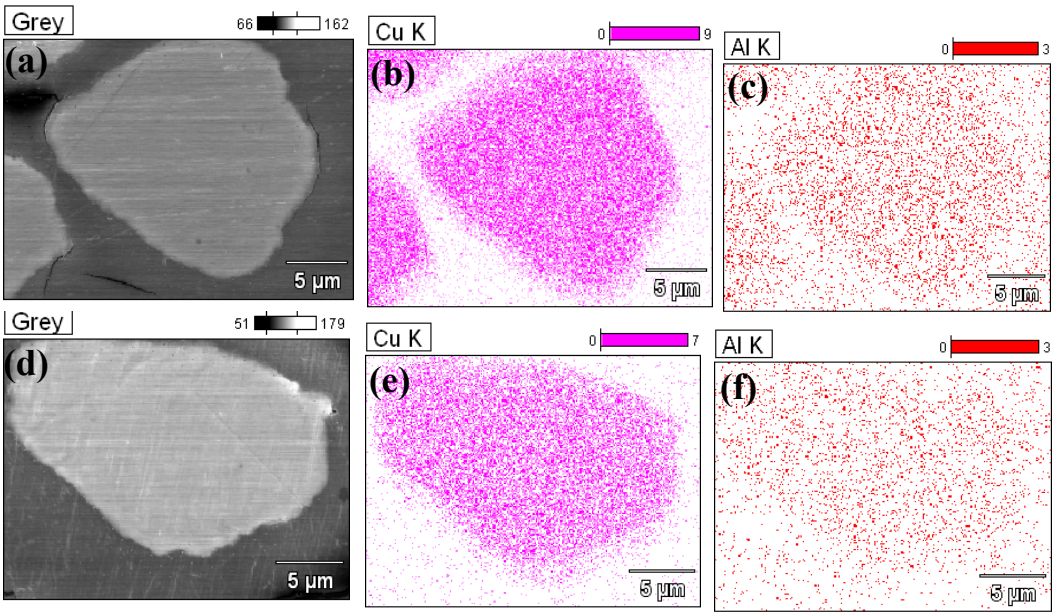


Figure 3.32: SEM micrographs and corresponding energy dispersive X-ray elemental maps (Cu and Al) of the cross section of as-milled Cu-10vol.%$Al_2O_3$ composite powder particles produced by HEMM, ((a)-(c)) after 12 hours milling, Route 1, ((d)-(f)) after 24 hours milling, Route 2, respectively.

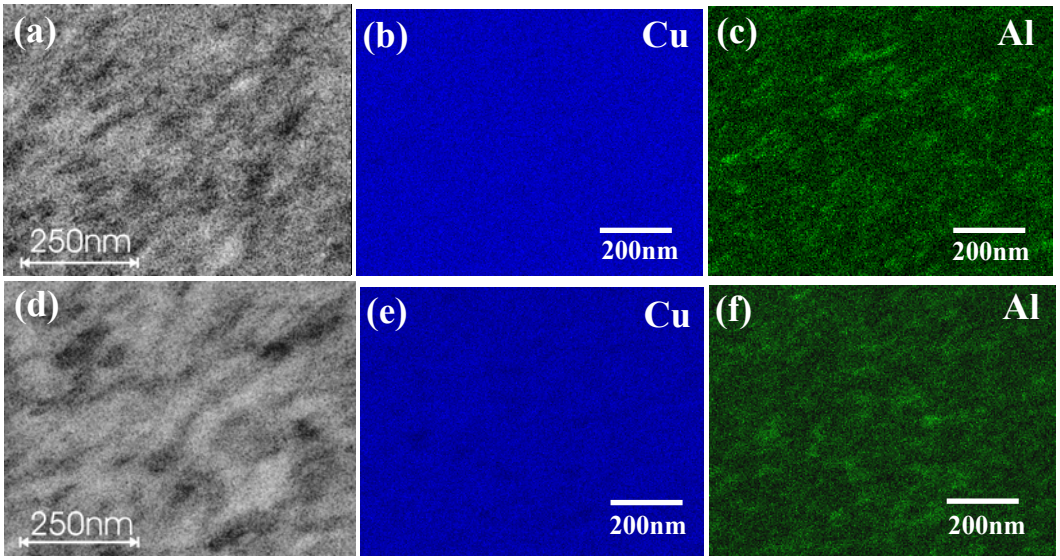


Figure 3.33: STEM images and X-ray elemental (Cu and Al) maps of Cu-10vol.%$Al_2O_3$ composite powder particles produced by HEMM with different milling times, ((a)-(c)) after 12 hours milling, Route 1, ((d)-(f)) after 24 hours milling, Route 2, respectively.

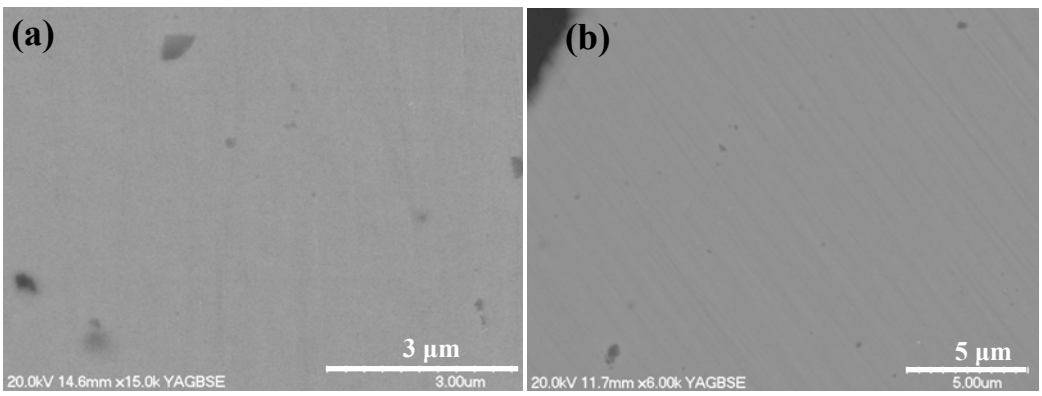


Figure 3.34: SEM backscattered electron images of the cross sections of Cu-10vol.%$Al_2O_3$ composite powder particles produced by HEMM after different milling times, (a) after 12 hours milling, Route 1, (b) after 24 hours milling, Route 2.

# 3.4 Microhardness

## 3.4.1 Distribution of Microhardness of Cu-$Al_2O_3$ Composite Balls/Granules

For each of the randomly selected Cu and Cu-2.5vol.%$Al_2O_3$ hollow balls, their through-centre cross sections were subjected to indentations along two perpendicular lines passing through the centre to determine the microhardness distribution. The indents were 100 μm apart along each line. Figures 3.35(a) and 3.35(b) show the distribution of the microhardness across the wall thickness of the selected Cu hollow balls produced after 6 hours and 12 hours of milling, respectively. As shown in Figure 3.35(a), the microhardness of the wall near the external surface of the balls produced after 6 hours of milling decreased from the external surface. The microhardness of the wall after 12 hours of milling was almost constant across the majority of the wall thickness, and then suddenly dropped to lower values, as shown in Figure 3.35(b). Figures 3.36(a) and 3.36(b) show the distribution of the microhardness across the wall thickness of the selected Cu-2.5vol.%$Al_2O_3$ composite hollow balls produced after 6 hours and 12 hours of milling, respectively. As shown in Figure 3.36(a), the microhardness of the wall material near the external surface of the ball produced after 6 hours of milling was clearly higher than that of the wall material away from the external surface. The microhardness of the wall after 12 hours of milling was more uniform, and it appeared that microhardness of the material near the internal surface of the balls was higher than that near the middle line of the wall and the external surface, as shown in Figure 3.36(b).

To determine the microhardness distribution for the randomly selected Cu-5vol.%$Al_2O_3$ composite granules, its through-centre cross section was subjected to indentations along two perpendicular lines passing through the centre. The indents were 150 μm apart along each line. Figures 3.37(a) and 3.37(b) show the distribution of the microhardness across the diameters of the selected Cu-5vol.%$Al_2O_3$ composite granules produced after 6 hours and 12 hours of milling, respectively. The microhardness investigation on the granules showed that for both 6 hours (Figure 3.37(a)) and 12 hours (Figure 3.37(b)) milled Cu-5vol.% $Al_2O_3$ composite granules, the microhardness distribution was fairly uniform. However, it appears that there might be an oscillation of the microhardness of the

material along the diameter of each granule, especially for the 6 hours milled granules (Figure 3.37(a)). This indicates that there might be a microstructure variation associated with the powder consolidation process during HEMM. Once again, there are some locations which show material microhardness much lower than average microhardness of the granules, which is likely caused by cracks lying underneath or very close to the indents produced at these locations.

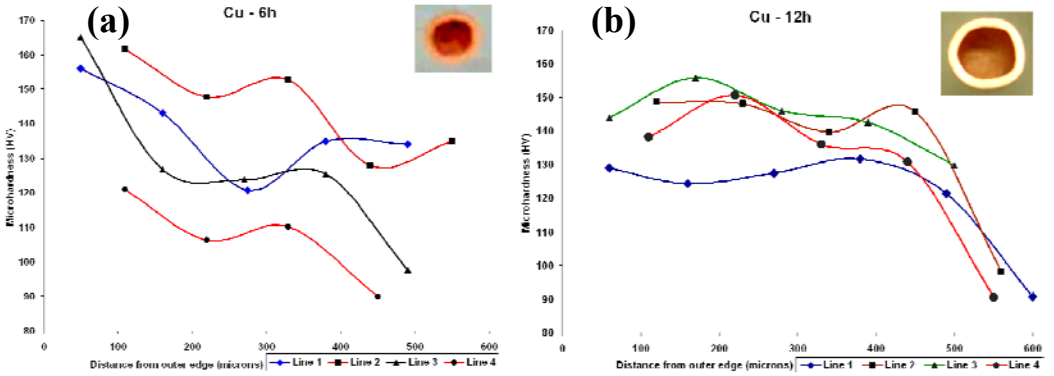


Figure 3.35: Microhardness vs distance from outer edge of the wall of Cu balls produced by HEMM with different milling times using Route 1, (a) after 6 hours milling, and (b) after 12 hours milling.

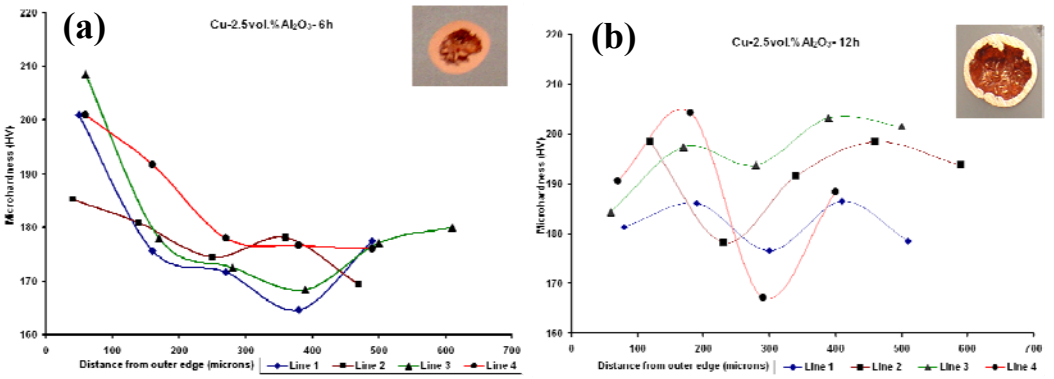


Figure 3.36: Microhardness vs distance from outer edge of the wall of Cu-2.5vol.%$Al_2O_3$ composite balls produced by HEMM with different milling times using Route 1, (a) after 6 hours milling, and (b) after 12 hours milling.

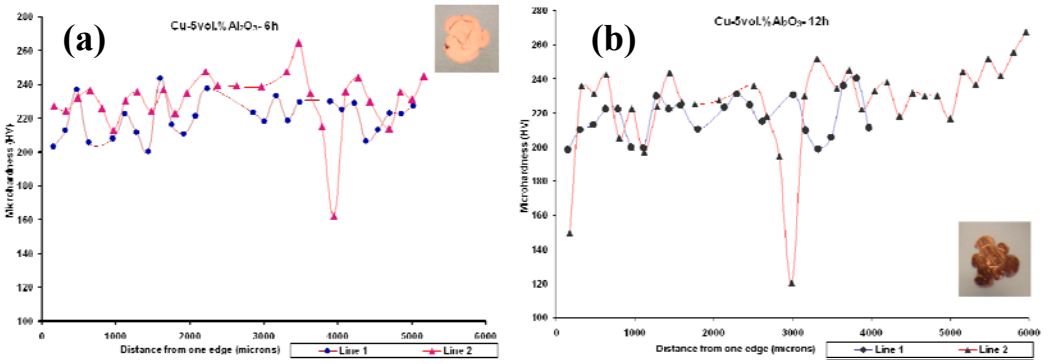


Figure 3.37: Microhardness vs distance from one edge along the diameter of Cu-5vol.%$Al_2O_3$ composite granule produced by HEMM with different milling times using Route 1, (a) after 6 hours milling, and (b) after 12 hours milling.

## 3.4.2 Effect of Composition and Milling Time

The as-received pure Cu powder particles showed an average microhardness of 100 HV. The average microhardness of Cu powder particles produced by 6 hours milling with 0.6wt%PCA was 72 HV. The microhardness increased dramatically to 176 HV with the increase of milling time from 6 hours to 12 hours, as shown in Figure 3.38. The average microhardness of the as-milled Cu balls produced by 6 hours milling without PCA was 137 HV and remain unchanged after 12 hours of milling (Route 1), as shown in Figure 3.38. Increasing the milling severity and milling time up to 18 hours and 24 hours, Route 2, caused a significant increase in the average microhardness.

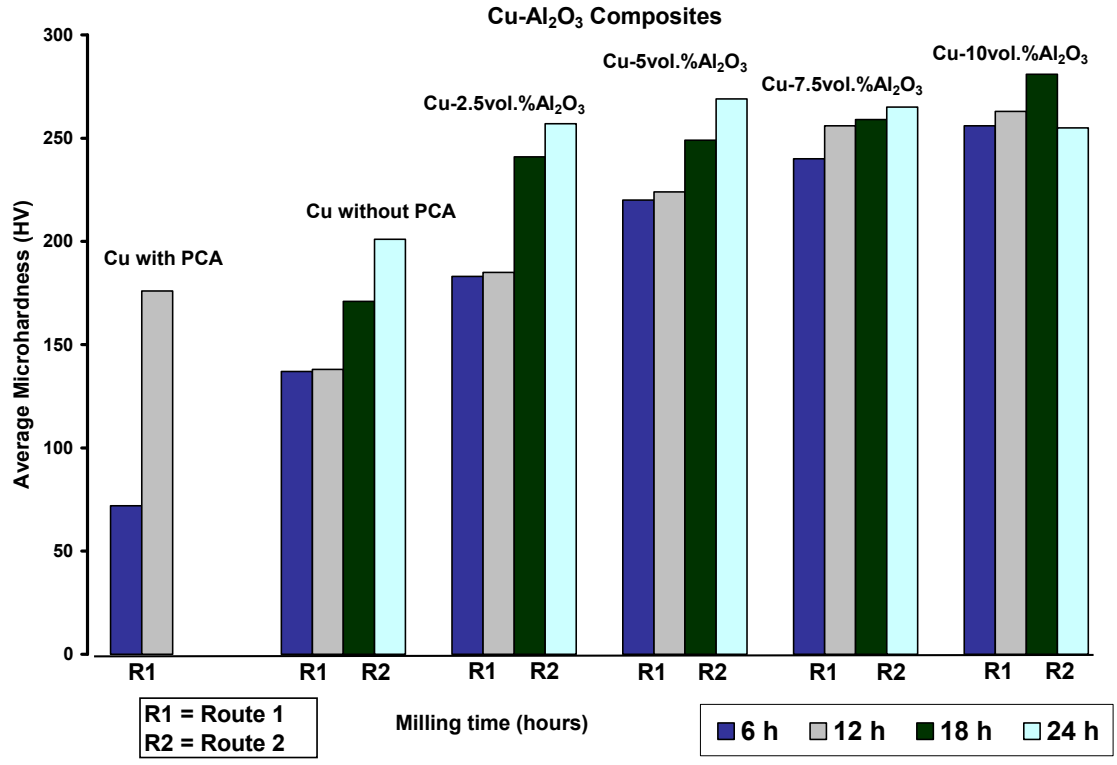


Figure 3.38: The average microhardness of as-milled Cu powder with 0.6wt%PCA, Cu balls/ powder particles and Cu-(2.5-10)vol.%$Al_2O_3$ composite balls/granules/powder particles produced by HEMM using Route 1 and Route 2, respectively.

The average microhardness of balls, granules and powder particles of Cu-(2.5-10) vol.%$Al_2O_3$ composites produced under different milling condition for different times was determined. Figure 3.38 also shows the average microhardness of as-milled Cu balls/powder particles and Cu-(2.5-10)vol.%$Al_2O_3$ composite balls/ granules/powder particles produced by HEMM after 12 hours (Route 1) and 24 hours (Route 2) of milling, respectively.

In the first 6 hours of milling (Route 1) and increasing the content of the $Al_2O_3$ nanoparticles from zero to 2.5vol.% of the balls, a significant increase in the

average microhardness was shown. Increasing the volume fraction of $Al_2O_3$ nanoparticles from 2.5% to 5%, the trend of increase in average microhardness continued. Further increasing the volume fraction of $Al_2O_3$ nanoparticles from 5% to 7.5% or 10%, a slight increase in average microhardness was shown in Figure 3.38.

Using Route 1, with 12 hours of milling and increasing the content of the $Al_2O_3$ nanoparticles from zero to 2.5vol.%, a significant increase in the average microhardness was shown. Increasing the volume fraction of $Al_2O_3$ nanoparticles from 2.5% to 5% or 7.5% caused a much more drastic increase of the average microhardness. Further increasing the volume fraction of $Al_2O_3$ nanoparticles from 7.5% to 10%, the increase of the average microhardness virtually stopped, as shown in Figure 3.38.

With the increase of milling severity and time of Cu and Cu-(2.5 and 5)vol.%$Al_2O_3$ composite powder particles (Route 2), a dramatic increase in the average microhardness was shown. This trend disappeared for Cu-(7.5 and 10)vol.%$Al_2O_3$ composite powder particles (Route 2).

Using Route 2, with 24 hours of milling which involves milling for a longer time under a more severe plastic deformation condition, the average microhardness of the powder particles increased significantly with increasing the content of $Al_2O_3$ nanoparticles from zero to 2.5vol.%, as shown in Figure 3.38. With increasing the volume fraction of $Al_2O_3$ nanoparticles from 2.5% to 5%, the increase of average microhardness was relatively smaller. Further increase in the volume fraction of $Al_2O_3$ nanoparticles from 5% to 7.5% or 10%, the average microhardness of the composite powder particles even decreased, suggesting that the dispersion of $Al_2O_3$ nanoparticles in the Cu matrix and milling severity has no effect on microhardness of powder particles.

In examining the effect of increasing milling time and milling severity on the microhardness of the Cu-$Al_2O_3$ powder particles, it was found that increasing the milling time from 12 hours (Route 1) to 24 hours (Route 2), the increase in average microhardness is significant for the Cu-2.5vol.%$Al_2O_3$ and Cu-5vol.%$Al_2O_3$ composite powder particles.

## 3.5 Discussion

High energy ball milling was previously used on consolidation of ductile powders such as Al, Cu and Zn [3-6]. The present study has shown that high energy mechanical milling is a versatile method for milling of Cu powder and to disperse nanoscaled $Al_2O_3$ particles into a microscaled Cu matrix [7], which is in agreement with Naser et al [8,9]. As-milled Cu after 12 hours milling was converted to nearly-spherical hollow balls, which is very similar to that which has been observed before [4,7]. A low volume fraction addition of hard and brittle $Al_2O_3$, 2.5% or 5%, to the ductile Cu matrix, led to the formation of hollow balls or granules, which is in agreement with Zhang et al [10]**.** Increasing the milling severity with more plastic deformation converted the hollow balls and granules into Cu-$Al_2O_3$ composite powders [7]. Based on the broadening of the XRD peaks and the Williamson-Hall method, the average grain size of Cu and Cu-(2.5-10)vol.%$Al_2O_3$ composites was calculated, as shown in Figure 3.39. Increasing the amount of $Al_2O_3$ from 5 to 10vol.% in the Cu matrix, the average grain size decreased significantly, as shown in Figure 3.39. The reduction of grain size stopped with the increase in milling time, milling severity and volume fraction of $Al_2O_3$ from 7.5% to 10%, as shown in Figure 3.39. The estimated grain sizes of Cu and Cu-$Al_2O_3$ composites (Figure 3.40) were calculated using the Scherrer equation which showed a better understanding of the grain size with the increase of milling hours.

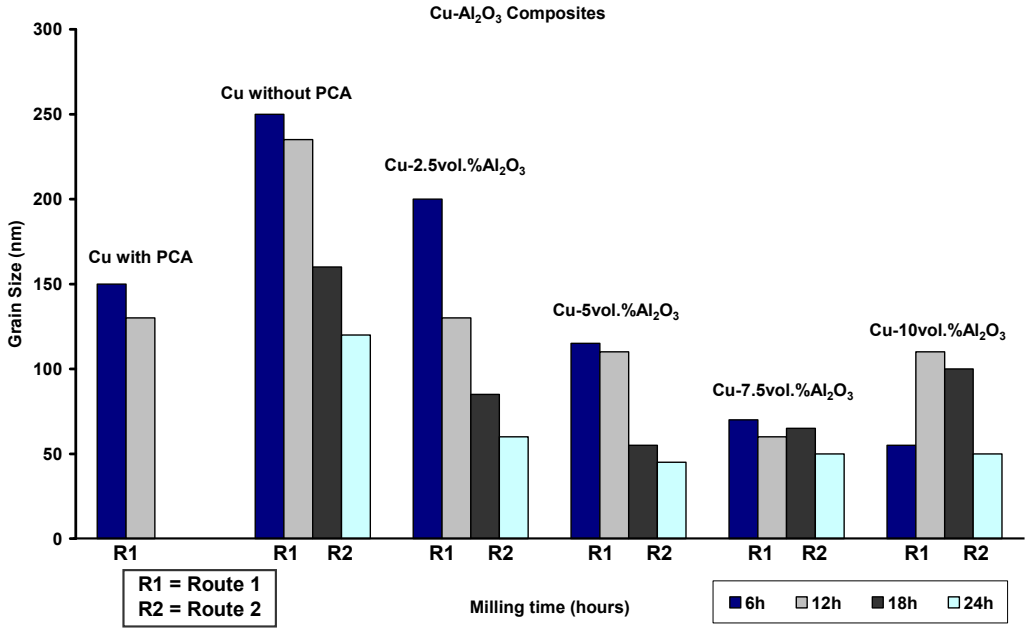


Figure 3.39: The average grain size of as-milled Cu powder with 0.6wt%PCA, Cu balls/powder particles and Cu-(2.5-10)vol.%$Al_2O_3$ composite balls/granules/powders produced by HEMM using Route 1 and Route 2, respectively.

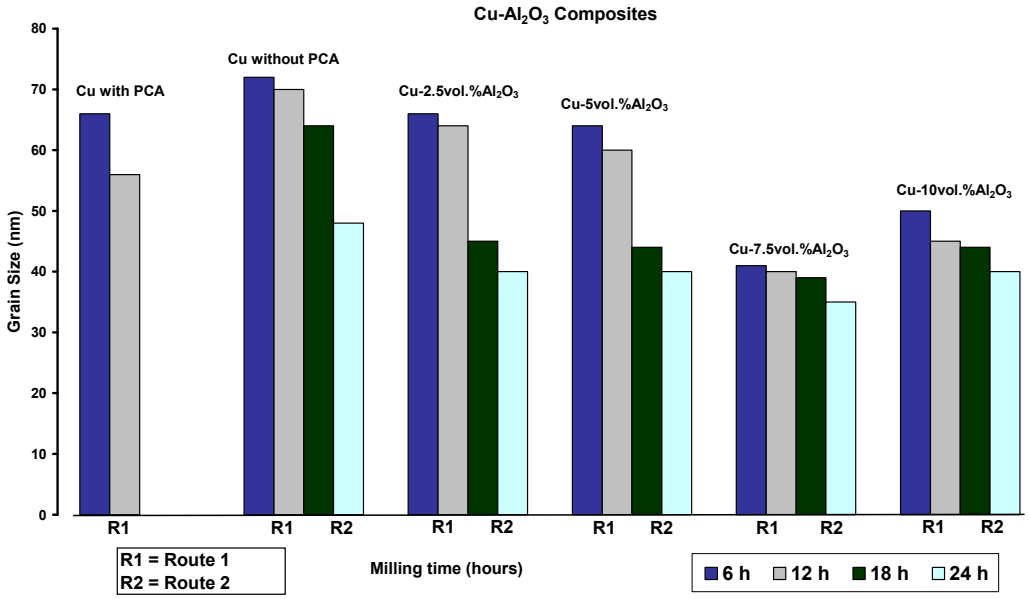


Figure 3.40: The estimated average grain size of as-milled Cu powder with 0.6wt%PCA, Cu balls/powder particles and Cu-(2.5-10)vol.%$Al_2O_3$ composite balls/granules/powders produced by HEMM using Route 1 and Route 2, respectively.

Figure 3.41 shows the lattice strain of Cu and Cu-(2.5-10)vol.%$Al_2O_3$ composites, which was calculated on the broadening of the XRD peaks and Williamson-Hall method. Based on this estimation, the lattice strain increased significantly for the Cu powder particles produced using Route 2. With the increase of the volume fraction of $Al_2O_3$ from 2.5% to 5%, lattice strain showed a decreasing trend. Increasing the volume fraction of $Al_2O_3$ from 7.5 to 10% and/or using more milling severity, the lattice strain started increasing due to strain hardening.

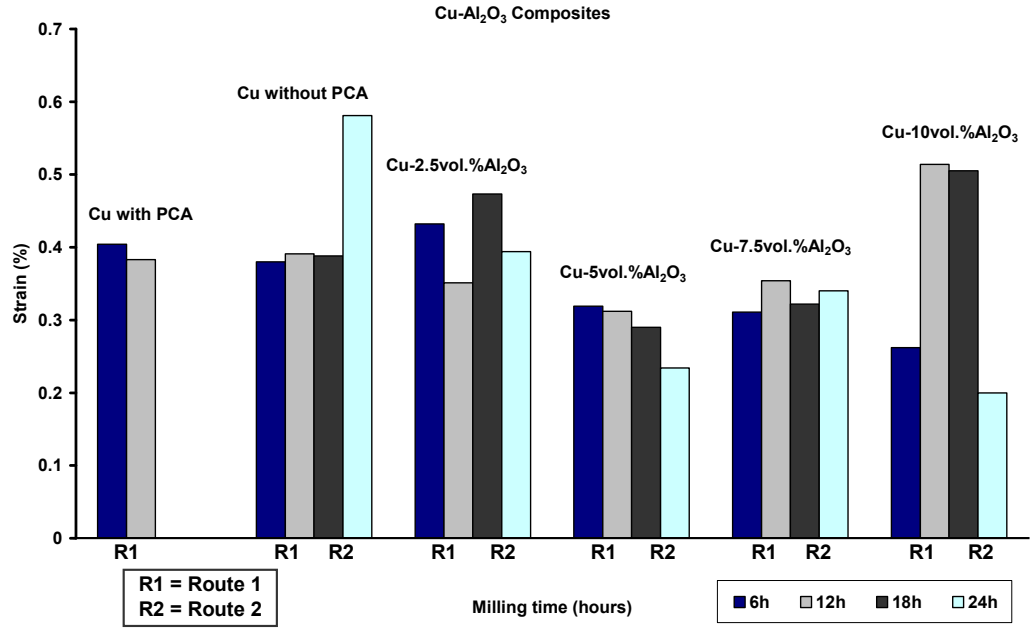


Figure 3.41: Lattice strain data of as-milled Cu powder with 0.6wt%PCA, Cu balls/powder particles and Cu-(2.5-10)vol.%$Al_2O_3$ composite balls/granules/powders produced by HEMM using Route 1 and Route 2, respectively.

$Al_2O_3$ nanoparticles were homogenously distributed in Cu matrix as observed before [8,9]. Increasing the volume fraction of $Al_2O_3$ powder in the starting mixture of Cu and $Al_2O_3$ powders led to enhanced effectiveness of milling in refining the Cu grains. As the grain size decreased with milling time, the hardness of the Cu-$Al_2O_3$ composite increased, as observed by Zhang et al [11]. For the bulk Cu-(2.5vol.% or 5vol.%)$Al_2O_3$ composite material, produced by HEMM of Cu and $Al_2O_3$ powders, the distribution of the microhardness was clearly affected by the composition of the material and the stages of the milling.

The distribution of the microhardness showed that the bulk Cu-(2.5vol.% or 5vol.%)$Al_2O_3$ composite material, produced by HEMM of Cu and $Al_2O_3$ powders, is clearly affected by the composition of the material and the stages of the milling. The microhardness increases for the Cu-$Al_2O_3$ composite powders with the dispersion of $Al_2O_3$ particles, which is in agreement with Rajkovic et al [12,13]. In examining the effect of increasing milling time and milling severity on the microhardness of the Cu-$Al_2O_3$ composites, the increase in average microhardness is significant for the volume fractions of 2.5% and 5% of $Al_2O_3$ nanoparticles. This study also reported that no stronger effect on the microhardness was observed with increasing the volume fraction of $Al_2O_3$ nanoparticles from 7.5% to 10% in Cu matrix.

## 3.6 Summary

In this study, HEMM consisting of two different routes was used to fabricate UFG and nanostructured Cu-(2.5-10)vol.%$Al_2O_3$ composites with a dispersion of $Al_2O_3$ nanoparticles. The microstructure of the composite powder particles was studied in detail to understand the morphological, macrostructural and microstructural evolution mechanisms of the granules and powder particles during HEMM and with the addition of volume fractions of $Al_2O_3$ nanoparticles. Change in microhardness was examined for the as-milled balls, granules and powder particles with the addition of volume fractions of $Al_2O_3$ nanoparticles. The average microhardness of Cu-(2.5-10)vol.%$Al_2O_3$ composites produced using Route 1, shows significant increase, with increasing volume fraction of $Al_2O_3$ nanoparticles from 2.5 to 7.5%.

## 3.7 References

1. B.D. Cullity, *Elements of X-ray Diffraction*, 1978, Addison-Wesley Publishing Company, Inc.

2. G.K. Williamson and W. Hall, *Acta Metallurgica* **1**, 1953, 22

3. A.M. Harris, G.B. Schaffer and N.W. Page, *J. Mater. Sci. Lett.,* **12**, 1993, 1103

4. A.M. Harris, G.B. Schaffer and N.W. Page, *Scripta. Mater.* **34**, 1996, 67

5. J.Y. Huang, Y.K. Wu and H.Q. Ye, *Mater. Sci. Eng. A* **199**, 1995, 165

6. X. Zhang, H. Wang, M. Kassem, J. Narayan and C.C. Koch, *Scripta Mater.*, **46(9)**, 2002, 661

7. D.L. Zhang, A. Mukhtar, C. Kong and P. Munroe, *J. Phys. Conference series* **144,** 2009, 012028

8. J. Naser, H. Ferkel and W. Riehemann, *Mater. Sci. Eng. A* **234–236**, 1997, 470

9. J. Naser, W. Riehemann and H. Ferkel, *Mater. Sci. Eng. A* **234–236**, 1997, 467

10. D.L. Zhang, S. Raynova, C.C. Koch, R.O. Scattergood and K.M. Youssef, *Mater. Sci. Eng. A* **410-411**, 2005, 375

11. D.L. Zhang, C.C. Koch, R.O. Scattergood and K.M. Youssef, *J. Metastable and Nanocrystalline Mater.*, **24-25**, 2005, 639

12. V. Rajkovic, D. Bozic and M.T. Jovanovic, *J. Mater. Process. Technol.,* **200**, 2008, 106

13. V. Rajkovic, D. Bozic and M.T. Jovanovic, *J. Alloys and Compd*., **459**, 2008, 177

# Chapter Four

# Thermal Stability of Cu-(2.5-10)vol.%$Al_2O_3$ Composite Balls/Granules/Powders Produced by HEMM

## 4.1 Introduction

The key factor to determine the thermal stability of nanostructured metallic materials is not only the stability of the microstructure, but also the stability of the structure of the grain boundaries. Grain growth and phase transformations will alter the properties of nanocrystalline materials when exposed at elevated temperatures. There are two ways in which grain growth can be minimized : the first one involves grain boundary pinning by various methods, which include pinning by impurity atom atmosphere drag, pores and second phases, while the second one involves a thermodynamic approach involving the reduction in grain growth by reducing the grain boundary energy. Since the ultrafine and nanostructured powders need to be consolidated at elevated temperatures [1], it is important to understand their microstructural stability at elevated temperatures. Thermal stability is considered as one of the most critical factors for consolidation of nanostructured powders without significantly coarsening the microstructure [2,3].

In this chapter the focus is on UFG and nanostructured Cu and Cu-$Al_2O_3$ composite balls/granules/powders, which were heat treated at 150, 300, 400 and 500°C for 1 hour, respectively, to determine the microstructural and microhardness changes of the Cu and Cu-$Al_2O_3$ composite powder particles produced by HEMM as a function of annealing temperature.

## 4.2 Microstructural Changes during Heat Treatment

### 4.2.1 Pure Cu

Figures 4.1 and 4.2 show the XRD patterns of UFG Cu balls/powder particles produced by HEMM after 12 hours (Route 1) and 24 hours (Route 2) and after annealing at different temperatures, respectively. For the balls produced using Route

1, annealing at 150°C caused clear further broadening of the Cu peaks in the XRD peaks, as shown in Figure 4.1, which indicates that the grain sizes of the Cu balls decreased after annealing, very likely due to recrystallisation. The estimated grain size of Cu balls and powder produced using Route 1 and Route 2 was determined using Scherrer Equation [4]. Based on this estimation, the Cu grain size of the 12 hours milled balls decreased and remained almost unchanged with the increase of annealing temperature from 150 to 500°C, as shown later in Figure 4.50. The average grain sizes and lattice strains of Cu balls and powder were determined using the Williamson-Hall method [5] and broadening of the XRD peaks. Based on this estimation, the Cu grain size of the 12 hours milled balls with the increase of annealing temperature from 150 to 500°C was in the range of 60-100 nm, as shown in Figure 4.3.

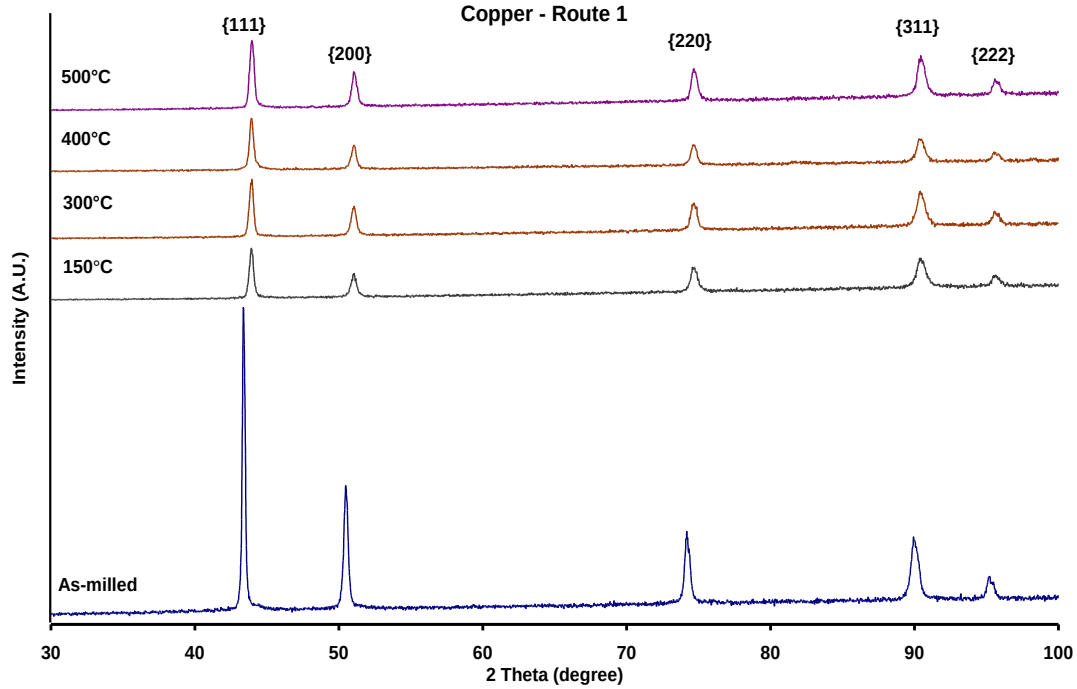


Figure 4.1: X-ray diffraction patterns of Cu balls produced by HEMM after 12 hours, Route 1, and after annealing at 150, 300, 400 and 500°C, respectively.

The lattice parameter, a, of Cu as a function of annealing temperature was calculated using the Cu{111} peaks of the XRD patterns. Figure 4.1 shows that Cu{111} peak shifted 0.55° to the larger angle for Cu balls produced after 12 hours and after annealing at 150°C, which caused the Cu lattice parameter to decrease by 0.0043 nm, this might be due to the diffusion of oxygen from furnace atmosphere.

For the as-milled powder particles produced using Route 2, broadening of the Cu peaks in the XRD pattern remained almost unchanged with increasing annealing temperature from 150 to 500°C, as shown in Figure 4.2, indicating that the grain sizes of the Cu powder particles had not increased significantly. Based on Scherrer equation, the Cu grain size of the 24 hours milled powder slightly increased with the increase of annealing temperature from 150 to 500°C, as shown in Figure 4.51. However, based on the broadening of the Cu peaks and Williamson-Hall Method, the Cu grain size of the 24 hours milled powder particles with the increase of annealing temperature from 150 to 500°C was in the range of 65-115 nm, as shown in Figure 4.3.

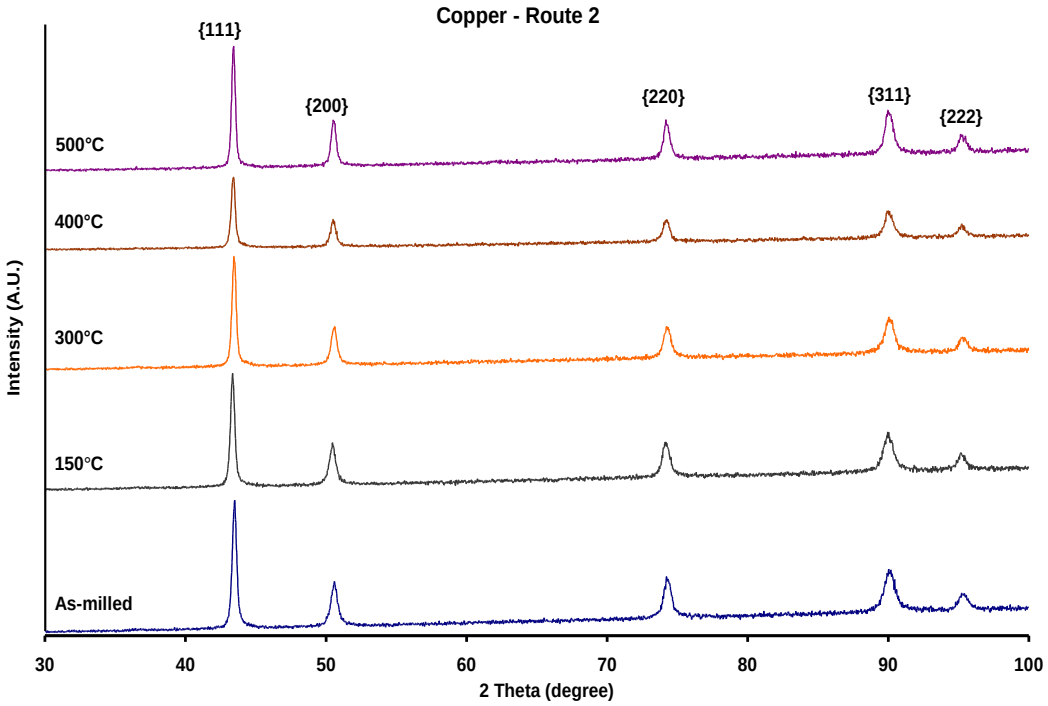


Figure 4.2: X-ray diffraction patterns of Cu powder produced by HEMM after 24 hours, Route 2, and after annealing at 150, 300, 400 and 500°C, respectively.

The average grain size and lattice strain data of the UFG Cu balls/powder particles produced using Route 1 and Route 2 and after annealing at different temperatures were estimated using the broadening of the XRD peaks and Williamson-Hall method, as shown in Figure 4.3. Grain sizes decreased significantly for the Cu balls produced using Route 1 and after heat treatment at 150°C, as compared to Cu powder particles produced using Route 2. However the grain size remained almost similar for UFG Cu

balls/powder particles produced using Route 1 and Route 2 after increasing the annealing temperatures from 150 to 500°C. On the other hand, lattice strain calculations showed a similar trend for the UFG Cu balls/powder particles produced using Route 1 and Route 2 after increasing the annealing temperature to 300°C, while the lattice strain was much higher for the Cu grains produced using Route 2 and annealed at 500°C.

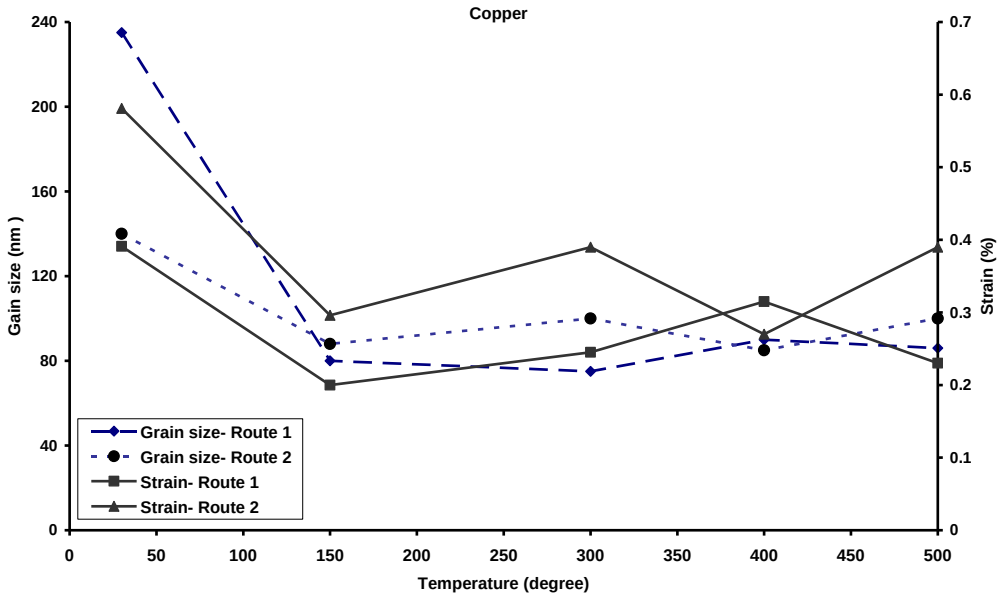


Figure 4.3: Average grain size and lattice strain data of Cu balls/powder particles produced by HEMM after 12 hours (Route 1) and 24 hours (Route 2) and after annealing at 150, 300, 400 and 500°C, respectively.

Based on TEM examination, the Cu grain size of the Cu powder particles produced after 24 hours reduced from 100-300 nm (Figure 3.9(c)) to 50-200 nm (Figures 4.4(a) and 4.4(c)) after annealing at 150 and 300°C, mainly due to recrystallisation. With the increase of annealing temperature from 300 to 500°C, the Cu grain sizes remained in the range of 50-250 nm, as shown in Figures 4.5(a) and 4.5(c), suggesting that there is less coarsening of the Cu grains during heat treatment. The majority of the Cu grains after annealing were smaller than the Cu grain sizes of as-milled powder particles. TEM bright field images also confirmed that the increase of the Cu grain size of Cu powder particles produced using Route 2 is very much less, as shown by the broadness of Cu peaks in XRD patterns (Figure 4.2). Almost continuous rings were observed in the selected area diffraction patterns (SADPs) for the UFG Cu

powder produced using Route 2 and annealed at 150, 300 and 400°C (Figures 4.4(b), 4.4(d) and 4.5(b)), showing strong reflections for Cu ({111}, {200}, {220}, {311}). The rings were replaced by discrete diffraction reflections for the 24 hours Cu powder particles, as shown in SADP (Figure 4.5(d)). This is presumably in relation to the normal grain growth during annealing, and only very limited number of large grains were present within the selected area.

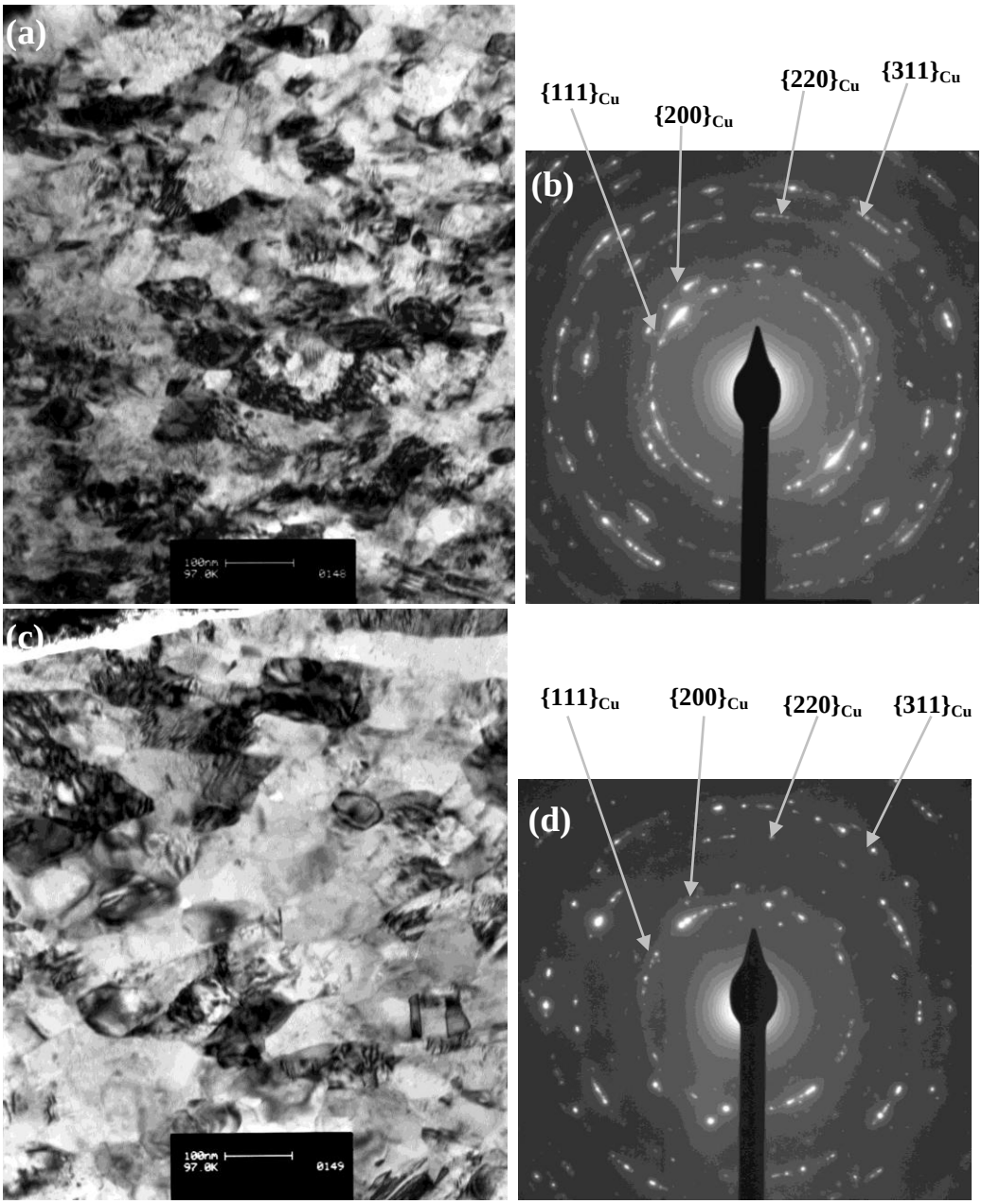


Figure 4.4: TEM bright field images and SADPs of Cu powder particles produced by HEMM after 24 hours, Route 2, and after annealing at 150 and 300°C, respectively.

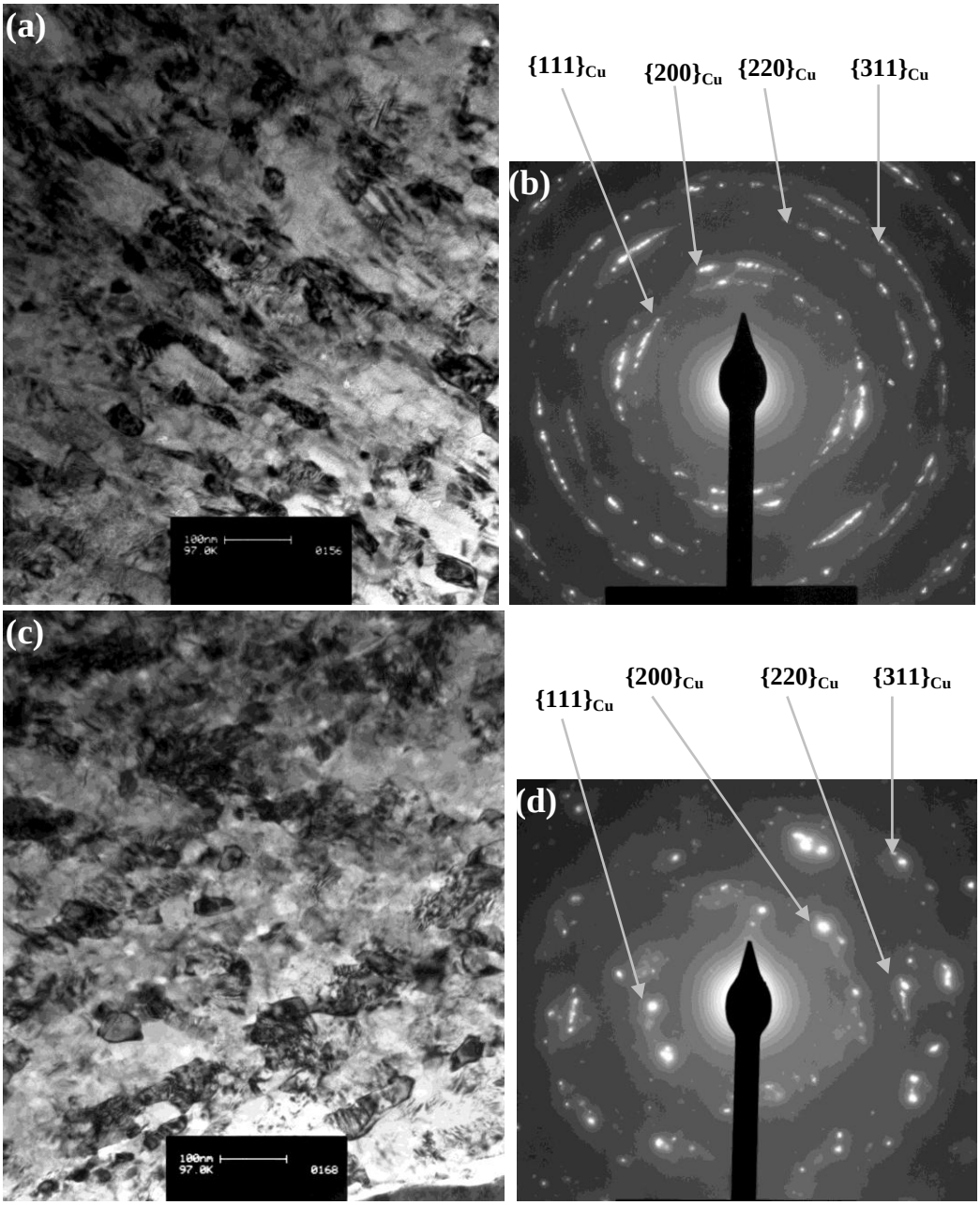


Figure 4.5: TEM bright field images and SADPs of Cu powder particles produced by HEMM after 24 hours, Route 2, and after annealing at 400 and 500°C, respectively.

Figure 4.6 shows the DSC traces obtained by heating the as-milled UFG Cu balls/ powder particles produced using 12 hours (Route 1) and 24 hours (Route 2) from 40 to 650°C. The onset temperatures of the first and second exothermic peaks produced using Route 1 were ~ 390°C and ~ 480°C, respectively. The tail of the second exothermic peak was extended beyond 650°C. With the increase of the milling time from 12 hours to 24 hours, the first exothermic peak became wider with an onset temperature of 370°C. The onset temperature for the second exothermic peak was ~

470°C and amount of heat released was 7.2 J/g with peak temperature at 565°C.

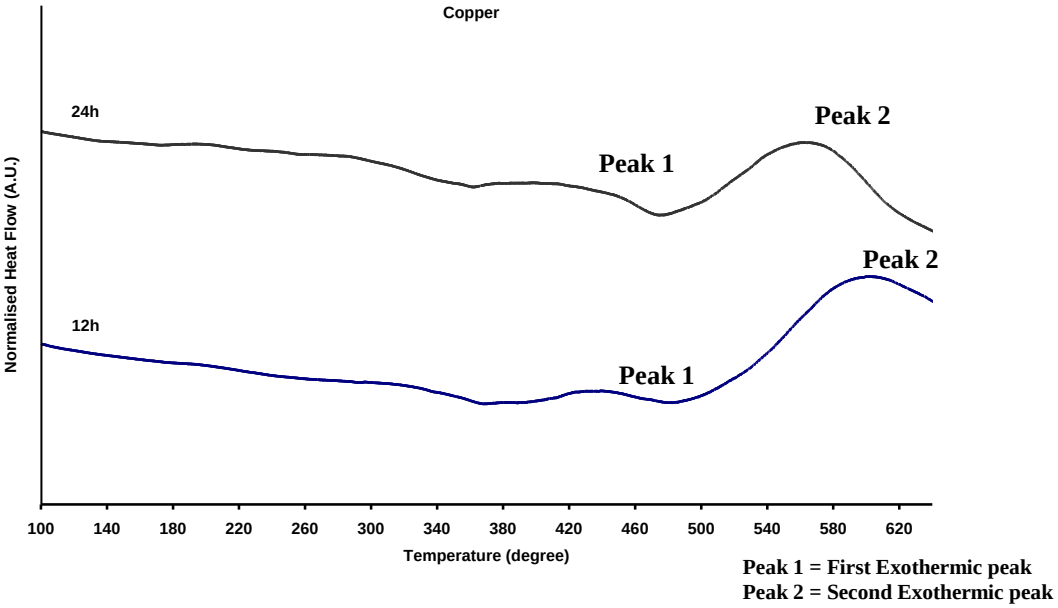


Figure 4.6: DSC traces obtained during heating of Cu balls/powder particles produced after 12 hours (Route 1) and 24 hours (Route 2).

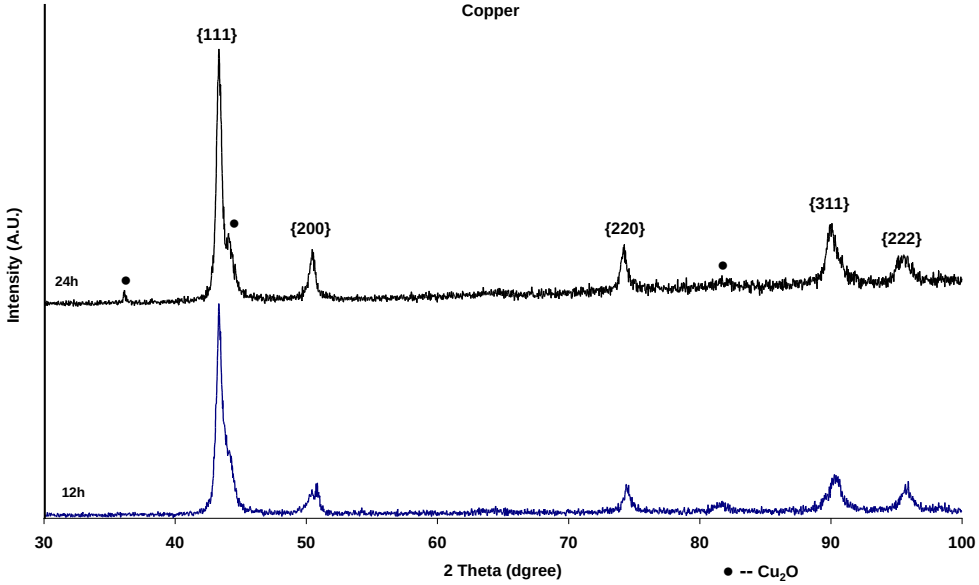


Figure 4.7: XRD patterns of Cu balls/powder produced after 12 hours (Route 1) and 24 hours (Route 2) and after the heating-cooling cycle (heated to 650°C).

After one heating-cooling cycle, the XRD patterns of the UFG Cu balls/powder produced using Route 1 and Route 2 and heated to 650°C showed the Cu peaks and small $Cu_2O$ peaks which are shown in Figure 4.7. The average grain sizes of Cu balls and powder, heated to 650°C, were determined using the Williamson-Hall method and broadening of the XRD peaks. Based on this estimation, the Cu grain size of the 12 hour balls and 24 hour powder particles was ~ 40 nm and 80 nm.

Figure 4.8 shows the XRD patterns of Cu powder with 0.6wt%PCA produced by HEMM after 12 hours (Route 1) and after annealing at different temperatures. The broadening effect for the powder was not significant after annealing at 150°C or higher annealing temperatures. The average grain size of the Cu was estimated using the broadening of the XRD peaks and Williamson-Hall method. Based on this estimation, the Cu grain size of the 12 hours milled powder with the increase of annealing temperature from 150 to 500°C was in the range of 100-125 nm.

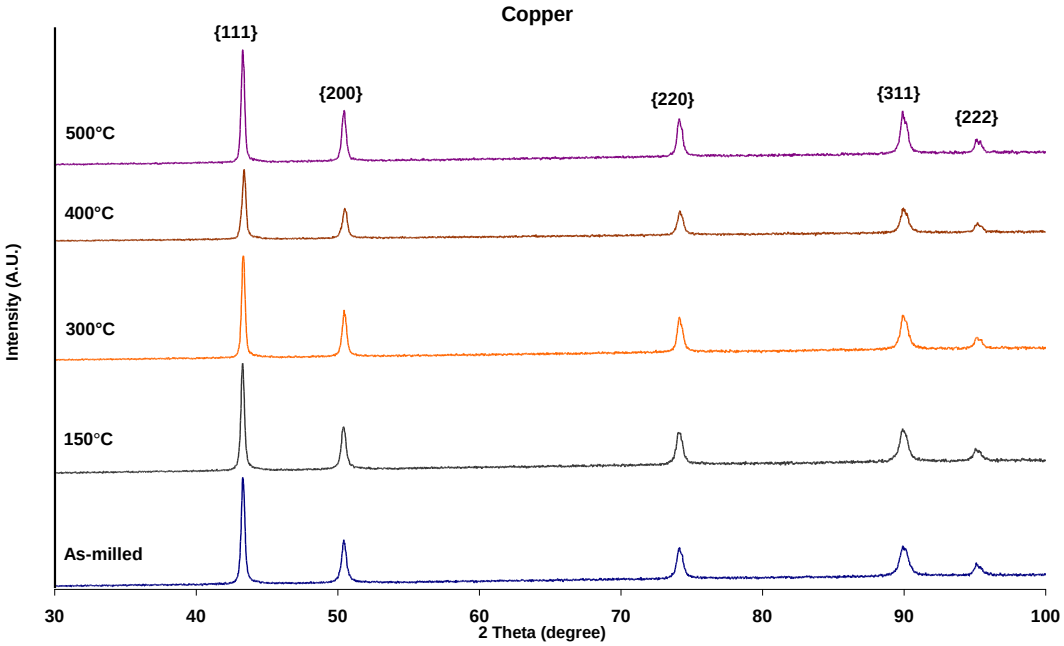


Figure 4.8: X-ray diffraction patterns of Cu powder with 0.6wt%PCA produced by HEMM after 12 hours, Route 1, and after annealing at 150, 300, 400 and 500°C, respectively.

Based on TEM examination, the elongated grains of the Cu powder with 0.6wt%PCA produced after 12 hours, Route 1, and after annealing at 150°C and 300°C, remained almost unchanged, as shown in Figures 4.9(a) and 4.9(c). With the increase of annealing temperature to 500°C, the size of the Cu grains increased in the range of 100-300 nm (Figure 4.9(e)), suggesting coarsening of the Cu grains during heat treatment. Almost continuous rings were observed in the selected area diffraction patterns (SADPs) for the UFG Cu powder 0.6wt%PCA produced using Route 2 and annealed at 150 and 300°C (Figures 4.9(b) and 4.9(d)), showing strong reflections for Cu ({111}, {200}, {220}, {311}). The rings were replaced by discrete diffraction reflections for Cu powder particles, as shown in SADP (Figure 4.9(f)). This is presumably in relation to the significant grain growth during annealing.

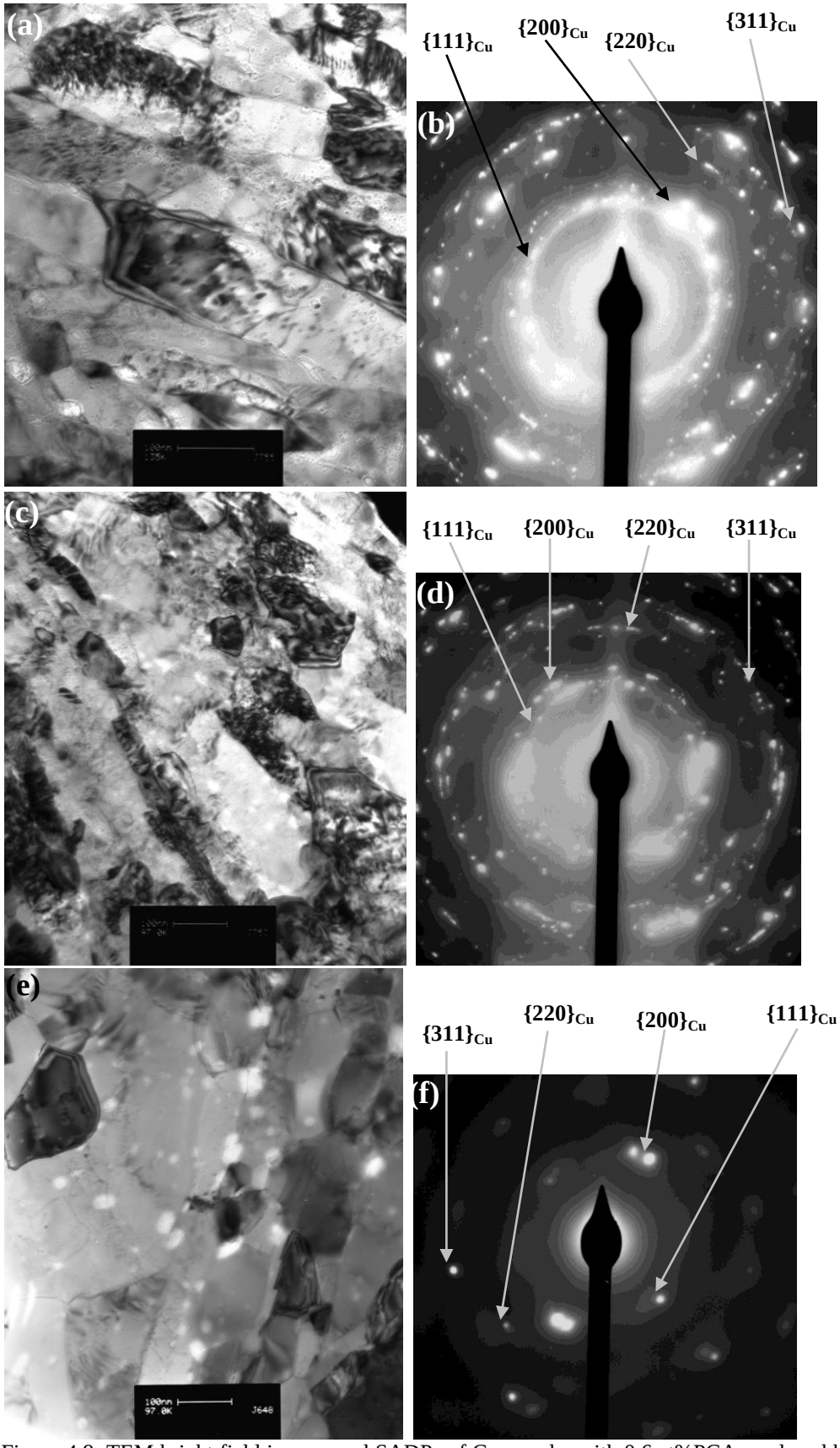


Figure 4.9: TEM bright field images and SADPs of Cu powder with 0.6wt%PCA produced by HEMM after 12 hours, Route 1, and after annealing at 150, 300 and 500°C, respectively.

### 4.2.2 Cu-2.5vol.%$Al_2O_3$ Composite

Figures 4.10 and 4.11 show the XRD patterns of UFG and nanostructured Cu-2.5vol.%$Al_2O_3$ composite balls/powder particles produced after 12 hours (Route 1) and 24 hours (Route 2) and after annealing at different temperatures, respectively. The XRD patterns (Figure 4.10) for the UFG composite balls produced using Route 1 only showed Cu peaks, mainly due to the extremely small size of $Al_2O_3$ nanoparticles. For the balls produced using Route 1, annealing at 150°C caused clear broadening of the Cu peaks in the XRD pattern, as shown in Figure 4.10, which indicated that the grain sizes decreased after annealing, very likely due to recrystallisation of the heavily deformed Cu matrix. Figure 4.10 shows that Cu{111} peak shifted 0.24° to a larger angle for balls produced using Route 1 and after annealing at 300°C, which caused the Cu lattice parameter to decrease 0.0018 nm, perhaps caused by diffusion of oxygen from furnace atmosphere into Cu. Further increase of the annealing temperature caused little change in the broadness of the Cu peaks of the XRD patterns. The estimated grain size of Cu-2.5vol.%$Al_2O_3$ composite balls/powder particles produced using Route 1 and Route 2 was determined using Scherrer Equation [4]. Based on this estimation, the Cu grain size of the 12 hours milled composite balls decreased and remained almost unchanged with the increase of annealing temperature from 150 to 500°C, as shown in Figure 4.50. The average grain sizes and lattice strains of UFG and nanostructured Cu-2.5vol.%$Al_2O_3$ composite balls/powder particles were determined using the Williamson-Hall method and broadening of the XRD peaks. Based on this estimation, the Cu grain size of the 12 hours milled balls with the increase of annealing temperatures from 150 to 500°C was in the range of 45-60 nm, as shown in Figure 4.12.

The XRD patterns (Figure 4.11) for the nanostructured composite powder particles produced using Route 2 showed Cu peaks and extremely small peaks of $Al_2O_3${104} after annealing at 300, 400 and 500°C. The broadness of the Cu peaks of the 24 hours milled composite powder remained almost unchanged with increasing the annealing temperature from 150 to 500°C, as shown by XRD patterns in Figure 4.11. Based on Scherrer equation, the estimated grain size of Cu-2.5vol.%$Al_2O_3$ composite powder particles produced using Route 2 slightly increased with the increase of annealing

temperature from 150 to 500°C, as shown in Figure 4.51. However, based on the Williamson-Hall method and broadening of the XRD peaks, the average Cu grain size of the 24 hours milled powder particles with the increase of annealing temperatures from 150 to 500°C was in the range of 60-150 nm, as shown in Figure 4.12.

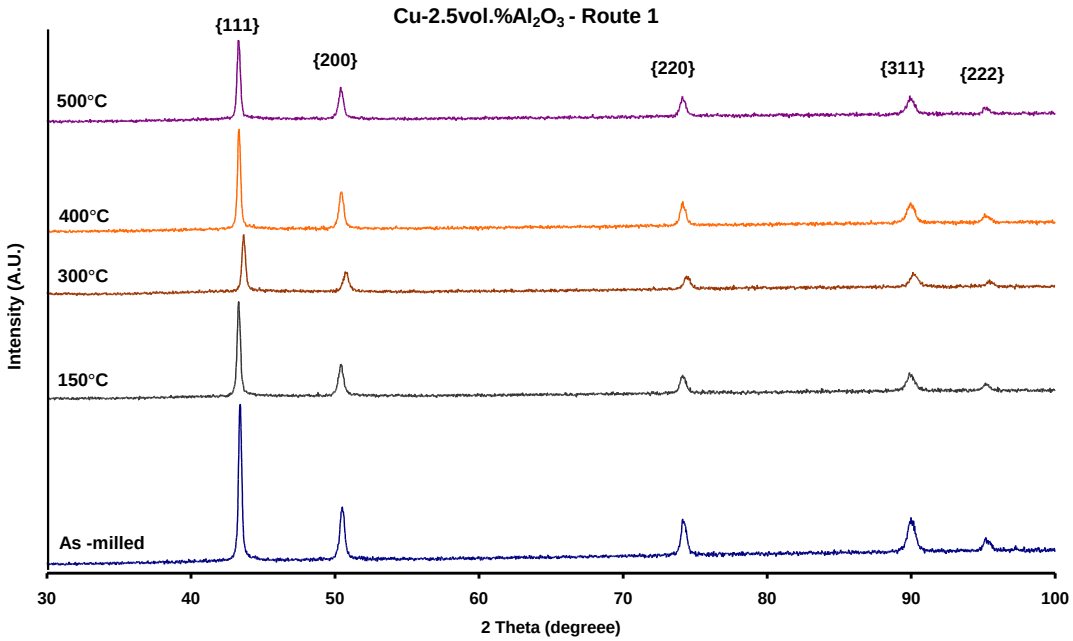


Figure 4.10: X-ray Diffraction patterns of Cu-2.5vol.%$Al_2O_3$ composite balls produced by HEMM after 12 hours, Route 1, and after annealing at 150, 300, 400 and 500°C, respectively.

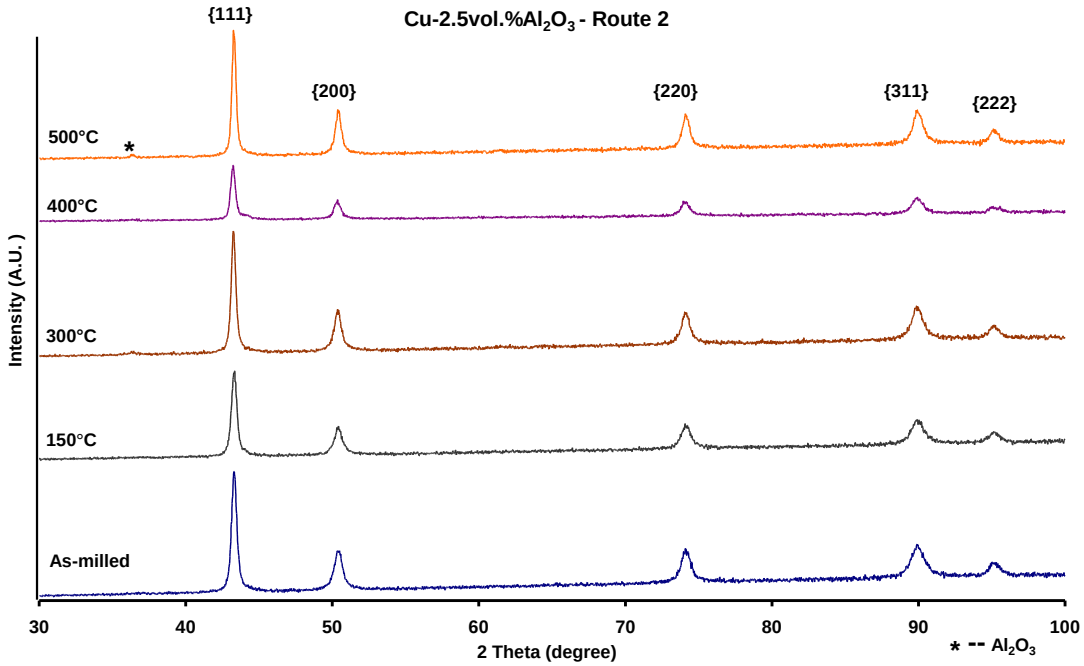


Figure 4.11: X-ray Diffraction patterns of Cu-2.5vol.%$Al_2O_3$ composite powder produced by HEMM after 24 hours, Route 2, and after annealing at 150, 300, 400 and 500°C, respectively.

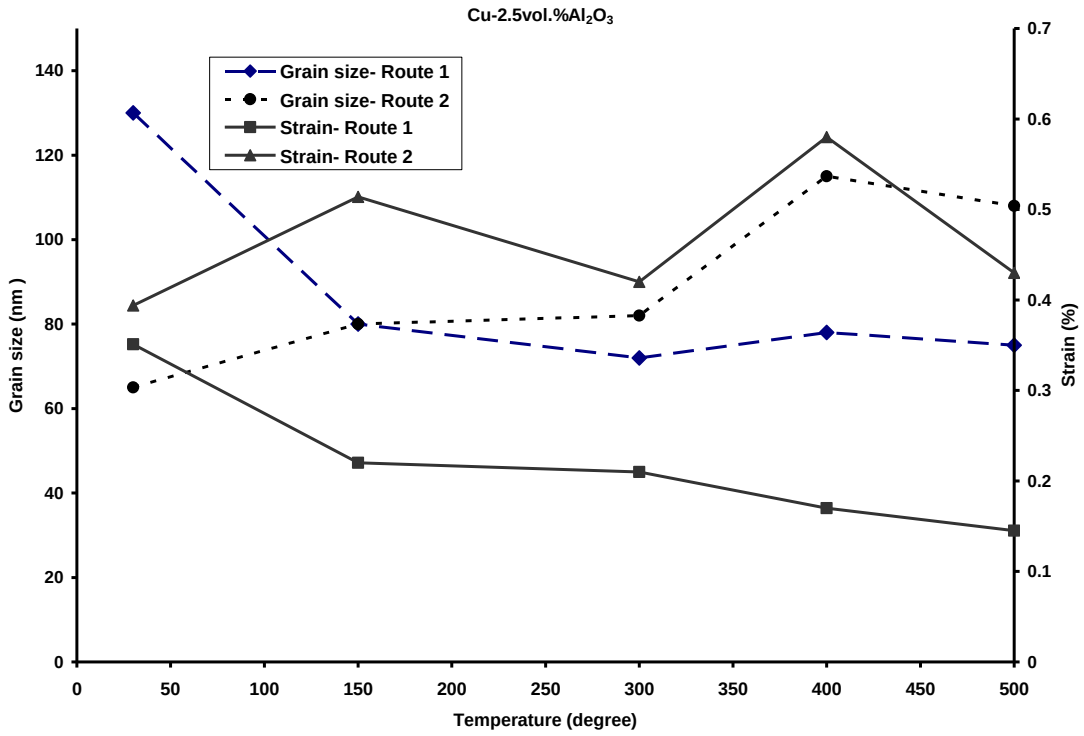


Figure 4.12: Average grain size and lattice strain data of Cu-2.5vol.%$Al_2O_3$ composite balls/powder particles produced by HEMM after 12 hours (Route 1) and 24 hours (Route 2) and after annealing at 150, 300, 400 and 500°C, respectively.

The average grain size and lattice strain data of the UFG and nanostructured Cu-2.5vol.%$Al_2O_3$ composite balls/powder particles produced using Route 1 and Route 2 and after annealing at different temperatures were estimated using the broadening of the XRD peaks and Williamson-Hall method, as shown in Figure 4.12. The grain sizes and lattice strains showed much higher values for the composite powder particles produced using Route 2, suggesting grain coarsening of the Cu matrix, as compared to the composite balls produced using Route 1 after annealing within the range of 150 to 500°C.

Backscattered electron SEM imaging of the cross section of the nanostructured Cu-2.5vol%$Al_2O_3$ composite powder particles produced using Route 2 was carried out to determine the volume fraction and distribution of $Al_2O_3$ nanoparticles. After annealing at 300 and 500°C, the volume fraction of the large $Al_2O_3$ particles with sizes in the range of 100-500 nm (Figures 4.13(a) and 4.13(b)) remained almost unchanged (Figures 3.15(a) and 3.15(b)).

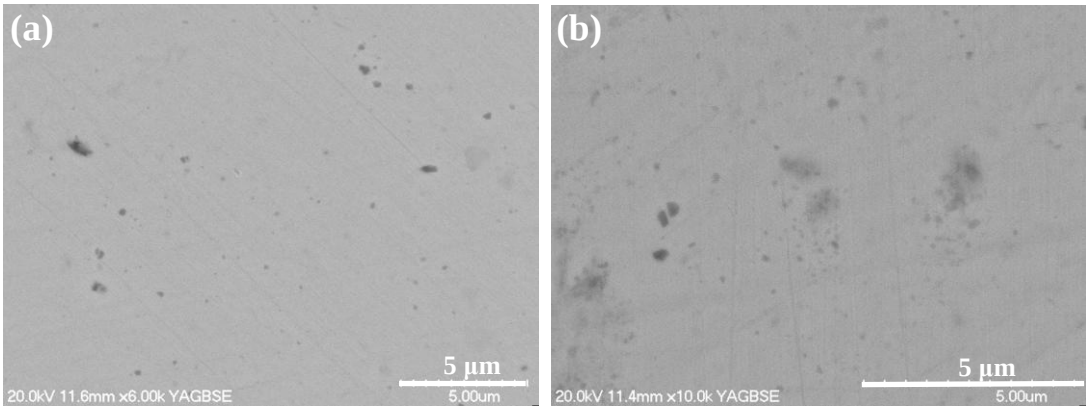


Figure 4.13: Backscattered electron SEM images of Cu-2.5vol.%$Al_2O_3$ composite powder particles produced by HEMM after 24 hours, Route 2, and after annealing at (a) 300°C and (b) 500°C.

Figures 4.14(a), 4.14(c) and 4.14(e) show the TEM bright field images of the UFG and nanostructured Cu-2.5vol.%$Al_2O_3$ composite balls produced using Route 1, and after annealing at different temperatures, respectively. TEM examination showed that grains of the Cu matrix decreased from the range of 100-500 nm (Figures 3.14(a)-(c)) to 100-300 nm (Figure 4.14(a)) due to recrystallisation after annealing at 150°C.

The microstructural refinement as a result of annealing at 150°C was confirmed by TEM examination, as shown in Figure 4.14(a). Increasing the annealing temperatures from 150 to 300°C and 500°C caused a slight increase of the grain sizes of the Cu matrix to 100-400 nm (Figures 4.14(c) and 4.14(e)), due to coarsening of the Cu grains. This showed that the average grain size of Cu matrix estimated using the broadening of the XRD peaks and Williamson-Hall method is clearly smaller than the actual average Cu grain size examined by TEM, and this discrepancy is likely due to overestimate of the broadness of XRD peaks which is directly attributed to the size of the grains. Figures 4.14((b), 4.14(d) and 4.14(f)) show the indexing of SADPs of UFG Cu-2.5vol.%$Al_2O_3$ composite balls produced after 12 hours (Route 1). Based on the SADPs it can be seen that strong reflections ({111}, {200}, {220}, {311}) could be correlated to Cu matrix while weak reflections ({012}, {104}, {300}, {116}) are probably in related to fine $Al_2O_3$ nanoparticles.

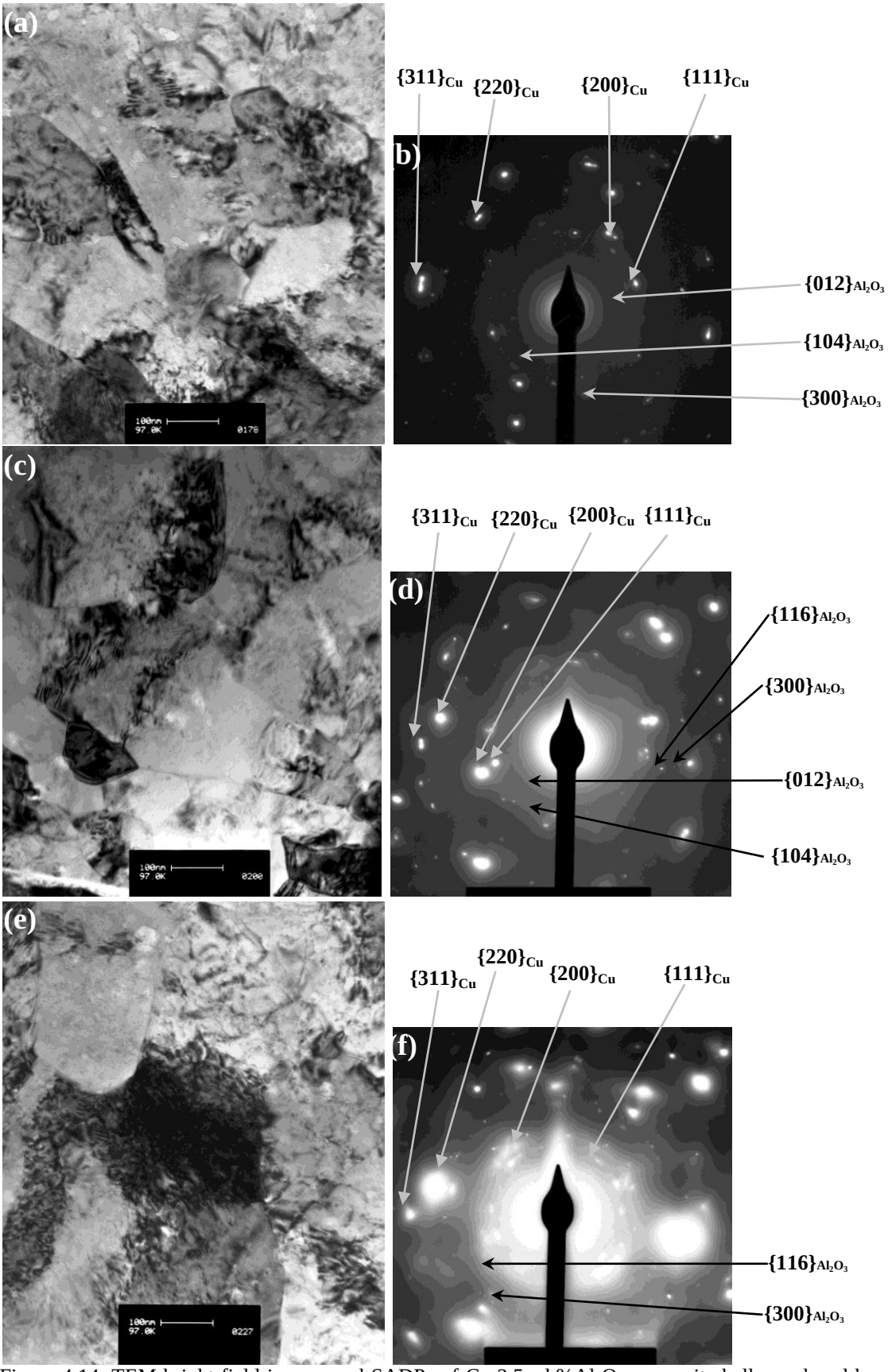


Figure 4.14: TEM bright field images and SADPs of Cu-2.5vol.%$Al_2O_3$ composite balls produced by HEMM after 12 hours, Route 1, and after annealing at 150, 300 and 500°C, respectively.

For the powder produced using Route 2, and based on TEM examination the grains of the Cu matrix slightly decreased to 50-120 nm (Figure 4.15(a)) due to recrystallisation after annealing at 150°C. After annealing at 150°C, the majority of the Cu grains had sizes smaller than 100 nm, showing that the Cu-2.5vol.%$Al_2O_3$ powder particles had a true nanostructured composite structure. With increasing the annealing temperature to 300°C, the sizes of the Cu grains increased to the range of 50-150 nm (Figure 4.15(c)). Annealing at 300°C had little effect on the grain sizes since the nanometer scaled Cu grains were already the result of recrystallisation that occurred during prolonged milling. Further increasing the annealing temperature to 500°C caused coarsening of the Cu grains, with the sizes of Cu grains increasing to 50-300 nm (Figure 4.15(e)), which again showed that the average grain size estimated using the XRD peaks and Williamson-Hall method is smaller than the actual average grain size. In comparison with the Cu-2.5vol.%$Al_2O_3$ balls made using Route 1 and annealed at 500°C, the microstructure of the composite powder produced using Route 2 and annealed at 500°C is much finer, and still in the UFG scale (grain sizes<500 nm).

Figures 4.15((b), 4.15(d) and 4.15(f)) show the indexing of SADPs of nanostructured Cu-2.5vol.%$Al_2O_3$ composite powder particles produced after 24 hours (Route 2). Based on the SADP it can be seen that strong reflections ({111}, {200}, {220}, {311}) could be correlated to Cu matrix while weak reflections ({104}, {300}, {116}) are probably in related to fine $Al_2O_3$ nanoparticles. Indexing of SADPs is recorded from JCPDS files of Cu (04-0836) and $Al_2O_3$ (46-1212), as shown in Appendix A. Almost continuous rings and discrete diffraction reflections for Cu powder particles were observed in the selected area diffraction patterns (SADPs) for the nanostructured composite powder produced using Route 2 and annealed at 150, 300 and 500°C. This is presumably in relation to the normal grain growth during annealing.

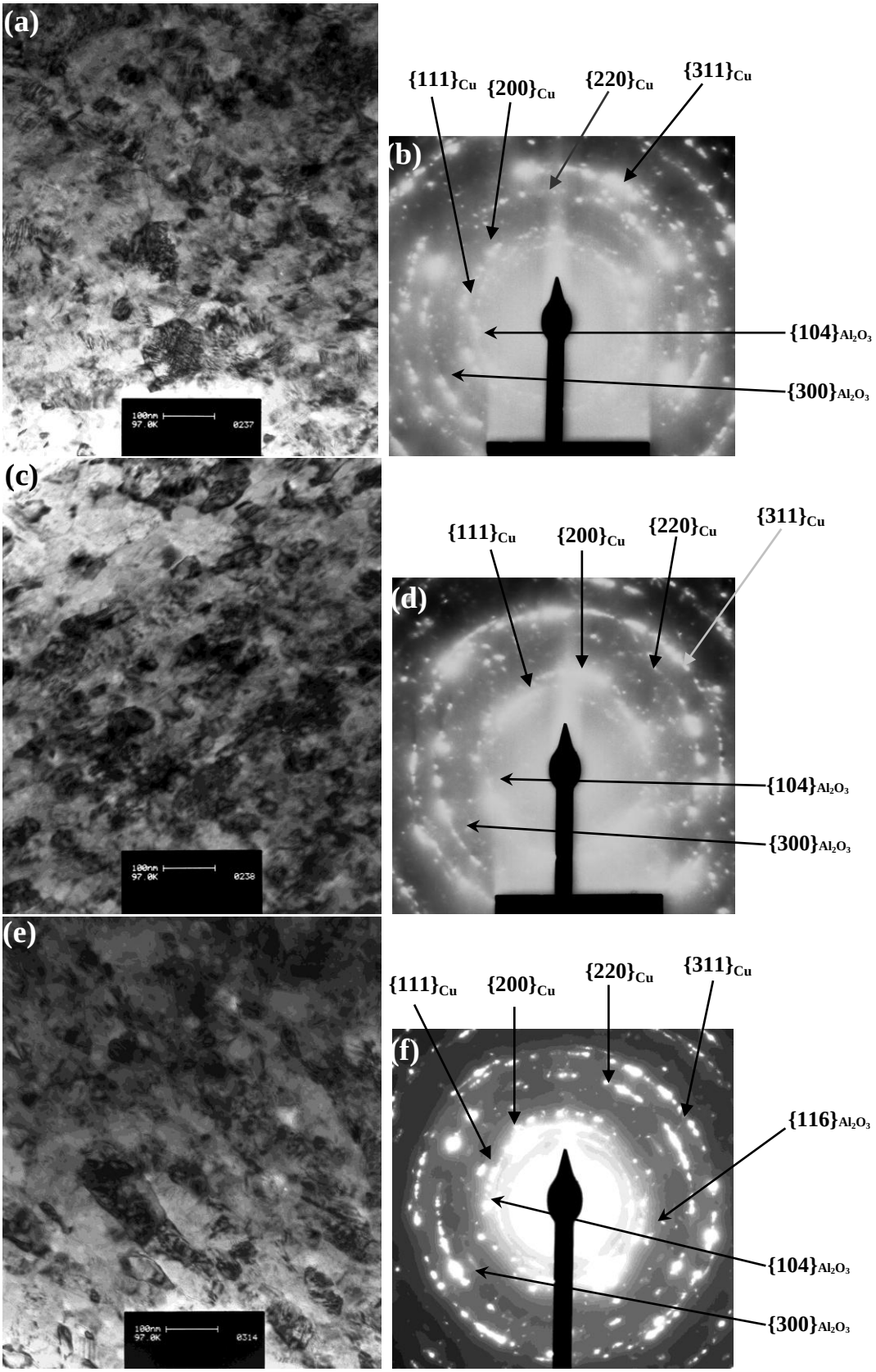


Figure 4.15: TEM bright field images and SADPs of Cu-2.5vol.%$Al_2O_3$ composite powder particles produced by HEMM after 24 hours, Route 2, and after annealing at 150, 300 and 500°C, respectively.

In the STEM images of the Cu-2.5vol.%$Al_2O_3$ composite balls produced after 12 hours, Route 1, as shown in Figures 4.16(a), 4.16(d) and 4.16(g), the bright particles are $Al_2O_3$ nanoparticles as confirmed from the X-ray elemental mapping for Al. The $Al_2O_3$ nanoparticles in Cu matrix formed clusters, with large sizes in the range of 80-100 nm after annealing at 150, 300 and 500°C. Increasing the annealing temperature from 300 to 500°C, more homogenous distribution of $Al_2O_3$ nanoparticles in Cu matrix was examined (Figure 4.16(i)), suggesting the coarsening of $Al_2O_3$ nanoparticles.

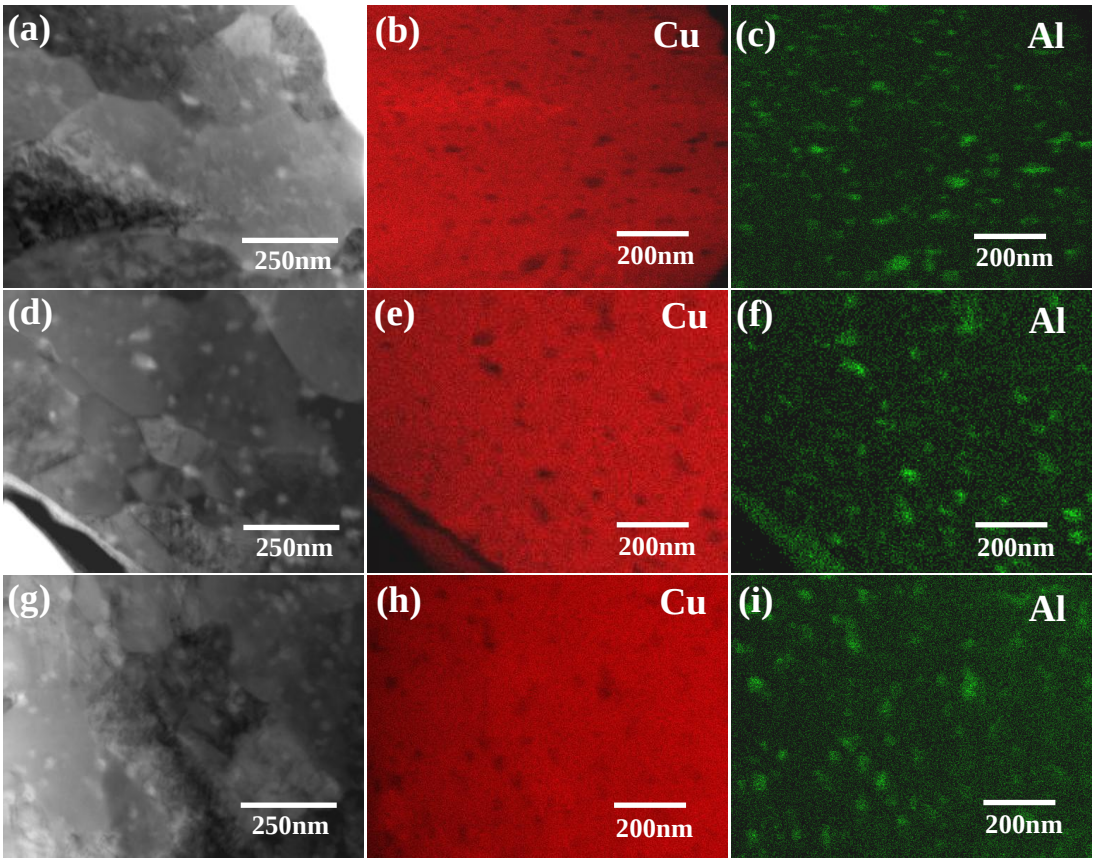


Figure 4.16: STEM images and X-ray elemental (Cu and Al) maps of Cu-2.5vol.%$Al_2O_3$ composite balls produced by HEMM after 12 hours, Route 1, and after annealing at ((a)-(c)) 150°C, ((d)-(f)) 300°C, and ((g)-(i)) 500°C, respectively.

Based on the STEM images and X-ray elemental mapping (Cu and Al) of the nanostructured Cu-2.5vol.%$Al_2O_3$ composite powder particles produced using Route 2 and after annealing at different temperatures, a more homogenous distribution and dispersion of $Al_2O_3$ nanoparticles in Cu matrix was obtained, as compared to composite balls produced using Route 1.

Increasing the annealing temperature from 150°C to 300 and 500°C, the $Al_2O_3$ nanoparticles are finely dispersed in the Cu matrix and with majority of sizes less than 100 nm as confirmed from the X-ray elemental mapping for Al, Figures 4.17(f) and 4.17(i), respectively. In comparison of the X-ray elemental mapping (Al) of the Cu-2.5vol.%$Al_2O_3$ balls made using Route 1 and annealed at different temperatures, the dispersion of $Al_2O_3$ nanoparticles of the composite powder produced using Route 2 and annealed at different temperatures was much finer.

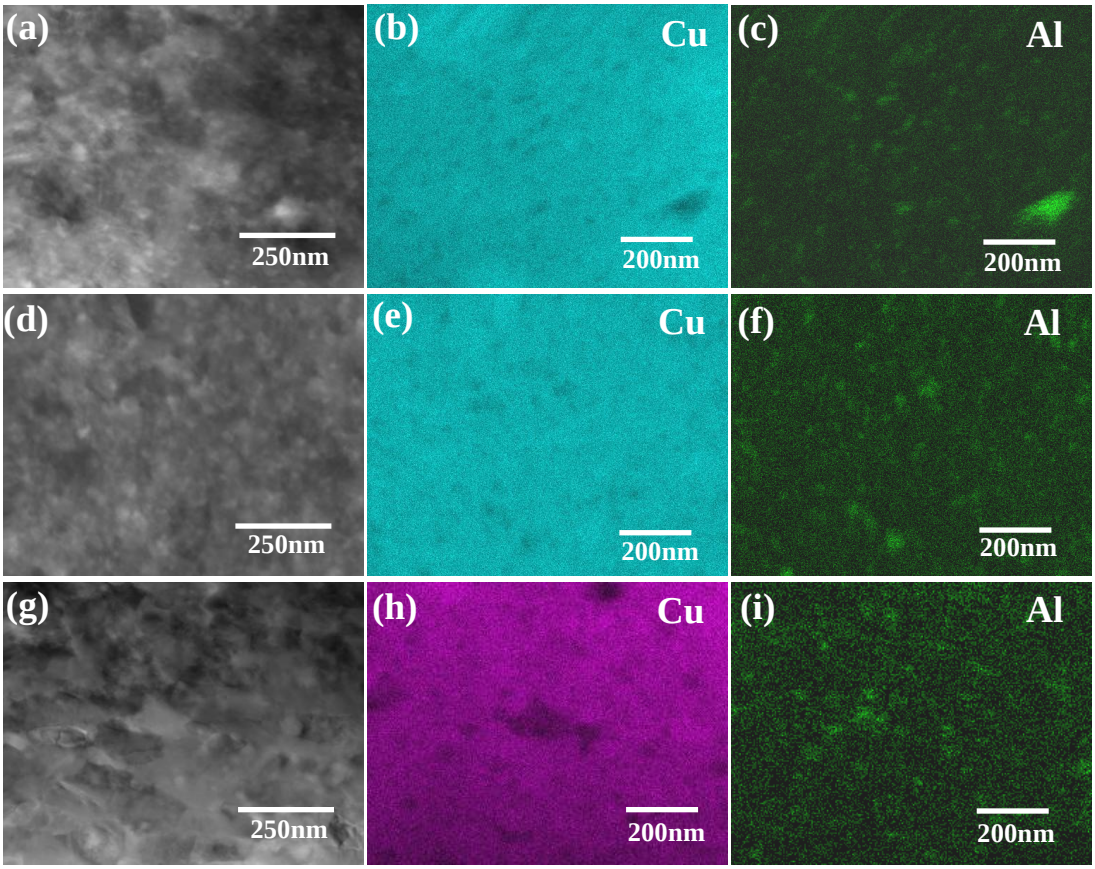


Figure 4.17: STEM images and X-ray elemental (Cu and Al) maps of Cu-2.5vol.%$Al_2O_3$ composite powder particles produced by HEMM after 24 hours, Route 2, and after annealing at ((a)-(c)) 150°C, ((d)-(f)) 300°C, and ((g)-(i)) 500°C, respectively.

Figure 4.18 shows the DSC traces obtained by heating the as-milled UFG and nanostructured Cu-2.5vol.%$Al_2O_3$ composite balls/powder particles produced using 12 hours (Route 1) and 24 hours (Route 2) from 40 to 650°C. The onset temperatures of the first and second exothermic peaks produced after 12 hours (Route 1) were ~ 400°C and ~ 490°C, respectively. The tail of the second exothermic peak is extended beyond 650°C. With the increase of the milling time from 12 hours to 24 hours (Route 2), the onset temperature of the first exothermic peak remained almost similar,

while the onset temperature of the second exothermic peak shifted to smaller temperature at ~ 460°C and amount of heat released was 11.6 J/g with peak temperature at 535°C.

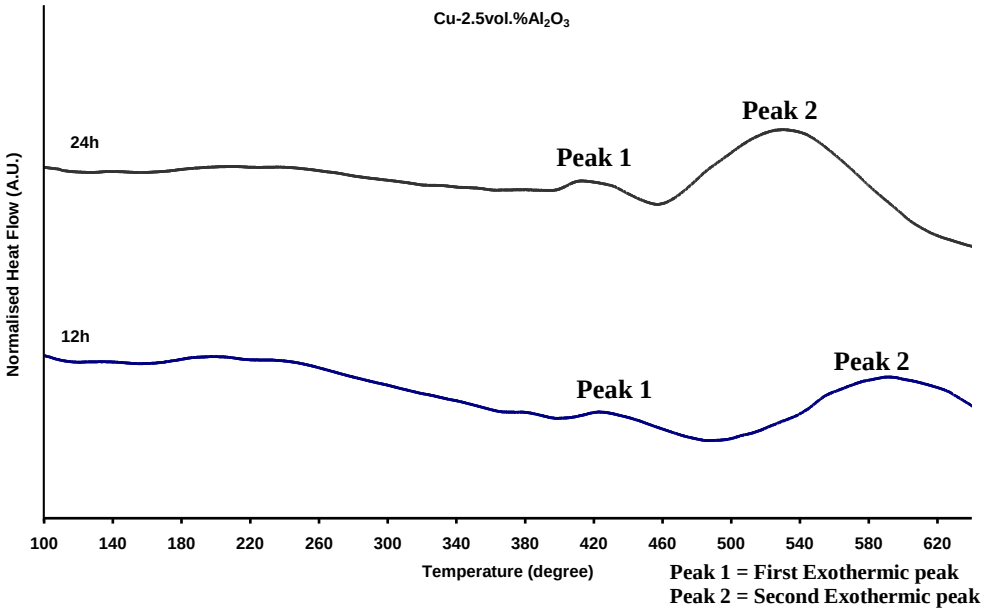


Figure 4.18: DSC traces obtained during heating of Cu-2.5vol.%$Al_2O_3$ composite balls/powder particles produced by HEMM after 12 hours (Route 1) and after 24 hours (Route 2).

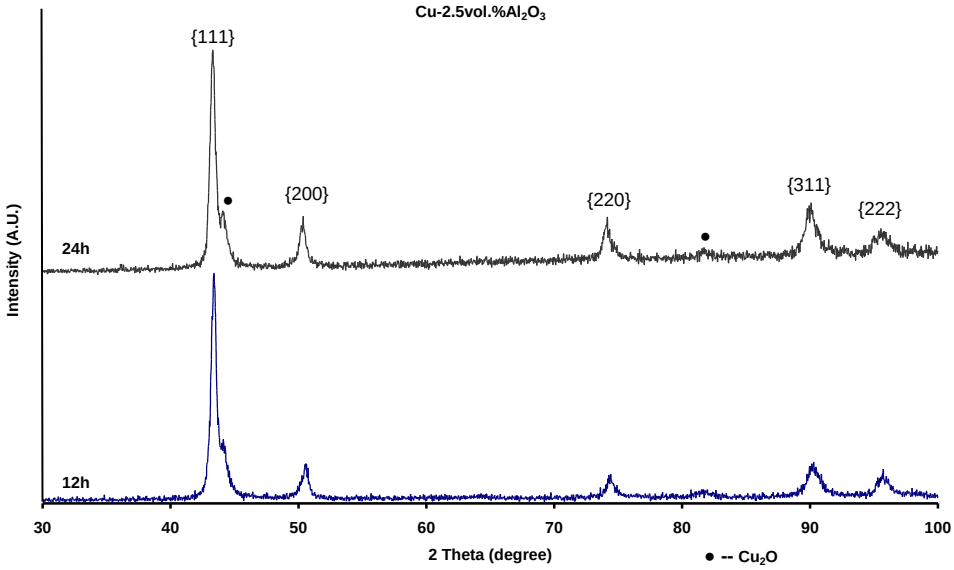


Figure 4.19: XRD patterns of Cu-2.5vol.%$Al_2O_3$ composite balls/powder produced after 12 hours (Route 1) and 24 hours (Route 2) and after the heating-cooling cycle (heated to 650°C ).

After one heating-cooling cycle, the XRD patterns of the UFG and nanostructured Cu-2.5vol.%$Al_2O_3$ composite balls/powder produced using Route 1 and Route 2 and heated to 650°C showed the Cu peaks and small $Cu_2O$ peaks, which are shown in Figure 4.19. The average grain sizes of the UFG and nanostructured Cu-

2.5vol.%$Al_2O_3$ composite balls/powder, heated to 650°C, were determined using the Williamson-Hall method and broadening of the XRD peaks. Based on this estimation, the Cu grain size of the 12 hour composite balls and 24 hour powder particles was ~ 55 nm and 75 nm.

### 4.2.3 Cu-5vol.%$Al_2O_3$ Composite

Figures 4.20 and 4.21 show the XRD patterns of UFG and nanostructured Cu-5vol.%$Al_2O_3$ composite granules/powder produced after 12 hours (Route 1) and 24 hours (Route 2) and after annealing at different temperatures, respectively. The XRD patterns only showed Cu peaks, due to the small fraction and extremely small size of $Al_2O_3$ nanoparticles. For the granules produced using Route 1, the broadening of the Cu peaks in the XRD pattern remained almost unchanged with increasing annealing temperature, as shown in Figure 4.20. The Cu{111} peak shifted 0.21° to a smaller angle after annealing at 300 and 500°C which meant that the Cu lattice parameter increased by 0.0016 nm, this might be because some of the $Al_2O_3$ was dissolved in the solution during the milling and then precipitated out after annealing at 300 and 500°C. The Cu{111} peak shifted 0.27° to a larger angle after annealing at 400°C, which meant that the Cu lattice parameter decreased by 0.0021 nm, this might be due to the diffusion of oxygen from furnace atmosphere. Based on Scherrer equation, the estimated grain size of Cu-5vol.%$Al_2O_3$ composite granules produced using Route 1 decreased and remained almost unchanged with the increase of annealing temperature from 150 to 500°C, as shown in Figure 4.50. However, based on Williamson-Hall method and broadening of the XRD peaks, the Cu grain size of the 12 hours milled granules with the increase of annealing temperatures from 150 to 500°C was in the range of 40-60 nm, as shown in Figure in 4.22.

The XRD patterns (Figure 4.21) for the nanostructured composite powder produced using Route 2 showed Cu peaks and extremely small peak of $Al_2O_3${104} after annealing at 500°C. For the composite powder produced using Route 2, the broadness of the Cu peaks changed little after annealing at different temperatures up to 500°C, and the lattice parameter remained almost same. Based on Scherrer equation, the estimated grain size of Cu-5vol.%$Al_2O_3$ composite powder particles produced using Route 2 slightly increased with the increase of annealing temperature from 150 to

500°C, as shown in Figure 4.51. However, based on the Williamson-Hall method and broadening of the XRD peaks, the average Cu grain size of the 24 hours milled powder particles with the increase of annealing temperatures from 150 to 500°C was in the range of 55-100 nm, as shown in Figure in 4.22.

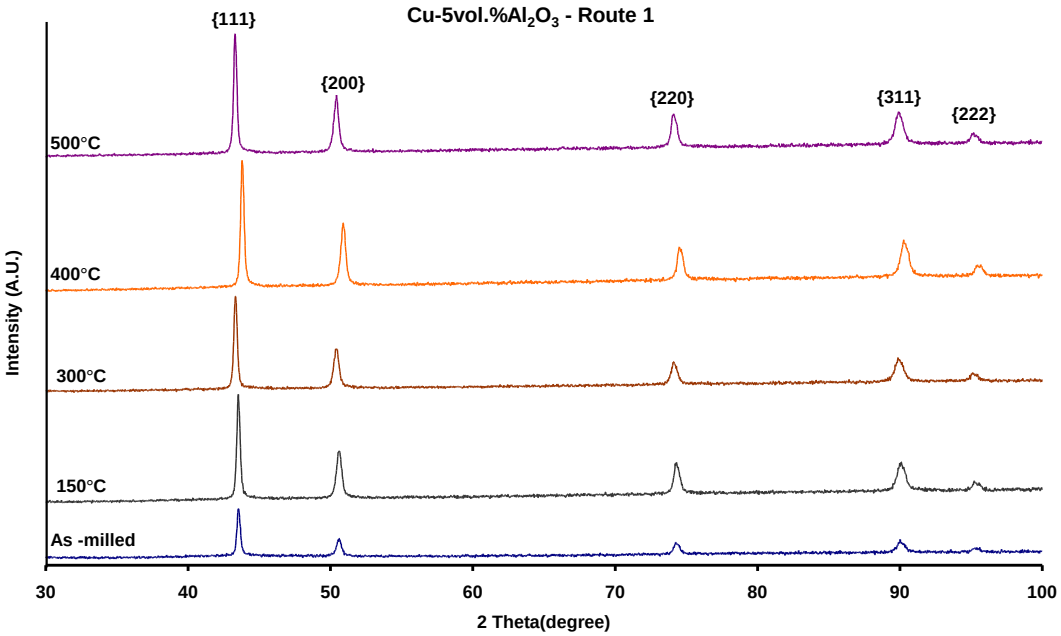


Figure 4.20: X-ray diffraction patterns of Cu-5vol.%$Al_2O_3$ composite granules produced by HEMM after 12 hours, Route 1, and after annealing at 150, 300, 400 and 500°C, respectively.

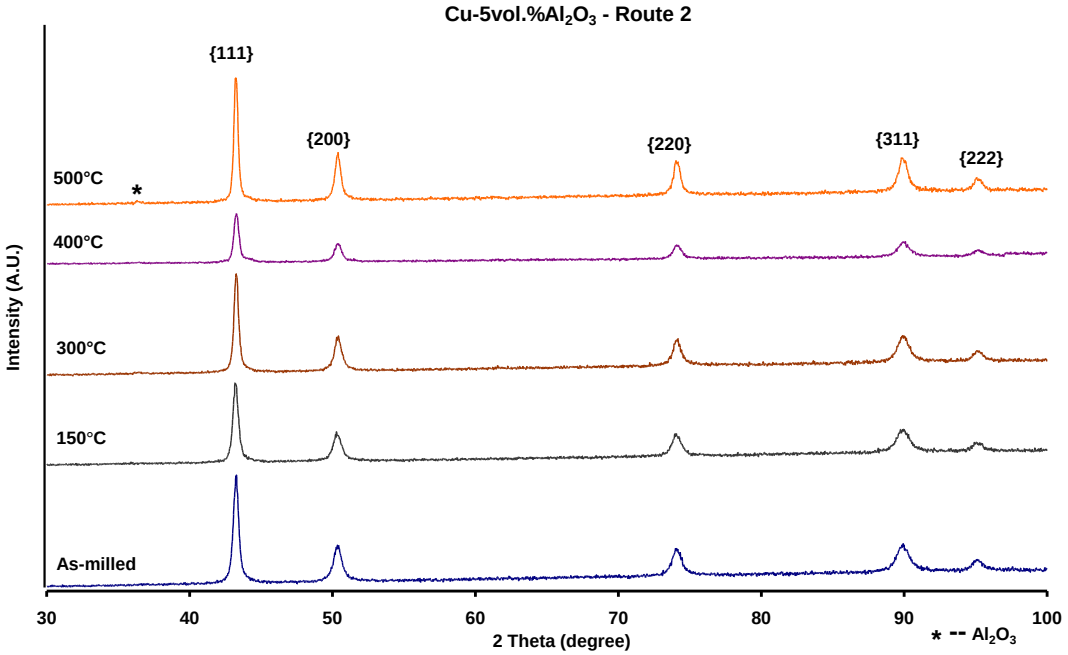


Figure 4.21: X-ray diffraction patterns of Cu-5vol.%$Al_2O_3$ composite powder produced by HEMM after 24 hours, Route 2, and after annealing at 150, 300, 400 and 500°C, respectively.

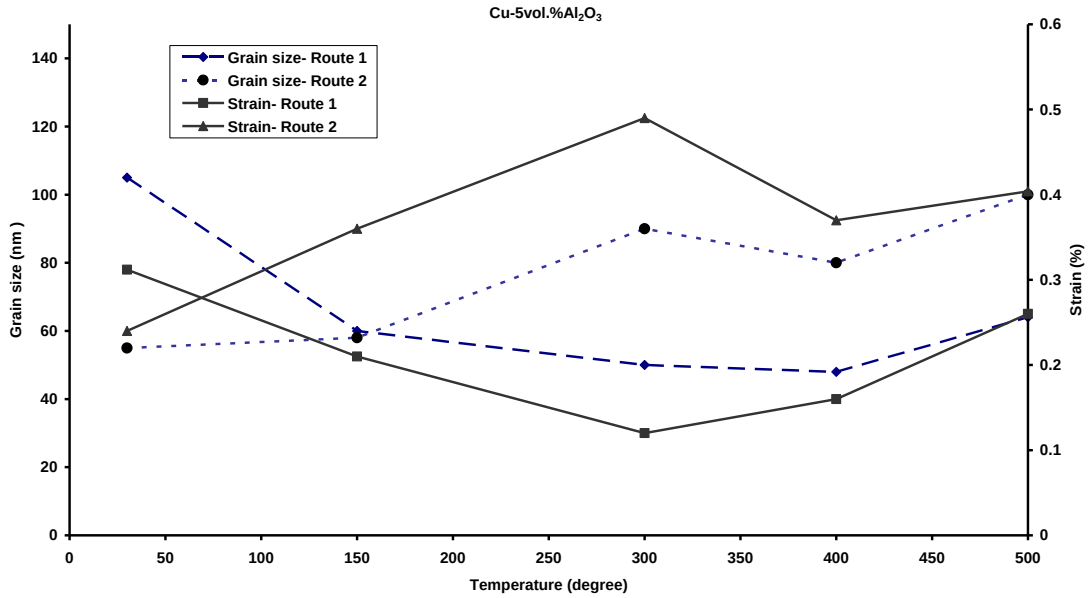


Figure 4.22: Average grain size and lattice strain data of Cu-5vol.%$Al_2O_3$ composite granules/powder particles produced by HEMM after 12 hours (Route 1) and 24 hours (Route 2) and after annealing at 150, 300, 400 and 500°C, respectively.

The average grain size and lattice strain data of the UFG and nanostructured Cu-5vol.%$Al_2O_3$ composite granules/powder particles produced using Route 1 and Route 2 and after annealing at different temperatures were estimated using the broadening of the XRD peaks and Williamson-Hall method, as shown in Figure 4.22. The grain sizes and lattice strain data showed almost a similar trend for the composite granules and powder particles annealed within the range of 150 to 500°C. However there was a significant increase in grain sizes and lattice strains for the composite powder particles, suggesting grain coarsening, produced using Route 2 as compared to granules produced using Route 1 after annealing at 300 and 500°C.

Backscattered electron SEM imaging of the cross section of the nanostructured Cu-5vol.%$Al_2O_3$ composite powder particles produced using Route 2 and after annealing at 300°C, showed a large size of $Al_2O_3$ particles in the range of 100-600 nm (Figure 4.23(a)), as compared to as-milled powder particles which showed 100-400 nm, (Figures 3.22). A homogenous distribution of $Al_2O_3$ particles was observed in the Cu matrix with further increasing the annealing temperature to 500°C. However, the volume fraction of the large $Al_2O_3$ particles increased significantly and grain sizes slightly increased to 100-700 nm, as shown in Figure 4.23(b). These large $Al_2O_3$

particles suggested coarsening of the $Al_2O_3$ nanoparticles occurred after annealing the powders at 300 and 500°C.

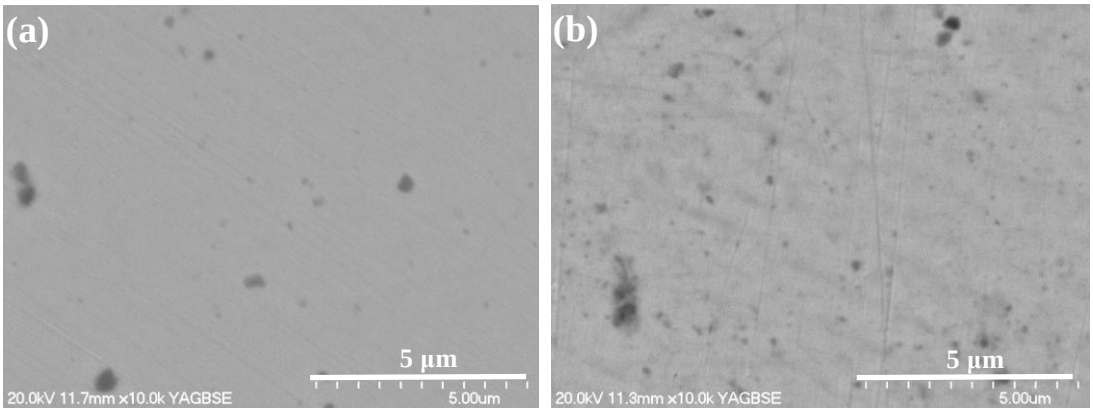


Figure 4.23: Backscattered electron SEM images of Cu-5vol.%$Al_2O_3$ composite powder particles produced by HEMM after 24 hours, Route 2, and after annealing at (a) 300°C and (b) 500°C.

Figures 4.24 and 4.25 show the TEM bright field images of UFG and nanostructured Cu-5vol.%$Al_2O_3$ composite granules/powder particles produced using Route 1 and Route 2, and after annealing at different temperatures, respectively. TEM examination of the microstructure of the granules produced using Route 1, confirmed the microstructural refinement as a result of annealing at 150°C. For the granules, the grains of the Cu matrix decreased from the range of 100-300 nm (Figure 3.17(a)) to 50-200 nm (Figure 4.24(a)) due to recrystallisation after annealing at 150°C. Increasing the annealing temperature from 150 to 300°C caused an increase of the grain sizes of the Cu matrix to 100-500 nm (Figure 4.24(c)). Further increasing the annealing temperature to 500°C caused a significant increase of the Cu matrix grain sizes to 100-800 nm (Figure 4.24(e)). Based on TEM examination of Cu grain size, that average grain size estimated using the XRD peaks and Williamson-Hall method is smaller than the actual average grain size, and this discrepancy is likely to be due to peak broadness of the inaccuracy of the measurement of XRD patterns. Figures 4.24((b), 4.24(d) and 4.24(f)) show the indexing of SADPs of UFG Cu-5vol.%$Al_2O_3$ composite granules produced after 12 hours (Route 1). Based on the SADPs it can be seen that strong reflections ({111}, {200}, {220}, {311}) could be correlated to the Cu matrix while weak reflections ({012}, {104}, {300}, {116}) are probably in related to fine $Al_2O_3$ nanoparticles. Indexing of SADPs is recorded from JCPDS files of Cu (04-0836) and $Al_2O_3$ (46-1212), as shown in Appendix A. Almost continuous rings were observed in the selected area diffraction patterns (SADPs) for the UFG

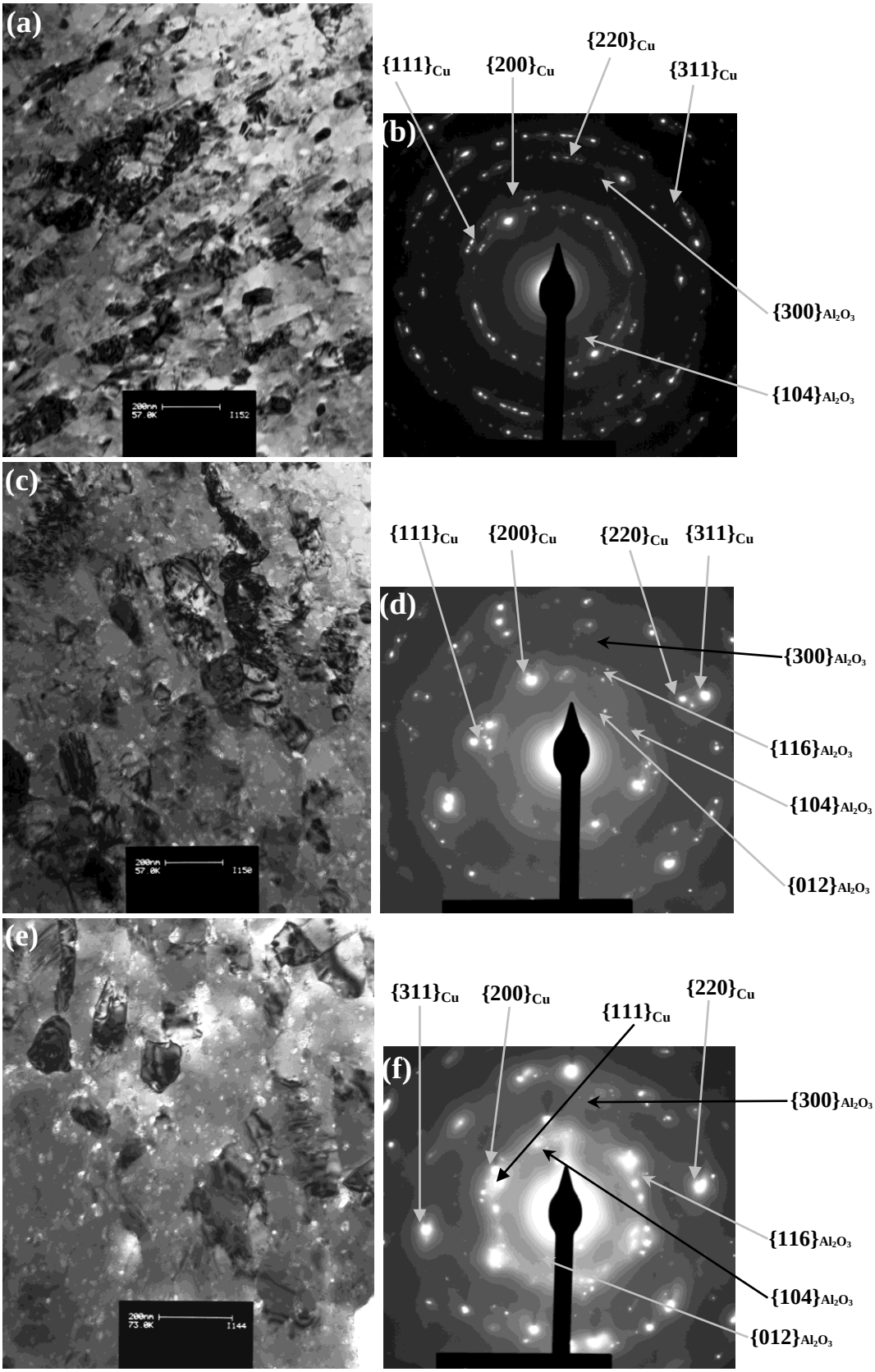


Figure 4.24: TEM bright field images and SADPs of Cu-5vol.%$Al_2O_3$ composite granules produced by HEMM after 12 hours, Route 1, and after annealing at 150, 300 and 500°C, respectively.

composite granules produced using Route 1 and annealed at 150°C. The rings were replaced by discrete diffraction reflections for Cu powder particles after annealed at 300 and 500°C. This is presumably in relation to the significant grain growth during annealing.

For the nanostructured composite powder produced with Route 2, the majority of the Cu grains of the as-milled powder particles had sizes smaller than 150 nm, confirming that Cu-5vol.%$Al_2O_3$ had a true nanostructured composite structure. After annealing at 150°C, the grain sizes changed very little (Figure 4.25(a)). XRD patterns in Figure 4.21 show annealing at 150°C has little effect on the grain sizes, since the nanometer scaled Cu grains are already the result of recrystallisation that occurs during prolonged milling, and the nanograins are fairly stable at temperatures up to 150°C, confirmed by TEM examination of the microstructure in Figure 4.25(a). With further increase of the annealing temperature to 300°C, the sizes of the Cu grains increased to the range of 50-300 nm (Figure 4.25(c)). Further increasing the annealing temperature to 500°C caused more significant coarsening of the Cu grains, with the sizes of the Cu grains increasing to 100-400 nm (Figure 4.25(e)). Figures 4.25((b), 4.25(d) and 4.25(f)) show the indexing of SADPs of nanostructured Cu-5vol.%$Al_2O_3$ composite powder particles produced after 24 hours (Route 2). Based on the SADPs it can be seen that strong reflections ({111}, {200}, {220}, {311}) could be correlated to Cu matrix while weak reflections ({012}, {104}, {300}) are probably in related to fine $Al_2O_3$ nanoparticles. Almost discrete diffraction reflections for Cu powder particles were observed in the selected area diffraction patterns (SADPs) for the nanostructured composite powder particles produced using Route 2 and annealed at 150, 300 and 500°C. This is presumably due to the normal grain growth during annealing. In comparison with the Cu granules made using Route 1 and annealed at 500°C, the microstructure of the nanostructured composite powder produced using Route 2 and annealed at 500°C is much finer, and still in the ultra fine grained scale (grain sizes < 500 nm).

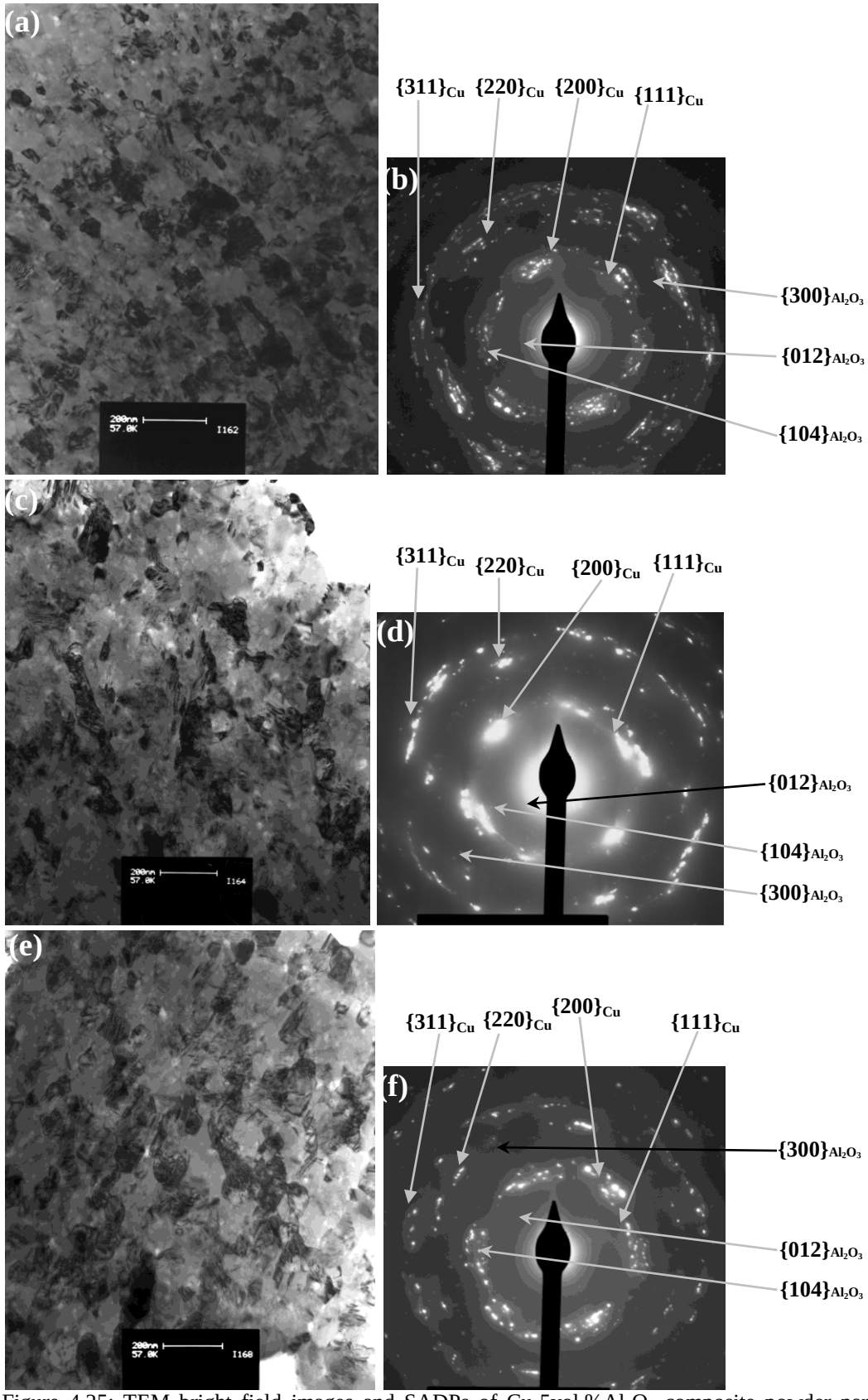


Figure 4.25: TEM bright field images and SADPs of Cu-5vol.%$Al_2O_3$ composite powder particles produced by HEMM after 24 hours, Route 2, and after annealing at 150, 300 and 500°C, respectively.

Figure 4.26 shows the DSC traces obtained by heating the as-milled UFG and nanostructured Cu-5vol.%$Al_2O_3$ composite granules/powder particles produced using 12 hours (Route 1) and 24 hours (Route 2) from 40 to 650°C. The onset temperatures of the first and second exothermic peaks of composite granules produced using Route 1 were ~ 410°C and ~ 490°C, respectively. The amount of heat released for the first exothermic peak was 1.08 J/g with peak temperature at 440°C. The second exothermic peak was extended beyond 650°C. With the increase of the milling time from 12 to 24 hours, a new exothermic peak appeared with an offset temperature of 170°C, while the onset temperatures for the second and third exothermic peaks shifted to lower temperatures ~ 390°C and 480°C. The amount of heat released for the first and second exothermic peaks was 3.8 J/g and 0.63 J/g with peak temperatures at 265°C and 420°C, respectively. The third exothermic peak was extended beyond 650°C.

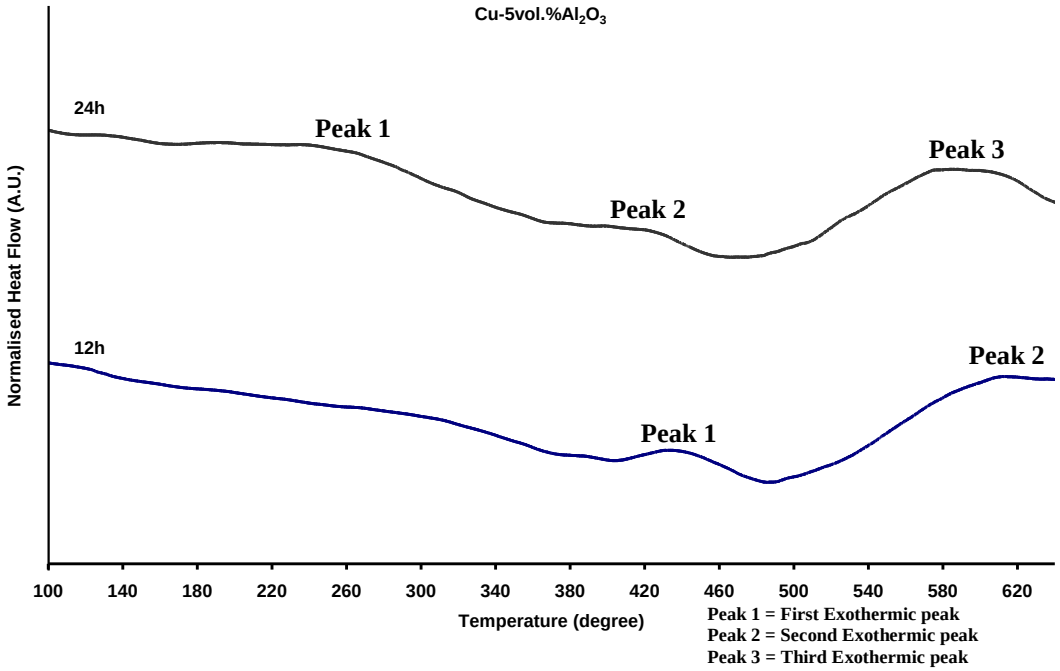


Figure 4.26: DSC traces obtained during heating of the Cu-5vol.%$Al_2O_3$ composite granules/powder particles produced by HEMM after 12 hours (Route 1) and 24 hours (Route 2).

After one heating-cooling cycle, the XRD patterns of UFG and nanostructured Cu-5vol.%$Al_2O_3$ composite granules/powder produced using Route 1 and Route 2 and heated to 650°C showed the Cu peaks and small $Cu_2O$ peaks, which are shown in Figure 4.27. Based on the broadening of the Cu peaks and Williamson-Hall Method,

the Cu grain size of the 12 hour composite granules and 24 hour composite powder, heated to 650°C, was ~ 55 nm.

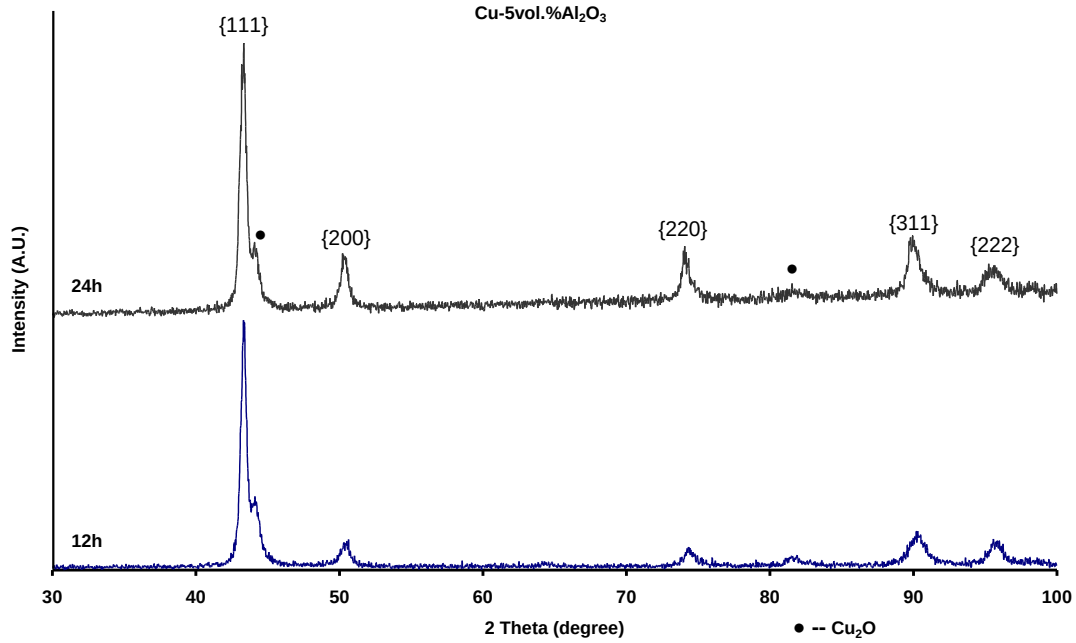


Figure 4.27: XRD patterns of Cu-5vol.%$Al_2O_3$ composite granules/powder produced after 12 hours (Route 1) and 24 hours (Route 2) and after the first heating-cooling cycle (heated to 650°C).

## 4.2.4 Cu-7.5vol.%$Al_2O_3$ Composite

Figures 4.28 and 4.29 show the XRD patterns of nanostructured Cu-7.5vol.%$Al_2O_3$ composite coarse and fine powders produced after 12 hours (Route 1) and 24 hours (Route 2) and after annealing at different temperatures, respectively. The XRD patterns showed Cu peaks and extremely small peaks of $Al_2O_3${104} after annealing at 300, 400 and 500°C, as shown in Figures 4.28 and 4.29. Increasing the annealing temperature from 150 to 500°C, caused little change in the broadness of the Cu peaks, as shown in the XRD patterns (Figure 4.28) of the coarse powders produced using Route 1, while the lattice parameter of Cu remained the same. Based on Scherrer equation, the estimated grain size of Cu-7.5vol.%$Al_2O_3$ composite powder particles produced using Route 1 slightly increased with the increase of annealing temperature from 150 to 400°C and then increased significantly with further increasing the annealing temperature to 500°C, as shown in Figure 4.50. The average grain sizes and lattice strain of nanostructured Cu-7.5vol.%$Al_2O_3$ composite powder particles were determined using the Williamson-Hall method and broadening of the XRD peaks.

Based on this estimation, the Cu grain size of the 12 hours milled powder particles with the increase of annealing temperatures from 150 to 500°C was in the range of 50-90 nm, as shown in Figure 4.30.

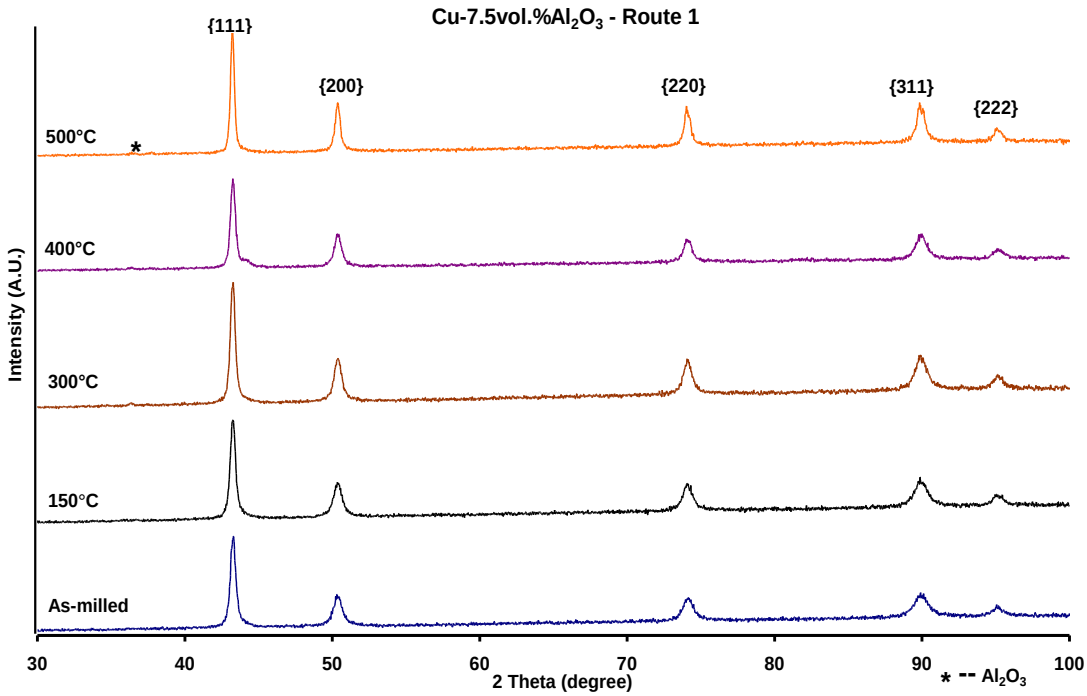


Figure 4.28: X-ray diffraction patterns of Cu-7.5vol.%$Al_2O_3$ composite powder produced by HEMM after 12 hours, Route 1, and after annealing at 150, 300, 400 and 500°C, respectively.

For the fine powder produced using Route 2, shown in Figure 4.29, the broadness of the Cu peaks remained unchanged after annealing at different temperatures up to 500°C. Based on Scherrer equation, the estimated grain size of Cu-7.5vol.%$Al_2O_3$ composite powder particles produced using Route 2 slightly increased with the increase of annealing temperature from 150 to 500°C, as shown in Figure 4.51. However, based on the Williamson-Hall method and broadening of the XRD peaks, the average Cu grain size of the 24 hours milled powder particles with the increase of annealing temperatures from 150 to 500°C was in the range of 50-110 nm, as shown in Figure 4.30.

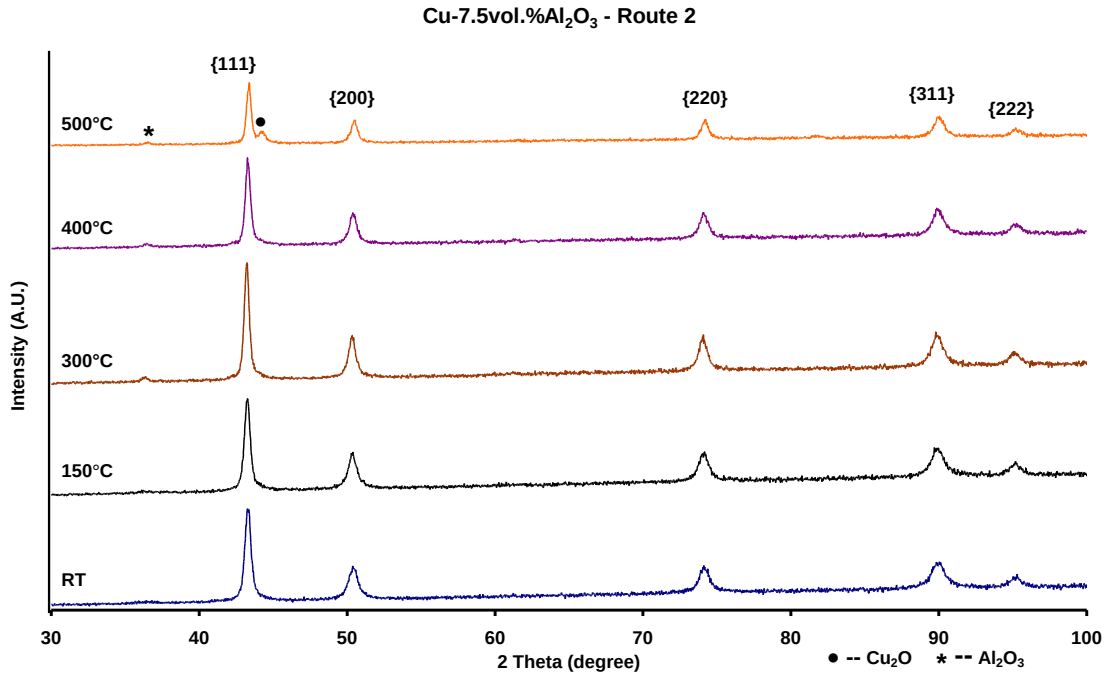


Figure 4.29: X-ray diffraction patterns of Cu-7.5vol.%$Al_2O_3$ composite powder produced by HEMM after 24 hours, Route 2, and after annealing at 150, 300, 400 and 500°C, respectively.

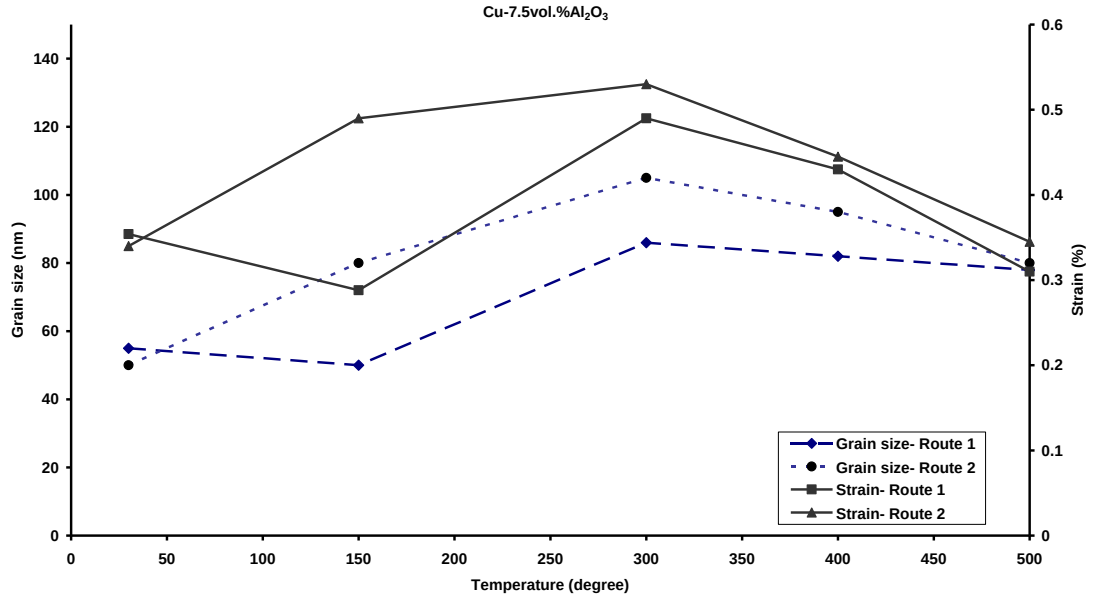


Figure 4.30: Average grain size and lattice strain data of Cu-7.5vol.%$Al_2O_3$ composite powder particles produced by HEMM after 12 hours (Route 1) and 24 hours (Route 2), and after annealing at 150, 300, 400 and 500°C, respectively.

The average grain size and lattice strain data of the nanostructured Cu-7.5vol.%$Al_2O_3$ composite powder particles produced using Route 1 and Route 2 and after annealing at different temperatures were estimated using the broadening of the XRD peaks and Williamson-Hall method, as shown in Figure 4.30. With the increase of the annealing temperature from 150 to 500°C, a similar trend of increase was observed in the grain

sizes and lattice strains for the composite powder particles produced using Route 1 and Route 2. However, the Cu grain size of composite powder particles produced using Route 2 slightly decreased with increasing the annealing temperature from 400 to 500°C.

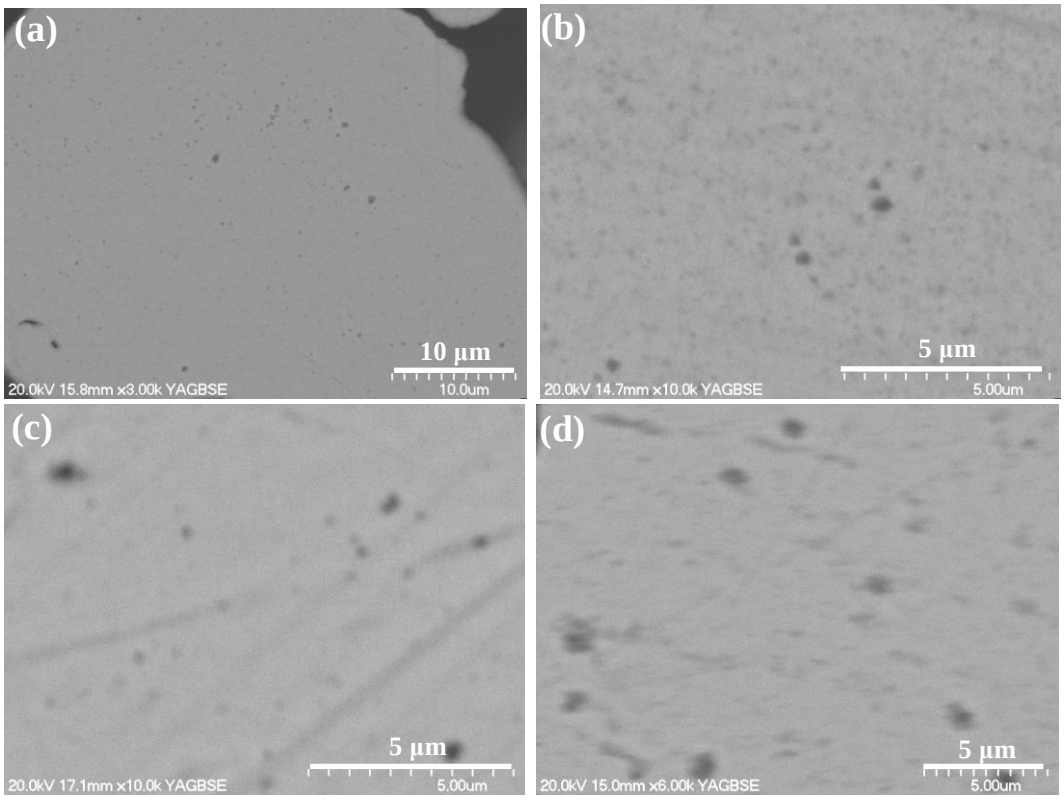


Figure 4.31: Backscattered electron SEM images of Cu-7.5vol.%$Al_2O_3$ composite powder particles produced by HEMM after 12 hours (Route1) and 24 hours (Route 2), (a) using Route 1 and after annealing at 300°C, (b) using Route 1 and after annealing at 500°C, (c) using Route 2 and after annealing at 300°C, and (d) using Route 2 and after annealing at 500°C.

Backscattered electron SEM imaging of the composite powder particles produced using Route 1 showed a small fraction of large $Al_2O_3$ particles (~ 1vol.%) with sizes in the range of 100-400 nm (Figure 4.31(a)) after annealing at 300°C, which is almost the same as as-milled powder particles of the corresponding material. Increasing the annealing temperature to 500°C, the volume fraction of such $Al_2O_3$ particles slightly increased (Figure 4.31(b)) suggesting that coarsening of the $Al_2O_3$ nanoparticles occurred. However for the composite powder particles produced using Route 2 and after annealing at 300°C, the volume fraction of large $Al_2O_3$ particles

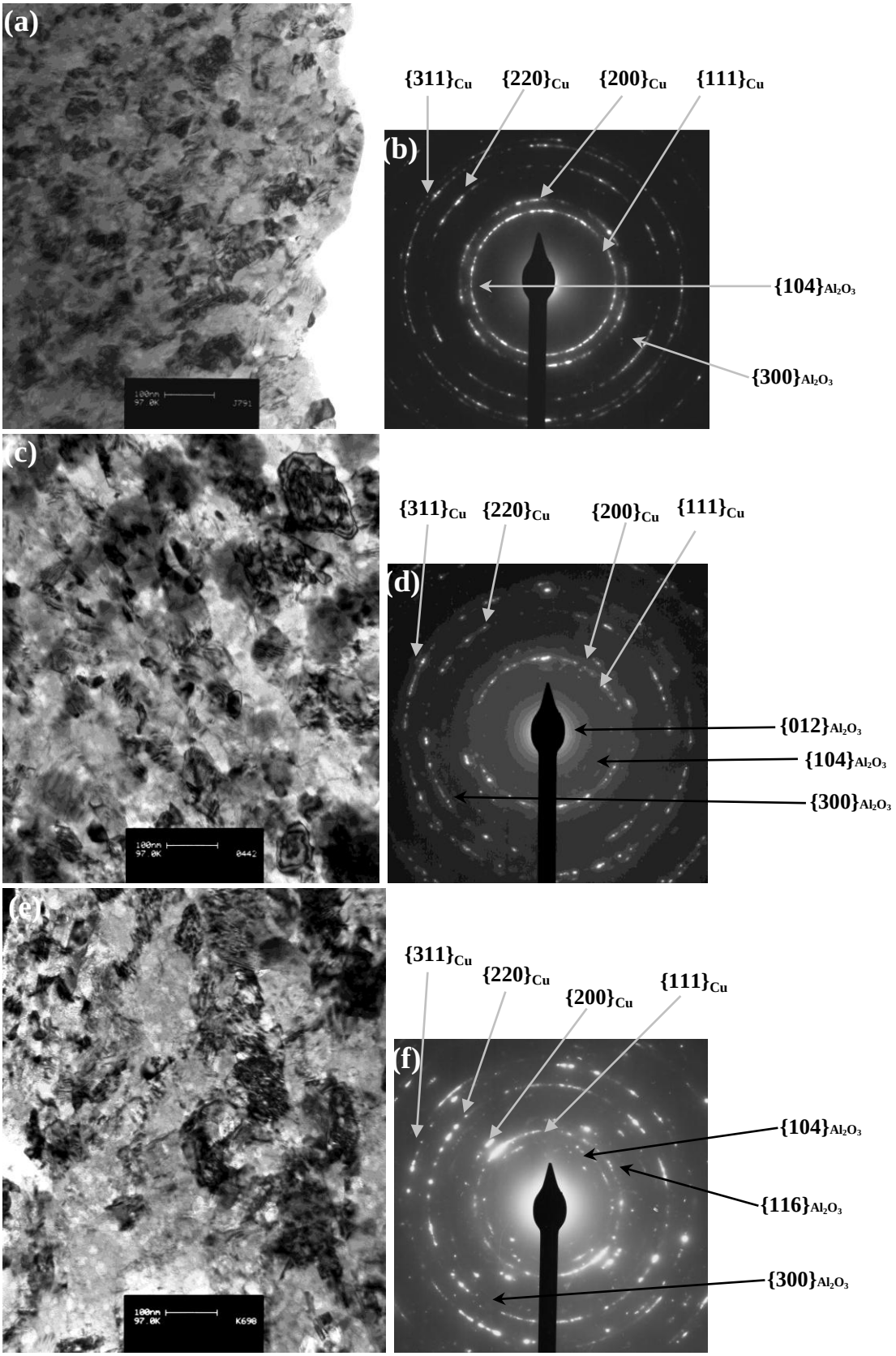


Figure 4.32: TEM bright field images and SADPs of Cu-7.5vol.%$Al_2O_3$ composite powder particles produced by HEMM after 12 hours, Route 1, and after annealing at 150, 300 and 500°C, respectively.

slightly increased (Figure 4.31(c)) as compared to as-milled nanostructured composite powder particles. With further increase in the annealing temperature to 500°C, the volume fraction of large $Al_2O_3$ particles was significantly increased (Figure 4.31(d)).

TEM bright field images and SADPs of nanostructured Cu-7.5vol.%$Al_2O_3$ composite powder particles produced by Route 1 and annealed at different temperatures are shown in Figures 4.32((a)-(f)). For the coarse powder produced with Route 1, TEM examination showed that grains of the Cu matrix decreased from the range of 50-150 nm (Figure (3.25(a)) to 50-100 nm (Figure (4.32(a)) after annealing at 150°C, due to recrystallisation. Increasing the annealing temperature to 300°C showed an increase of the grain sizes of the Cu matrix to 50-200 nm (Figure (4.32(c)) and further increasing the annealing temperature to 500°C caused a significant increase of the Cu matrix grain sizes in the range of 300-500 nm (Figure (4.32(e)), as the result of grain coarsening. Figures 4.32(b), 4.32(d) and 4.32(f) show the indexing of SADPs of nanostructured Cu-7.5vol.%$Al_2O_3$ composite powder particles produced after 12 hours (Route 1). Based on the SADPs it can be seen that strong reflections ({111}, {200}, {220}, {311}) could be correlated to Cu matrix while weak reflections ({012}, {104}, {300}, {116}) are probably in related to fine $Al_2O_3$ nanoparticles. Indexing of SADPs is recorded from JCPDS files of Cu (04-0836) and $Al_2O_3$ (46-1212), as shown in Appendix A. Almost continuous rings were observed in the selected area diffraction patterns (SADPs) for the composite powder particles produced using Route 1 and annealed at 150, 300 and 500°C, suggesting not significant grain growth during annealing.

Based on the TEM examination fine powder produced using Route 2 and after annealing at 150°C, the Cu grain sizes increased from the range of 50-150 nm (Figure (3.25(c)) to the range of 100-200 nm (Figure (4.33(a)). With the increase of annealing temperature from 150 to 300 and 500°C, the Cu grain sizes increased to 100-300 nm (Figures (4.33(c) and 4.33(e)), suggesting normal coarsening of grains during annealing.

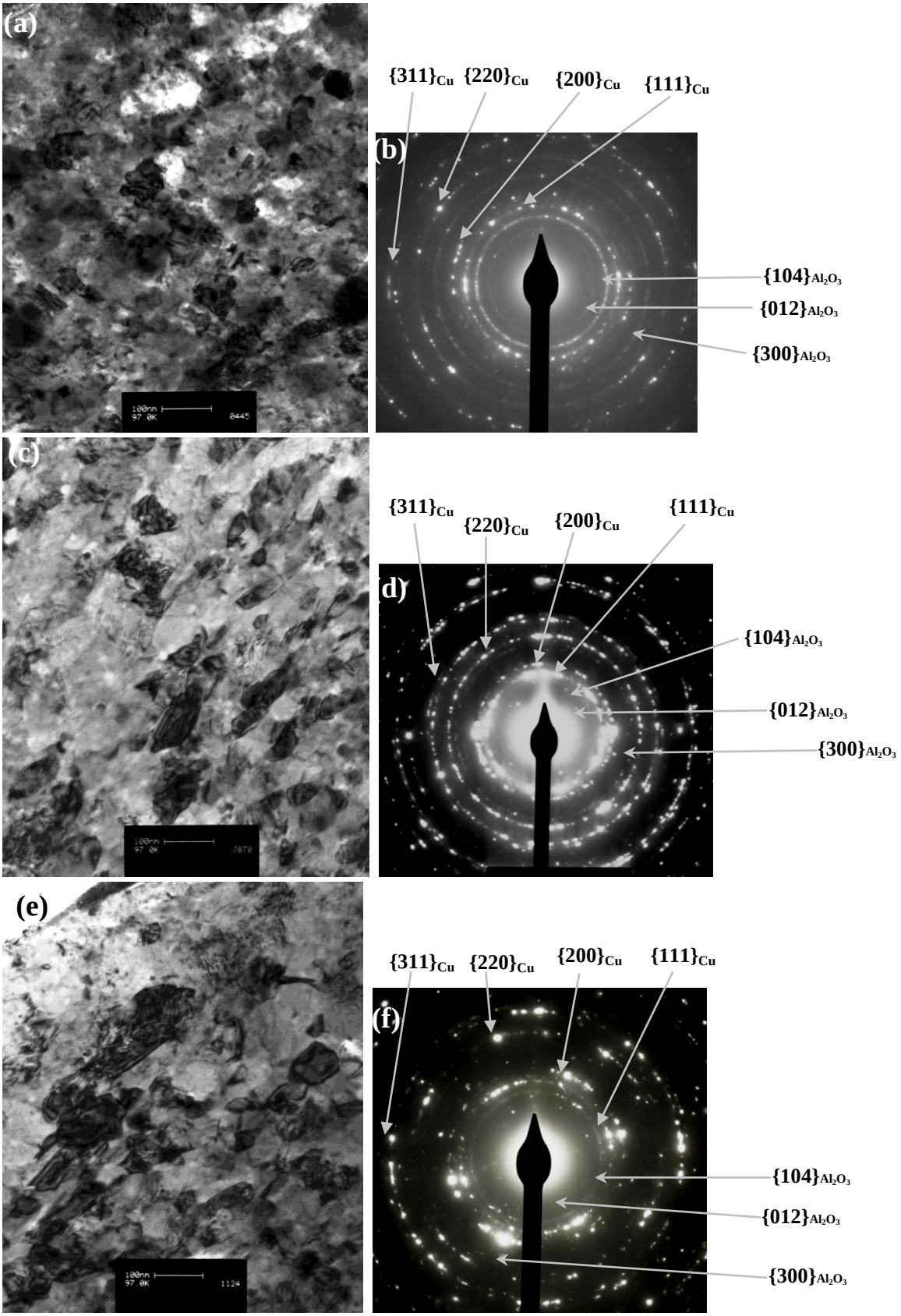


Figure 4.33: TEM bright field images and SADPs of Cu-7.5vol.%$Al_2O_3$ composite powder particles produced by HEMM after 24 hours, Route 2, and after annealing at 150, 300 and 500°C respectively.

Based on the SADPs (Figures 4.33 (b), 4.33(d) and 4.33(f)) it can be seen that strong reflections ({111}, {200}, {220}, {311}) could be correlated to Cu matrix while weak reflections ({012}, {104}, {300}) are probably due to fine $Al_2O_3$ nanoparticles. Almost continuous rings were observed in the SADPs for the composite powder particles produced using Route 2 and annealed at 150 and 300°C, suggesting Cu grains are thermally stable. The rings produced slight discrete diffraction reflections for composite powder particles after annealed at 500°C, suggesting significant grain growth during annealing. In comparison with the nanostructured Cu-7.5vol.%$Al_2O_3$ composite powder made using Route 1 and annealed at 500°C, the microstructure of the composite powder produced using Route 2 and annealed at 500°C was slightly finer, as most of the Cu grains were in the range of nanoscale (<100 nm).

In the STEM images of the nanostructured Cu-7.5vol.%$Al_2O_3$ composite coarse powder produced using Route 1 and annealed after different temperatures, as shown in Figures 4.34(a), 4.34(d) and 4.34(g), the bright particles are $Al_2O_3$ nanoparticles as confirmed from the X-ray elemental mapping for Al. The $Al_2O_3$ nanoparticles are homogenously distributed in Cu matrix after annealing, confirmed by X-ray elemental mapping for Al, as shown in Figures 4.34(c), 4.34(f) and 4.34(i). Increasing the annealing temperature from 150 to 300°C, more homogenous distribution of $Al_2O_3$ nanoparticles in Cu matrix was examined (Figure 4.34(f)), and predominately along the grain boundaries. With further increase of the annealing temperature to 500°C, the size of $Al_2O_3$ nanoparticles increased in the range of 10-40 nm (Figure 4.34(i)), suggesting the coarsening of grains.

Based on the STEM image and X-ray elemental mapping (Cu and Al) of the nanostructured Cu-7.5vol.%$Al_2O_3$ composite powder particles produced using Route 2 and after annealing at 300°C, show a homogenous distribution of the $Al_2O_3$ nanoparticles in Cu matrix. The size of $Al_2O_3$ nanoparticles was ~ 10 nm and a large cluster of $Al_2O_3$ nanoparticles ~ 100 nm was also observed (Figure (4.35(c)), suggesting coarsening of few grains.

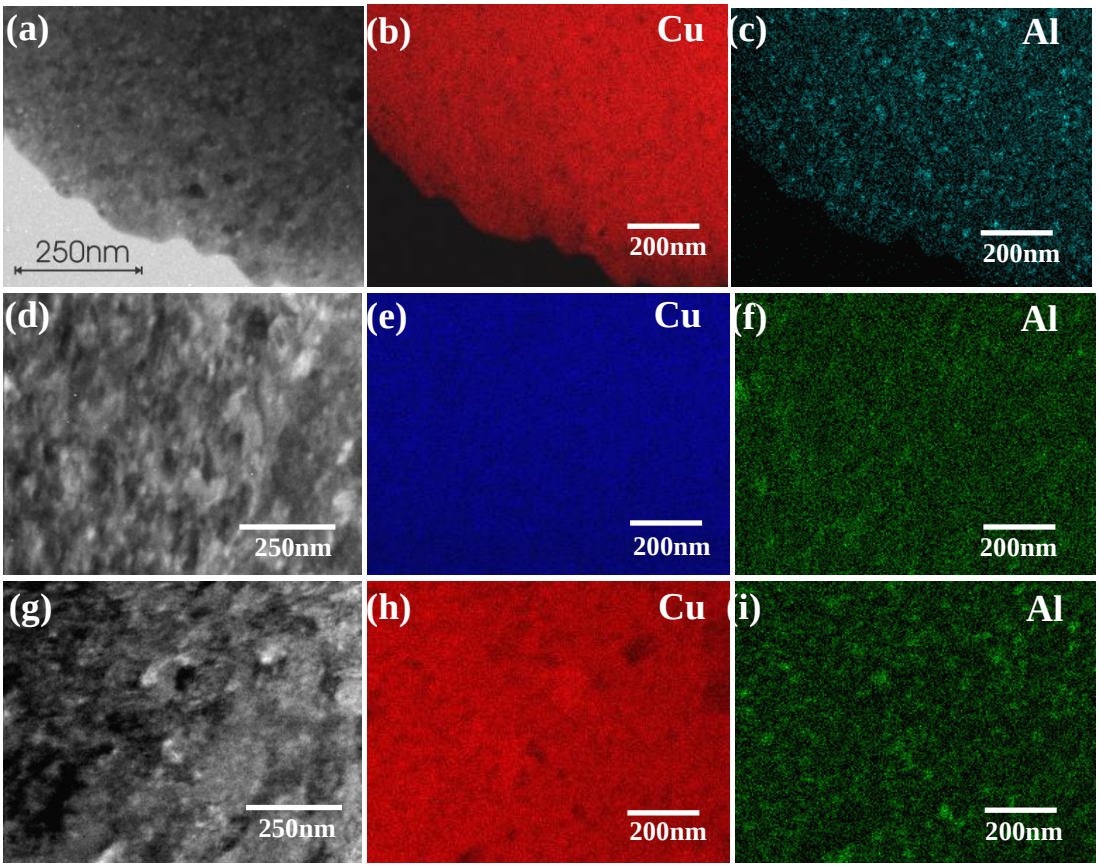


Figure 4.34: STEM images and X-ray elemental (Cu and Al) maps of Cu-7.5vol.%$Al_2O_3$ composite powder particles produced by HEMM after 12 hours, Route 1, and after annealing at ((a)-(c)) 150°C, ((d)-(f)) 300°C, and ((g)-(i)) 500°C, respectively.

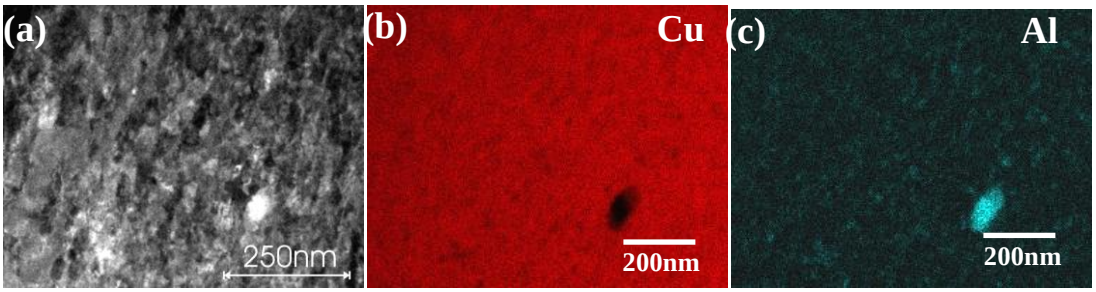


Figure 4.35: STEM image and X-ray elemental (Cu and Al) maps of Cu-7.5vol.%$Al_2O_3$ composite powder particles produced by HEMM after 24 hours, Route 2, and after annealing at 300°C.

Figure 4.36 shows the DSC traces obtained by heating the as-milled nanostructured Cu-7.5vol.%$Al_2O_3$ composite powder particles produced using 12 hours (Route 1) and 24 hours (Route 2) from 40 to 650°C. The onset temperatures of the first and second exothermic peaks produced after 12 hours were ~ 170°C and ~ 400°C, respectively. The amount of heat released for the first and second exothermic peaks was 5.1 J/g and 0.48 J/g with peak temperatures at 250°C and 410°C, respectively. The third exothermic peak has an onset temperature of ~ 470°C and the tail might

extended beyond 650°C and the amount of heat released was 11.1 J/g with peak temperature at 548°C. With the increase of the milling time from 12 hours to 24 hours (Route 2), the first exothermic peak became smaller with an onset temperature ~ 235°C and the amount of heat released was 0.49 J/g with peak temperature at 255°C. The second exothermic peak was almost finished, while the onset temperature of the third exothermic peak shifted slightly to a smaller angle ~ 460°C. The amount of heat released for the third exothermic peak was 10.25 J/g with peak temperature at 537°C.

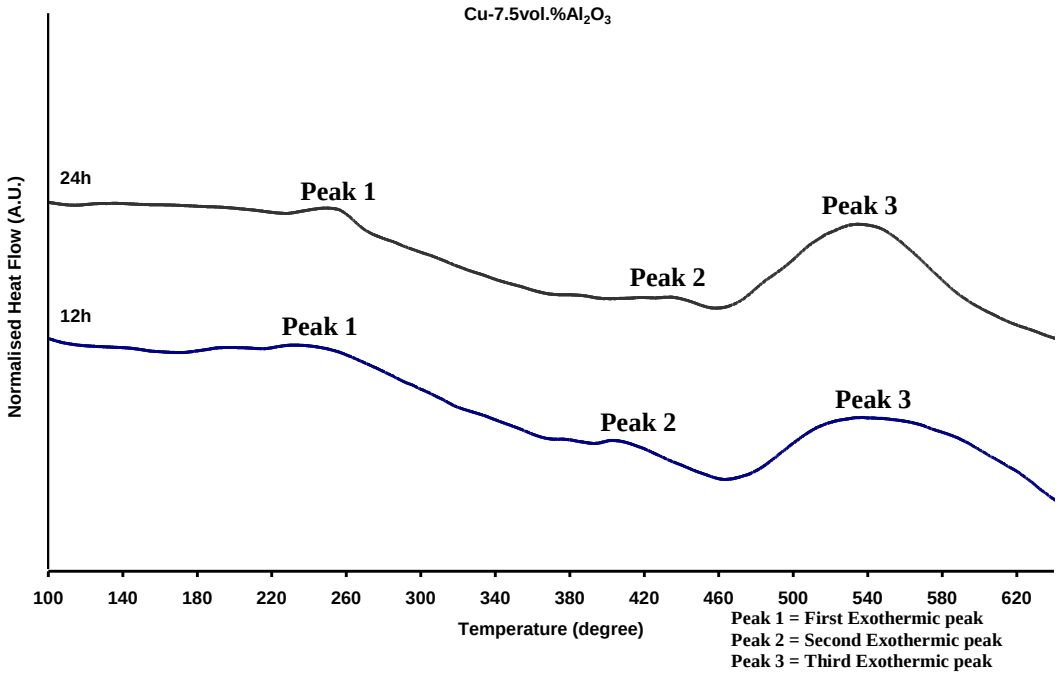


Figure 4.36: DSC traces obtained during heating of the Cu-7.5vol.%$Al_2O_3$ composite powder particles produced by HEMM after 12 hours (Route 1) and 24 hours (Route 2).

After one heating-cooling cycle, the XRD patterns of the nanostructured Cu-7.5vol.%$Al_2O_3$ composite powder produced using Route 1 and Route 2 and heated to 650°C showed the Cu peaks and small $Cu_2O$ peaks, as shown in Figure 4.37. Based on the broadening of the Cu peaks and Williamson-Hall Method, the Cu grain size of the 12 hour and 24 hour composite powders, heated to 650°C, was ~ 55 nm and 65 nm.

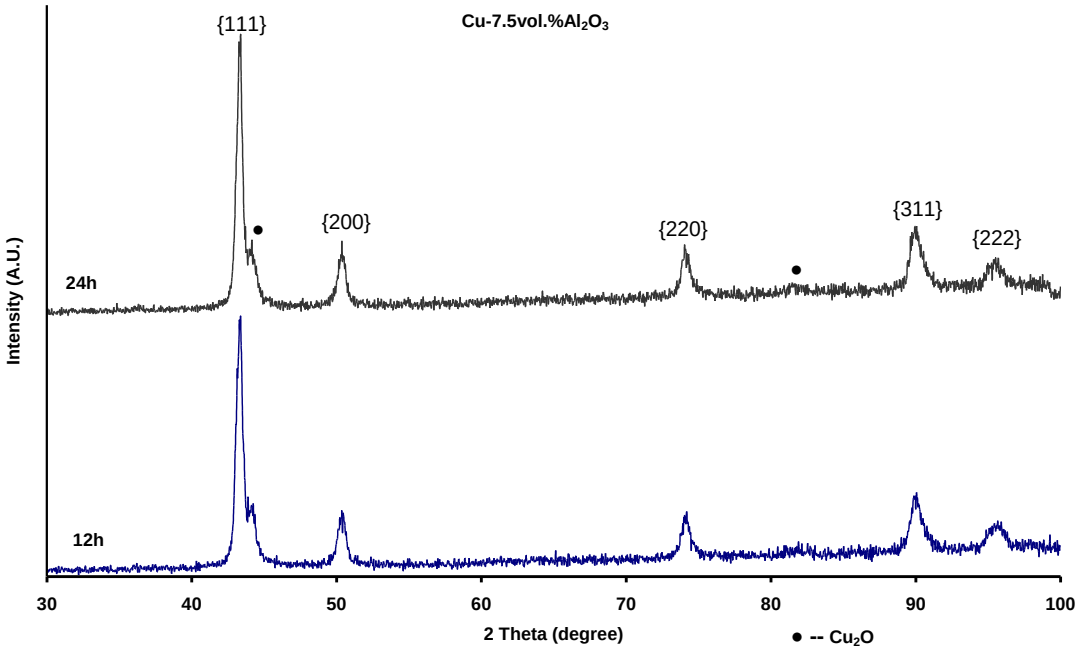


Figure 4.37: XRD patterns of Cu-7.5vol.%$Al_2O_3$ composite powder produced after 12 hours (Route 1) and 24 hours (Route 2) and after the first heating-cooling cycle (heated to 650°C).

## 4.2.5 Cu-10vol.%$Al_2O_3$ Composite

Figures 4.38 and 4.39 show the XRD patterns of nanostructured Cu-10vol.%$Al_2O_3$ composite powders produced after 12 hours (Route 1) and 24 hours (Route 2) and after annealing at different temperatures, respectively. The XRD patterns only showed Cu peaks, due to the small fraction and extremely small size of $Al_2O_3$ nanoparticles. The broadness of the Cu peaks of the XRD patterns remained almost unchanged with increasing the annealing temperature of the composite powder produced using Route 1. Based on Scherrer equation, the estimated grain size of Cu-10vol.%$Al_2O_3$ composite powder particles produced using Route 1 remained almost unchanged with the increase of annealing temperature from 150 to 400°C and then slightly decreased with further increasing the annealing temperature to 500°C, as shown in Figure 4.50. The average grain sizes and lattice strain of nanostructured Cu-10vol.% $Al_2O_3$ composite powder particles were determined using the Williamson-Hall method and broadening of the XRD peaks. Based on this estimation, the Cu grain size of the 12 hours milled powder with the increase of annealing temperatures from 150 to 500°C was in the range of 80-125 nm, as shown in Figure 4.40.

Annealing of the 24-hour milled nanostructured Cu-10vol.%$Al_2O_3$ composite powder at temperatures in the range of 150-500°C caused little change in the degree of broadening of the Cu peaks of the XRD patterns, as shown in Figure 4.39. The Cu{111} peak shifted 0.87° to a larger angle after annealing at 500°C, which caused the Cu lattice parameter to decrease by 0.0068 nm, perhaps by diffusion of $Al^{3+}$ and $O^{2-}$ into the Cu lattice or some of the $Al_2O_3$ was dissolved in the solution during the milling and then precipitated out after annealing at 500°C. Based on Scherrer equation, the estimated grain size of Cu-10vol.%$Al_2O_3$ composite powder particles produced using Route 2 increased with the increase of annealing temperature from 150 to 400°C and then increased significantly with further increase of the annealing temperature to 500°C, as shown in Figure 4.51. However, based on the Williamson-Hall method and broadening of the XRD peaks, the average Cu grain size of the 24 hours milled powder particles with the increase of annealing temperatures from 150 to 500°C was in the range of 50-200 nm, as shown in Figure 4.40.

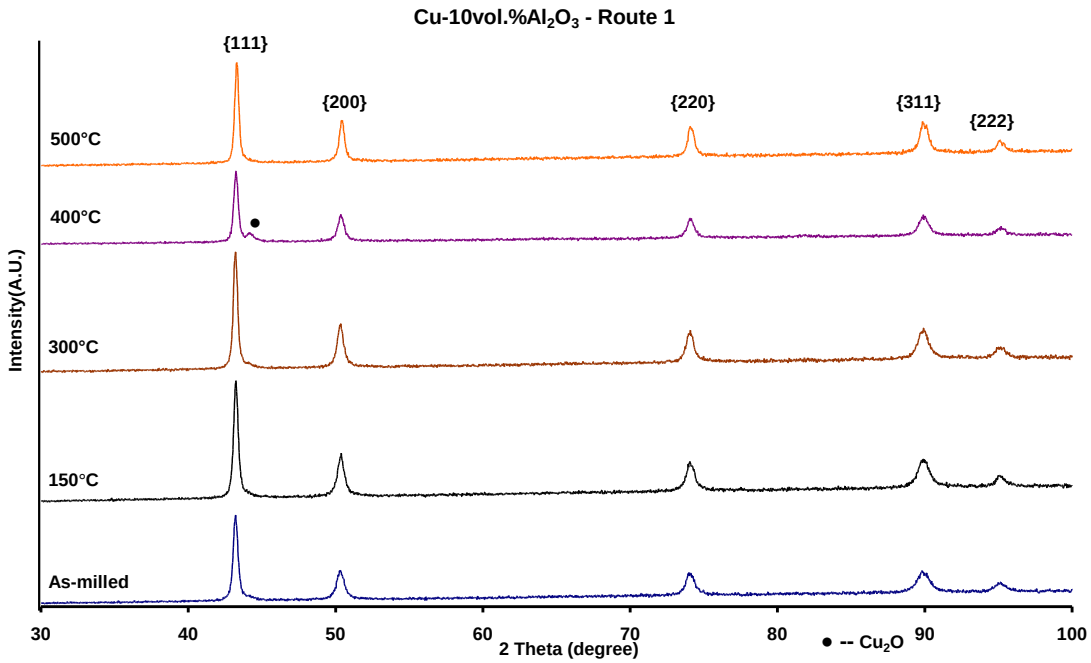


Figure 4.38: X-ray diffraction patterns of Cu-10vol.%$Al_2O_3$ composite powder produced by HEMM after 12 hours, Route 1, and after annealing at 150, 300, 400 and 500°C, respectively.

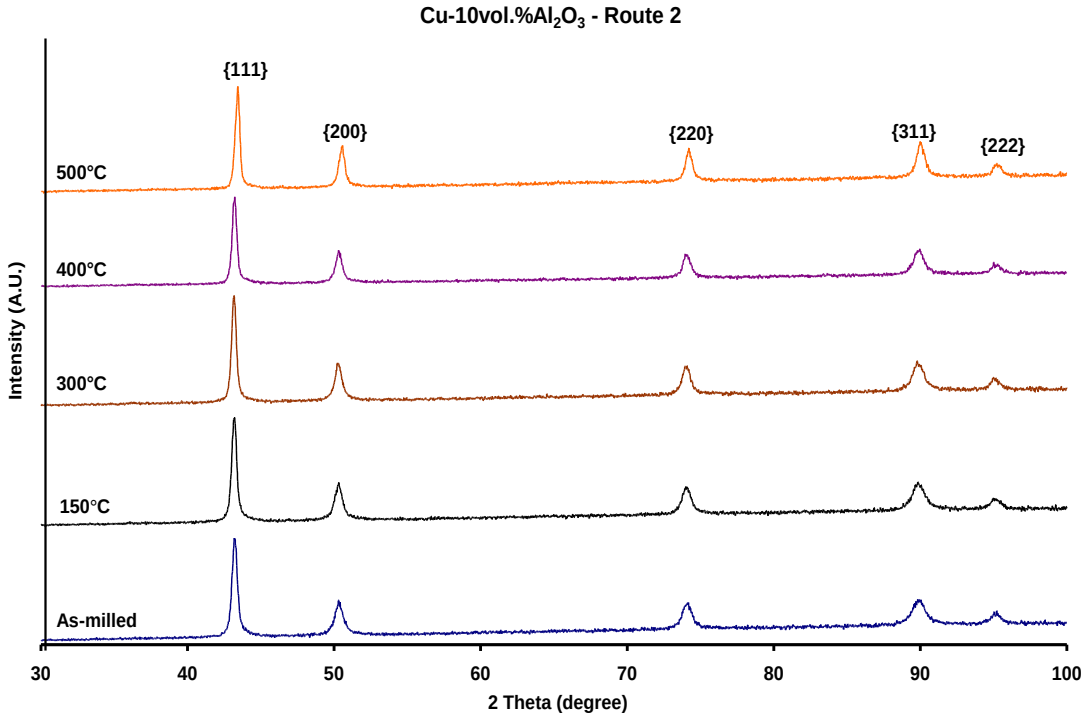


Figure 4.39: X-ray diffraction patterns of Cu-10vol.%$Al_2O_3$ composite powder produced by HEMM after 24 hours, Route 2, and after annealing at 150, 300, 400 and 500°C, respectively.

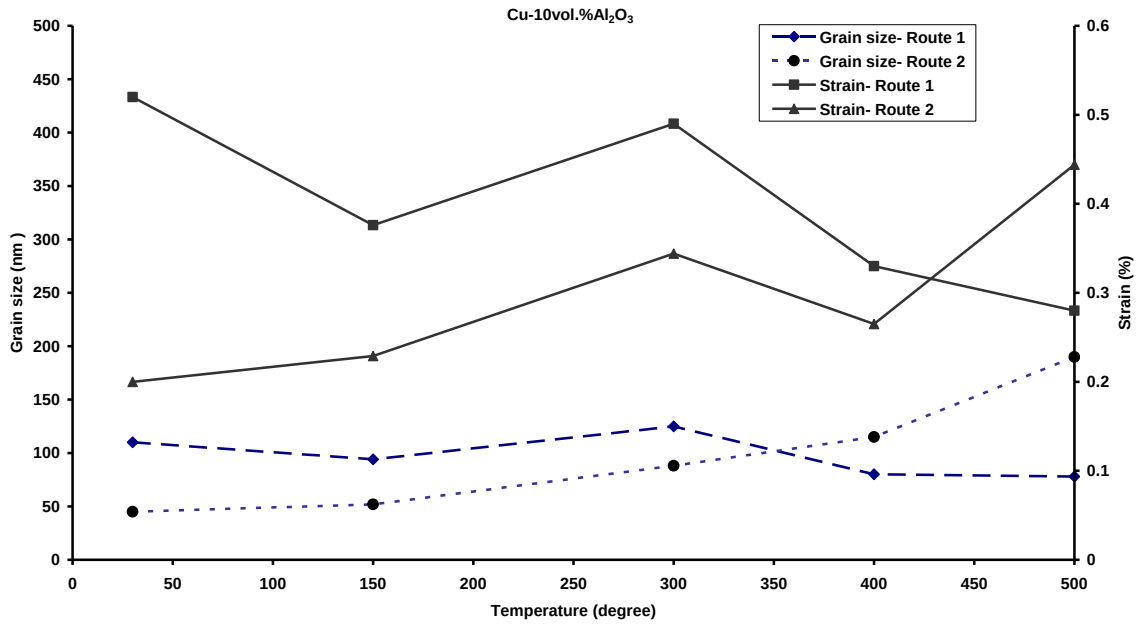


Figure 4.40: Average grain size and lattice strain data of Cu-10vol.%$Al_2O_3$ composite powder particles produced by HEMM after 12 hours (Route 1) and 24 hours (Route 2) and after annealing at 150, 300, 400 and 500°C, respectively.

The average grain size and lattice strain data of the nanostructured Cu-10vol.%$Al_2O_3$ composite powder particles produced using Route 1 and Route 2 and after annealing at different temperatures were estimated using the broadening of the XRD peaks and Williamson-Hall method, as shown in Figure 4.40. Grain sizes and lattice strain calculations of the composite powder particles produced using Route 1 and Route 2 showed almost a similar trend after increasing annealing temperatures to 300°C. The average Cu grain size increased for the composite powder produced using Route 2 compared to the composite powder produced using Route 1, when increasing the annealing temperature from 300 to 500°C. However, the lattice strain also increased for the composite powder produced using Route 2, when increasing the annealing temperature from 400 to 500°C.

Backscattered electron SEM imaging of the cross section of the powder particles was carried out to determine the volume fraction and distribution of $Al_2O_3$ particles after annealing at different temperatures. For the powder produced using Route 1 and after annealing at 300°C, the volume fraction of $Al_2O_3$ particles with sizes in the range of 100-600 nm (Figure 4.41(a)) increased, compared to as-milled powder particles, suggesting significant coarsening of the $Al_2O_3$ nanoparticles occurred. With further increase of the annealing temperature to 500°C, the volume fraction of large $Al_2O_3$ particles increased significantly (Figure 4.41(b)). The large sized $Al_2O_3$ particles in the 500°C annealed powder particles were homogenously distributed in the Cu matrix, with their size reaching ~ 700 nm. The fraction of the $Al_2O_3$ particles clearly increased for the powder particles produced using Route 2 annealed at 300°C for 1 hour (Figure 4.41(c)). With increasing the annealing temperature to 500°C, a substantially higher amount of larger sized $Al_2O_3$ particles in the range of 100-500 nm, appeared in the microstructure, suggesting coarsening of the $Al_2O_3$ nanoparticles occurred during annealing. These large sized $Al_2O_3$ particles were homogenously distributed, as shown in Figure 4.41(d). SEM examination of the cross sections of the annealed nanostructured composite powder particles with a volume fraction of 7.5% or 10% $Al_2O_3$, using the backscattered electron imaging mode showed that with increasing the annealing temperature to 500°C, the volume fraction of the $Al_2O_3$ particles larger than 100 nm increased significantly, suggesting coarsening of the $Al_2O_3$ nanoparticles occurred.

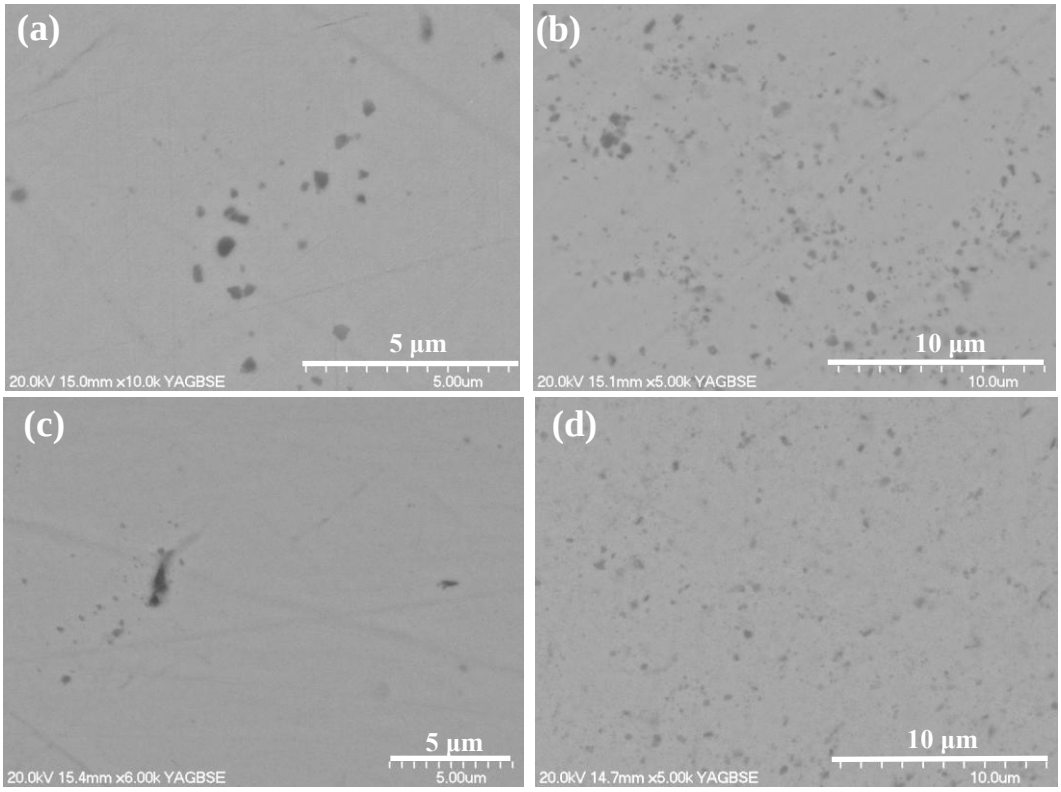


Figure 4.41: Backscattered electron SEM images of Cu-10vol.%$Al_2O_3$ composite powder particles produced by HEMM after 12 hours (Route1) and 24 hours (Route 2), (a) using Route 1 and after annealing at 300°C, (b) using Route 1 and after annealing at 500°C, (c) using Route 2 and after annealing at 300°C, and (d) using Route 2 and after annealing at 500°C.

Figures 4.42((a)-(f)) show the TEM bright field images and SADPs of nanostructured Cu-10vol.%$Al_2O_3$ composite powder particles after annealing at different temperatures. For the coarse powder produced using Route 1, TEM examination showed that grains of the Cu matrix decreased from the range of 50-150 nm (Figure 3.31(a)) to 50-100 nm (Figure 4.42(a)) due to recrystallisation after annealing at 150°C. Increasing the annealing temperature from 150 to 500°C the grain sizes of the Cu matrix increased within the range of 50-250 nm (Figures 4.42(c) and 4.42(e)), suggesting the coarsening of the Cu grains. Indexing of SADPs of nanostructured Cu-10vol.%$Al_2O_3$ composite powder particles produced after 12 hours (Route 1) showed that strong reflections ({111}, {200}, {220}, {311}) could be correlated to Cu matrix while weak reflections ({012}, {104}, {300}, {116}) are probably related to fine $Al_2O_3$ nanoparticles. Indexing of SADPs is recorded from JCPDS files of Cu (04-0836) and $Al_2O_3$ (46-1212), as shown in Appendix A. Almost continuous rings were observed in the selected area diffraction patterns (SADPs) for the composite powder particles produced using Route 1 and annealed at 150 and 300°C.

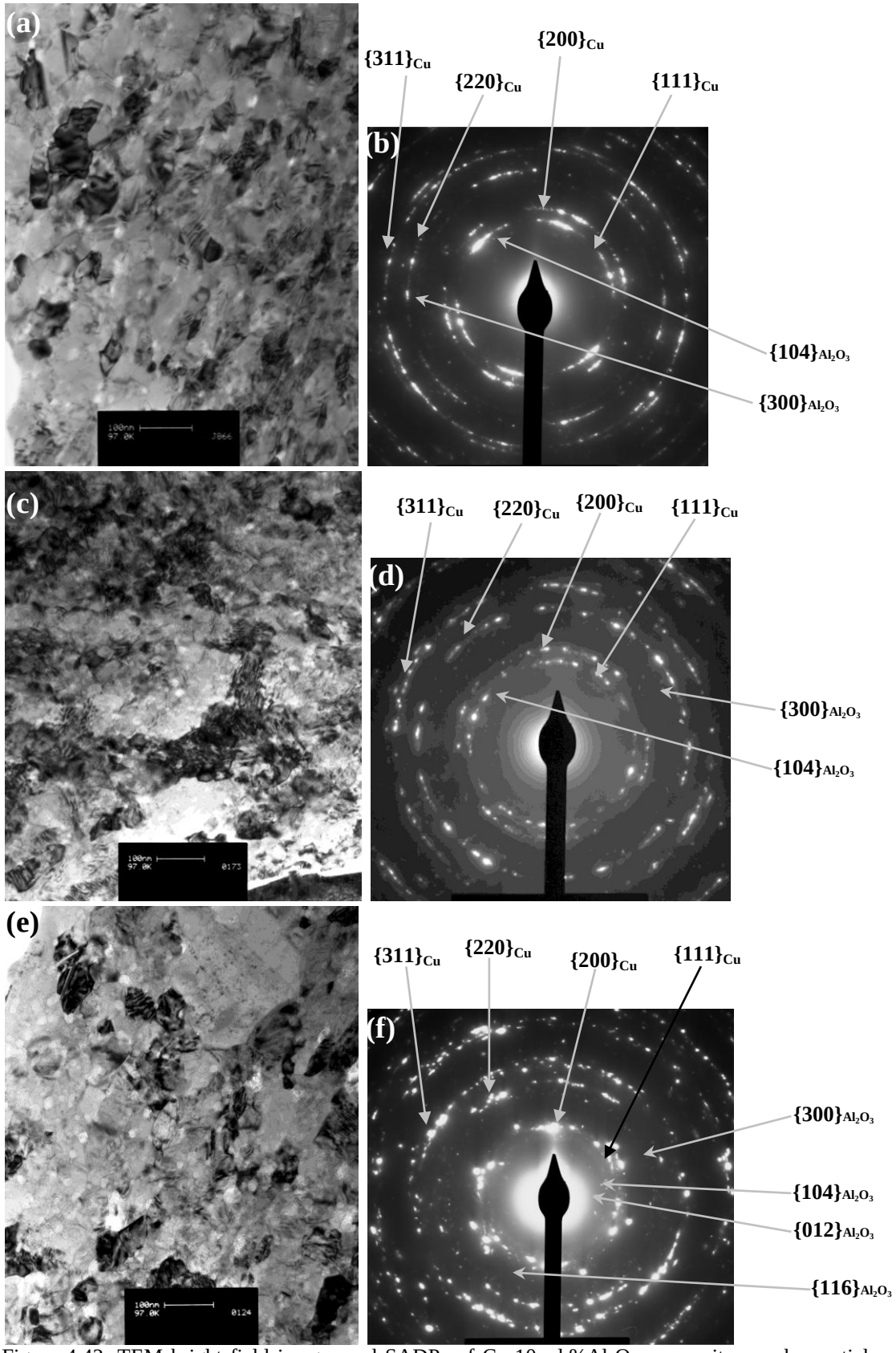


Figure 4.42: TEM bright field images and SADPs of Cu-10vol.%$Al_2O_3$ composite powder particles produced by HEMM after 12 hours, Route 1, and after annealing at 150, 300 and 500°C, respectively.

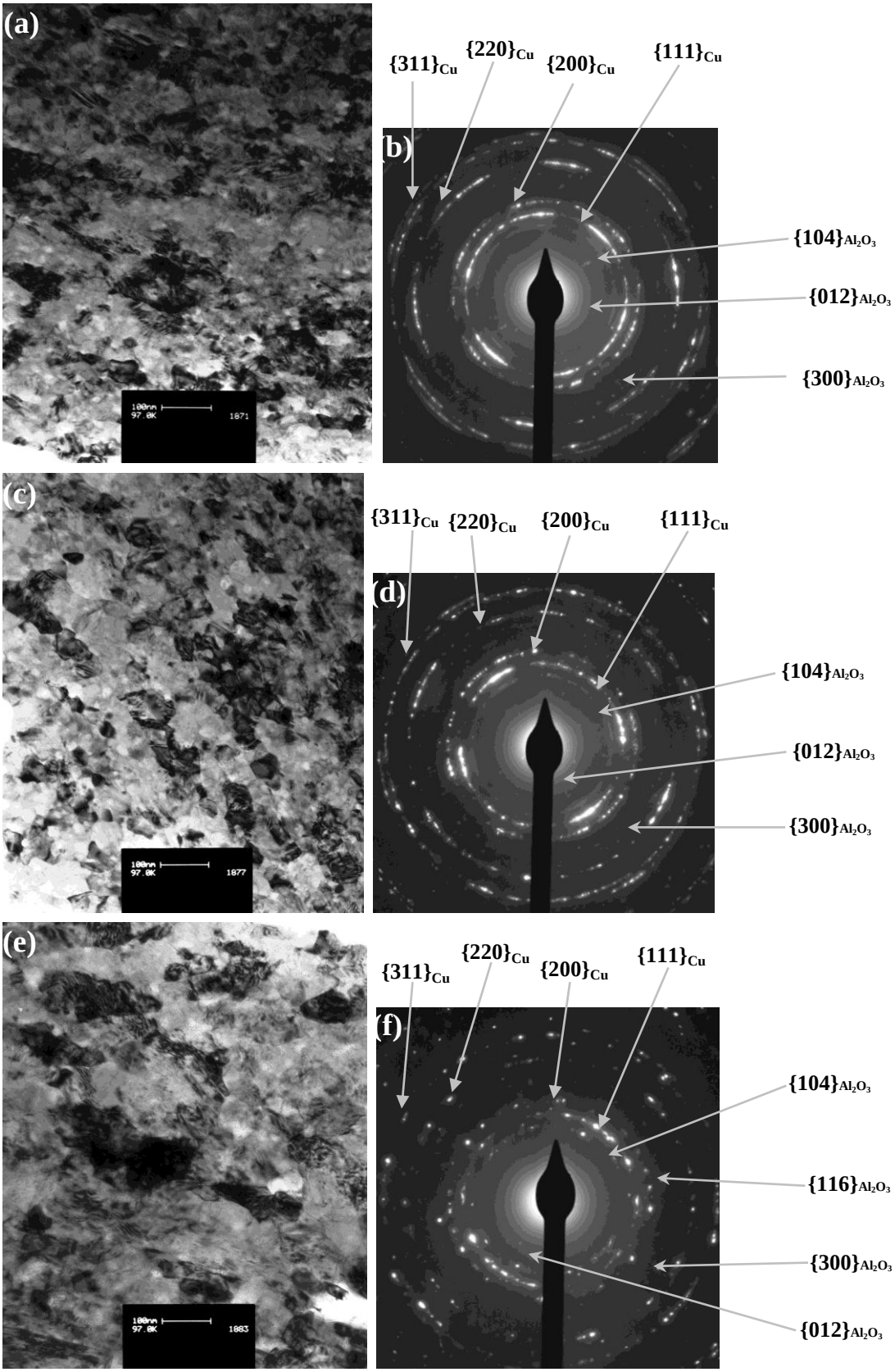


Figure 4.43: TEM bright field images and SADPs of Cu-10vol.%$Al_2O_3$ composite powder particles produced by HEMM after 24 hours, Route 2, and after annealing at 150, 300 and 500°C, respectively.

The diffraction rings were less complete and slight discrete diffraction reflections were observed for Cu powder particles after annealing at 500°C. This is presumably in relation to the grain growth during annealing.

On the other hand, for the fine powder produced with Route 2, the grain sizes of the as-milled powder particles increased very little to the range of 50-150 nm (Figure 4.43(a)) after annealing at 150°C. With further increase of the annealing temperature to 300°C, a slight increase of the Cu grains to the range of 100-200 nm was observed (Figure 4.43(c)). Further increasing the annealing temperature to 500°C caused more significant coarsening of the Cu grains, with the sizes of the Cu grains increasing to 100-350 nm (Figure 4.43(e)). Figures 4.43((b), 4.43(d) and 4.43(f)) show the indexing of SADPs of nanostructured Cu-10vol.%$Al_2O_3$ composite powder particles produced after 24 hours (Route 2). Based on the SADPs it can be seen that strong reflections ({111}, {200}, {220}, {311}) could be correlated to Cu matrix while weak reflections ({012}, {104}, {300}, {116}) are probably in related to fine $Al_2O_3$ nanoparticles. In comparison with the nanostructured Cu-10vol.%$Al_2O_3$ composite powder made using Route 2 and annealed at 500°C, the microstructure of the corresponding composite powder produced using Route 1 and annealed at 500°C was much finer, and most of the grains were in the range of nanoscale (<100 nm).

Figure 4.44 shows the STEM images and X-ray elemental mapping (Cu and Al) of the nanostructured Cu-10vol.%$Al_2O_3$ composite powder produced using Route 1 and annealed after different temperatures. The bright particles are $Al_2O_3$ nanoparticles as confirmed from the X-ray elemental mapping for Al. The $Al_2O_3$ nanoparticles are homogenously distributed in Cu matrix after annealing at 150°C, confirmed by X-ray elemental mapping for Al, as shown in Figure 4.44(c). Increasing the annealing temperature from 150 to 300°C, gave a more homogenous distribution of $Al_2O_3$ nanoparticles in Cu matrix (Figure 4.44(f)). Further increasing the annealing temperatures to 400 and 500°C, the size of $Al_2O_3$ nanoparticles increased in range of 10-50 nm, as shown in Figures 4.44(i) and 4.44(l), suggesting the coarsening of grains.

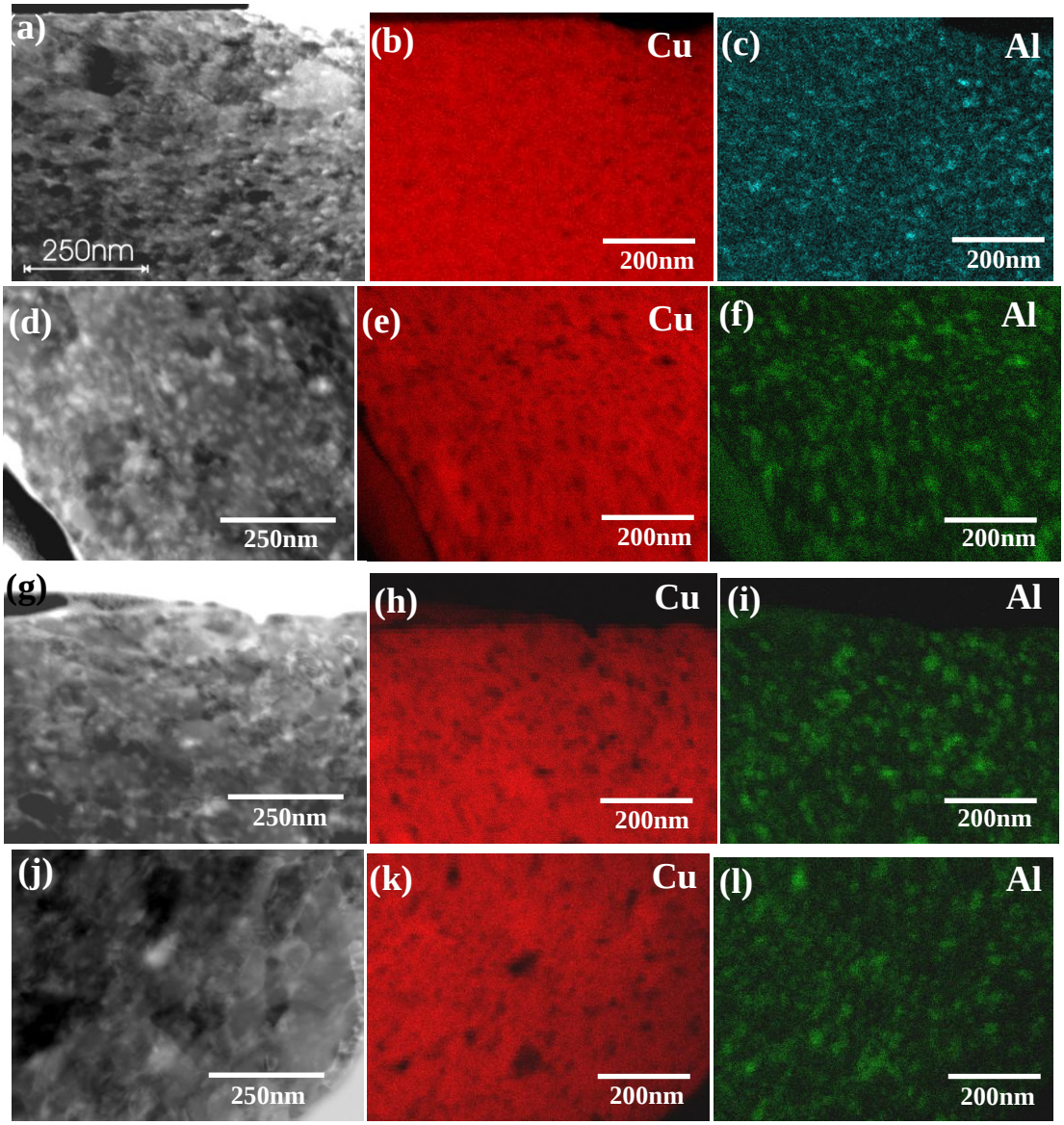


Figure 4.44: STEM images and X-ray elemental (Cu and Al) maps of Cu-10vol.%$Al_2O_3$ composite powder particles produced by HEMM after 12 hours, Route 1, and after annealing at ((a)-(c)) 150°C, ((d)-(f)) 300°C, ((g)-(i)) 400°C, and ((j)-(l)) 500°C, respectively.

X-ray elemental mapping (Al) of the nanostructured Cu-10vol.%$Al_2O_3$ composite powder particles produced using Route 2 and after annealing at 150°C, confirmed a homogenous distribution of the $Al_2O_3$ nanoparticles in the Cu matrix (Figure 4.45(c)). Increasing the annealing temperature from 150 to 500°C, the size of $Al_2O_3$ nanoparticles increased significantly, as confirmed by the X-ray elemental mapping for Al (Figure 4.45(f)). The large $Al_2O_3$ particles were in the range of 100-200 nm, suggesting significant coarsening of grains.

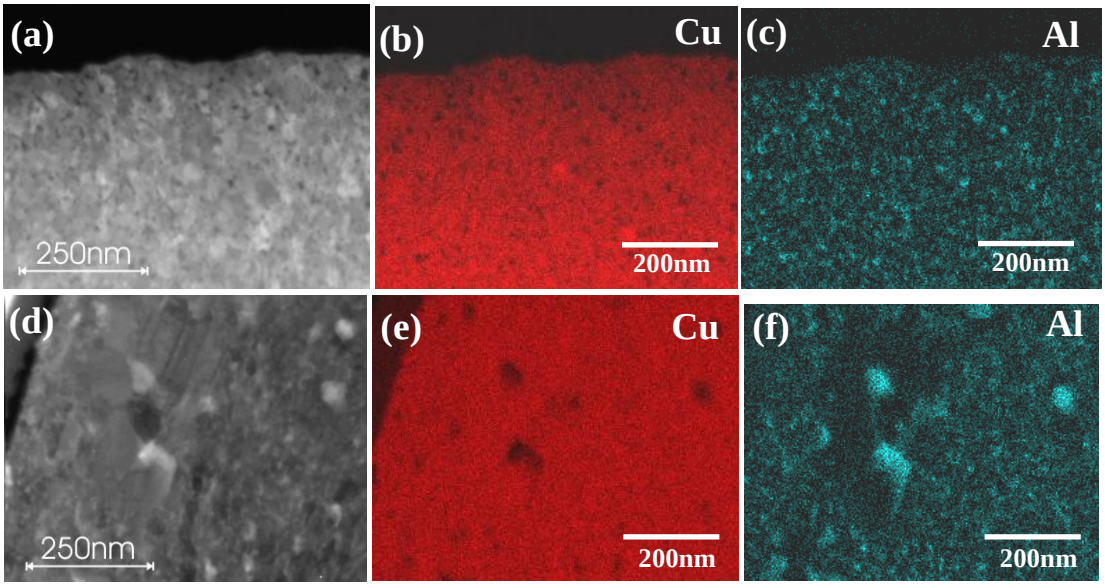


Figure 4.45: STEM images and X-ray elemental (Cu and Al) maps of Cu-10vol.%$Al_2O_3$ composite powder particles produced by HEMM after 24 hours, Route 2, and after annealing at ((a)-(c)) 150°C, and ((d)-(f)) 500°C, respectively.

Figure 4.46 shows the DSC traces obtained by heating the as-milled nanostructured Cu-10vol.% $Al_2O_3$ composite powder particles produced using 12 hours (Route 1) and 24 hours (Route 2) from 40 to 650°C. Each of the DSC traces showed exothermic peaks which were caused by precipitation of $Al_2O_3$ nanoparticles. The onset temperatures of the first and second exothermic peaks produced after 12 hours (Route 1) were ~ 220°C and ~ 370°C, respectively. The amount of heat released for the first and second exothermic peaks was 1.17 J/g and 0.86 J/g with peak temperatures at 266°C and 404°C, respectively. The onset temperature of the third small exothermic peak was ~ 450°C and the amount of heat released was 0.42 J/g with peak temperature at 476°C. However the onset temperature of the fourth incomplete exothermic peak was ~ 530°C, and the remaining part of the fourth exothermic peak is extended beyond 650°C. With the increase of the milling time from 12 hours to 24 hours (Route 2), the onset temperature of the first exothermic peak was ~ 220°C and the amount of heat released was 0.65 J/g with peak temperature at 242°C, while the second exothermic peak disappeared. The third exothermic peak became clearer and broad with an onset temperature of ~ 445°C and the amount of heat released was 2.03 J/g with peak temperature at 476°C. However the onset temperature of the fourth incomplete exothermic peak was ~ 535°C and remaining half part of the fourth exothermic peak is extended beyond 650°C.

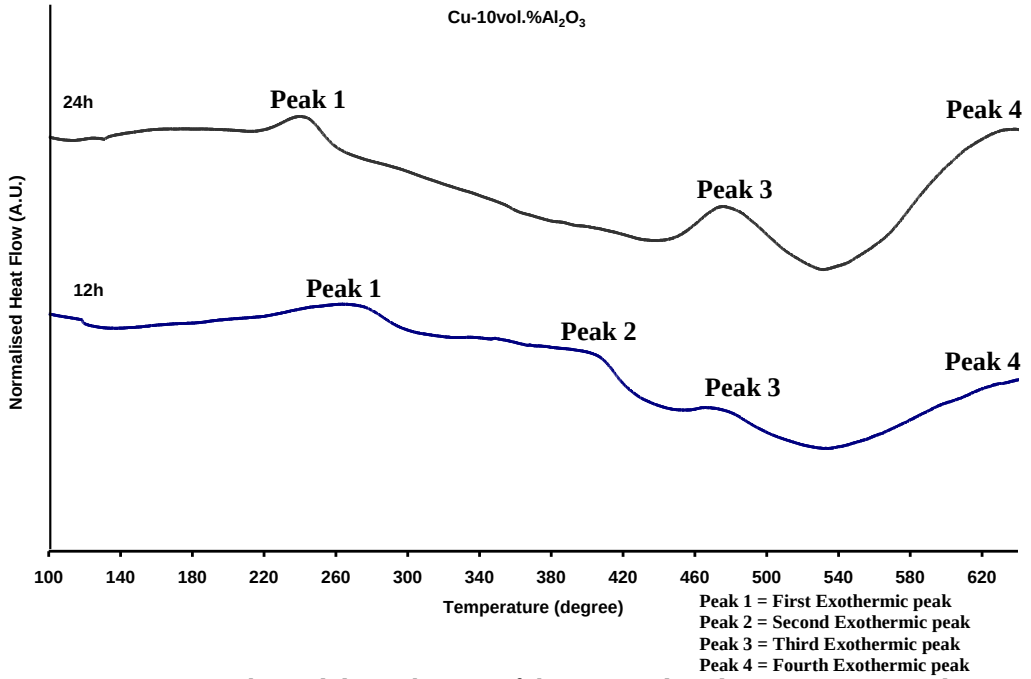


Figure 4.46: DSC traces obtained during heating of the Cu-10vol.%$Al_2O_3$ composite powder particles produced by HEMM after 12 hours (Route 1) and 24 hours (Route 2).

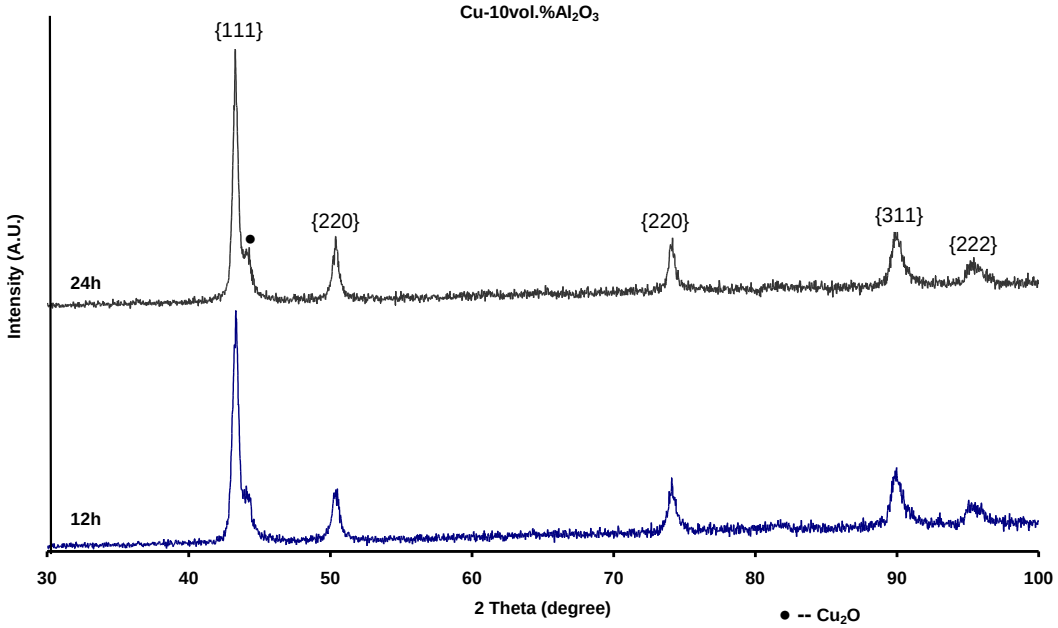


Figure 4.47: XRD patterns of Cu-10vol.%$Al_2O_3$ composite powder produced after 12 hours (Route 1) and 24 hours (Route 2) and after the first heating-cooling cycle (heated to 650°C).

After one heating-cooling cycle, the XRD patterns of the nanostructured Cu-10vol.%$Al_2O_3$ composite powder produced using Route 1 and Route 2 and heated to 650°C showed Cu peaks and a $Cu_2O$ peak, as shown in Figure 4.47. Based on the broadening of the Cu peaks and Williamson-Hall Method, the Cu grain size of the 12 hour and 24 hour composite powder, heated to 650°C, was ~ 150 nm and 450 nm.

## 4.3 Microhardness

### 4.3.1 Cu and Cu-$Al_2O_3$ Composites Produced using Route 1

Figure 4.48 shows the change of the average microhardness of the Cu and Cu-(2.5-10)vol.%$Al_2O_3$ composite balls/granules/powder particles produced by HEMM using Route 1 as a function of annealing temperature. The average microhardness of the UFG Cu balls produced using Route 1 remained almost unchanged after annealing at 150°C and 300°C. With increasing the annealing temperature from 300 to 400°C, the average microhardness decreased slightly perhaps due to reduction in dislocation density. However, for some reason the average microhardness increased with increasing the annealing temperature from 400 to 500°C, as shown in Figure 4.48. For Cu-2.5vol.%$Al_2O_3$ composite, after annealing at 150°C the average microhardness first decreased slightly, and then remained almost unchanged at 175 HV with increasing the annealing temperature from 150 to 500°C. After heat treatment at 150°C, the average microhardness of Cu-5vol.%$Al_2O_3$ granules decreased slightly and then remained almost unchanged with increasing the annealing temperature to 400°C. After this point the microhardness decreased with increasing the annealing temperature from 400 to 500°C.

For Cu-7.5vol.%$Al_2O_3$ composite, the average microhardness of the as-milled powder particles remained almost unchanged at around 255 HV after increasing the annealing temperatures from 150 to 400°C. While a sharp decrease in the average microhardness of the powder particles was observed with increasing the annealing temperature from 400 to 500°C. For Cu-10vol.%$Al_2O_3$ composite, after heat treatment at 150°C the average microhardness of powder particles clearly decreased, and then the average microhardness remained almost unchanged with increasing the annealing temperatures to 400°C. A sharp decrease in average microhardness from 232 HV to 180 HV was observed with increasing the annealing temperature from 400 to 500°C. For some reason, after annealing at temperatures in the range of 150 to 400°C, the microhardness of the Cu-10vol.%$Al_2O_3$ composite is lower than that of Cu-7.5vol.%$Al_2O_3$ composite.

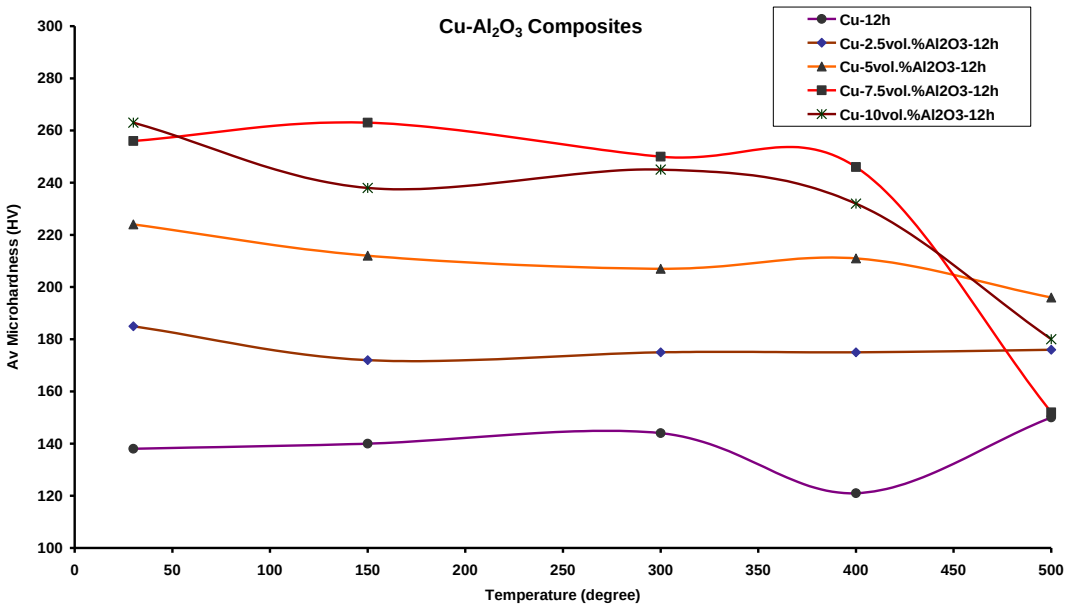


Figure 4.48: Average microhardness of Cu balls and Cu-(2.5-10)vol.% $Al_2O_3$ composite balls/granules/ powder particles produced by HEMM after 12 hours, Route 1, as a function of annealing temperature.

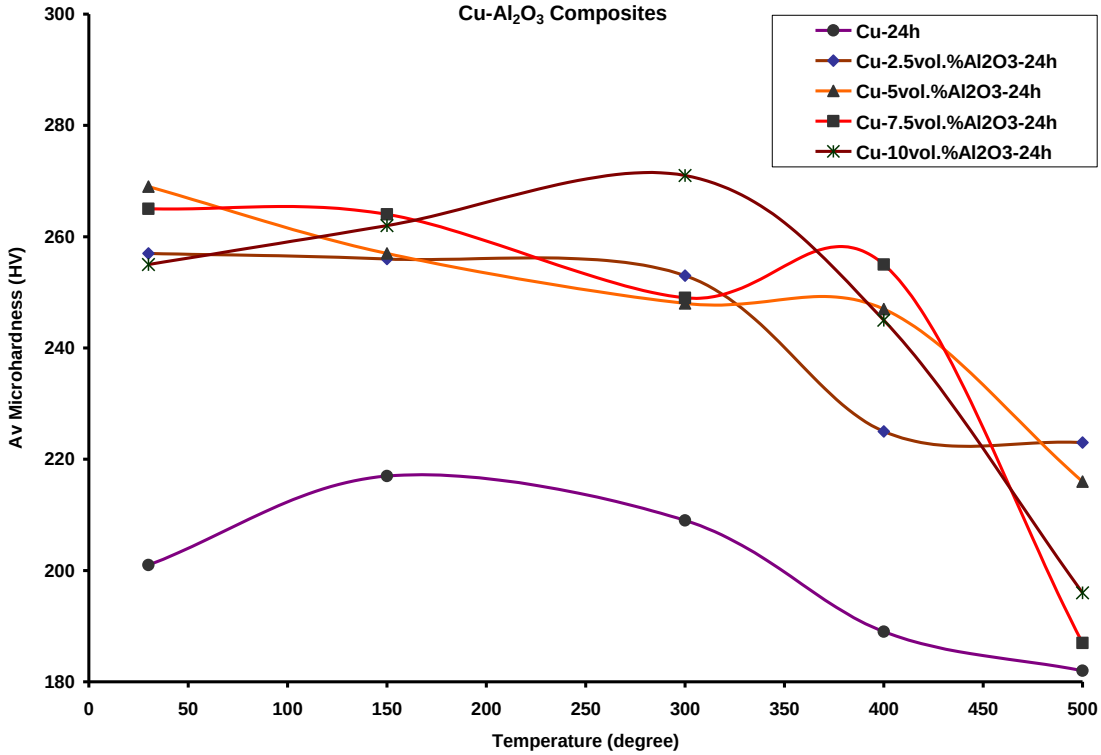


Figure 4.49: Average microhardness of Cu powder particles and Cu-(2.5-10)vol.%$Al_2O_3$ composite powder particles produced by HEMM after 24 hours, Route 2, as a function of annealing temperature.

## 4.3.2 Cu and Cu-$Al_2O_3$ Composites Produced using Route 2

Figure 4.49 shows the change of the average microhardness of the UFG Cu powder particles and nanostructured Cu-(2.5-10)vol.%$Al_2O_3$ composite powder particles

produced by HEMM using Route 2 as a function of annealing temperature. The average microhardness of the UFG Cu powder particles produced using Route 2 increased after annealing at 150°C, and then decreased little with increasing the annealing temperature to 300°C. After this the average microhardness decreased more sharply with increasing the annealing temperature to 500°C, as shown in Figure 4.49. For Cu-2.5vol.%$Al_2O_3$ composite, the average microhardness remained unchanged after annealing at 150°C and 300°C, but decreased sharply with further increasing the annealing temperature to 400°C and then again remained unchanged with increasing the annealing temperature from 400°C and 500°C. For Cu-5vol.%$Al_2O_3$ composite, the average microhardness decreased slightly and almost linearly from 260 HV to 250 HV with increasing the annealing temperature up to 300°C, then remained unchanged with increasing the annealing temperature from 300 to 400°C, but decreased sharply with increasing the annealing temperature from 400 to 500°C.

For Cu-7.5vol.%$Al_2O_3$ composite, the average microhardness remained unchanged after annealing at 150°C, and then slightly decreased from 265 HV to 250 HV with increasing the annealing temperature to 300°C. After this point, the average microhardness of the composite powder particles slightly increased to 255 HV with increasing the annealing temperature from 300 to 400°C and then decreased sharply with increasing the annealing temperature from 400 to 500°C. For Cu-10vol.%$Al_2O_3$ composite, the average microhardness increased slightly and almost linearly from 265 HV to 270 HV with increasing annealing temperature up to 300°C. After this point, the average microhardness decreased sharply and almost linearly from 270 HV to 195 HV with increasing the annealing temperature from 300 to 500°C.

# 4.4 Discussion

## 4.4.1 Microstructural Reasons of the Hardness

In the present study, Cu-2.5vol.%$Al_2O_3$ composite balls produced using Route 1 and after annealing at 150°C causes recrystallisation of the Cu matrix, resulting in formation of finer grains. The average microhardness of the annealed samples decreased, which is very similar that was observed before [6], even after the

refinement of grains, suggesting that in the as-milled condition, a substantial fraction of the high hardness is due to high dislocation density in the heavily cold worked material. Cu-10vol.%$Al_2O_3$ composite powder showed that the grain sizes of the Cu matrix are almost thermally stable at temperature up to 500°C (0.46 $T_m$), while the average microhardness decreased sharply after increasing the annealing temperature from 400 to 500°C, due to reduction of dislocation density.

For the nanostructured Cu-5vol.%$Al_2O_3$ composite powder produced using Route 2, annealing at 150°C has little effect on the grain sizes, since the nanometer scaled Cu grains are already the result of recrystallisation that occur during prolonged milling, while the slight decrease in average microhardness is likely to be due to decrease of dislocation density during annealing. Increasing the annealing temperature to 500°C for the Cu-(7.5 and 10)vol.%$Al_2O_3$ composite powders causes significant decrease in microhardness, partly due to coarsening of Cu grains and partly due to coarsening of $Al_2O_3$ nanoparticles. It appears that the coarsening of the grains and the associated microhardness decrease are not significant after annealing at temperatures up to 400°C. This suggests that the nanostructured Cu-$Al_2O_3$ composite powders can be consolidated at temperature around 400°C without totally losing the nanostructure.

### 4.4.2 Effect of $Al_2O_3$ Fraction on Thermal Stability

By comparing the change of Cu grain sizes with increasing annealing temperature for nanostructured Cu-$Al_2O_3$ composites, it can be seen that with increasing the volume fraction of $Al_2O_3$ particles from 2.5% to 10%, the coarsening of Cu grains with annealing at elevated temperature becomes clearly less severe. This can at least partly be attributed to the enhancement of the grain boundary pinning effect of the $Al_2O_3$ nanoparticles when their volume fraction is higher. Figures 4.50 and 4.51 show the estimated grain size of UFG and nanostructured Cu and Cu-(2.5-10)vol.%$Al_2O_3$ composite balls/granules/powder particles produced by HEMM using Route 1 and Route 2 and with the increase of annealing temperature from 150 to 500°C. Based on Scherrer equation, a more reliable understanding of the grain size with the increase of annealing temperature was observed, given in Figures 4.50 and 4.51.

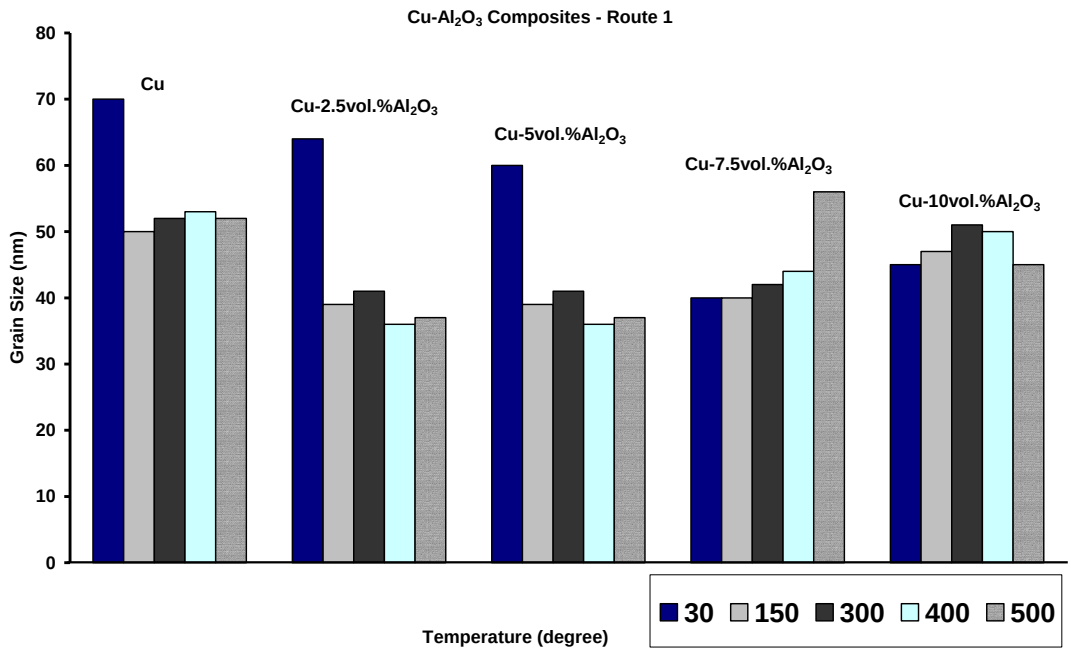


Figure 4.50: The estimated grain size of Cu balls and Cu-(2.5-10)vol.%$Al_2O_3$ composite balls/granules/ powders produced by HEMM after 12 hours, Route 1, and after annealing at 150, 300, 400 and 500°C, respectively.

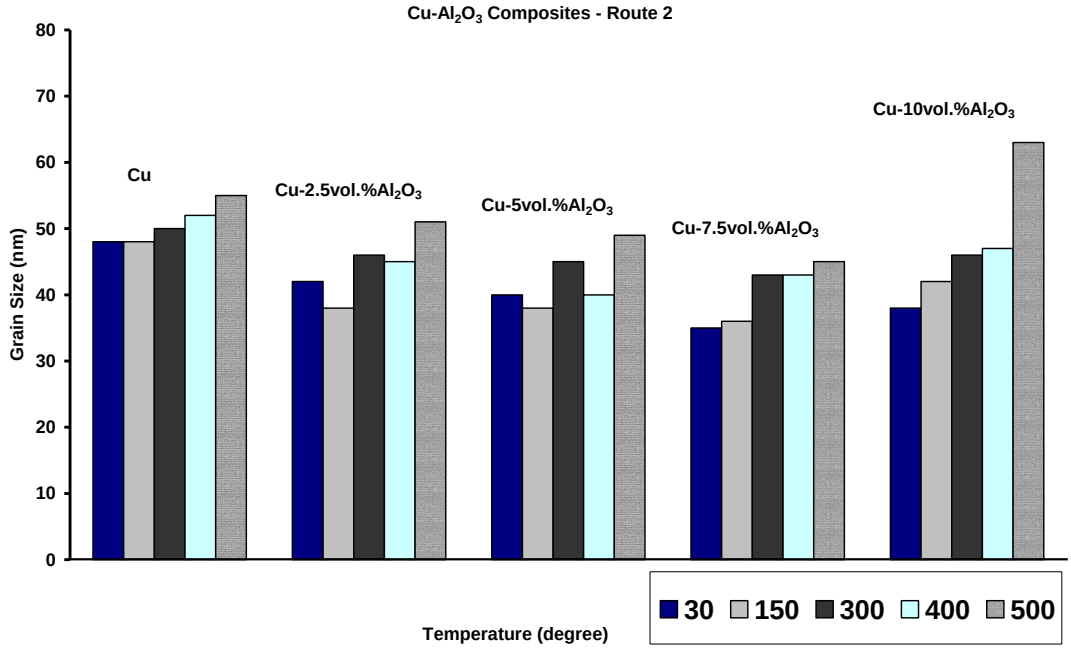


Figure 4.51: The estimated grain size of Cu powder particles and Cu-(2.5-10)vol.%$Al_2O_3$ composite powders produced by HEMM after 24 hours, Route 2, and after annealing at 150, 300, 400 and 500°C, respectively.

Based on TEM examination, the range of the grain sizes of UFG and nanostructured Cu and Cu-(2.5-10)vol.%$Al_2O_3$ composite balls/granules/powder particles produced by HEMM using Route 1 and Route 2, are shown in Table 4.1 and Table 4.2,

respectively. The degree of microstructure coarsening with the increase of annealing temperature for the Cu-$Al_2O_3$ composites produced using Route 2 was clearly smaller than that of Cu-$Al_2O_3$ composites produced using Route 1 annealed under the same condition. It is reported that decrease in average microhardness is less significant with the increase of annealing temperature from 400 to 500°C for the Cu-2.5vol.%$Al_2O_3$ composite and Cu-5vol.%$Al_2O_3$ composite powder particles produced using Route 2 as compared to the composites with a volume fractions of 7.5% and 10%. It is also reported that Cu-7.5vol.%$Al_2O_3$ composite and Cu-10vol.%$Al_2O_3$ composite powder particles produced using Route 2 were less thermally stable because of coarsening of the Cu grains and sharp decrease in average microhardness, due to reduction in dislocation density.

Table 4.1: Range of the grain size of the Cu-(2.5-10)vol.%$Al_2O_3$ composite balls/granules/powder particles produced by HEMM after 12 hours, Route 1.

| **Material** | Grain Size (nm) | | | |
|---|---|---|---|---|
| | **As-milled** | **150ºC** | **300ºC** | **500ºC** |
| Cu-2.5vol.%$Al_2O_3$ | 100-500 | 100-300 | 100-400 | 100-400 |
| Cu-5vol.%$Al_2O_3$ | 100-300 | 50-200 | 100-500 | 100-800 |
| Cu-7.5vol.%$Al_2O_3$ | 50-150 | 50-100 | 50-200 | 300-500 |
| Cu-10vol.%$Al_2O_3$ | 50-150 | 50-100 | 50-250 | 50-250 |

Table 4.2: Range of the grain size of the Cu and Cu-(2.5-10)vol.%$Al_2O_3$ composite powder particles produced by HEMM after 24 hours, Route 2.

| **Material** | Grain Size (nm) | | | |
|---|---|---|---|---|
| | **As-milled** | **150ºC** | **300ºC** | **500ºC** |
| Cu | 100-300 | 50-200 | 50-200 | 50-250 |
| Cu-2.5vol.%$Al_2O_3$ | 50-150 | 50-120 | 50-150 | 50-300 |
| Cu-5vol.%$Al_2O_3$ | 50-150 | 50-200 | 50-300 | 100-400 |
| Cu-7.5vol.%$Al_2O_3$ | 50-150 | 100-200 | 100-300 | 100-300 |
| Cu-10vol.%$Al_2O_3$ | 50-120 | 50-150 | 100-200 | 100-350 |

## 4.4.3 Effect of Initial Microstructure

Cu grain sizes first decreased due to recrystallisation after heat treatment at 150°C, then slight coarsening was observed at 300°C and lastly significant coarsening with

increasing the annealing temperature to 500°C. On the other hand, coarsening of $Al_2O_3$ nanoparticles occurs during the annealing at temperature in the range of 300-500°C, and the rate of coarsening became quite dramatic at 500°C. Increasing the volume fraction of $Al_2O_3$ nanoparticles, the microstructure of the Cu matrix became more refined, and the coarsening of Cu grains in the composite powder particles after annealing at 500°C became less severe. It is reported that Cu-2.5vol.%$Al_2O_3$ and Cu-5vol.%$Al_2O_3$ composites produced using Route 2 were more thermally stable up to 300°C, as Cu grain coarsening and decrease in average microhardness was less severe. On the other hand, Cu-7.5vol.%$Al_2O_3$ and Cu-10vol.%$Al_2O_3$ composites produced using Route 1 were more thermally stable up to 300°C and 500°C, respectively, as slight growth of Cu grains and decrease in average microhardness was not significant for the corresponding material.

## 4.5 Summary

In this study, the thermal stability and microhardness change of the Cu-(2.5-10)vol.% $Al_2O_3$ composite balls/granules/powder particles produced by HEMM and caused by annealing at temperatures in the range of 150-500°C is reported. It was found that after heat treatment at 150°C, the Cu grain sizes decreased due to recrystallisation, and slight coarsening of the Cu grains was observed with increasing the annealing temperature to 300°C. Further increasing the annealing temperature to 500°C caused significant coarsening of the Cu grains and the $Al_2O_3$ nanoparticles and significant decrease in microhardness due to reduction in dislocation density. The coarsening of the Cu grains and the associated microhardness decrease were not significant after annealing at temperatures up to 400°C, suggesting that the composite powder can be consolidated at temperatures around 400°C without totally losing the nanostructure. Cu-$Al_2O_3$ composite powder particles produced using Route 2 showed that with the increase of the volume fraction of $Al_2O_3$ nanoparticles and refinement in the microstructure of the Cu matrix both increased the thermal stability of the composite structure.

## 4.6 References

1. Z. Zhang, B.Q. Han, Y. Zhou and E.J. Lavernia, *Mater. Sci. Eng. A,* **493,** 2008, 221

2. K.A. Darling et al, *Intermetallics* , **16,** 2008, 378

3. J.M. Hernandez et al, *J. Alloys Compd.*, **388,** 2005, 266

4. B.D. Cullity, *Elements of X-ray Diffraction*, 1978, Addison-Wesley Publishing Company, Inc.

5. G.K. Williamson and W. Hall, *Acta Metallurgica* **1**, 1953, 22

6. J. Naser, W. Riehemann and H. Ferkel, *Mat. Sci. Eng. A* **234–236**, 1997, 467

# Chapter Five
# Microstructural Evolution and Thermal Stability of Cu-(1-4)at.%Pb Alloy Powders Produced by HEMM

## 5.1 Introduction

In this chapter, the results of the microstructural evolution during HEMM and heat treatment of nanostructured Cu-Pb alloy powders are described. The change in microhardness of the Cu-Pb powder particles of different compositions and milled for different milling times caused by annealing at different temperatures was also examined.

## 5.2 Microstructural Evolution during HEMM

HEMM was performed for 12 hours (Route 1) to prepare powders with three nominal compositions : Cu-1at.%Pb, Cu-2at.%Pb and Cu-4at.%Pb. The mixture of Cu and Pb powders failed to be consolidated in-situ during HEMM and the powder mixtures were converted into fine Cu-Pb alloy powders after 6 hours and 12 hours of milling (Route 1). Figures 5.1(a) and 5.1(b) show the XRD patterns of Cu-(1-4)at.%Pb alloy powders produced after 6 hours and 12 hours of milling, Route 1. After 6 hours of milling, XRD patterns (Figure 5.1(a)) showed Cu peaks and Pb{111} peak. With the increase of the Pb content from 1at.% to 4at.%, the Pb{111} peak became more prominent with increasing the milling time from 6 hours to 12 hours, the XRD patterns of the Cu-Pb alloy powders (Figure 5.1(b)) showed only Cu peaks and the Pb peak disappeared, which indicated a large fraction of Pb was dissolved in the Cu matrix. It was also noted that with increasing the milling time from 6 to 12 hours, the Cu peaks became notably broader, suggesting the decrease of Cu grain size.

The average grain sizes and lattice strains of the Cu powder with 0.6wt%PCA and Cu-(1-4)at.%Pb alloy powder particles were estimated using the Williamson-Hall method [1] and broadening of the XRD peaks of the Cu phase, as shown in Figures 5.2 and 5.3. Based on this estimation, the grain size of the Cu matrix of the Cu-(1-4)at.%Pb alloy powder particles produced after 6 hours and 12 hours of milling was in the range of 30-160 nm, as shown in Figure 5.2. For the 6 hours milled powders, the grain size decreased with increasing the Pb content to 2at.% and

increased with increasing the Pb content to 4at.% as compared with 6 hour milled powders. For the 12 hours milled powders, the grain size decreased significantly for all Cu-Pb compositions, as shown in Figure 5.2. The grain sizes of the 12 hour milled powder decreased with increasing Pb content. The lattice strain for the 6 hours milled powders remained unchanged with increasing the Pb content to 2at.% and then increased significantly with increasing the Pb content to 4at.%. For the 12 hours milled powders, the lattice strain showed a decreasing trend, as shown in Figure 5.3.

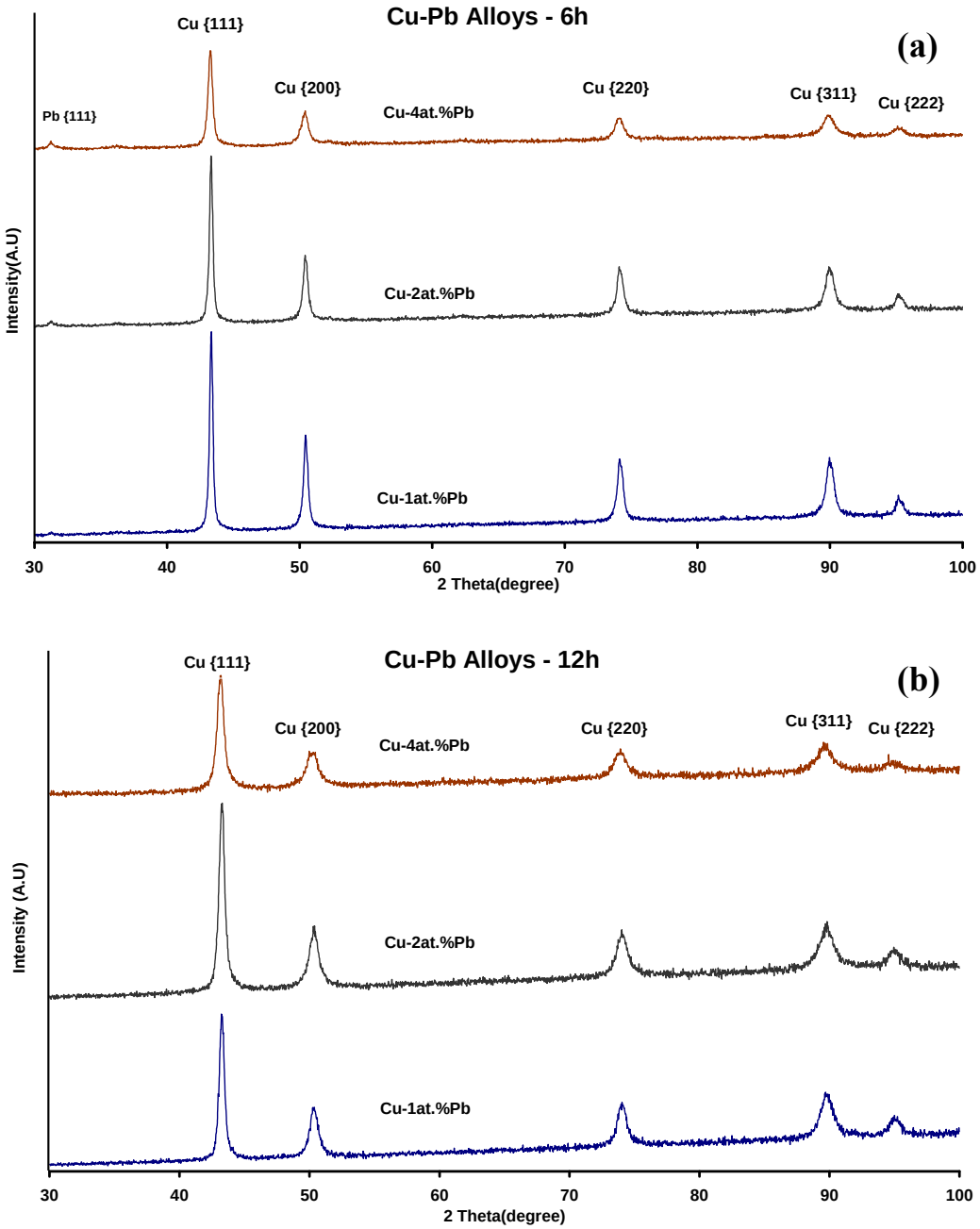


Figure 5.1: X-ray diffraction patterns of Cu-(1-4)at.%Pb alloy powders produced by HEMM using, Route 1, (a) after 6 hours milling, and (b) after 12 hours milling.

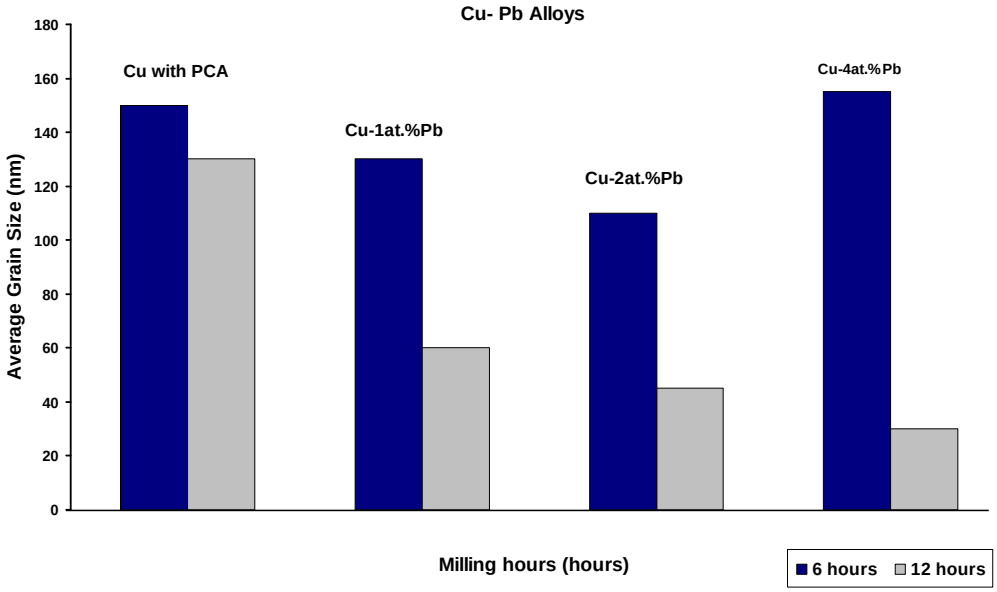


Figure 5.2: The average grain size of as-milled Cu powder with 0.6wt%PCA and Cu-(1-4)at.%Pb alloy powders produced by HEMM after 6 hours and 12 hours using Route 1.

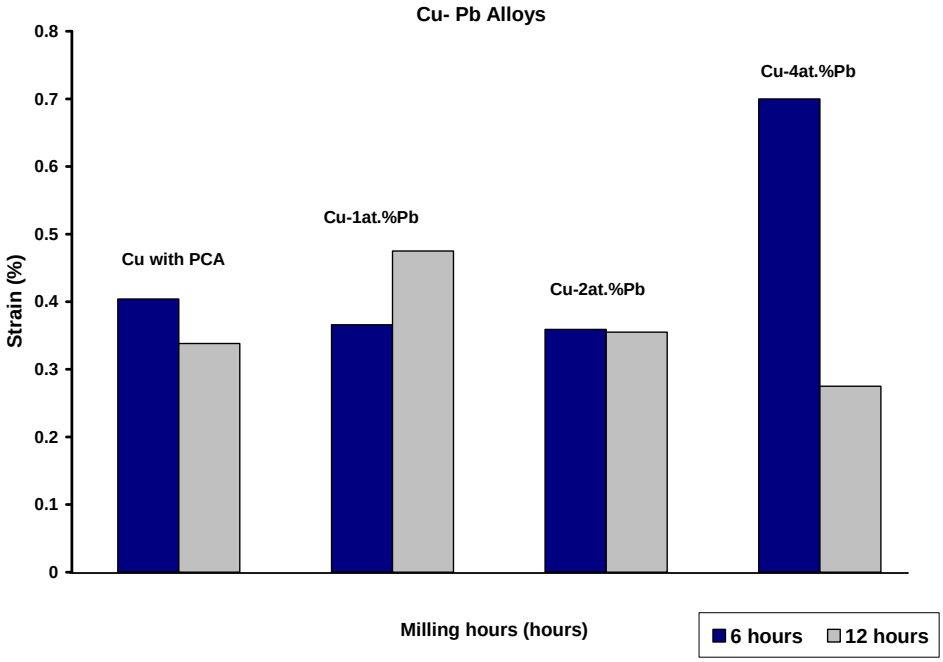


Figure 5.3: The lattice strain of as-milled Cu powder with 0.6wt%PCA and Cu-(1-4)at.%Pb alloy powders produced by HEMM after 6 hours and 12 hours using Route 1.

TEM examination of the Cu-1at.%Pb alloy powder particles confirmed that cellular substructures were formed in the powder particles due to plastic deformation after 6 hours of milling (Figure 5.4(a)). After 12 hours of milling, nanograins formed through recrystallisation with grain size in the range of 100-150 nm (Figure 5.4(c)). TEM examination confirmed the reduction of the grain size with the increase of the milling from 6 to 12 hours, with the formation of nanograins from UFG cellular substructures. The refinement of the microstructure with increasing milling time is also shown by the selected area diffraction patterns (SADPs) in Figures 5.4(b) and 5.4(d).

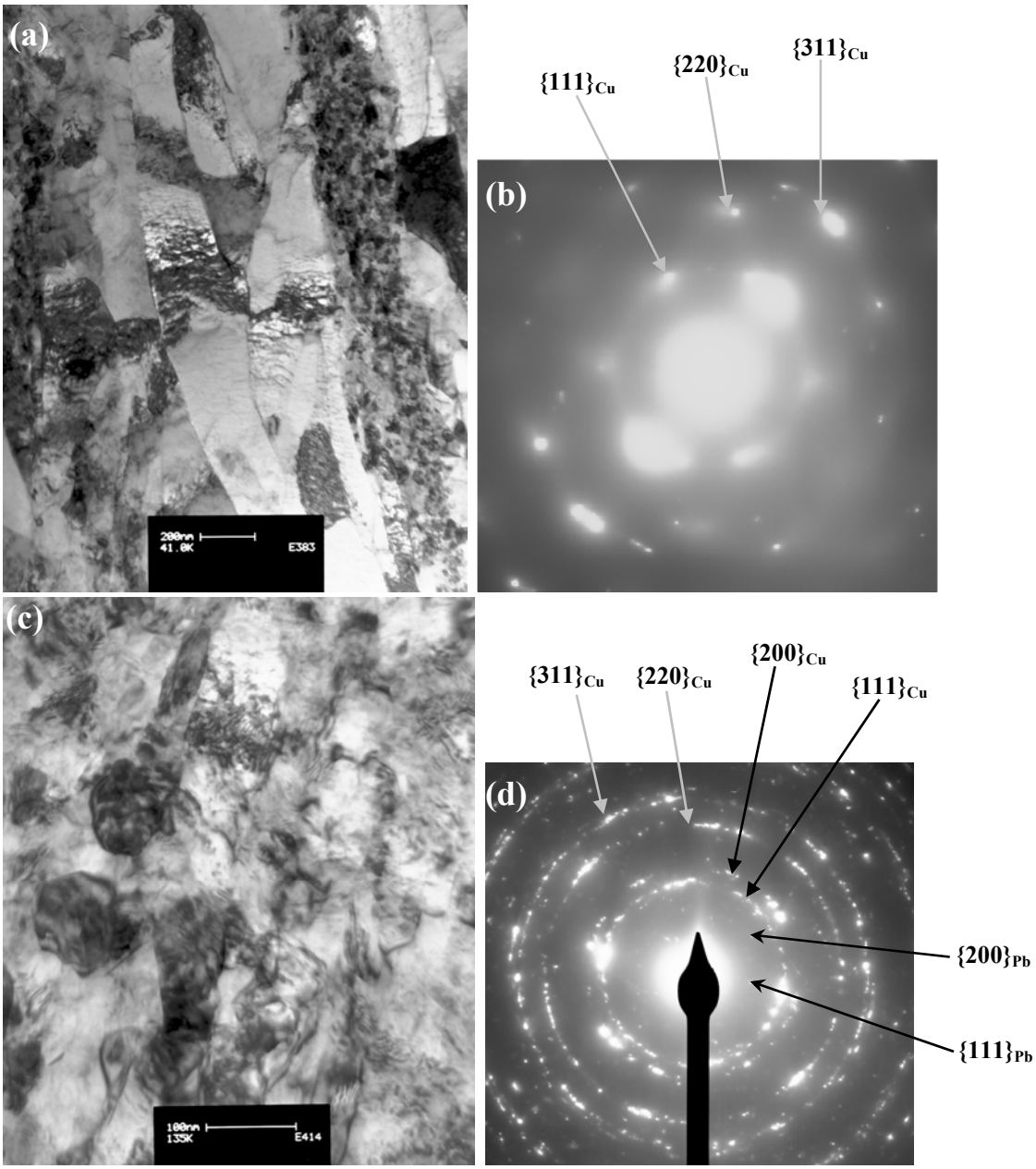


Figure 5.4: TEM Bright field images and SADPs of Cu-1at.%Pb alloy powder particles produced by HEMM using Route 1, ((a) and (b)) after 6 hours, and ((c) and (d)) after 12 hours milling.

Almost continuous rings for Cu powder particles were observed in the SADP for the alloy powder after 12 hours, while discrete diffraction reflections for Cu powder particles produced after 6 hours were observed. Based on the SADPs it can be seen that strong reflections ({111}, {200}, {220}, {311}) could be correlated to Cu matrix while weak reflections ({111}, {200}) are probably in related to Pb particles. Indexing of SADPs is recorded from JCPDS files of Cu (04-0836) and Pb (04-0686), as shown in Appendix A.

TEM examination of the 12 hours milled powder particles showed that with increasing Pb content from 1 to 2at.%, the grain sizes of the Cu matrix decreased slightly to the range of 50-150 nm (Figure 5.5(a)). The majority of the Cu grains of the as-milled Cu-2at.%Pb powder particles produced after 12 hours had sizes ~

100nm. On the other hand, the Cu grains of the as-milled Cu-4at.%Pb powder particles produced after 12 hours had sizes in the range of 150-250 nm (Figure 5.5(c)). The average grain size, which was calculated using the XRD peaks and Williamson-Hall method for the Cu-(1-4)at.%Pb alloy powders is smaller than the actual average Cu grain size examined by TEM, and this discrepancy is likely due to overestimate of the broadness of XRD peaks which is directly attributed to the size of the grains. Based on the TEM examination, the Cu grain sizes remained almost unchanged with the increase of the Pb content from 1at.% to 2at.% for the 12 hours of milled Cu-Pb alloy powders and almost continuous rings of the Cu powder were observed in the SADP, as shown in Figure 5.5(b). However these rings were replaced by discrete diffraction reflections for Cu-4at.%Pb powder particles, presumably in relation to the grain growth with the increase of Pb content, as shown in Figure 5.5(d).

Energy dispersive X-ray spectrum analysis of 12 hours milled Cu-1at.%Pb and Cu-2at.%Pb alloy powder particles, respectively, showed that the Pb particles were incorporated into each of the powder particles, as shown in Figures 5.6(a) and 5.6(b), forming a nanostructured Cu-Pb alloy. The peak which is not labeled in the energy dispersive X-ray spectrum analysis (Figures 5.6(a) and 5.6(b)) is for Platinum. SEM examination showed that the Pb particles were incorporated into each of the as-milled powder particles, forming a nanostructured Cu-Pb alloy structure, as confirmed by energy dispersive X-ray elemental (Cu and Pb) mapping of the as-milled Cu-2at.%Pb powder particles produced after 6 hours and 12 hours. Figures 5.7(a) and 5.7(d) show the SEM micrographs of the as-milled Cu-2at.%Pb alloy powder particles produced after 6 hours and 12 hours (Route 1) of milling, respectively, while Figures 5.7((b) and (c)) and 5.7((e) and (f)) show their corresponding energy dispersive X-ray elemental mapping (Cu and Al). Cu-2at.%Pb alloy powder particles produced after 12 hours (Figure 5.7(f)) showed more homogenous distribution of Pb in Cu-rich powder particle as compared to 6 hours (Figure 5.7(c)) of milling. On the other hand, figures 5.8(a) and 5.8(d) show the SEM micrographs of the as-milled Cu-4at.%Pb alloy powder particles produced after 6 hours and 12 hours (Route 1) of milling, respectively, while Figures 5.8((b) and (c)) and 5.8((e) and (f)) show their corresponding energy dispersive X-ray elemental mapping (Cu and Al). The energy dispersive X-ray elemental (Cu and Pb) mapping of the as-milled Cu-4at.%Pb powder particles produced after 6 hours and 12 hours of milling, shown at a higher magnification

in Figures 5.8(c) and 5.8(f), respectively, showed a homogenous distribution of Pb in each of the Cu-rich powder particles.

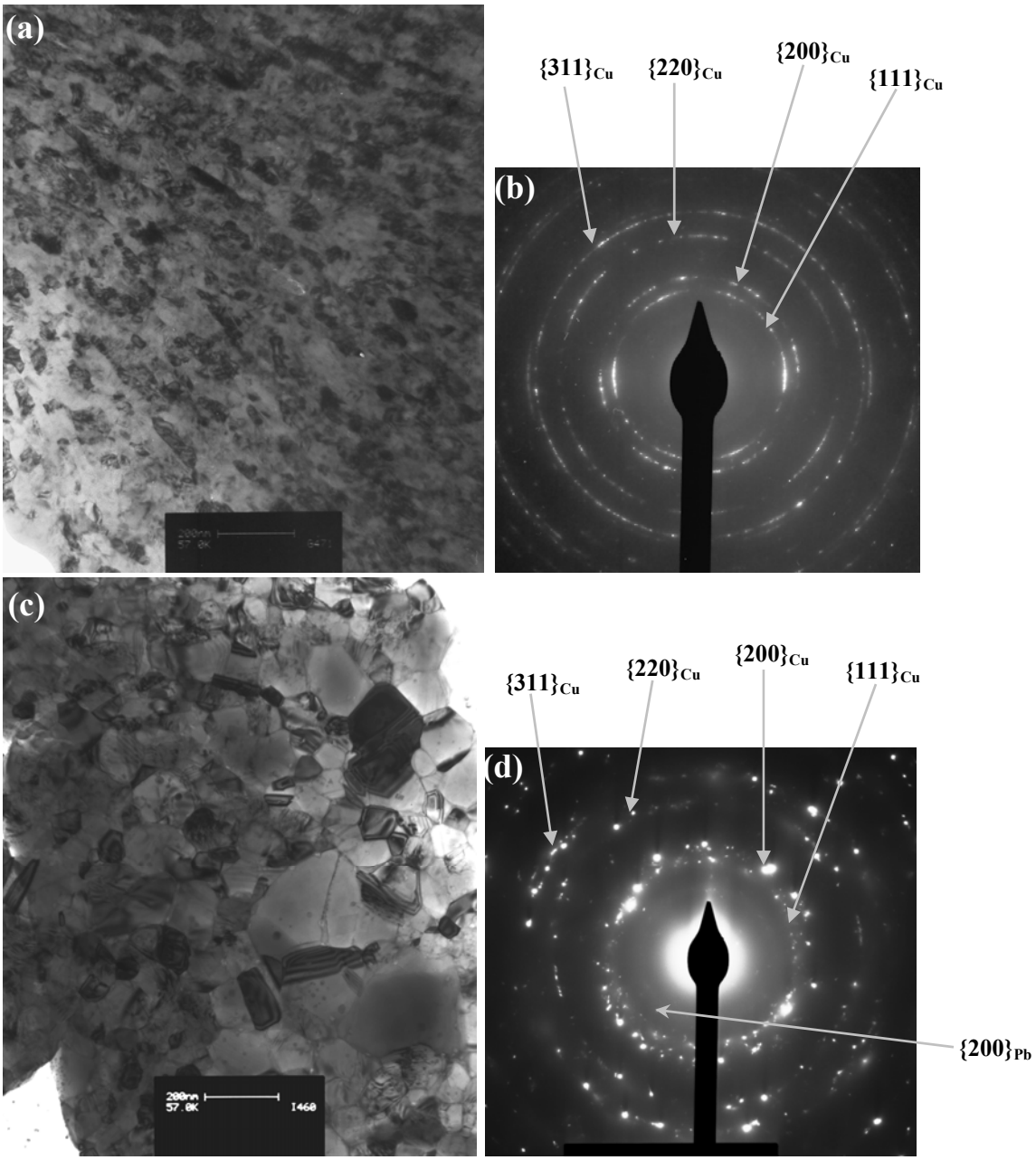


Figure 5.5: TEM Bright field images and SADPs of Cu-Pb alloy powders produced by HEMM after 12 hours using Route 1, ((a) and (b)) Cu-2at.%Pb alloy and ((c) and (d)) Cu-4at.%Pb alloy.

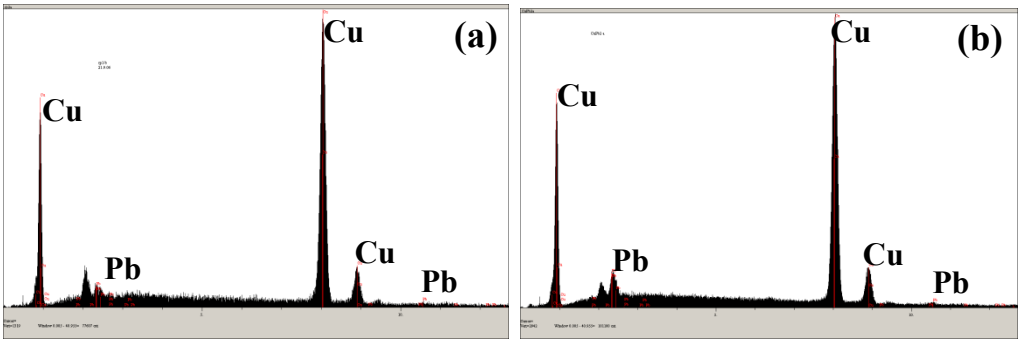


Figure 5.6: EDX spectrum, Intensity vs Energy (keV), of Cu-Pb alloy powder particles produced by HEMM after 12 hours, Route 1, (a) Cu-1at.%Pb alloy, and (b) Cu-2at.%Pb alloy.

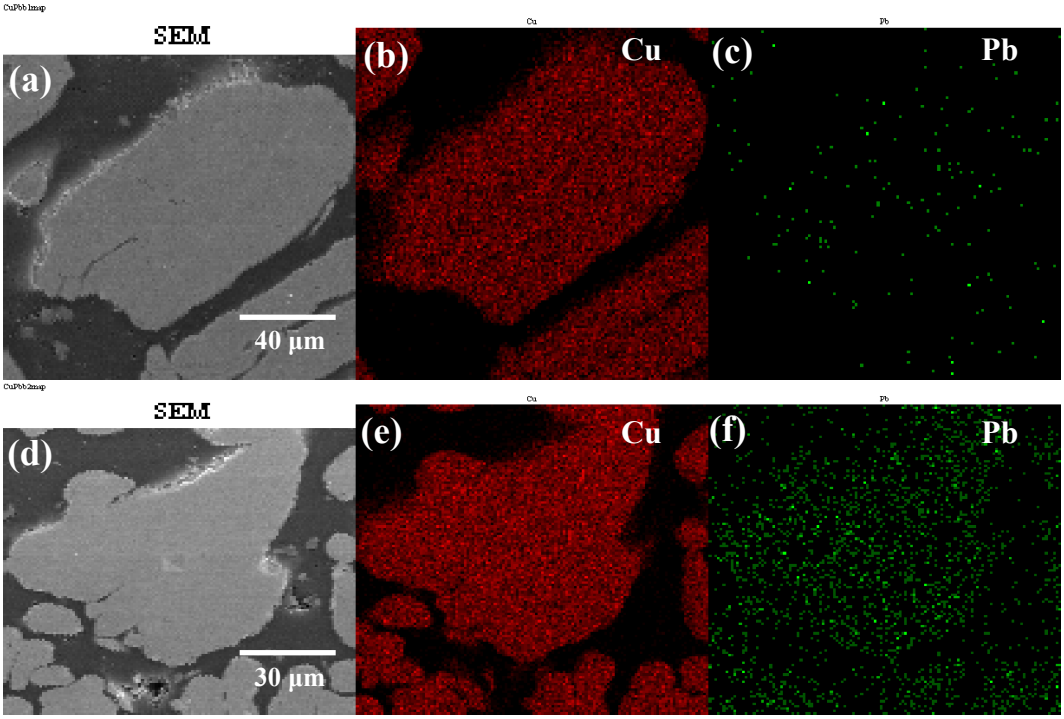


Figure 5.7: SEM micrographs and corresponding Energy Dispersive X-ray elemental (Cu and Pb) maps of the cross section of Cu-2at.%Pb alloy powder particles produced by HEMM using Route 1, (a) after 6 hours milling, and (b) after 12 hours milling.

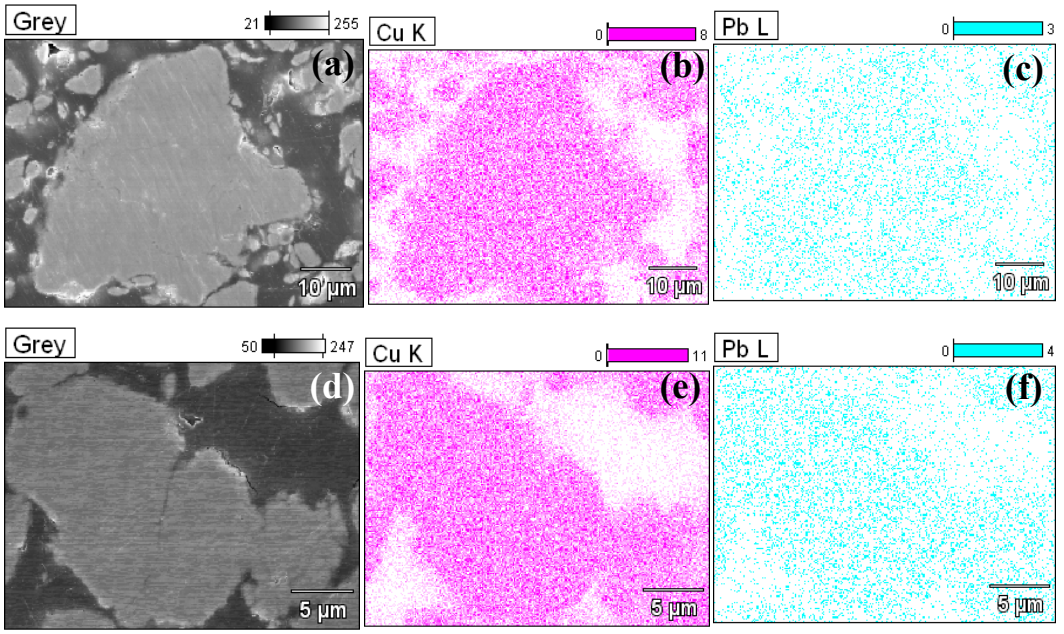


Figure 5.8: SEM micrographs and corresponding Energy Dispersive X-ray elemental maps (Cu and Pb) of the cross section of Cu-4at.%Pb alloy powder particles produced by HEMM using Route 1, (a) after 6 hours milling, and (b) after 12 hours milling.

Based on the STEM images and X-ray elemental mapping (Cu and Pb) of the nanostructured Cu-2at.%Pb alloy powder particles produced using Route 1, a more homogenous distribution and dispersion of Pb particles in Cu matrix was observed in 12 hours milled alloy powder particles, as compared to 6 hours milled alloy powder particles. Elongated subgrains (Figure (5.9(c)) of the Pb particles in

the Cu matrix were converted to a homogenous distribution (Figure (5.9(f)) of Pb particles, as confirmed by x-ray elemental mapping of Pb. The size of the Cu-2at.%Pb alloy powder particles produced after 12 hours reached within the range of 50-150 nm.

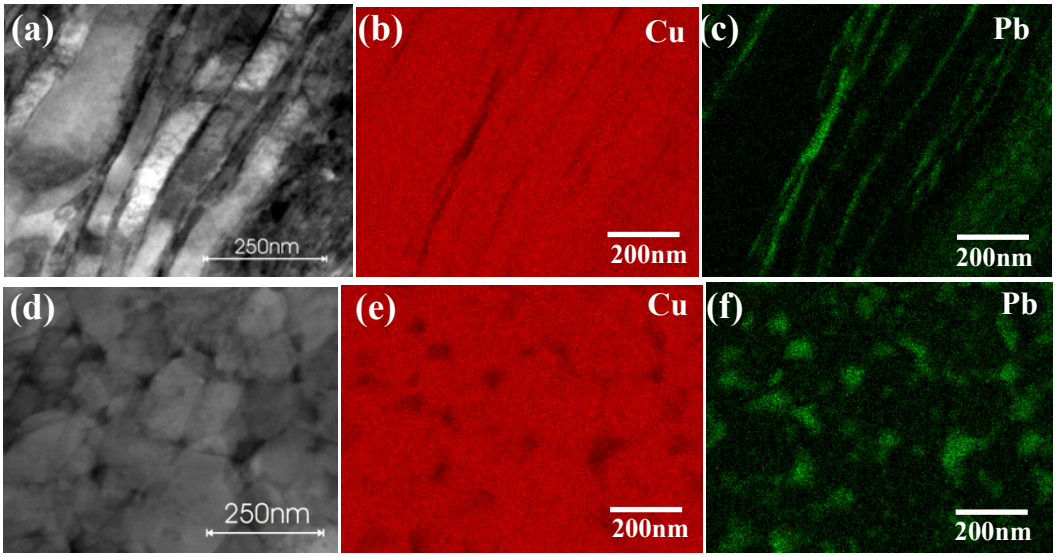


Figure 5.9: STEM images and X-ray elemental (Cu and Pb) maps of Cu-2at.%Pb alloy powder particles produced by HEMM with different milling times using Route 1, ((a)-(c)) after 6 hours, and ((d)-(f)) after 12 hours.

## 5.3 Microhardness

Figure 5.10 shows the average microhardness of Cu powder with 0.6wt%PCA and Cu-(1-4)at.%Pb alloy powder particles produced by HEMM after 6 hours and 12 hours, respectively. Using Route 1, and increasing the content of the Pb particles from zero to 1at.%, a significant increase in average microhardness was observed after 6 hours and 12 hours of milling, as shown in Figure 5.10. The average microhardness of Cu-2at.%Pb powder particles produced after 6 hours of milling decreased to about the average microhardness of the pure Cu starting powder (100 HV). However, a dramatic increase of average microhardness was observed with the increase of milling time from 6 hours to 12 hours. Cu-Pb alloy powder particles with the Pb content of 1at.% or 4at.% showed higher average microhardness for the initial 6 hours of milling, suggesting a homogenous distribution of Pb powder particles. With the same milling time the microhardness of Cu-2at.%Pb alloy powder was significantly lower and with a further increase of Pb content from 2at.% to 4at.%, the average microhardness decreased significantly for the powder particles produced after 12 hours of milling, as shown in Figure 5.10.

The following are the possible reasons for the changes of microhardness of the Cu-Pb alloy powders with milling time and Pb content :

● With increasing milling time from 6 to 12 hours, more Pb is alloyed with Cu to form Cu-Pb solid solutions. This leads to a higher degree of solution strengthening and in the meantime a smaller fraction of soft Pb particles.

● For a given milling time, a higher content of Pb in the starting can have two opposite effects : (i) More Pb goes into solid solution if all Pb can be alloyed into the solid solution. This leads of a higher hardness. (ii) More Pb is left out in the incomplete alloying and this fraction of Pb exists in the form of Pb particles in the powder, making the powder softer. This is the case for Cu-4at.%Pb alloy powders.

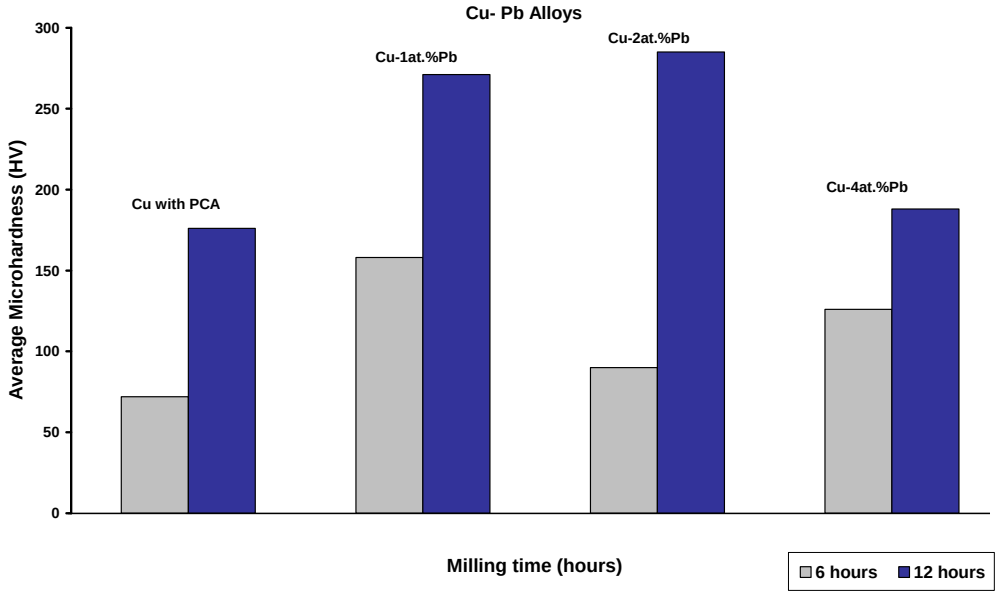


Figure 5.10: The average microhardness of Cu powder with 0.6wt%PCA and Cu-(1-4)at.%Pb alloy powder particles produced by HEMM after 6 hours and 12 hours, Route 1, respectively.

# 5.4 Microstructural Evolution during Heat Treatment

## 5.4.1 XRD Analysis

Figure 5.11 shows the XRD patterns of Cu-1at.%Pb alloy powder produced by HEMM after 12 hours (Route 1) and after annealing at different temperatures, respectively. The XRD patterns only showed Cu peaks for the as-milled and after annealing at 150°C and 300°C, due to the small fraction of Pb powder. However, a small peak of Pb{111} appeared after annealing at 400°C, which became more prominent after annealing at 500°C. The broadening effect of Cu peaks in the XRD patterns decreased for the powder annealed at 500°C, very likely due to increase of grain size of Cu matrix.

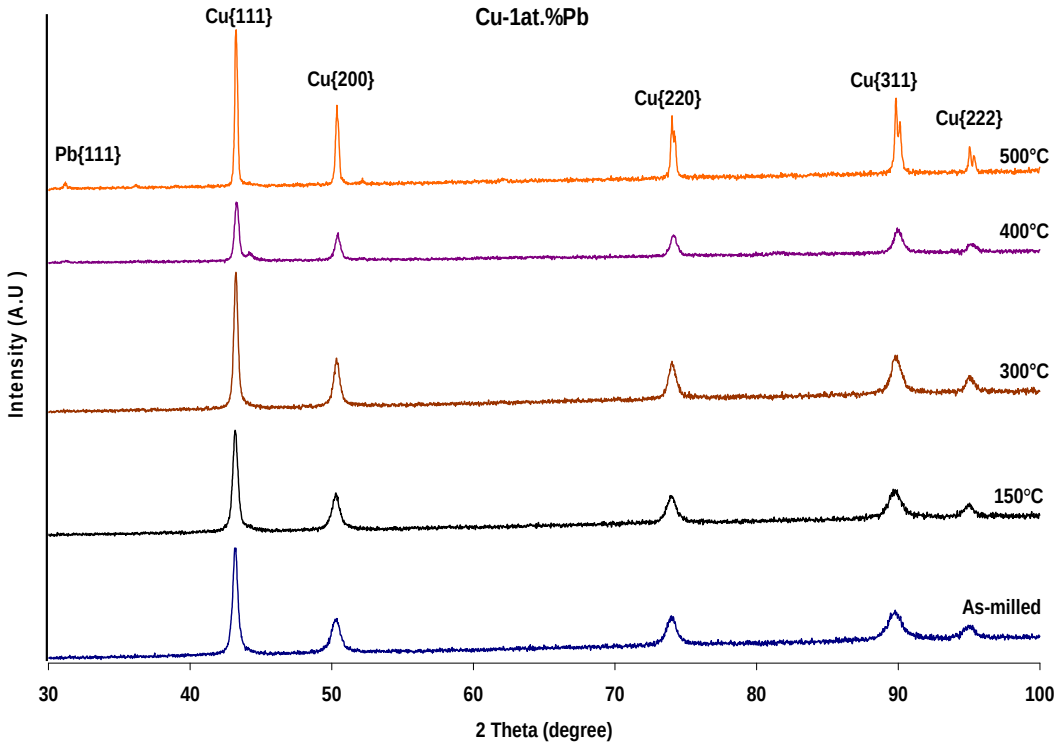


Figure 5.11: X-ray diffraction patterns of Cu-1at.%Pb alloy powder produced by HEMM after 12 hours, Route 1, and after annealing at 150, 300, 400 and 500°C, respectively.

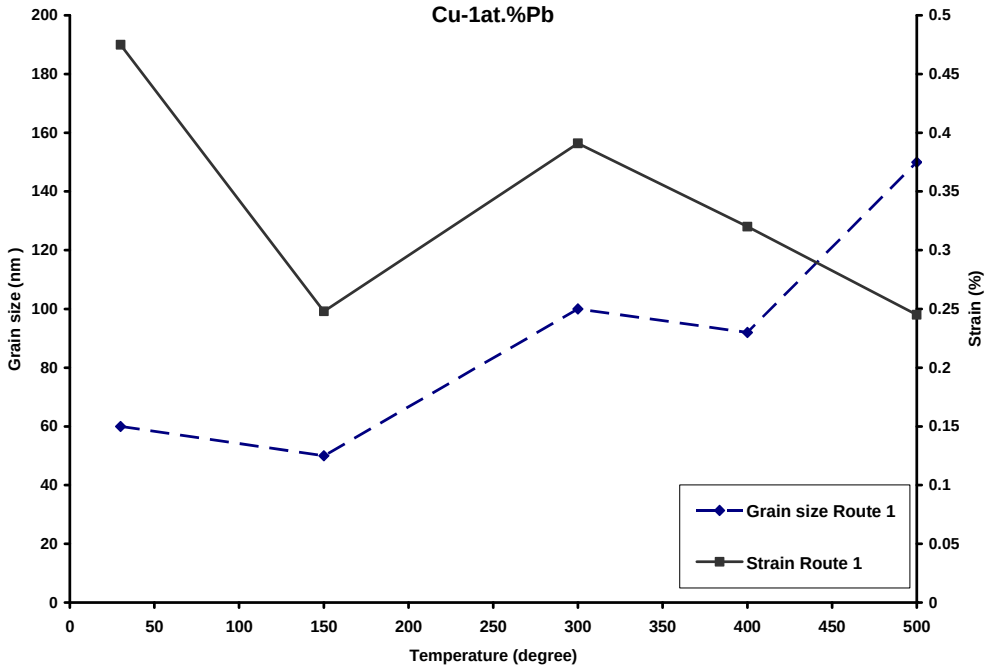


Figure 5.12: Average grain size and lattice strain of Cu-1at.%Pb alloy powder particles produced by HEMM after 12 hours, Route 1, and after annealing at 150, 300, 400 and 500°C, respectively.

The average grain size and lattice strain data of the nanostructured Cu-1at.%Pb alloy powder particles produced using Route 1 and after annealing at different temperatures were estimated using the broadening of the XRD peaks and Williamson-Hall method, as shown in Figure 5.12. Based on this estimation, the

Cu grain size of the 12 hours milled powder with the increase of annealing temperature from 150 to 500°C was in the range of 50-150 nm. Grain sizes and lattice strain data of the alloy powder particles showed a similar trend after annealing up to 300°C. However a decrease in lattice strain of the powder particles was observed after annealing at 400 and 500°C.

Figure 5.13 shows the XRD patterns of nanostructured Cu-2at.%Pb alloy powder produced by HEMM after 12 hours (Route 1) and after annealing at different temperatures, respectively. The XRD patterns only showed Cu peaks for the as-milled and after annealing in the range of 150 to 400°C, due to the small fraction of Pb powder. However, after annealing at 500°C, small Pb peaks appeared in the XRD pattern, very likely due to the precipitation of Pb particles. The broadening effect of Cu peaks in XRD patterns after annealing at 500°C decreased, very likely due to increase of grain size of Cu matrix. The Cu{111} peak shifted 0.15º to a larger angle after annealing at 500°C which caused the lattice parameter to decrease by 0.0012 nm for powder particles produced using Route 1. This change of Cu lattice parameter perhaps caused by some of the Pb dissolved in the solution during the milling and then precipitating out after annealing at 500°C.

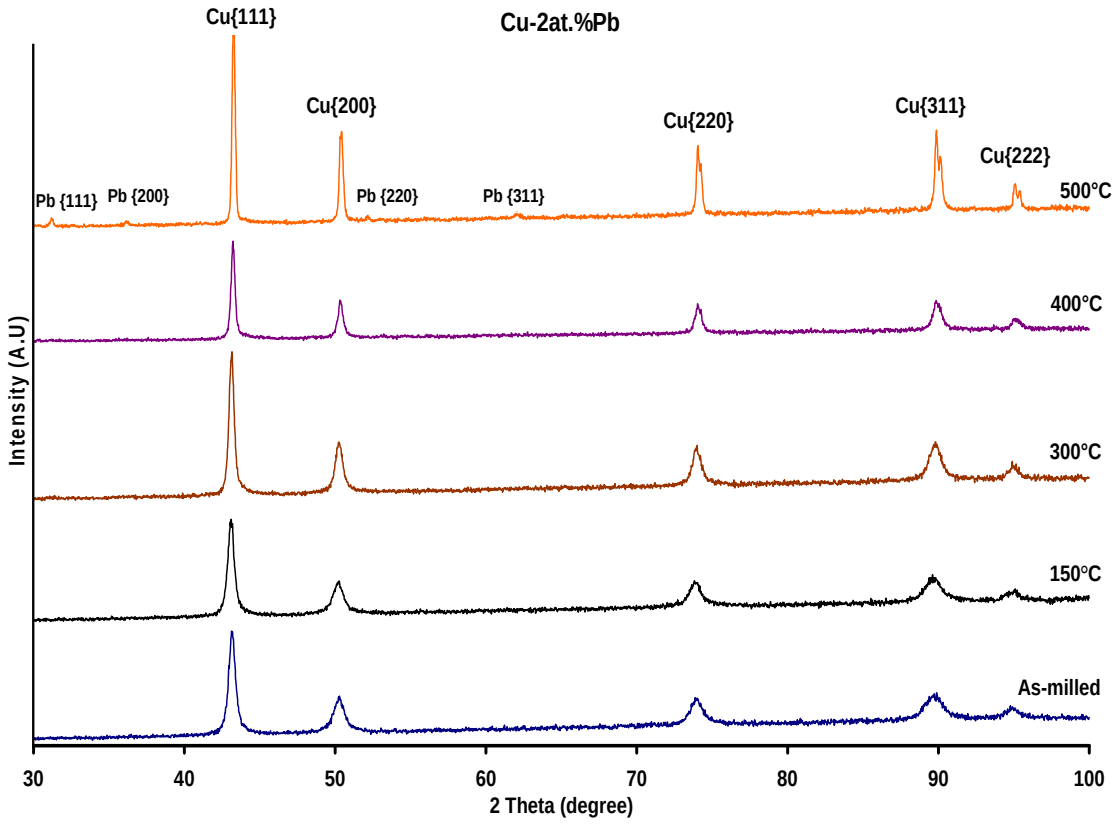


Figure 5.13: X-ray diffraction patterns of Cu-2at.%Pb alloy powder produced by HEMM after 12 hours, Route 1, and after annealing at 150, 300, 400 and 500°C, respectively.

The average grain size and lattice strain data of the nanostructured Cu-2at.%Pb alloy powder particles produced using Route 1 and after annealing at different temperatures were estimated using the broadening of the XRD peaks and Williamson-Hall method, as shown in Figure 5.14. Based on the Williamson-Hall method and broadening of the XRD Cu peaks, the estimated Cu grain size of the 12 hours milled powder with the increase of annealing temperature from 150 to 500°C was in the range of 50-180 nm. Grain sizes and lattice strain data of the alloy powder particles showed a similar trend after annealing up to 300°C. However a significant increase in grain size of the powder particles was observed after annealing at 400°C while lattice strain showed the decreasing trend.

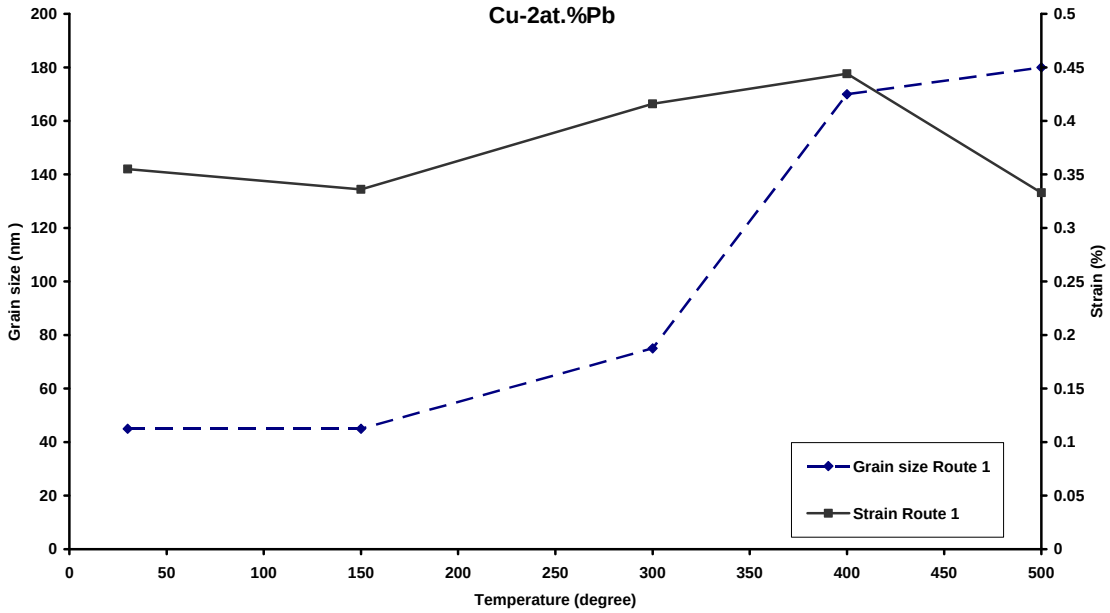


Figure 5.14: Average grain size and lattice strain of Cu-2at.%Pb alloy powder particles produced by HEMM after 12 hours, Route 1, and after annealing at 150, 300, 400 and 500°C, respectively.

Figure 5.15 shows the XRD patterns of Cu-4at.%Pb powder produced by HEMM after 12 hours (Route 1) and after annealing at different temperatures, respectively. The XRD patterns only showed Cu peaks for the as-milled and after annealing at 150°C, due to the small fraction of Pb powder. However, with the increase of annealing temperature from 150 to 300°C and 400°C, small Pb peaks appeared, which became more prominent after annealing at 500°C, as shown in Figure 5.15, very likely due to the precipitation of Pb particles. For the Cu-4at.%Pb alloy powder annealed in the range of 300 to 500°C, the broadening effect of the Cu

peaks decreased in the XRD pattern, very likely due to increase of grain size of Cu matrix.

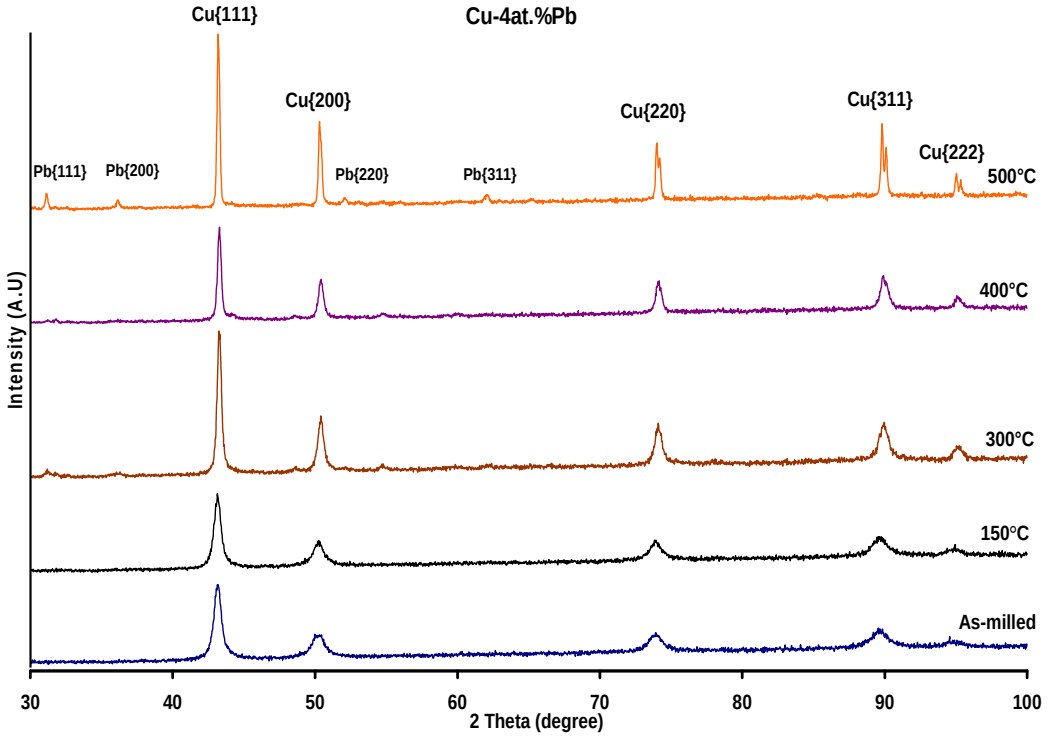


Figure 5.15: X-ray diffraction patterns of Cu-4at.%Pb alloy powder produced by HEMM after 12 hours, Route 1, and after annealing at 150, 300, 400 and 500°C, respectively.

The average grain size and lattice strain data of the nanostructured Cu-4at.%Pb alloy powder particles produced using Route 1 and after annealing at different temperatures were estimated using the broadening of the XRD peaks and Williamson-Hall method, as shown in Figure 5.16. Based on the Williamson-Hall method and broadening of the XRD Cu peaks, the estimated Cu grain size of the 12 hours milled powder with the increase of annealing temperature from 150 to 500°C was in the range of 50-160 nm. Grain sizes and lattice strain data of the alloy powder particles showed a similar trend after annealing up to 300°C. However an increase in grain sizes of the powder particles was observed after annealing at 500°C and the lattice strain decreased after annealing at 400 and 500°C.

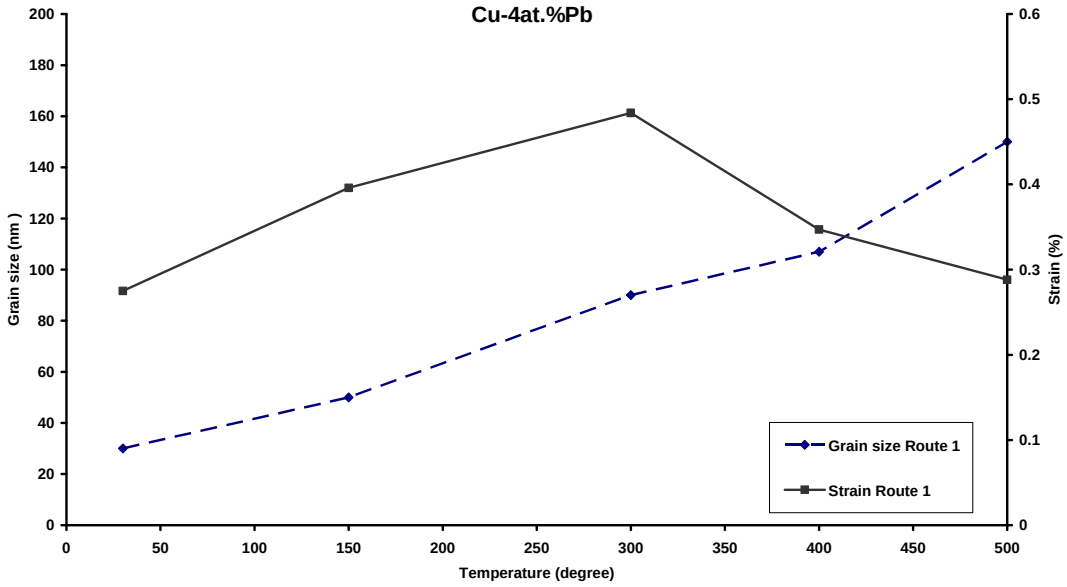


Figure 5.16: Average grain size and lattice strain of Cu-4at.%Pb alloy powder particles produced by HEMM after 12 hours, Route 1, and after annealing at 150, 300, 400 and 500°C, respectively.

## 5.4.2 TEM Examination

Figures 5.17(a), 5.17(c) and 5.17(e) show the TEM bright field images of Cu-1at.%Pb alloy powder particles annealed at different temperatures. TEM examination of Cu-1at.%Pb alloy powder particles showed that grains of the Cu matrix increased after annealing at 150°C, due to coarsening of Cu grains (Figure 5.17(a)). Increasing the annealing temperature to 300°C showed a further increase of the grain sizes of the Cu matrix to 50-300 nm (Figure 5.17(c)). Further increasing the annealing temperature to 500°C caused a significant increase of the Cu matrix grain sizes in the range of 150-450 nm (Figure (5.17(e)), as the result of grain coarsening. Figures 5.17(b), 5.17(d) and 5.17(f) show the indexing of SADPs of nanostructured Cu-1at.%Pb powder particles produced after 12 hours (Route 1) and after annealing at different temperatures. Based on the SADPs it can be seen that strong reflections ({111}, {200}, {220}, {311}) could be correlated to Cu matrix while weak reflections ({111}, {200}, {220}, {311}) are probably in related to Pb particles. Indexing of SADPs is recorded from JCPDS files of Cu (04-0836) and Pb (04-0686), as shown in Appendix A. Almost continuous rings were observed in the selected area diffraction patterns (SADPs) for the alloy powder particles annealed at 150 and 300°C, suggesting normal grain growth during annealing. However discrete diffraction reflections for alloy powder particles were observed in the SADP annealed at 500°C. This is presumably in relation to the significant grain growth during annealing.

Figures 5.18(a), 5.18(c) and 5.18(e) show the TEM bright field images of Cu-2at.%Pb alloy powder particles annealed at different temperatures. TEM examination showed that the grain sizes of the Cu matrix increased from the range of 50-150 nm (Figure (5.5(a)) to 100-250 nm (Figure (5.18(a)) after annealing at 150°C, due to coarsening of Cu grains. Increasing the annealing temperature to 300°C caused a more significant increase of the Cu grain sizes to 150-500 nm (Figure 5.18(c)). With further increasing the annealing temperature to 500°C, the trend of increase of the Cu matrix grain sizes continued and the Cu matrix grain sizes reached ~ 800 nm (Figure (5.18(e)), as the result of significant grain coarsening. Figures 5.18((b), 5.18(d) and 5.18(f)) show the indexing of SADPs of nanostructured Cu-2at.%Pb powder particles produced after 12 hours (Route 1) and after annealing at different temperatures. Based on the SADPs it can be seen that strong reflections ({111}, {200}, {220}, {311}) could be correlated to Cu matrix while weak reflections ({111}, {200}, {220}, {311}) are probably in related to Pb particles. Indexing of SADPs is recorded from JCPDS files of Cu (04-0836) and Pb (04-0686), as shown in Appendix A. Discrete diffraction reflections or rings for alloy powder particles were observed in the SADP annealed at 150°C. With the increase of annealing temperature from 150 to 300°C and 500°C, the discrete reflections or rings were replaced by weak or discrete diffraction reflections, suggesting significant grain growth during annealing.

Figures 5.19(a), 5.19(c) and 5.19(e) show the TEM bright field images of nanostructured Cu-4at.%Pb alloy powder particles annealed at different temperatures. TEM examination showed that grains of the Cu matrix increased from the range of 100-200 nm (Figure (5.5(c)) to 200-400 nm (Figures 5.19(a) and 5.19(c)) after annealing at 150°C and 300°C, due to coarsening of Cu grains. Further increasing the annealing temperature to 500°C, the Cu matrix grain sizes reached ~ 500 nm (Figure (5.19(e)), as the result of significant grain coarsening.

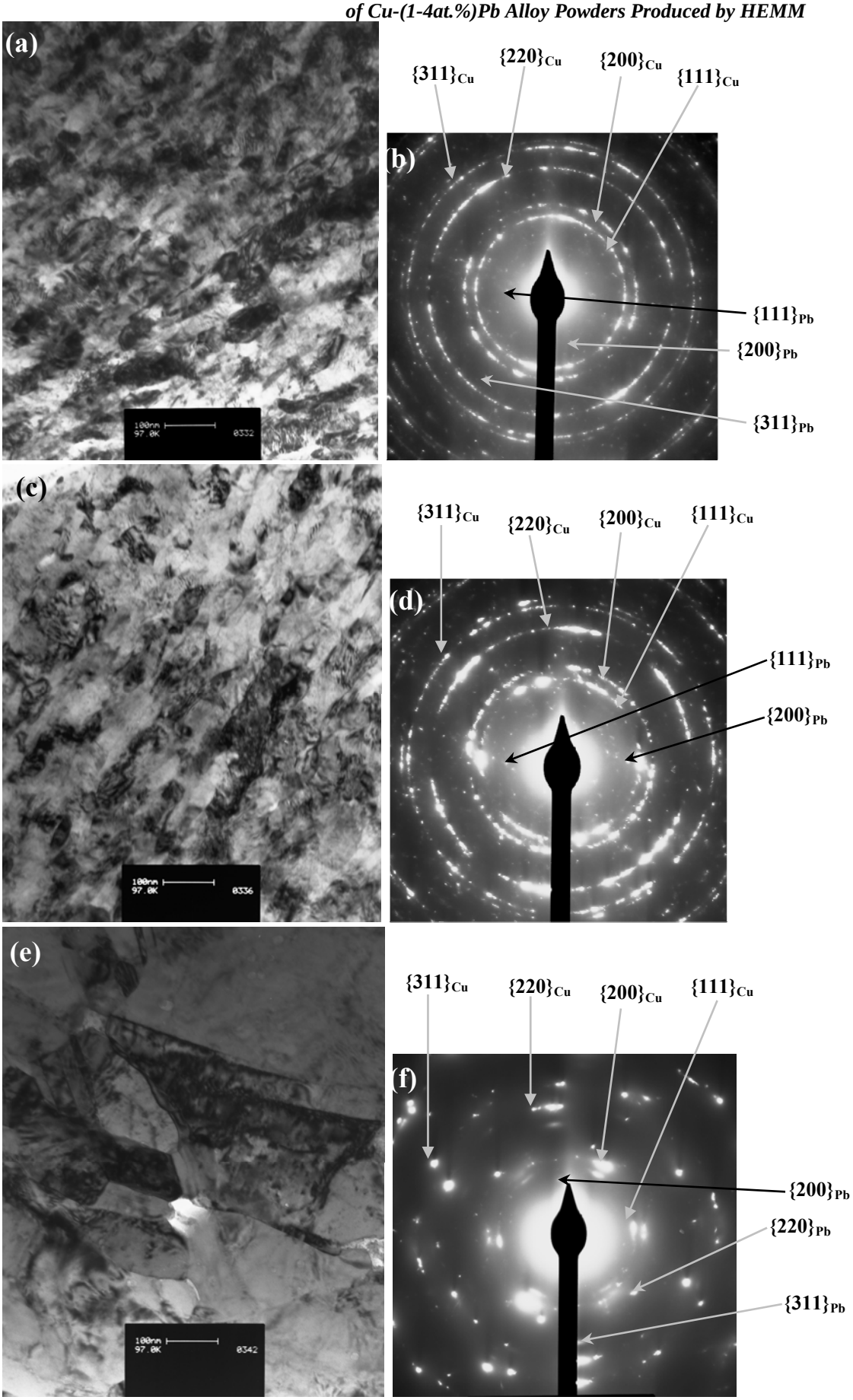


Figure 5.17: TEM bright field images and SADPs of Cu-1at.%Pb alloy powder particles produced by HEMM after 12 hours, Route 1, and after annealing at 150, 300 and 500°C, respectively.

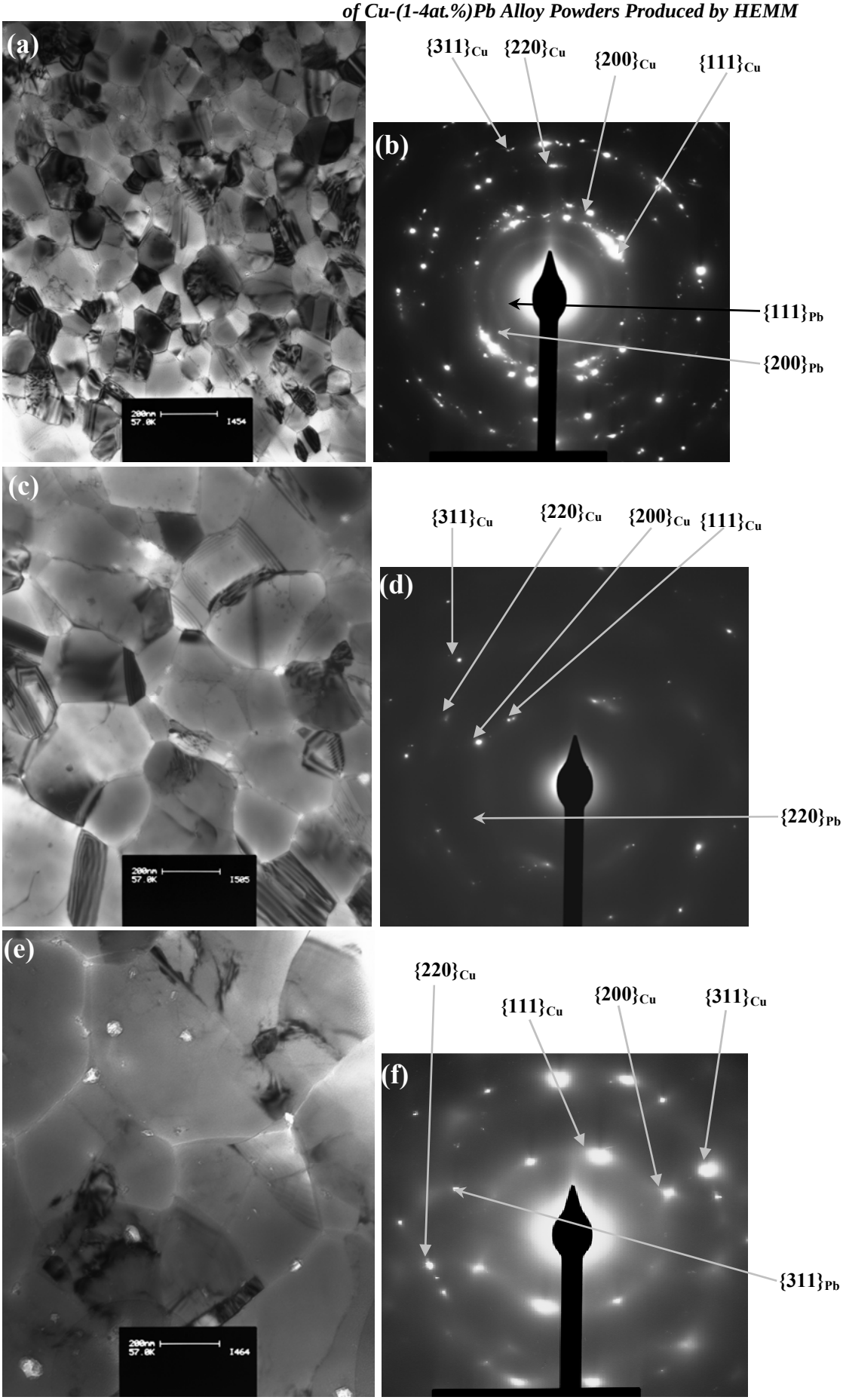


Figure 5.18: TEM bright field images and SADPs of Cu-2at.%Pb alloy powder particles produced by HEMM after 12 hours, Route 1, and after annealing at 150, 300 and 500°C, respectively.

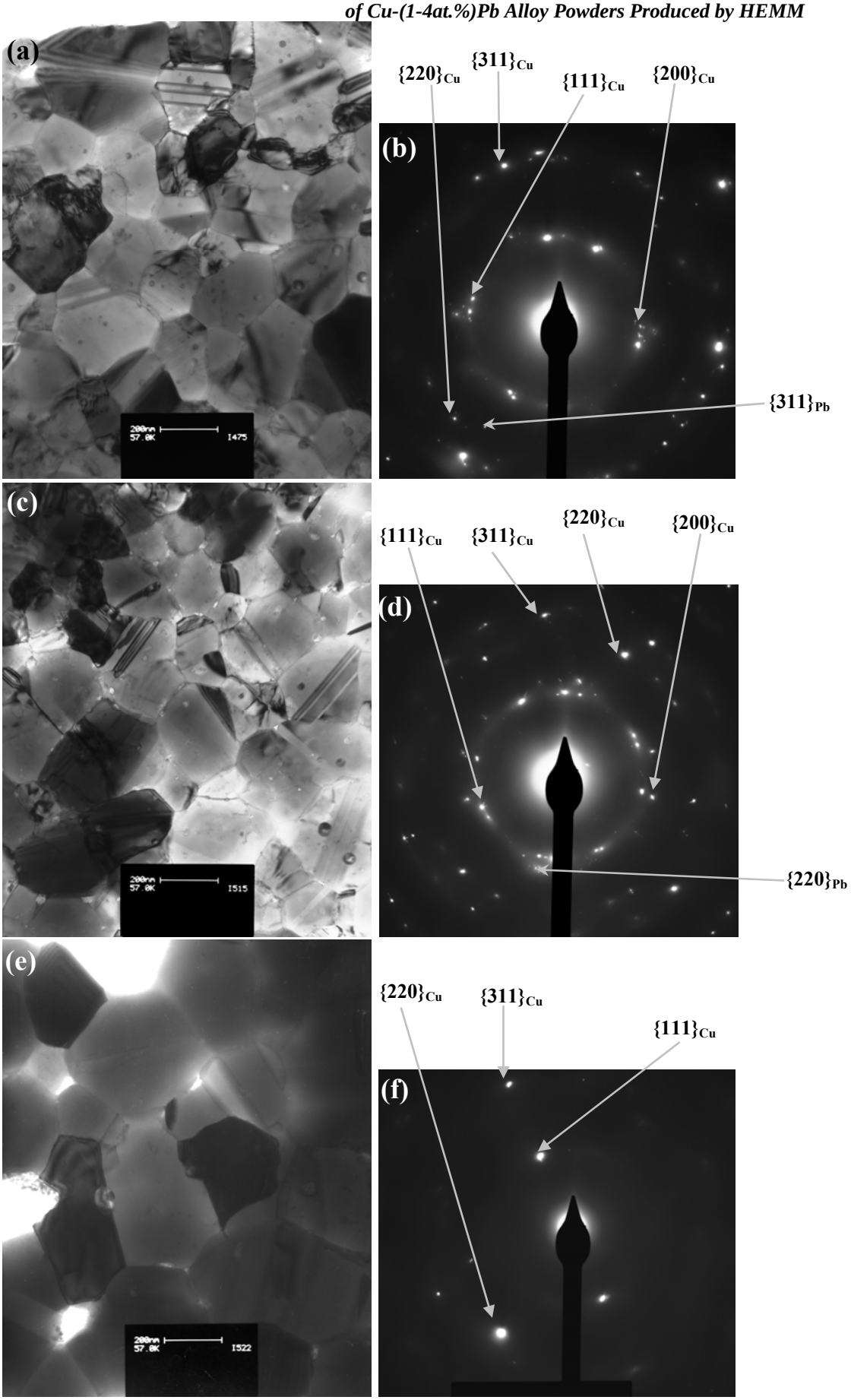


Figure 5.19: TEM bright field images and SADPs of Cu-4at.%Pb alloy powder particles produced by HEMM after 12 hours, Route 1, and after annealing at 150°C, 300°C and 500°C, respectively.

Figures 5.19((b), 5.19(d) and 5.19(f)) show the indexing of SADPs of nanostructured Cu-4at.%Pb powder particles produced after 12 hours (Route 1) and after annealing at different temperatures. Based on the SADPs it can be seen that strong reflections ({111}, {200}, {220}, {311}) could be correlated to Cu matrix while weak reflections ({220}, {311}) are probably in related to Pb particles. Indexing of SADPs is recorded from JCPDS files of Cu (04-0836) and Pb (04-0686), as shown in Appendix A. Discrete and weak diffraction reflections for alloy powder particles were observed in the SADPs annealed at 150, 300 and 500°C, suggesting significant grain growth during annealing.

## 5.4.3 DSC Analysis

Figures 5.20 (a)-(c) show the DSC traces of Cu-(1-4)at.%Pb alloy powders produced after 12 hours obtained in two heating-cooling cycles. In both heating-cooling cycles, Cu-Pb alloy powders were heated to 500°C, held for only one min, and then cooled down to 100°C. In the first heating cycle, the overall amount heat released within the range of 100-500°C for Cu-1at.%Pb alloy powder was 12 J/g. With the increase of Pb content from 1at.% to 2at.%, the amount of heat released increased significantly to 24 J/g. However, with the increase of Pb content from 2at.% to 4at.%, the amount of heat released increased slightly to 29J/g within the range of 100-500°C. In the second heating cycle, the amount of heat intake caused by Pb melting increased from 325 mJ/g (Figure 5.20(a)) to 665 mJ/g (Figure 5.20(b)) with the increase of Pb content from 1at.% to 2at.% in the Cu-Pb alloy powder. For Cu-4at.%Pb alloy powder, the amount of heat intake was 1.11 J/g (Figure 5.20(c)). The amount of heat released during cooling of the Cu-1at.%Pb alloy powder, caused by the precipitation of Pb particles, was 300 mJ/g (Figure 5.20(a)), as measured by exothermic peaks. The amount of heat released increased from 730 mJ/g (Figure 5.20(b)) to 1.0 J/g (Figure 5.20(c)) with the increase of Pb content from 2at.% to 4at.% in the Cu-Pb alloy powder. It was clear that heat of Pb melting was proportional to the Pb content in the powder, indicating that Pb was not lost during the milling process and heat treatment in DSC.

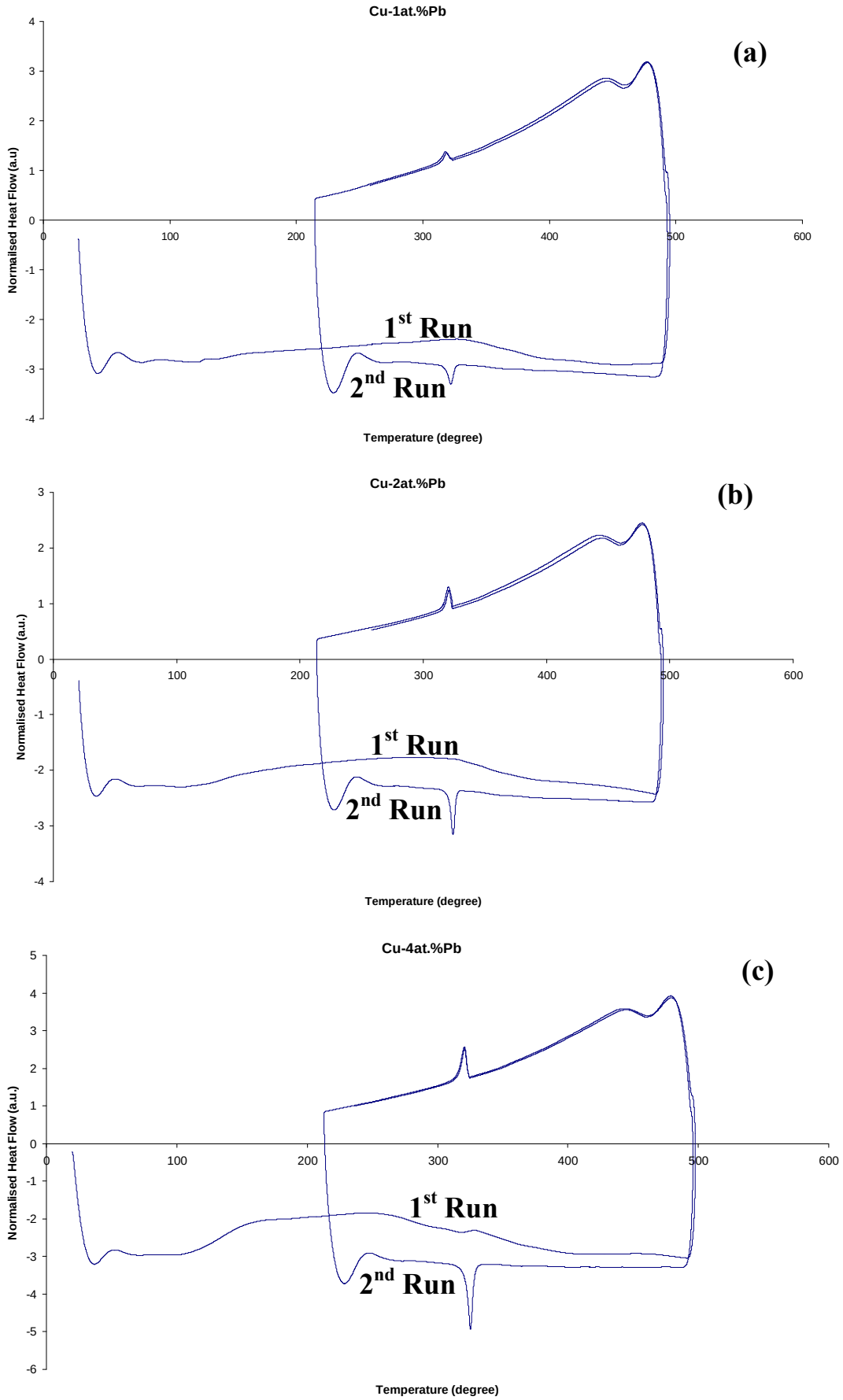


Figure 5.20: DSC traces of Cu-Pb alloy powders produced by HEMM after 12 hours, Route 1 and obtained in the first to second heating-cooling cycle, (a) Cu-1at.%Pb, (b) Cu-2at.%Pb, and (c) Cu-4at.%Pb.

Figure 5.21 shows the DSC traces obtained during heating in the first heating-cooling cycle of the as-milled Cu-(1-4)at.%Pb alloy powders produced after 6 hours of milling using Route 1, from 40 to 500°C. The DSC trace of Cu-1at.%Pb alloy powder (Figure 5.21(a)) exhibited an exothermic and endothermic peak, followed by second exothermic peak. The first exothermic peak was rather small and its onset and peak temperatures were ~ 130°C and 160°C, respectively. The endothermic peak was small and its onset and peak temperatures were ~ 315°C and 325°C, respectively. It is likely that the endothermic peak was caused by melting of an Pb(Cu) solution with very high Cu content. This solution might be formed during heating due to inhomogeneous distribution of Pb and Cu among different powder particles. The second exothermic peak was small again and its onset and peak temperatures were ~ 360°C and 380°C, respectively.

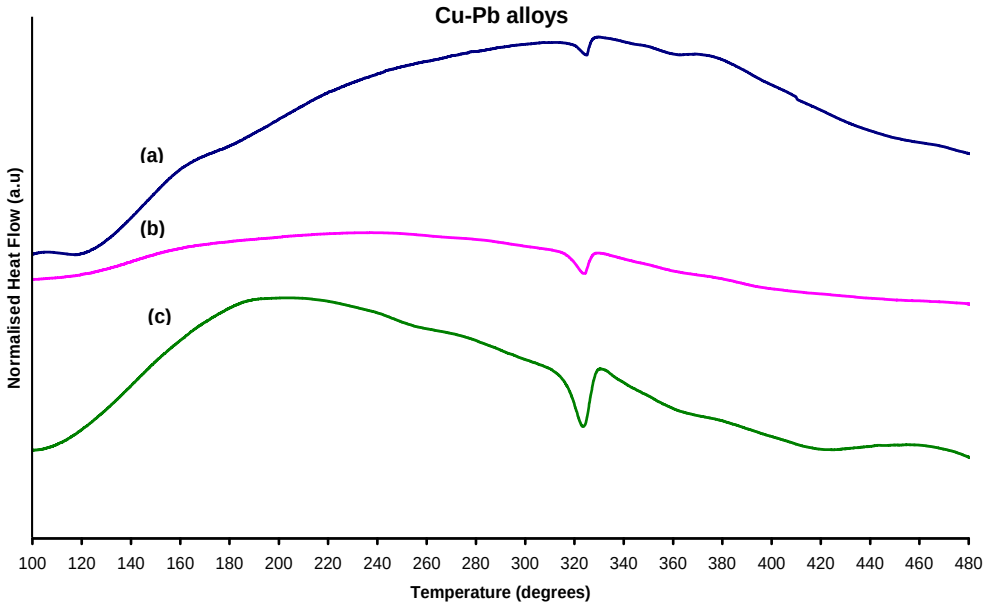


Figure 5.21: DSC traces of Cu-Pb alloy powders produced by HEMM after 6 hours, Route 1 and obtained during heating in the first heating-cooling cycle, (a) Cu-1at.%Pb, (b) Cu-2at.%Pb, and (c) Cu-4at.%Pb.

With the increase of Pb content from 1 to 2at.%, first exothermic peak became extremely small having the same onset and peak temperatures, while second exothermic peak disappeared. However, the endothermic peak became slightly broader, having the onset and peak temperatures ~ 305°C and 324°C, respectively. Further increasing the Pb content to 4at.%, a broad exothermic peak appeared having an onset temperature ~ 120°C, while its peak temperature shifted to a higher temperature ~ 190°C. However, the endothermic peak became sharper and its onset and peak temperatures were ~ 285°C and 323.5°C, respectively (Figure 5.21(c)).

Figure 5.22 shows the DSC traces obtained during heating in the first heating-cooling cycle of the as-milled Cu-Pb alloy powders produced after 12 hours of milling using Route 1, from 40 to 500°C. The DSC trace of Cu-1at.%Pb alloy powder exhibited two overlapping exothermic peaks (Figure 5.22(a)). The first exothermic peak was rather small and its onset and peak temperatures were ~ 130°C and 160°C, respectively. The second endothermic peak was broader and its onset and peak temperatures were ~ 290°C and 335°C, respectively.

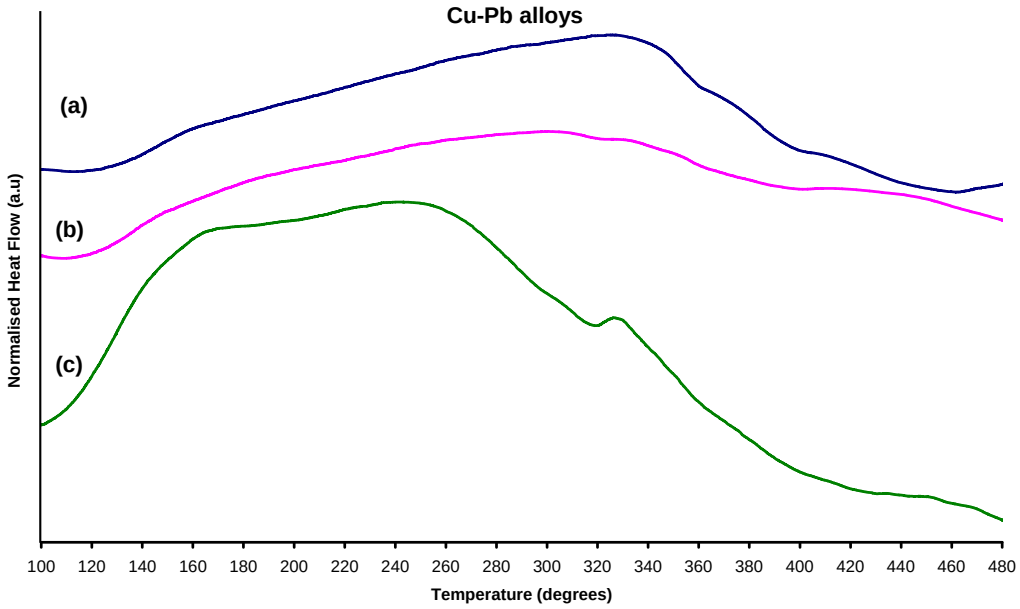


Figure 5.22: DSC traces of Cu-Pb alloy powders produced by HEMM after 12 hours, Route 1 and obtained during heating in the first heating-cooling cycle, (a) Cu-1at.%Pb, (b) Cu-2at.%Pb, and (c) Cu-4at.%Pb.

With the increase of Pb content from 1at.% to 2at.%, onset and peak temperatures of both overlapping exothermic peaks almost remained unchanged. The onset and peak temperatures of the first exothermic peak remained similar, while the onset temperature of the second exothermic peak increased to ~ 320°C and peak temperature remained same. Further increasing the Pb content to 4at.%, the two overlapping exothermic peaks were followed by one endothermic peak (Figure 5.22(c)). The onset and peak temperatures of the first exothermic peak were ~ 110°C and 150°C, respectively, while the onset and peak temperatures of the second exothermic peak were ~ 205°C and 255°C, respectively. However, the onset and peak temperature of the endothermic peak were ~ 290°C and 314°C respectively. For the Cu-4at.%Pb alloy powder the amount of heat intake caused by Pb melting was about 225 mJ/g (per gram of lead), while the amount of heat release caused by precipitation of Pb particles was 181 mJ/g.

## 5.5 Changes in Microhardness during Heat Treatment

Figure 5.23 shows the change of the average microhardness of the Cu powder with 0.6wt%PCA and Cu-(1-4)at.%Pb alloy powders produced by HEMM after 12 hours (Route 1) as a function of annealing temperature. The average microhardness of the Cu powder milled with 0.6wt% PCA decreased from 176 HV to 150 HV after heat treatment at 150°C, and remained almost unchanged with increase in annealing temperature from 150 to 500°C.

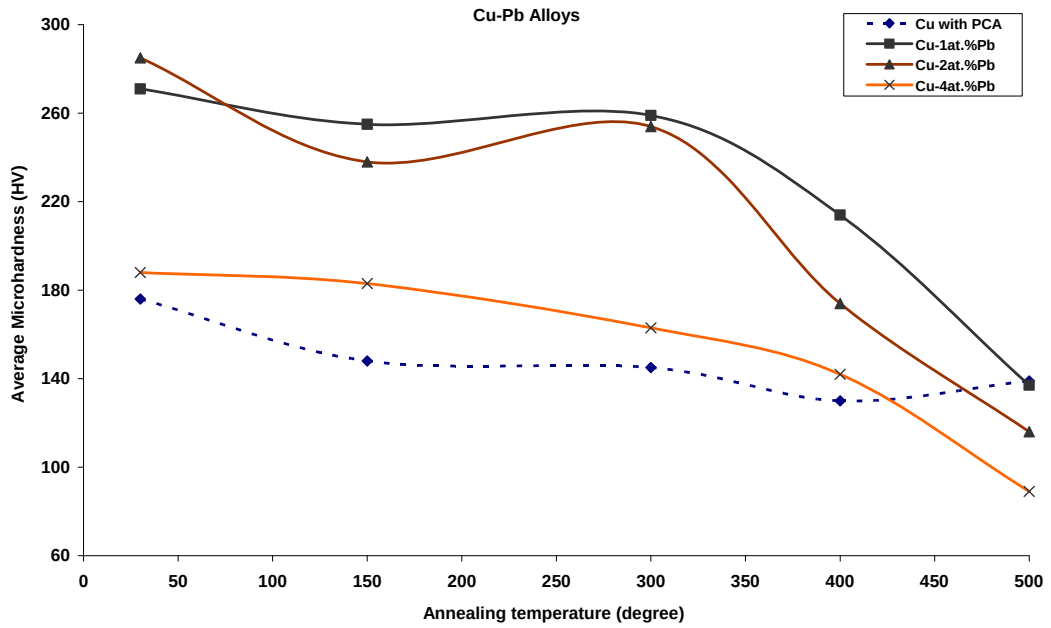


Figure 5.23: Average Microhardness of Cu powder with 0.6wt%PCA and Cu-(1-4)at.%Pb alloy powders produced by HEMM after 12 hours, Route 1, as a function of annealing temperature.

For 12 hours milled Cu-1at.%Pb alloy powder, the average microhardness decreased slightly from 270 HV to 255 HV after annealing at 150°C and remained almost unchanged with increasing the annealing temperature from 150 to 300°C. After this point, the average microhardness of this alloy powder decreased sharply and almost linearly from 260 HV to 140 HV with increasing annealing temperature from 300 to 500°C, as shown in Figure 5.23. The average microhardness of 12 hours milled Cu-2at.%Pb alloy powder decreased sharply from 285 HV to 240 HV after annealing at 150°C and then slightly increased with increasing the annealing temperature from 150 to 300°C. A significant decrease in average microhardness was observed from 255 HV to 116 HV with increasing annealing temperature from 300 to 500°C. For 12 hours milled Cu-4at.%Pb alloy powder, the average microhardness decreased slightly from 188 HV to 182 HV after annealing at 150°C and then a slow decreasing trend in average microhardness was observed with increasing the annealing temperature from 150

to 400°C. After this point, the average microhardness decreased sharply and almost linearly from 142 HV to 90 HV with increasing annealing temperature from 400 to 500°C.

From the investigation of microhardness change as a function of annealing temperature, it is clear that the 12 hours milled Cu-(1-4)at.%Pb alloy powder is thermally stable at temperatures of up to 300°C. This is in agreement with the microstructure observation and which shows that significant grain coarsening does not occur during annealing at 150 and 300°C. A sharp decrease of microhardness was observed for Cu-1at.%Pb and Cu-2at.%Pb alloy powder particles when the annealing temperature was increased from 300 to 500°C. The reasons for this are Cu matrix grain coarsening and Pb atom precipitation from the solid solution to form soft Pb particles as shown by the TEM microstructure examination (Figures 5.17-5.19) and DSC analysis (Figures 5.20-5.23).

## 5.6 Summary

In this study, HEMM was used to fabricate nanostructured Cu-Pb alloy powders and the microstructure of the as-milled powder particles is reported. The thermal stability and microhardness change of Cu-Pb alloy powder particles as a function of annealing temperature was examined. Cu-2at.%Pb alloy powder particles were homogenously distributed in Cu matrix with the increase of milling. With the increase of annealing temperature from 150 to 500°C, coarsening of the Cu grains was observed, which was more significant within the range of 300-500°C. The average microhardness decreased significantly after annealing at 400°C and 500°C, due to the reduction of dislocation density and coarsening of the Cu grains. The amount of heat intake increased for the Cu-(1-4)at.%Pb alloy powder particles with increasing the Pb content from 1at.% to 4at.%.

## 5.7 Reference

1. G.K. Williamson and W. Hall, *Acta Metallurgica* **1**, 1953, 22

# Chapter Six

# Consolidation of Cu Powder and Cu-(2.5-10)vol.% $Al_2O_3$ Composite Powders Produced by HEMM

## 6.1 Introduction

As the consolidation process directly influences the mechanical properties of the consolidate materials, it is legitimate to optimize the parameters of consolidation process, such as pressure, time and temperature. This chapter reports the results of a preliminary study on the consolidation behaviour of Cu and Cu-(2.5-10)vol.%$Al_2O_3$ composite powders and the mechanical properties of the consolidated samples.

## 6.2 Consolidation of Cu and Cu-$Al_2O_3$ Composite Powders

As received pure copper powder and nanostructured Cu-(2.5-10)vol.%$Al_2O_3$ composite powders produced using Route 2 milling were first compacted at 350°C for 20 minutes under pressure of 300 MPa. The Cu powder and Cu-$Al_2O_3$ composite compacts produced after hot pressing had a diameter of 25 mm and height in the range of 18-28 mm, as given in Table 6.1. A typical Cu-$Al_2O_3$ compact with side and top view is shown in Figures 6.1(a) and 6.1(b). The density of the Cu-$Al_2O_3$ composite compacts were measured by measuring their weights and dimensions.

Table 6.1: Theoretical and relative densities of Cu-$Al_2O_3$ composites and the corresponding compacts.

| Material | Theoretical Density ($g/cm^3$) | Density of Compact ($g/cm^3$) | Relative Density of Compact | Compact Height (mm) |
|---|---|---|---|---|
| Cu | 8.93 | 8.78 | 97% | 18.1 |
| Cu-2.5vol.%$Al_2O_3$ | 8.81 | 7.84 | 88% | 20.7 |
| Cu-5vol.%$Al_2O_3$ | 8.68 | 6.61 | 76% | 26.4 |
| Cu-7.5vol.%$Al_2O_3$ | 8.56 | 6.68 | 78% | 25.6 |
| Cu-10vol.%$Al_2O_3$ | 8.44 | 6.77 | 80% | 27.7 |

The theoretical density of Cu-$Al_2O_3$ composites was calculated using the rule of mixture :

$$\rho_{composite} = \rho_{Cu} f_{Cu} + \rho_{Al_2O_3} f_{Al_2O_3} \quad \text{.....Equation 6.1}$$

where $\rho$ is the density of the material and $f$ is the volume fraction. The relative densities of the compacts for Cu and Cu-2.5vol.%$Al_2O_3$ composite were higher, due to softer compacts powder particles. However, the relative densities decreased with the increase of $Al_2O_3$ content in the milled Cu-$Al_2O_3$ composite powder, due to the increased hardness of the mechanically milled Cu-$Al_2O_3$ composite powder particles as shown in Chapter 3.

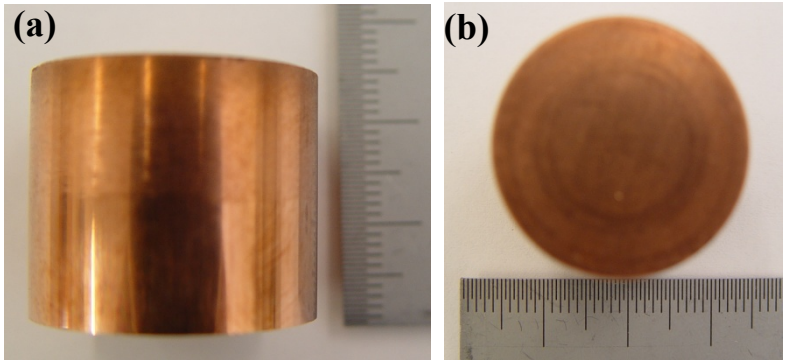


Figure 6.1: (a) Side view and (b) top view of Cu-$Al_2O_3$ composite compact produced after hot pressing.

Table 6.2: Average Heating rate of Cu-$Al_2O_3$ composite compacts and dimensions of the Forged Cu-$Al_2O_3$ composite disks.

| Material | Compact Temperature (°C ) | Average Heating Rate (°C.min$^{-1}$) | Dimensions of Forged Disk (mm) | |
|---|---|---|---|---|
| | | | Diameter (mm) | Height (mm) |
| Cu | 500 | 300 | 40 | 6.2 |
| Cu-2.5vol.%$Al_2O_3$ | 700 | 350 | 38 | 8.2 |
| Cu-5vol.%$Al_2O_3$ | 700 | 650 | 33 | 6.8 |
| Cu-7.5vol.%$Al_2O_3$ | 700 | 500 | 34 | 6.5 |
| Cu-10vol.%$Al_2O_3$ | 800 | 450 | 36 | 7.2 |

The Cu powder and Cu-(2.5-10)vol.%$Al_2O_3$ composite compacts were heated from room temperature to sintering temperature in the range of 500-800°C, under an argon atmosphere. The compacts temperatures and average heating rates for the samples are given in Table 6.2. The heating curves using the induction heating method of the Cu-$Al_2O_3$ composite powder compacts during induction heating are shown in Figure 6.2.

The average heating rate of the Cu-$Al_2O_3$ composite compacts was in the range of ~ 300-650°C.min$^{-1}$. After the powder compact reached its designated temperature, it was upset forged to form a disk with a thickness in the range of 6.2-8.2 mm, shown in Table 6.2. Figures 6.3 (a)-(d) show the forged Cu-$Al_2O_3$ composite disks. The height reduction caused by the forging was in the range of 65-75%. Tensile testing specimens were cut from the material in the centre region of the disk.

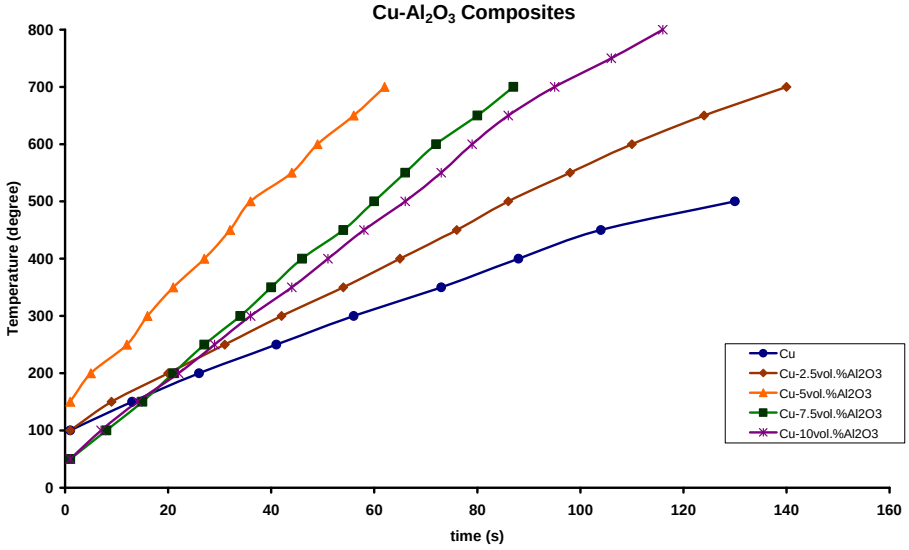


Figure 6.2: Heating curves of Cu-$Al_2O_3$ composite powder compacts.

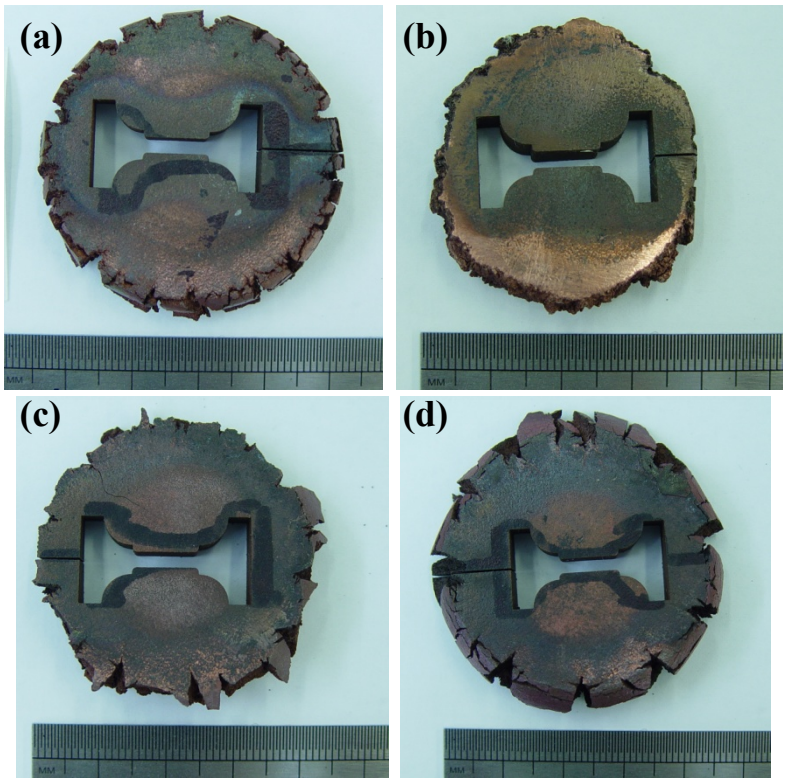


Figure 6.3: Planar view of the forged Cu-$Al_2O_3$ composite disk (a) (a) Cu-2.5vol.%$Al_2O_3$ composite, (b) Cu-5vol.%$Al_2O_3$ composite, (c) Cu-7.5vol.%$Al_2O_3$ composite, and (d) Cu-10vol.%$Al_2O_3$ composite.

Figures 6.4(a)-(e) show the SEM micrographs of the Cu and Cu-(2.5-10)vol.%$Al_2O_3$ forged disks. It was clear that there were no pores in the samples.

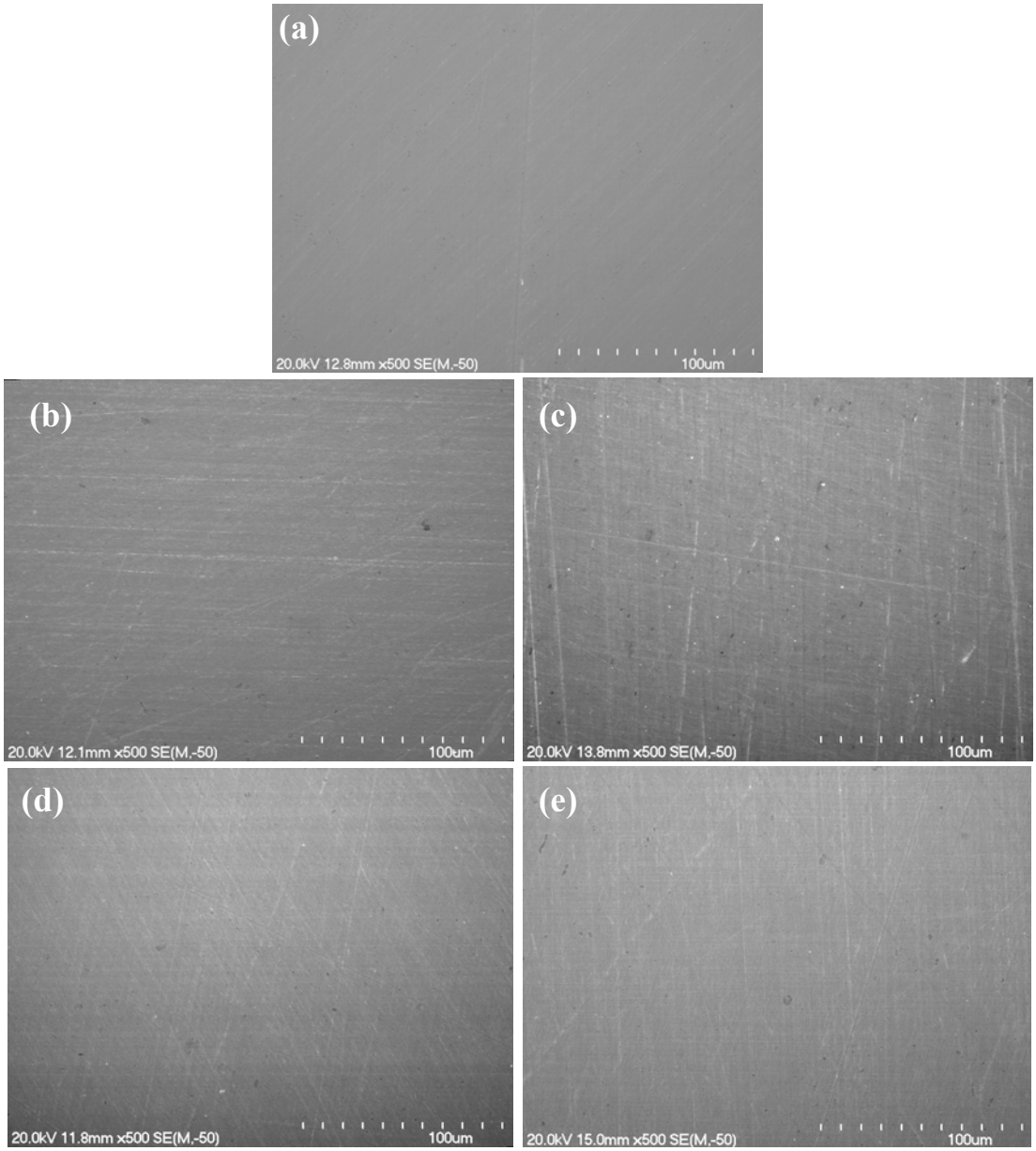


Figure 6.4: SEM micrographs for the forged Cu powder and Cu-$Al_2O_3$ composites, (a) Cu powder, (b) Cu-2.5vol.%$Al_2O_3$ composite, (c) Cu-5vol.%$Al_2O_3$ composite, (d) Cu-7.5vol.%$Al_2O_3$ composite, and (e) Cu-10vol.%$Al_2O_3$ composite.

Figure 6.5 shows the XRD patterns of Cu powder and Cu-$Al_2O_3$ composites forged in the range of 500-800°C. Comparing Cu{111} peak with the as-milled powder particles produced using Route 2, the Cu{111} peak for Cu-2.5vol.%$Al_2O_3$ and Cu-7.5vol.%$Al_2O_3$ composites shifted to a larger angle after forging. The Cu{111} peak shifted 0.33° and 0.64° to a larger angle for Cu-2.5vol.%$Al_2O_3$ and Cu-7.5vol.%$Al_2O_3$ composites after forging, which caused the Cu lattice parameter to

decrease by 0.0026 nm and 0.005 nm, respectively. This might be due to diffusion of oxygen in the argon atmosphere into the powder compact during heating and forging. The average grain size and lattice strain data of the Cu powder and Cu-$Al_2O_3$ composites were estimated using the broadening of the XRD peaks and Williamson-Hall method, as shown in Figure 6.6. Average grain size and lattice strain of Cu matrix increased significantly for the Cu-7.5vol.%$Al_2O_3$ composite after forging.

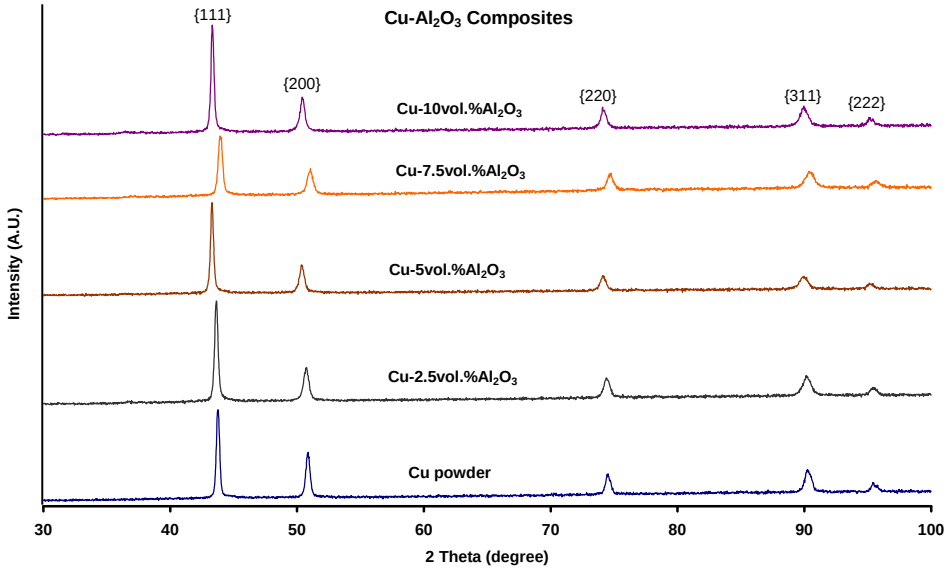


Figure 6.5: X-ray diffraction patterns of forged Cu powder and Cu-$Al_2O_3$ composites.

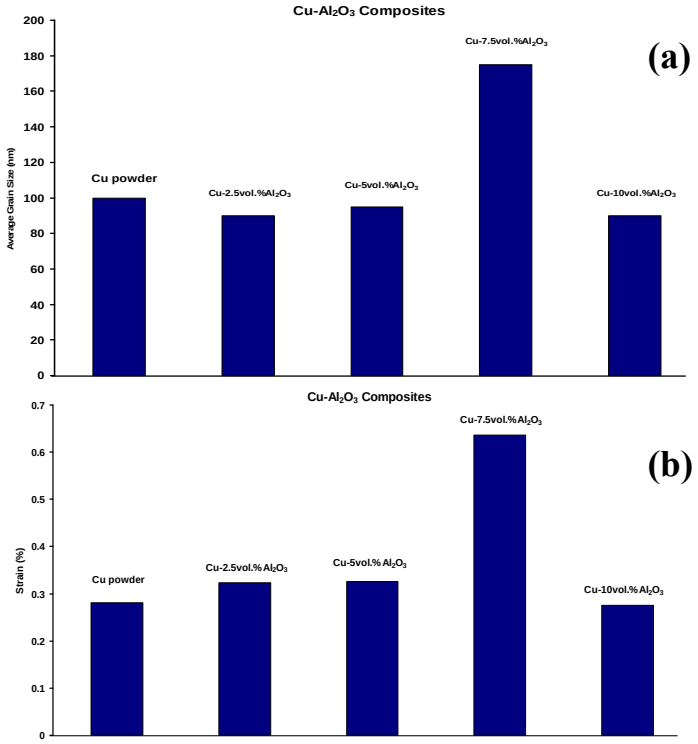


Figure 6.6: (a) Grain size and (b) lattice strain data of the forged Cu powder and Cu-(2.5-10)vol.% $Al_2O_3$ composites.

# 6.3 Mechanical Properties of Forged Cu and Cu-$Al_2O_3$ Composites

Figure 6.7 shows the average microhardness of the Cu and Cu-$Al_2O_3$ composites after forging. The average microhardness of the Cu powder after forging was 115 HV, which is higher than the Cu material as-received (100 HV). With an increase of $Al_2O_3$ content from 2.5 to 5vol.% in Cu-$Al_2O_3$ composites after forging, the average microhardness was around 200 HV, which is lower than the as-milled powder particles for the same material (~ 265 HV). The average microhardness increased slightly for the Cu-$Al_2O_3$ composites after forging to 212 HV and 218 HV with the increase of volume fraction of $Al_2O_3$ to 7.5% and 10%, respectively, as shown in Figure 6.7. The average microhardness of the Cu-(7.5 and 10)vol.%$Al_2O_3$ composites after forging is also lower than the as-milled powder particles for the same material (~ 260 HV).

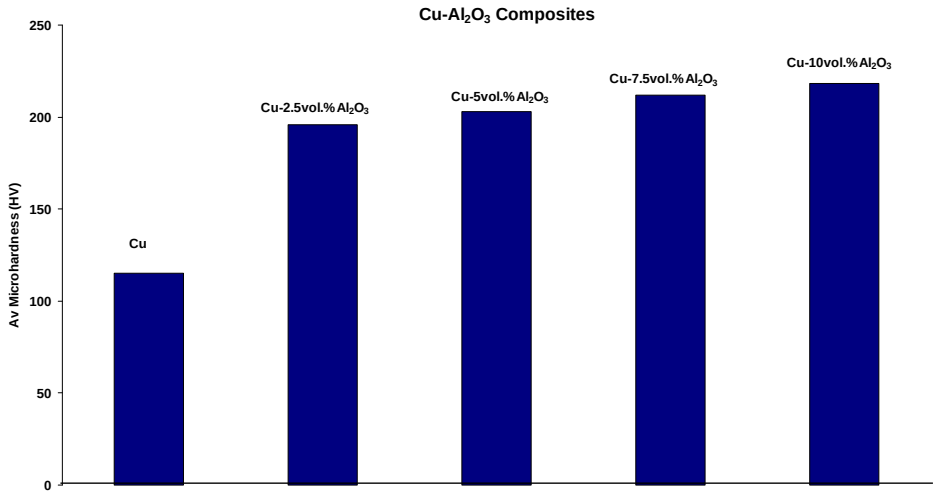


Figure 6.7: The average microhardness of forged Cu and Cu-$Al_2O_3$ composites.

## 6.3.1 Pure Cu

Figure 6.8 shows the engineering stress-strain curve of the Cu specimen at room temperature. Curve show plastic yielding of the material. The specimen showed high tensile yield strength ($\sigma_y$), of 340 MPa, as shown in Figure 6.8. In addition to high tensile yield strength, Cu specimen showed a clean ductility. The broken tensile specimen for the forged Cu powder showed that the specimen eventually necked before fracturing (Figure 6.9).

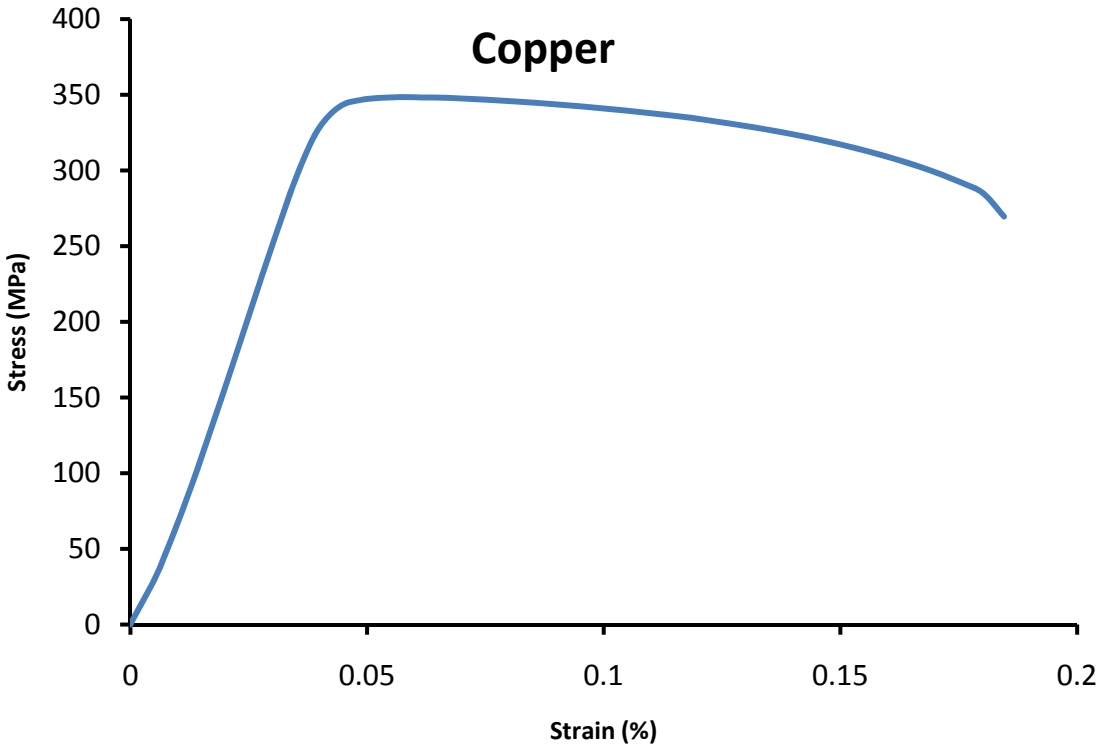


Figure 6.8: Tensile Stress-strain curves for the forged Cu powder.

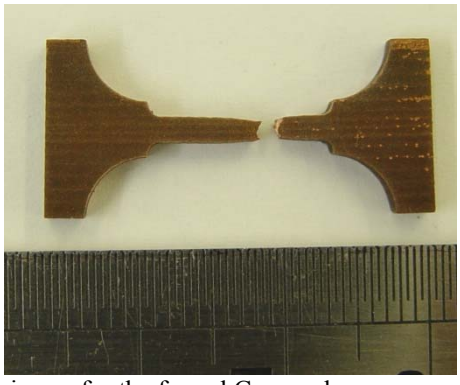

Figure 6.9: Broken tensile specimens for the forged Cu powder.

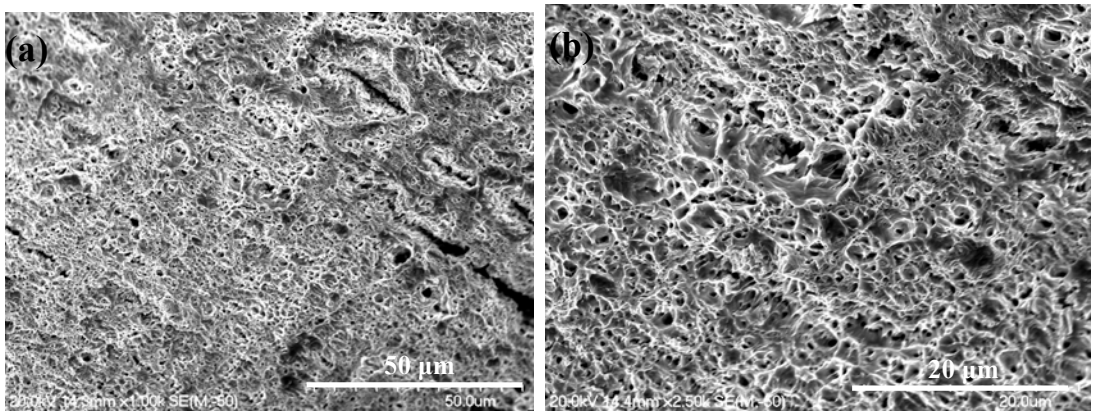


Figure 6.10: (a) and (b) Fracture surface of a Cu specimen after the tensile testing.

Figures 6.10 show the fracture surface of a Cu specimen. The high magnification micrograph showed a typical ductile fracture surface with a large clarity of dimples (Figure 6.10(b)). The formation of dimples on the fracture surface is the typical process for ductile crack propagation. This shows that the powder particles are well bonded in the powder compact forged disk.

### 6.3.2 Cu-$Al_2O_3$ Composites

Figures 6.11 (a)-(d) show engineering stress-strain curves for the Cu-(2.5-10)vol.% $Al_2O_3$ tensile testing specimens. All the curves did not show any macroscopic yielding of the consolidated material. Cu-2.5vol.%$Al_2O_3$ specimen showed an average fracture strength of 542 MPa, as shown in Figure 6.12. With increasing volume fraction of $Al_2O_3$ from 2.5 to 10%, the tensile fracture strength decreased almost linearly to 112 MPa as shown in Figures 6.11 and 6.12. Figures 6.13 (a)-(d) show the images of the broken tensile specimens for the forged Cu-(2.5-10)vol.%$Al_2O_3$ composites. From them, it can be seen that the fracture surface was very flat and the fracture mostly occurred at the locations of section change.

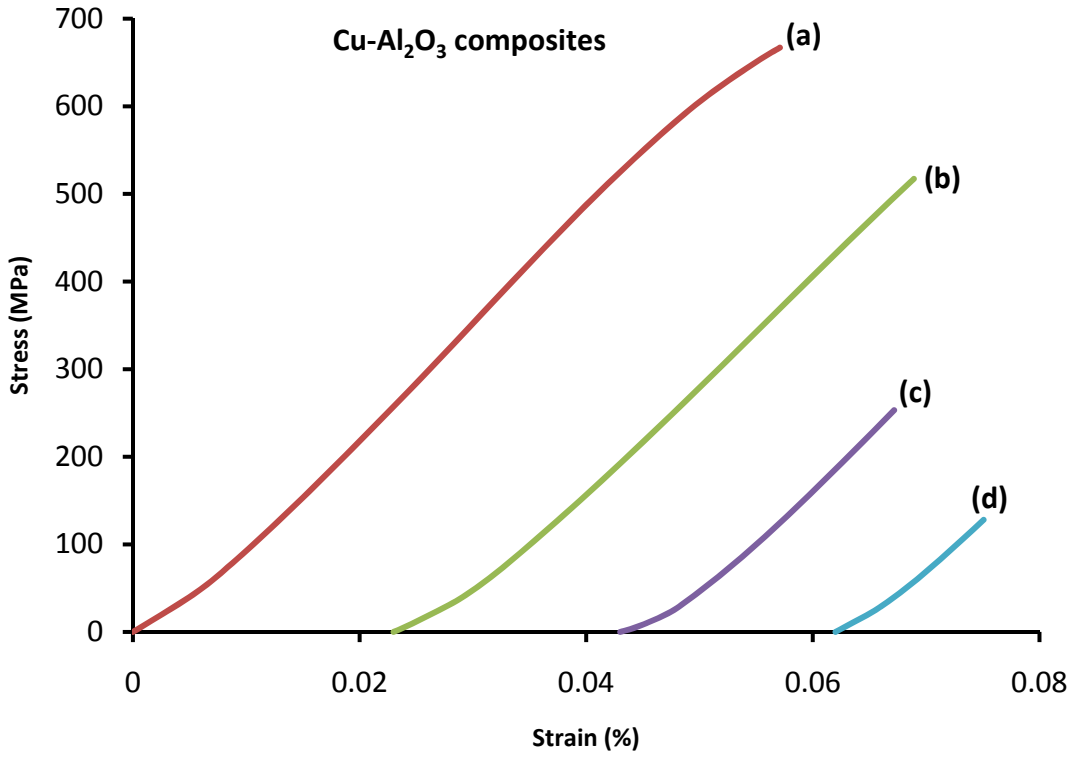


Figure 6.11: Tensile Stress-strain curves for forged Cu-$Al_2O_3$ composites, (a) Cu-2.5vol.%$Al_2O_3$ composite, (b) Cu-5vol.%$Al_2O_3$ composite, (c) Cu-7.5vol.%$Al_2O_3$ composite, and (d) Cu-10vol.% $Al_2O_3$ composite.

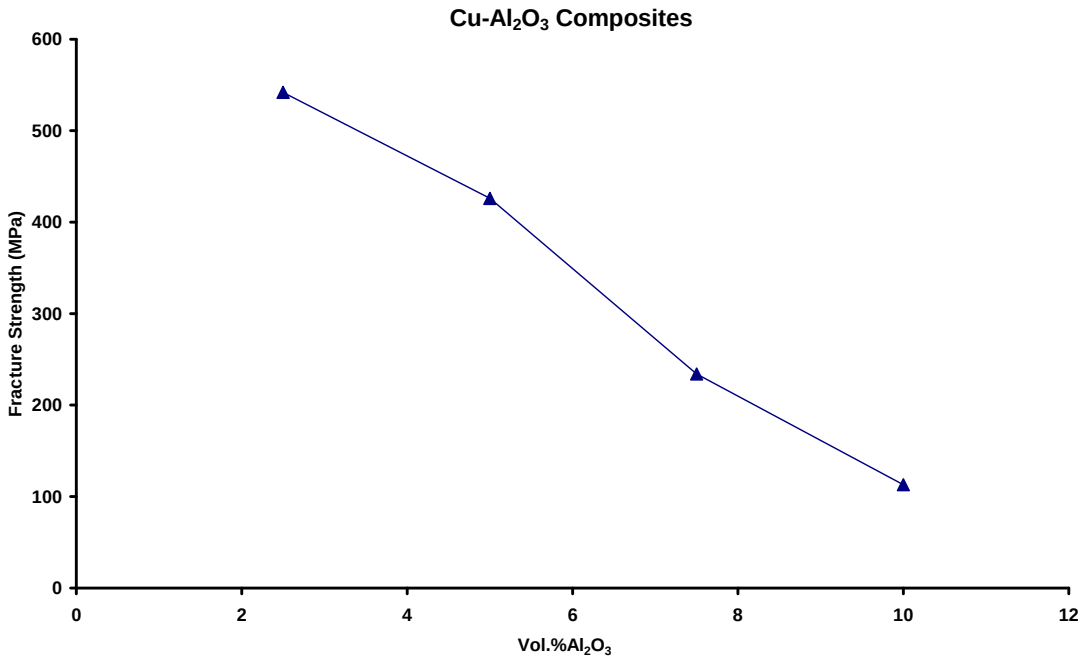


Figure 6.12: Fracture strength for forged Cu-$Al_2O_3$ composites.

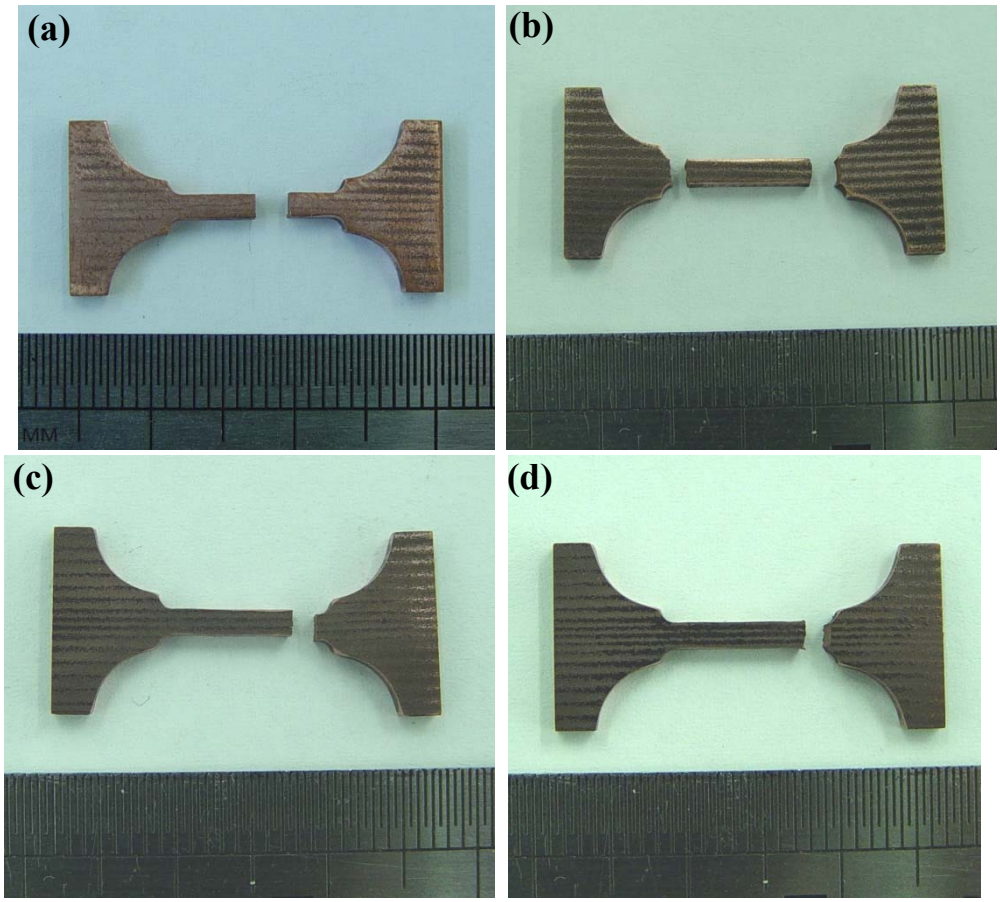


Figure 6.13: Broken tensile specimens for the forged Cu-$Al_2O_3$ composites, (a) Cu-2.5vol.%$Al_2O_3$ composite, (b) Cu-5vol.%$Al_2O_3$ composite, (c) Cu-7.5vol.%$Al_2O_3$ composite, and (d) Cu-10vol.% $Al_2O_3$ composite.

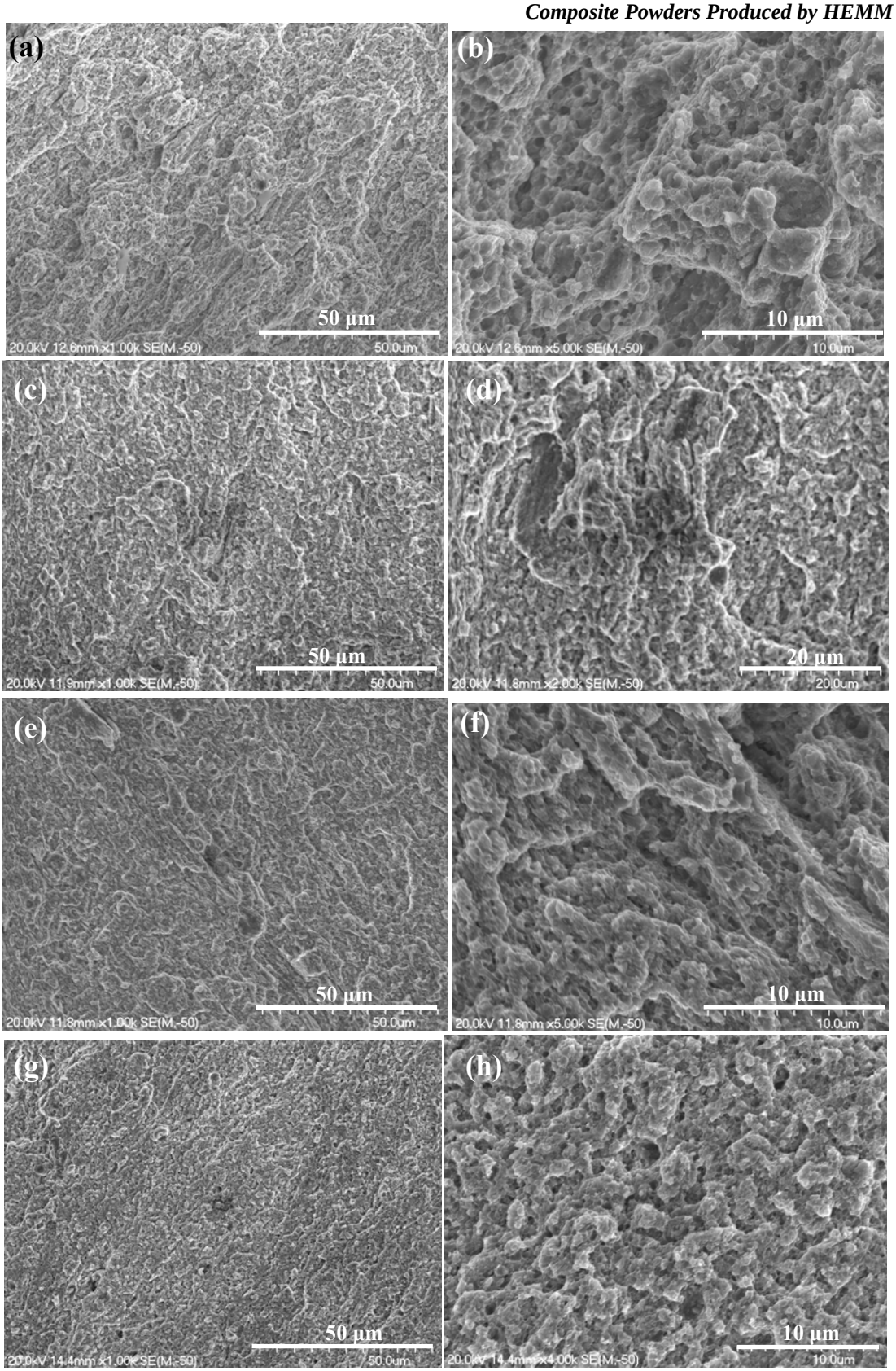


Figure 6.14: SEM micrographs showing the fracture surfaces of the Cu-$Al_2O_3$ composite tensile testing specimens, ((a) and (b)) Cu-2.5vol.%$Al_2O_3$ composite, ((c) and (d)) Cu-5vol.%$Al_2O_3$ composite, ((e) and (f)) Cu-7.5vol.%$Al_2O_3$ composite, and ((g) and (h)) Cu-10vol.%$Al_2O_3$ composite.

Figures 6.14 (a)-(h) show the fracture surfaces of the Cu-(2.5-10)vol.%$Al_2O_3$ composite tensile testing specimens. The feature of the fracture surface changes with the increase of $Al_2O_3$ content in the composite. With the increase of the volume fraction of $Al_2O_3$ from 2.5 to 5% the fracture surface exhibited less dimples indicating a smaller degree of microscopic ductile fracture. (Figures 6.14(b) and 6.14(d)). These micrographs of the fracture surfaces further revealed that fractured particles were surrounded by ductile regions described as 'tear ridges' and voids were intermingled with isolated regions of dimpled rupture. However, fracture surfaces showed the presence of river and vein type patterns (Figures 6.14(a) and 6.14(c)). With the increase of the volume fraction of $Al_2O_3$ to 10%, the fracture surfaces of the composite tensile testing specimens showed the brittle failure which dominated the inter-particle regions, as shown in Figures 6.14 (e)-(h). Fracture of the brittle $Al_2O_3$ particles and concurrent failure of the surrounding matrix resulted in the formation of microvoid coalesce, observed as shallow dimples on the fractured surface. The fracture surface resulted from decohesion between the adjacent particles due to incomplete densification of the composite, as the voids were clearly observed. The cracks initiated at the voids, and propagated along the particle boundaries. The morphologies of the fracture surfaces of Cu-10vol.%$Al_2O_3$ composite tensile testing specimen (Figures 6.14(g) and 6.14(h)) showed microvoids and dimples, suggesting the larger size particles fractured first, followed by fracture of smaller size particles. Larger dimples on the fracture surface indicated considerable void growth and plastic deformation before failure. However, smaller dimples indicated a fracture with less void growth and plastic deformation.

In this study, the Cu-$Al_2O_3$ composite compacts showed lower relative density with the increase of volume fraction of $Al_2O_3$ nanoparticles in the Cu matrix, which cannot be attributed only due to the hardness of the brittle $Al_2O_3$ in ductile Cu. One of the possible explanation for the difference in the relive densities of the Cu-$Al_2O_3$ powder compacts is that the level of the powder particle softening that occurred during hot pressing at 350$^oC$ is much higher for the 2.5vol.%$Al_2O_3$ in Cu matrix than that for the other three Cu-$Al_2O_3$ composite compacts due to the increased thermal stability of microstructure of the powder particles with increasing fraction of $Al_2O_3$. Cu-$Al_2O_3$

samples produced by forging the powder compacts showed low tensile fracture strength with increasing the volume fraction of $Al_2O_3$ from 2.5% to 10%. The decrease of the fracture strength of the forged disks with increasing $Al_2O_3$ volume fraction shows that the level of interparticle atomic bonding decreases with increasing $Al_2O_3$ volume fraction. This indicates that some correlation exist between the two. More work is needed to understand principles underlying this correlation.

## 6.4 Summary

Cu-$Al_2O_3$ composite powders produced using HEMM were consolidated at 350°C by hot pressing and then forged at 700/800°C with microstructure showing no pores in the sample. The average microhardness of the forged Cu-$Al_2O_3$ composites increased with increasing the volume fraction of $Al_2O_3$. However, tensile fracture strength of the Cu-$Al_2O_3$ composites decreased almost linearly with the increase of $Al_2O_3$ from 2.5% to 10%.

# Chapter Seven
# Conclusions and Recommendations

## 7.1 Conclusions

● Two high energy mechanical milling routes were used to produce Cu and Cu-(2.5-10)vol.%$Al_2O_3$ composite balls/granules/powder particles. It was found that $Al_2O_3$ nanoparticles can be easily dispersed into the microscaled Cu matrix, and increasing the volume fraction of $Al_2O_3$ nanoparitcles enhances the effectiveness of milling in refining the Cu grains and increasing the thermal stability of the Cu grains in the nanostructured composite.

● High energy mechanical milling of pure Cu powder results in formation of nearly spherical hollow balls, while adding 0.6wt%PCA to Cu powder failed to consolidate in-situ and turned the mixture into fine Cu powder with same milling condition. Using larger diameter balls or increasing the milling severity, the hollow balls were converted into ultrafine grained powder particles.

● High energy mechanical milling of powder mixtures of Cu and $Al_2O_3$ with compositions of 2.5vol.%$Al_2O_3$ and 5vol.%$Al_2O_3$ results in formation of nearly spherical hollow balls and granules of a few millimeters in diameter respectively. Distribution of the microhardness across the wall thickness of the Cu-2.5vol.% $Al_2O_3$ composite hollow balls and along the diameter of Cu-5vol.%$Al_2O_3$ composite granules showed that with increasing milling time and volume fraction of $Al_2O_3$ the microhardness distribution became more uniform. Increasing the volume fraction of $Al_2O_3$ from 5% to 7.5 or 10%, coarse and fine powders were produced.

● Using larger diameter balls or increasing the milling severity from 12 hours (Route 1) to 24 hours (Route 2), as-milled Cu-(2.5 and 5)vol.%$Al_2O_3$ composite hollow balls and granules were converted into ultrafine grained powder particles, while a significant decrease in the average grain size of the Cu matrix and increase in average microhardness was observed. The trend of decrease in average grain size and increase in average microhardness virtually stopped for nanostructured Cu-10vol.%$Al_2O_3$ composite powder particles produced using Route 2.

● Cu-2.5vol.%$Al_2O_3$ composite hollow balls and powder particles produced using Route 1 and Route 2 and after annealing at 150°C caused recyrstallisation of Cu grains, while microhardness remained almost unchanged for both hollow balls and powder particles. For both the hollow balls and the powder particles, increasing the annealing temperature from 150 to 300°C caused slight coarsening of the Cu grains while the microhardness remained almost unchanged. The effect of increasing the annealing temperature from 300 to 500°C on the microstructure coarsening of the hollow balls was significant compared to the powder particles, while microhardness decreased for powder particles due to reduction of dislocation density.

● Cu-5vol.%$Al_2O_3$ composite granules and powder particles produced using Route 1 and Route 2 and after annealing at 150°C caused recyrstallisation and slight coarsening of Cu grains, respectively, while a decrease of microhardness for both granules and powder particles was due to a reduction of dislocation density. For both the granules and the powder particles, increasing the annealing temperature from 150 to 300°C caused slight coarsening of the grains and slight decrease of microhardness. The effect of increasing the annealing temperature from 300 to 500°C on the microstructure coarsening and the microhardness of the powder particles was much more significant when compared to the granules.

● Coarse and fine powders of Cu-7.5vol.%$Al_2O_3$ composite produced using Route 1 and Route 2 showed little increase of the Cu matrix grain sizes and decrease of microhardness after annealing at 150°C and 300°C. However significant coarsening of Cu grains and $Al_2O_3$ nanoparticles and a sharp decrease of microhardness occured with increasing the annealing temperature to 500°C. The degree of microstructure coarsening and microhardness decrease with annealing of the 24 hours milled (Route 2) powder was clearly smaller than that of the 12 hours milled (Route 1) powder annealed under the same conditions.

● Cu-10vol.%$Al_2O_3$ composite powder produced using Route 1 and Route 2 and after annealing up to 300°C showed little increase of the Cu matrix grain sizes and decrease of the microhardness. A significant coarsening of the Cu grains and $Al_2O_3$ nanoparticles and sharp decrease of microhardness were observed for the composite powder with increasing the annealing temperature up to 500°C.

● The change of average microhardness of Cu-(2.5-10)vol.%$Al_2O_3$ composites produced using Route 2 as a function of annealing temperature showed that the powder particles were thermally stable after annealing at temperatures in the range of 150-400°C, suggesting that consolidation is feasible at temperatures around 400°C without totally losing the nanostructure. The average microhardness decreased significantly for the Cu-(7.5-10)vol%$Al_2O_3$ composite powder particles after heat treatment at 500°C, mainly due the reduction of dislocation density.

● Cu-(2.5-10)vol.%$Al_2O_3$ composite powders produced using Route 2 were compacted at 350°C and then forged at 700/800°C with the microstructure showing no pores in the sample. The tensile fracture strength decreased almost linearly with the increase of $Al_2O_3$ from 2.5% to 10%.

● High energy mechanical milling was used to produce nanostructured Cu-(1-4)at.%Pb alloy powder particles using Route 1. With the increase of Pb content from 2at.% to 4at.%, the average grain size of the Cu matrix slightly increased and the average microhardness decreased significantly for the Cu-Pb alloy powder particles. An increase of the annealing temperature to 150°C, caused a slight coarsening of the Cu grains and decrease in average microhardness. Further increasing of the annealing temperatures to 400°C and 500°C caused significant coarsening of the Cu grains and decrease in average microhardness due to reduction in dislocation density.

## 7.2 Recommendations for Future Work

● Extend the grain size examination for the annealed Cu-$Al_2O_3$ composites from different positions of the sample.

● Extend the heating temperature to higher value for Cu-$Al_2O_3$ composite powders during hot-pressing to obtain/examine mechanical properties.

● Apply more tensile testing for the forged Cu-$Al_2O_3$ composite disks at room temperature to study the mechanical behaviour and extend the tensile testing to elevated temperatures to study the effect of temperature on the mechanical behaviour of Cu-$Al_2O_3$ forged disks.

● Apply EDX analysis and elemental mapping to examine the distribution of the $Al_2O_3$ nanoparticles in the initial microstructure of the forged Cu-$Al_2O_3$ composites and extend the grain size examination using TEM.

● Apply extrusion for the Cu-$Al_2O_3$ composite compacts to obtain samples for studying their mechanical behaviour and compare that with the mechanical behaviour of the forged Cu-$Al_2O_3$ composite disks.

● Obtain the electrical properties of Cu-$Al_2O_3$ composite forged disks to study the effect of nanoparticles on the electrical conductivity of the Cu-$Al_2O_3$ composites.

● Use the warm powder compaction and hot forging to consolidate the as-milled Cu-Pb alloy powders to produce samples to study the mechanical behaviour of ultrafine grained Cu-Pb alloys.

# Appendix A

## Phase diagrams

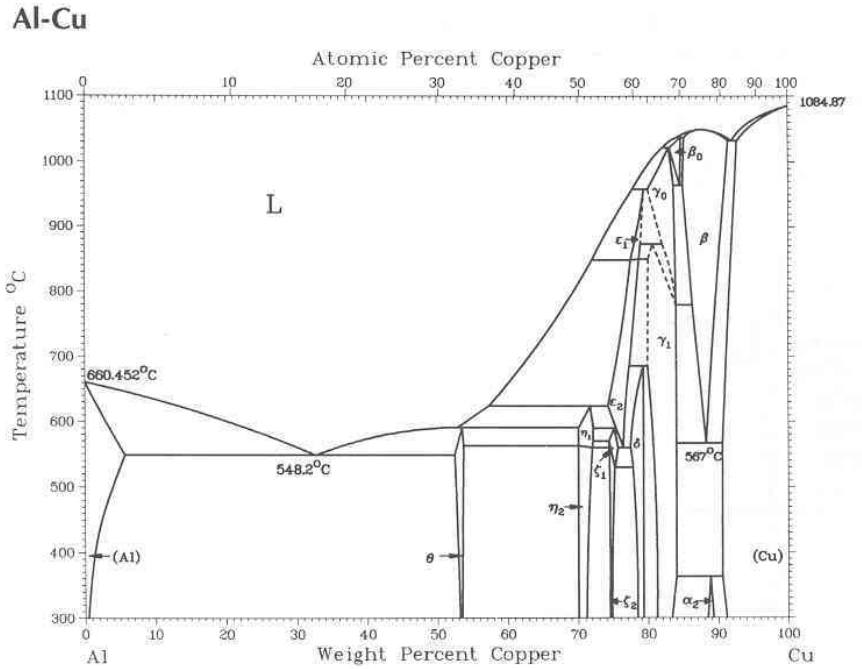


Reference : J.L. Murray, *Alloy Phase Diagrams*, ASM Handbook, (Ed. Hugh Baker), Vol. 3, pg-2.44, 1997, ASM International, Materials Park, OH

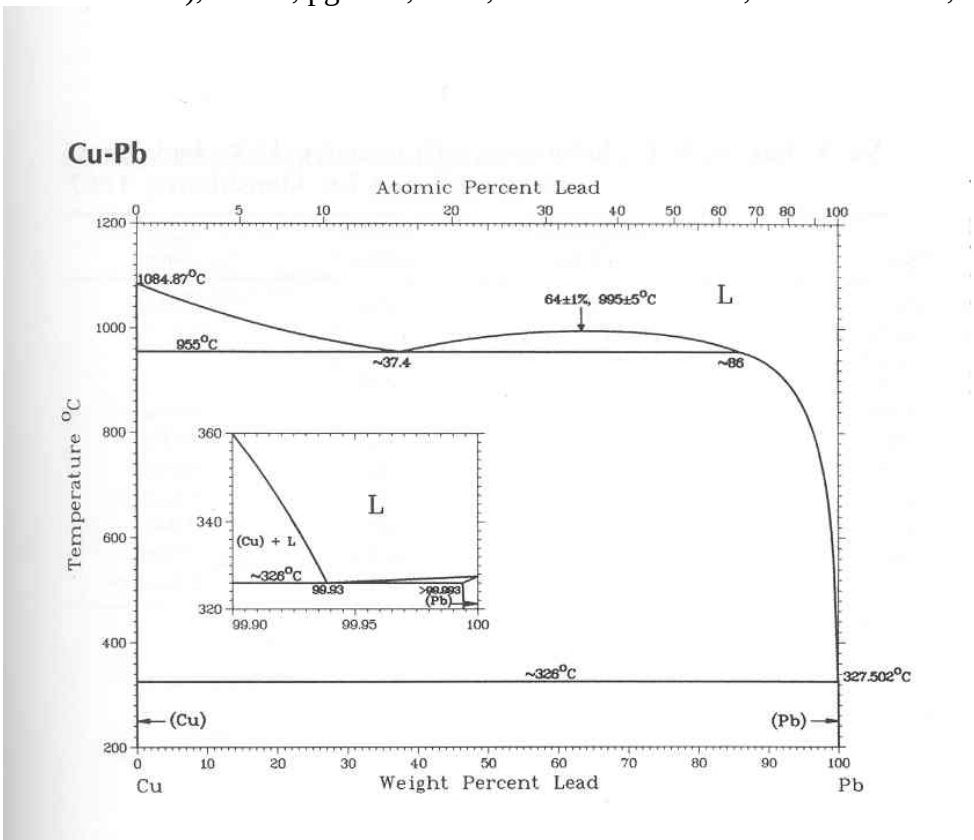


Reference : D.J. Chakarbarti and D.E. Laughlin, *Alloy Phase Diagrams*, ASM Handbook, (Ed. Hugh Baker), Vol. 3, pg-2.175, 1997, ASM International, Materials Park, OH

Cu

Copper

Copper, syn

Rad.: CuKa1λ: 1.5405 Filter: Ni Beta d-sp:

Cut off: Int.: Diffract. I/Icor.:

Ref: Swanson, Tatge, I, 15 (1953)

Sys.: Cubic S.G.: Fm$\bar{3}$m (225)

a: 3.6150 b: c: A: C:

α: β: γ: Z: 4 mp: 1083

Ref: Ibid.

Dx: 8.935 Dm: 8.950 SS/FOM: $F_8$ = 89(.0112, 8 )

Color: Red

Pattern taken at 26 C. Sample from metallurgical laboratory of NBS, Gaithersburg, Maryland, USA. CAS #: 7440-50-8. It had been heated in an H2 atmosphere at 300 C. Impurities from 0.001-0.01%, Ag, Al, Bi, Fe, Si, Zn. Measured density and color from Dana's System of Mineralogy, 7th Ed., I 99. Cu type. PSC: cF4. See ICSD 64699 (PDF 85-1326). Opaque mineral optical data on specimen from unspecified locality, R3R%=60.65, Disp.=Std. VHN100=96-104, Mwt: 63.55. Volume[CD]: 47.24.

| 2θ | Int | h | k | l |
|---|---|---|---|---|
| 43.297 | 100 | 1 | 1 | 1 |
| 50.433 | 46 | 2 | 0 | 0 |
| 74.130 | 20 | 2 | 2 | 0 |
| 89.931 | 17 | 3 | 1 | 1 |
| 95.139 | 5 | 2 | 2 | 2 |
| 116.919 | 3 | 4 | 0 | 0 |
| 136.507 | 9 | 3 | 3 | 1 |
| 144.714 | 8 | 4 | 2 | 0 |

Al2O3

Aluminum Oxide

Corundum, syn

Rad.: CuKa1λ: 1.540562 Filter: d-sp: Diff.

Cut off: 4.4 Int.: Diffract. I/Icor.:

Ref: Huang, T et al., 33, 295 (1990)

Sys.: Rhombohedral S.G.: $R\bar{3}c$ (167)

a: 4.7587(1) b: c: 12.9929(3) A: C: 2.7303

α: β: γ: Z: 6 mp:

Ref: Ibid.

Dx: 3.987 Dm: SS/FOM: $F_{25}$ = 357(.0028, 25 )

εα: 1.7604 ηωβ: 1.7686 εγ: Sign:- 2V:

Ref: Ibid.

| 2θ | Int | h | k | l |
|---|---|---|---|---|
| 25.578 | 45 | 0 | 1 | 2 |
| 35.152 | 100 | 1 | 0 | 4 |
| 37.776 | 21 | 1 | 1 | 0 |
| 41.675 | 2 | 0 | 0 | 6 |
| 43.355 | 66 | 1 | 1 | 3 |
| 46.175 | 1 | 2 | 0 | 2 |
| 52.549 | 34 | 0 | 2 | 4 |
| 57.496 | 89 | 1 | 1 | 6 |
| 59.739 | 1 | 2 | 1 | 1 |
| 61.117 | 2 | 1 | 2 | 2 |
| 61.298 | 14 | 0 | 1 | 8 |
| 66.519 | 23 | 2 | 1 | 4 |
| 68.212 | 27 | 3 | 0 | 0 |
| 70.418 | 1 | 1 | 2 | 5 |
| 74.297 | 2 | 2 | 0 | 8 |
| 76.869 | 29 | 1 | 0 | 10 |
| 77.224 | 12 | 1 | 1 | 9 |
| 80.419 | 1 | 2 | 1 | 7 |
| 80.698 | 2 | 2 | 2 | 0 |
| 83.215 | 1 | 3 | 0 | 6 |
| 84.356 | 3 | 2 | 2 | 3 |
| 85.140 | <1 | 1 | 3 | 1 |
| 86.360 | 2 | 3 | 1 | 2 |
| 86.501 | 3 | 1 | 2 | 8 |
| 88.994 | 9 | 0 | 2 | 10 |

The sample is an alumina plate as received from ICDD.
Unit cell computed from dobs. Al2 O3 type. PSC: hR10.
Mwt: 101.96. Volume[CD]: 254.81.

Pb

Lead

Lead, syn

Rad.: CuKa1λ: 1.54056 Filter: Ni Beta d-sp:

Cut off: Int.: Diffract. I/Icor.:

Ref: Swanson, Tatge, I, 34 (1953)

Sys.: Cubic S.G.: $Fm\bar{3}m$ (225)

a: 4.9506 b: c: A: C:

α: β: γ: Z: 4 mp:

Ref: Ibid.

Dx: 11.343 Dm: 11.365 SS/FOM: $F_{13}$ = 68(.0148, 13 )

Color: Light gray metallic
Pattern taken at 26 C. Sample obtained from American Smelting and Refining Company. CAS #: 7439-92-1. It was annealed for 1 hour and 180 C in petrolatum.
Spectrographic analysis shows faint traces of Bi and Mg.
Purity >99.999%. Cu type. PSC: cF4. Mwt: 207.20.
Volume[CD]: 121.33.

| 2θ | Int | h | k | l |
|---|---|---|---|---|
| 31.305 | 100 | 1 | 1 | 1 |
| 36.266 | 50 | 2 | 0 | 0 |
| 52.228 | 31 | 2 | 2 | 0 |
| 62.119 | 32 | 3 | 1 | 1 |
| 65.236 | 9 | 2 | 2 | 2 |
| 76.954 | 2 | 4 | 0 | 0 |
| 85.394 | 10 | 3 | 3 | 1 |
| 88.196 | 7 | 4 | 2 | 0 |
| 99.331 | 6 | 4 | 2 | 2 |
| 107.920 | 5 | 5 | 1 | 1 |
| 123.313 | 1 | 4 | 4 | 0 |
| 133.968 | 9 | 5 | 3 | 1 |
| 137.993 | 4 | 6 | 0 | 0 |